

REPORT DOCUMENTATION PA

AFRL-SR-BL-TR-98-

PD
4-0188

Public reporting burden for this collection of information is estimated to average 1 hour per review, gathering and maintaining the data needed, and completing and reviewing the collection of information, including suggestions for reducing this burden, to Washington Headquarters, Davis Highway, Suite 1204, Arlington, VA 22202-4302, and to the Office of Management and Budget, Paperwork Project, Washington, DC 20503.

0544

existing data sources,
other aspects of this
series, 1215 Jefferson
20503.

1. AGENCY USE ONLY (Leave blank)		2. REPORT DATE 30 Jul 97		3. REPORT TYPE AND DATES COVERED FINAL REPORT 01 Jun 93 - 31 May 97	
4. TITLE AND SUBTITLE (AASERT-92) MBE Growth and Characterization of GaN/AlN Structures Under Hydrostatic Pressure				5. FUNDING NUMBERS 61103D 3484/TS	
6. AUTHOR(S) Professor Hauenstein					
7. PERFORMING ORGANIZATION NAME(S) AND ADDRESS(ES) Department of Physics Oklahoma State University Stillwater, OK 74078				8. PERFORMING ORGANIZATION REPORT NUMBER	
9. SPONSORING / MONITORING AGENCY NAME(S) AND ADDRESS(ES) AFOSR/NE 110 Duncan Avenue Suite B115 Bolling AFB DC 20332-8050				10. SPONSORING / MONITORING AGENCY REPORT NUMBER F49620-93-1-0389	
11. SUPPLEMENTARY NOTES					
12a. DISTRIBUTION / AVAILABILITY STATEMENT APPROVED FOR PUBLIC RELEASE: DISTRIBUTION UNLIMITED					
13. ABSTRACT (Maximum 200 words) We present the results of a series of studies on the optical properties of GaN and AlGaIn/GaN heterostructures using a variety of spectroscopic techniques. Strain effects were found to have a strong influence in determining the energies of excitonic transitions. The observations of spectral features associated with the transitions involving the ground and excited excitation states make it possible to directly estimate binding energy for the excitations in GaN. Optical pumping experiments were performed on AlGaIn/GaN separate confinement heterostructures (SCH) grown on sapphire by MBE and SiC by MOCVD. the threshold pumping powers were found to be an order of magnitude lower than that for regular GaN epilayers. Nonlinear four-wave-mixing experiments were carried out in both femtosecond and picosecond regimes to study the intensity and time response of scattering efficiency, as well as the pump-induced nonlinear refractive index change.					
14. SUBJECT TERMS				15. NUMBER OF PAGES	
				16. PRICE CODE	
17. SECURITY CLASSIFICATION OF REPORT UNCLASSIFIED		18. SECURITY CLASSIFICATION OF THIS PAGE UNCLASSIFIED		19. SECURITY CLASSIFICATION OF ABSTRACT UNCLASSIFIED	
20. LIMITATION OF ABSTRACT					

19980730 142

FINAL REPORT

Program Director:

Dr. Mike Prairie

**Project Title:
(AASERT)**

**MBE Growth & Characterization
of GaN/AlN Structures Under
Hydrostatic Pressure**

Contract No:

F49620-93-1-0389

Principal Investigator:

**Dr. R.J. Hauenstein
Dept. of Physics
Oklahoma State University
Stillwater, OK 74078
405-744-5812**

Co-Principal Investigator:

**Dr. J.J. Song
Dept. of Physics & Center for
Laser & Photonics Research
Oklahoma State University
Stillwater, OK 74078
405-744-6575**

Reporting Period

6/1/93 - 5/31/97

Reporting Date:

7/30/97

DTIC QUALITY INSPECTED 1

DEGREES COMPLETED

John M. Hays

Department of Physics, Oklahoma State University

Ph.D. Thesis:

Linear and Nonlinear Spectroscopy of Selected Compound Bulk and Quantum-Confined Structures

Mark L. O'Steen

Department of Physics, Oklahoma State University

Master's Thesis:

X-Ray Diffraction Characterization of Epitaxial Thin Films

PUBLICATIONS

"Optical Properties and Lasing in GaN", in Physics and Applications of Group III Nitrides Semiconductor Compounds", J. J. Song and W. Shan; B. Gil, Ed. (Oxford University Press, London) 1997 (in press). [Invited Review Book Chapter]

"Correlation of Biaxial Strains, Bound Exciton Energies, and Defect Microstructures in GaN Films Grown on AlN/6H-SiC (0001) Substrates", W.G. Perry, T. Zheleva, M.D. Bremser, R.F. Davis, W. Shan, and J.J. Song, J. Electr. Mats. **26**, 224 (1997).

"Linear and Nonlinear Optical Investigations of GaN and AlGaIn/GaN Heterostructures", J.J. Song, A.J. Fischer, W. Shan, B. Goldenberg, and G.E. Bulman, Inst. Phys. Conf. Ser. **155**, 355 (1997).

"Binding Energy for the Intrinsic Excitons in Wurtzite GaN", W. Shan, B.D. Little, A.J. Fischer, J.J. Song, B. Goldenberg, W.G. Perry, M.D. Bremser, and R.F. Davis, Phys. Rev. B **54**, 16369, (1996).

"Optical Transitions in $\text{In}_x\text{Ga}_{1-x}\text{N}$ Alloys Grown by Metalorganic Chemical Vapor Deposition", W. Shan, B. Little, J.J. Song, Z.C. Feng, M. Schurman, and R.A. Stall, Appl. Phys. Lett. **69**, 3315 (1996).

"Optical Studies of GaN and GaN/AlGaIn Heterostructures on SiC Substrates," W. Shan, A. J. Fischer, J. J. Song, G. E. Bulman, H. S. Hong, M. T. Leonard, W. G. Perry, M. D. Bremser, and R. f. Davis, Appl. Phys. Lett. **69**, 740 (1996).

"Optical Properties of Mg-GaN, GaN/AlGaIn SCH Structures, and GaN on ZnO Substrates", H. Morkoc, W. Kim, O. Aktas, A. Salvador, D.C. Reynolds, M. Smith, G.D. Chen, J.Y. Lin, H.X. Jiang, T.J. Schmidt, X.H. Yang, W. Shan, J.J. Song, B. Goldenberg, C.W. Litton, and K. Evans, Mat. Res. Soc. Symp. Proc. **395**, 527 (1996).

"Growth of GaN by Gas-Source Molecular Beam Epitaxy by Ammonia and by Plasma Generated Nitrogen Radicals", W.S. Wong, N.Y. Li, H.K. Dong, F. Deng, S.S. Lau, C.W. Tu, J. Hays, S. Bidnyk, and J.J. Song, J. of Crystal Growth **164**, 159 (1996).

"Molecular Beam Epitaxial Growth of Eu-doped CaF_2 and BaF_2 on Si", X.M. Fang, T. Chatterjee, P.J. McCann, W.K. Liu, M.B. Santos, W. Shan, and J.J. Song, J. Vac. Sci. Technol. B **14**, 2267 (1996).

"Optical Studies of Epitaxial GaN Based Materials," J. J. Song, W. Shan, T. J. Schmidt, X. H. Yang, A. J. Fischer, S. J. Hwang, and B. Taheri, SPIE Proc., **2693**, 86 (1996).

"Picosecond Four-Wave Mixing in GaN Epilayers at 532 nm," B. Taheri, J. Hays, J. J. Song, and B. Goldenberg, *Appl. Phys. Lett.* **68**, 587 (1996).

"Room-Temperature Stimulated Emission in GaN/AlGa_N Separate Confinement Heterostructures Grown by Molecular Beam Epitaxy," T. J. Schmidt, X. H. Yang, W. Shan, and J. J. Song, *Appl. Phys. Lett.* **68**, 1820 (1996).

"Intensity Scan Determination of Two Photon Absorption and Nonlinear Refraction of C₆₀ in Toulene", B. Taheri, D. Appling, B. Jassemnejad, R. Powell, and J.J. Song, *Appl. Phys. Lett.* **68**, 1317 (1996).

"Spectroscopic Studies of GaN Grown by Metalorganic Chemical Vapor Deposition", W. Shan, J.J. Song, T.J. Schmidt, X.H. Yang, and B. Goldenberg, to be published in *International Journal of Solid State Electronics (TWN'95 Proceedings)* (1996).

"Optical Properties of Wurtzite GaN Grown by Low-Pressure Metalorganic Chemical-Vapor Deposition", W. Shan, T. Schmidt, X.H. Yang, J.J. Song, and B. Goldenberg, *J. Appl. Phys.* **79**, 3691 (1996).

"Recent Progress in Optical Studies of Wurtzite GaN Grown by Metalorganic Chemical Vapor Depositon", W. Shan, T. Schmidt, X.H. Yang, J.J. Song, and B. Goldenberg, *Inst. Phys. Conf. Ser.* **145**, 1151 (1996).

"Strain Effects on Excitonic Transitions in GaN: Deformation Potentials," W. Shan, R. J. Hauenstein, A. J. Fischer, J. J. Song, W. G. Perry, M. D. Bremser, R. F. Davis, and B. Goldenberg, *Phys. Rev. B* **54**, 13460 (1996).

"Going Beyond the Mean-Filed Approximations of Alloys and Alloy Superlattices: A Few Puzzles Solved?" D.S. Kim, H.S. Ko, Y.S. Lim, Y.M. Kim, J.S. lee, S.J. Rhee, W.S. Kim, S.C. Hong, Y.H. Yee, J.S. Khim, J.M. Jung, S. Huhr, J.H. Lee, J.S. Chang, B.D. Choe, J.C. Woo, P.H. Song, H.J. Choi, S.H. Jhi, J. Ihm, E.J. Shin, D. Kim, D.H. Woo, K.N. Kang, J.J. Song, *J. Opt. Soc. Am. B* **13**, 1210 (1996).

"Spatial and Dynamical Properties of Optical Phonons in Al_x/Ga_{1-x}As and GaAs/Al_x/Ga_{1-x}As Supperlattices: Beyond the Mean Field Approach", D.S. Kim, P.H. Song, S.H. Jhi, Y.S. Lim, E.J. Shin, Y.H. Yee, J.S. Khim, J. Ihm, J.H. Lee, J.S. Chang, D.H. Woo, K.N. Kang, D. Kim, J.J. Song, *Physica B* **219**, 684 (1996).

"Dynamics of Photoexcited Carriers in GaN", J.J. Song, W. Shan, B. Goldenberg, G.E. Bulman, and J.A. Edmond, to be published in *International Journal of Solid State Electronics (TWN'95 Proceedings)* (1996).

"Microscopic Processes during Electron Cyclotron Resonance Microwave Nitrogen Plasma-Assisted Molecular Beam Epitaxial Growth of GaN/GaAs Heterostructures: Experiments and Kinetic Modeling," Z. Z. Bandic, R. J. Hauenstein, M. L. O'Steen, and T. C. McGill, *J. Vac. Sci. Technol. A*, **14**, 2948 (1996).

"Atomic-Scale Structure and Electronic Properties of GaN/GaAs Superlattices", R. S. Goldman, B. G. Briner, R. M. Feenstra, M. L. O'Steen, and R. F. Hauenstein, *Appl. Phys. Lett.*, **69**, 3698 (1996).

"Kinetic Modeling of Microscopic Processes during Electron Cyclotron Resonance Microwave Plasma-Assisted Molecular Beam Epitaxial Growth of GaN/GaAs Heterostructures," Z. Z. Bandic, R. J. Hauenstein, M. L. O'Steen, and T. C. McGill, *Appl. Phys. Lett.* **68**, 1510 (1996).

"Reflection High Energy Electron Diffraction Study of Nitrogen Plasma Interactions with a GaAs (100) Surface," R. J. Hauenstein, D. A. Collins, X. P. Cai, M. L. O'Steen, and T. C. McGill, *Appl. Phys. Lett.* **66**, 2861 (1995).

"Schottky-Based Band Lineups for Refractory Semiconductors," M. W. Wang, J. O. McCaldin, J. F. Swenberg, T. C. McGill, and R. J. Hauenstein, *Appl. Phys. Lett.* **66**, 1974 (1995).

"Anion Exchange Reactions and Initial GaN Epitaxial Layer Formation under Nitrogen Plasma Exposure of a GaAs Surface," R. J. Hauenstein, D. A. Collins, M. L. O'Steen, Z. Bandic, S. J. Hwang, and T. C. McGill, *Mater. Res. Soc. Symp. Proc.* **388**, 259 (1995).

"Time-resolved Exciton Luminescence in GaN Grown by Metalorganic Chemical Vapor Deposition", W. Shan, X.C. Xie, J.J. Song, and B. Goldenberg, *Appl. Phys. Lett.* **67**, 2512 (1995).

"Temperature Dependence of Interband Transitions in GaN Grown by Metalorganic Chemical Vapor Deposition", W. Shan, T.J. Schmidt, X.H. Yang, S.A. Hwang, J.J. Song and B. Goldenberg, *Appl. Phys. Lett.* **66**, 985, (1995).

"Above Room Temperature Near Ultraviolet Lasing From an Optically Pumped GaN Film Grown on Sapphire", X.H. Yang, T.J. Schmidt, W. Shan, J.J. Song, and B. Goldenberg, *Appl. Phys. Lett.* **66**, 1, (1995).

"Pressure-dependent Photoluminescence Study of Wurtzite GaN", W. Shan, T.J. Schmidt, R.J. Hauenstein, J.J. Song and B. Goldenberg, *Appl. Phys. Lett.* **66**, 3492, (1995).

"Hot-Phonon Generation in GaAs/Al_xGa_{1-x}As Superlattices: Observations and Implications on the Coherence Length of LO Phonons", D.S. Kim, A. Bouchalkha, J.M. Jacob, J.J. Song, J.F. Klem, H.Hou, C.W. Tu, and H. Morkoc, Phys. Rev. B **51**, 5449 (1995).

"Eu-Doped CaF₂ Grown on Si(100) Substrates by Molecular Beam Epitaxy", X.M. Fang, T. Chatterjee, P.J. McCann, W.K. Liu, M.B. Santos, W. Shan, and J.J. Song, Appl. Phys. Lett. **67**, 1891 (1995)

Correlation of Biaxial Strains, Bound Exciton Energies, and Defect Microstructures in GaN Films Grown on AlN/6H-SiC(0001) Substrates

WILLIAM G. PERRY, T. ZHELEVA, M.D. BREMSER, and R.F. DAVIS

Department of Materials Science, North Carolina State University, Raleigh, NC 27695

W. SHAN and J.J. SONG

Center for Laser Research, Oklahoma State University, Stillwater, OK 74078

Biaxial strains resulting from mismatches in thermal expansion coefficients and lattice parameters in 22 GaN films grown on AlN buffer layers previously deposited on vicinal and on-axis 6H-SiC(0001) substrates were measured via changes in the c-axis lattice parameter. A Poisson's ratio of $\nu = 0.18$ was calculated. The bound exciton energy (E_{bx}) was a linear function of these strains. The shift in E_{bx} with film stress was 23 meV/GPa. Threading dislocations densities of $\sim 10^{10}/\text{cm}^2$ and $\sim 10^8/\text{cm}^2$ were determined for GaN films grown on vicinal and on-axis SiC, respectively. A 0.9% residual compressive strain at the GaN/AlN interface was observed by high resolution transmission electron microscopy (HRTEM).

Key words: Biaxial strain, donor bound excitons, gallium nitride (GaN), organometallic vapor phase epitaxy (OMVPE), photoluminescence (PL), Poisson's ratio, transmission electron microscopy (TEM), x-ray diffraction

INTRODUCTION

Mismatches in the lattice parameters (a and c) and the coefficients of thermal expansion (α) exist between heteroepitaxial GaN films and all of the presently used substrates. These mismatches result in interfacial biaxial strain which leads to misfit dislocations and associated threading defects that degrade film quality. Measurement and analysis of these strains have been the goals of the research reported herein.

The most common substrate used for GaN film growth is sapphire (0001). Buffer layers of AlN and GaN have been used to improve GaN film quality, although significant mismatches in the lattice parameters between these layers and sapphire exist ($\Delta a/a_0 \approx 13.6$ and 16.1%, respectively, [see Table I]). The resulting lattice mismatch strain is compressive for both GaN on AlN and GaN on sapphire and alters the values of both a (decreases) and c (increases) of the films.^{1,2} Hiramatsu et al.³ have assumed this strain to be relieved after several nanometers of growth ac-

cording to the critical thickness theory. The primary relief mechanism is the formation of dislocations at the film/substrate interface during film growth. Upon cooling, the difference in thermal expansion coefficients ($\alpha_{\text{sapphire}} > \alpha_{\text{AlN}} > \alpha_{\text{GaN}}$) results in additional compressive stresses which are often assumed^{1,4} to be wholly responsible for the observed compressive strain. However, high resolution transmission electron microscopy (HRTEM) analysis of the GaN/AlN interface on sapphire⁵ suggests that the lattice mismatch stress in GaN is not fully relieved. This residual stress was assumed⁵ to be accommodated elastically and to give rise to biaxial stresses in the GaN films. However, it is difficult to substantiate this through other characterization techniques since both thermal and lattice mismatch stresses are compressive, and there is a marked variation in published thermal expansion coefficients that could be used in calculations. Moreover, none of these coefficients applies to temperatures above 900°C, where most GaN thin films are deposited.

Recent work^{6,7} has used a SiC(0001) substrate/AlN(0001) buffer layer combination. The lattice mismatch strains at both the GaN/AlN and AlN/SiC

(Received October 18, 1996; accepted November 4, 1996)

Table I. Comparison of III-Nitride Material Properties with 6H-SiC and Sapphire^a

Material	Lattice Parameter at RT(Å)	In-Plane Mismatch with GaN (%)	Coefficients of Thermal Expansion 10 ⁻⁶ /K
GaN	$a = 3.1891^b$ $c = 5.1855^b$	—	5.59; 3.1, 6.2 ^d 7.75 ^c ; 2.8, 6.1 ^d
AlN	$a = 3.112$ $c = 4.982$	2.5	4.15 5.27
6H-SiC	$a = 3.08$ $c = 15.12$	3.5	4.2; 3.2, 4.2 ^d 4.68; 3.2, 4.0 ^d
Sapphire	$a = 4.758$ $c = 12.99$	16.1	7.5; 4.3, 9.2 ^d 8.5; 3.9, 9.3 ^d

^aLandolt-Börnstein, ed. O. Madelung (New York: Springer, 1982), Vol. 17.

^bC.M. Balkas, C. Basceri and R.F. Davis, *Powder Diffraction* 10, 266 (1995).

^cProperties of Group III Nitrides, ed. J.H. Edgar (London: INSPEC, 1994)

^dM. Leszczynski, T. Suski, P. Perlin, H. Teisseyre, I. Grzegory, M. Bockowski, J. Jun, S. Porowski and J. Major, *J. Phys. D: Appl. Phys.* 28, A149 (1995), For T = 300–350 and 700–750K, respectively.

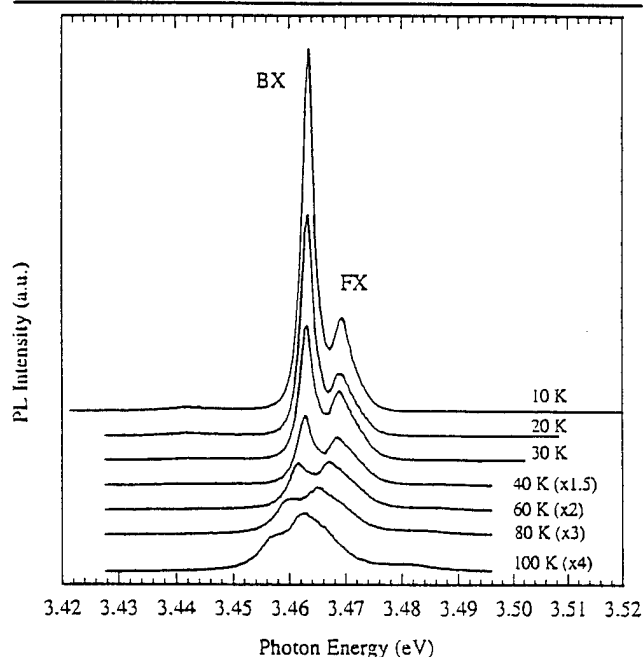


Fig. 1. PL of a 3.7 μm thick GaN film on an AlN buffer layer previously grown on a SiC(0001) wafer at 10, 20, 30, 40, 60, 80, and 100K. The peaks labeled BX and FX are due to the recombination of bound and free excitons, respectively.

interfaces are compressive ($a_{\text{GaN}} > a_{\text{AlN}} > a_{\text{SiC}}$), but the reduced lattice mismatch between AlN and SiC (~1%) compared to AlN and sapphire leads to improved GaN film quality. This mismatch is expected to be at least partially relieved by the formation of misfit dislocations, as the calculated critical thickness for AlN(0001) on SiC(0001) is only 47 Å.⁸ The differences in thermal expansion coefficients are opposite in sign ($\alpha_{\text{GaN}} > \alpha_{\text{SiC}} \approx \alpha_{\text{AlN}}$) to that for GaN on sapphire and result in a biaxial tensile stress contribution. Hence, the two

main stresses in the GaN/AlN/SiC heteroepitaxial system are opposite in sign, which offer the potential to substantiate if residual lattice mismatch stress exists through lattice parameter measurements and other techniques. Li and Ni⁹ measured the lattice parameters for thick GaN films grown directly on both SiC(0001) and sapphire(0001). They observed that the film on SiC was in tension while that on sapphire was in compression. They attributed this variation in strain to the difference in thermal expansion coefficients between the two substrates.

One consequence of film strain is a shift in the band-gap energy (E_g).¹⁰ The biaxial strain can be viewed as an isotropic cubic component together with a uniaxial component along the c -axis of the GaN film.¹¹ The cubic, or hydrostatic term influences the band-gap directly, while the uniaxial component introduces subtle shifts between individual lines in the spectrum. However, it is difficult to measure E_g directly in GaN due the strong excitonic features at the absorption edge.¹² Changes in E_g may be detected by shifts in these excitonic features using low temperature photoluminescence (PL). At $T \leq 4.2\text{K}$, the PL of high-quality GaN reveals intense near-band edge emission attributed to the recombination of both free excitons and/or excitons bound to shallow neutral donors.^{4,6,7,12,13} The bound exciton feature is often the dominant feature due to the nature of GaN, which is always n -type for undoped films. The identity of the shallow donor(s) is unknown, although recent work suggests that both native defects and extrinsic impurities are possibilities.^{14–16} Amano et al.¹ observed a shift of the bound exciton energy (E_{BX}) to higher energies that was attributed to biaxial compressive strain for GaN films deposited on sapphire(0001). Reported E_{BX} values range from 3.467 to 3.494 eV for GaN on sapphire,^{12,13,17,18} and from 3.463 to 3.472 for GaN on SiC.^{4,6,7,18,19} The disparity between the two energy ranges has been attributed to the difference in thermal expansion coefficients of the two substrates.^{4,18}

In this research, the relationship between E_{BX} and lattice parameters (and hence strain) was determined for 22 GaN films grown on AlN buffer layers previously deposited on 6H-SiC(0001). A value of E_{BX} for relaxed GaN was determined. Poisson's ratio was calculated from lattice parameter measurements and used to determine the shift of E_{BX} with biaxial stress (σ_x). The roles of the AlN buffer layer and the tilt of the SiC substrate on film stress and the associated PL spectra were also determined. Transmission electron microscopy (TEM) was employed to compare and contrast the crystal structure of GaN films grown on the vicinal (off-axis) and on-axis SiC wafers. The GaN/AlN interface was analyzed via high resolution (HR)TEM to determine if any residual lattice mismatch stress occurred.

EXPERIMENTAL PROCEDURES

The GaN/AlN films were grown in an organometallic vapor phase epitaxial (OMVPE) system described previously^{6,7} on both on-axis and vicinal (2–4° off-axis)

6H-SiC(0001) substrates. The GaN films ranged in thickness from 0.3–3.7 μm and were grown at temperatures ranging from 950–1100°C. The AlN buffer layer for each sample was 1000Å thick and grown at 1100°C. All of the GaN films were unintentionally doped, with n-type carrier concentrations ranging from $<1 \times 10^{16}$ – $1 \times 10^{17}/\text{cm}^3$.

Absolute lattice constants values were measured using a Philips X'Pert MRD x-ray diffractometer in the triple-axis mode. The technique used was originally proposed by Fewster²⁰ and is comparable to, and in many ways more accurate than, the commonly used "Bond" method. The high resolution of the triple-bounce analyzer crystal and the steps taken to eliminate inaccuracies due to the 2θ zero error and sample centering account for this. The data were collected using 2θ - ω scans, with corrections made for refraction. The accuracy of the lattice parameters measured using this system was 0.0002Å. The c-axis lattice parameter (c) was measured using the (002) reflection. Measurements of the a-axis lattice parameter (a) were made using both the (002) and (015) reflections; however, the low count rate for the asymmetric reflections limited the number of samples that could be measured accurately.

Photoluminescence measurements of the GaN films on SiC were made at 4.2K using a He-Cd laser ($\lambda = 325$ nm) as the excitation source, unless otherwise noted. TEM studies were performed using a TOPCON EM-002B HRTEM, operated at 200 kV with a point-to-point resolution 0.18 nm. The cross-sectional samples in the $[11\bar{2}0]$ orientation were prepared by conventional techniques using mechanical grinding and polishing, and Ar⁺ ion-milling at a low angle in the final stage.^{21,22}

RESULTS AND DISCUSSION

Low temperature PL of the GaN(0001) films grown in this research exhibited strong near-band-edge emission due to the recombination of both free and donor-bound excitons, as shown in the spectrum from a 3.7 μm thick film in Fig. 1. The emission from the donor-bound exciton (BX) decreased in intensity much faster than that from the free excitons (FX) as the temperature was increased from 10 to 100K. This behavior is due to the small localization energy (E_b) of the donor-bound excitons compared to the binding energy of the free excitons (E_x). From this data, E_b was estimated to be 5.9 meV, which agrees favorably with earlier measurements.^{7,13} Recent work on this and other samples measured E_b to be 21 ± 1 meV for the A- and B- free excitons,²³ although earlier work suggested a higher (26 meV) value.¹³ The PL of the GaN films in this study was dominated by the bound exciton emission, and its dependence on lattice strain as manifest in changes in lattice parameters will be described below.

The bound exciton energies (E_{BX}) determined at 4.2K as a function of the c-axis lattice parameter (c) for 22 GaN films on SiC are shown in Fig. 2. The lattice parameter measurements were performed at room

temperature. It is expected that the tensile strain in the GaN films due to thermal expansion mismatch will increase as the temperature is decreased from room temperature to 4.2K, but lattice parameter measurements are not possible at these temperatures. A linear relationship between c and E_{BX} was observed, where the bound exciton peak shifted to lower energies as c decreased. Any change in c is in response to a strain (ϵ_a) along the a-axis (a), $\Delta a/a_0$, which results from the biaxial stress produced in the plane of the film by residual stresses. Thus, a decrease in the value of c indicates that the biaxial tensile strain in the film is increasing, which causes E_g to decrease and E_{BX} to shift to lower energies.

The value of c for relaxed GaN has recently been measured to be 5.1855Å.²⁴ As shown in Fig. 2, six of the GaN films grown on SiC(0001) have values of c greater than this, which indicates they are compressively strained. This suggests that the compressive strain due to lattice mismatch has not been fully relieved by defect formation in these samples. The highest value of c observed was 5.190Å, and the bound exciton energy for this sample was 3.484 eV. The highest reported E_{BX} value previously reported for GaN grown on 6H-SiC was 3.472 eV.¹⁹ The n-type carrier concentration of this film was reported to be $1 \times 10^{18} \text{ cm}^{-3}$; thus it is possible that this value was slightly shifted to higher energies by the Burstein-Moss²⁵ effect rather than by strain. The free carrier concentration for the samples in this study was less than $1 \times 10^{17}/\text{cm}^3$; therefore, it is assumed that the shift observed in E_{BX} in this study was not due to this effect.

Values of E_{BX} can be estimated from a linear regression of the data in Fig. 2, which yielded $E_{\text{BX}} = (-14.91 + 3.545 \cdot c) \text{ eV}$, where c is in angstroms. Using this relationship, $E_{\text{BX}0}$ was predicted to be 3.469 eV for relaxed GaN. This compares favorably to reported

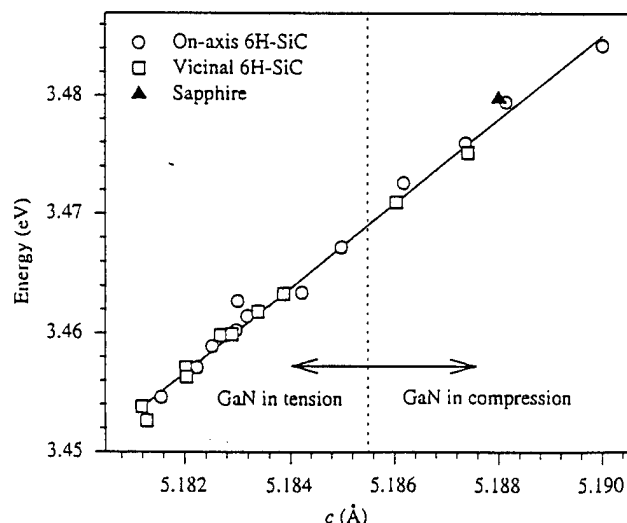


Fig. 2. Lattice constant c vs the bound exciton energy (E_{BX}) for GaN/AlN/SiC. The PL was performed at 4.2K and the lattice parameter measurements at room temperature. The dashed line indicates the relaxed value of c_0 (5.1855Å) for GaN. A data point for GaN grown on sapphire is included.

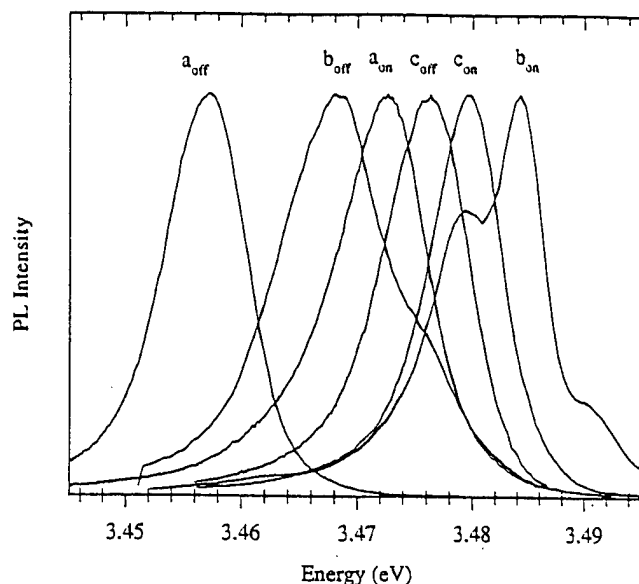


Fig. 3. Lattice constant a vs c for GaN/AIn/SiC. The lattice parameter measurements were performed at room temperature. The Poisson's ratio calculated using this data was $\nu = 0.18 \pm .02$.

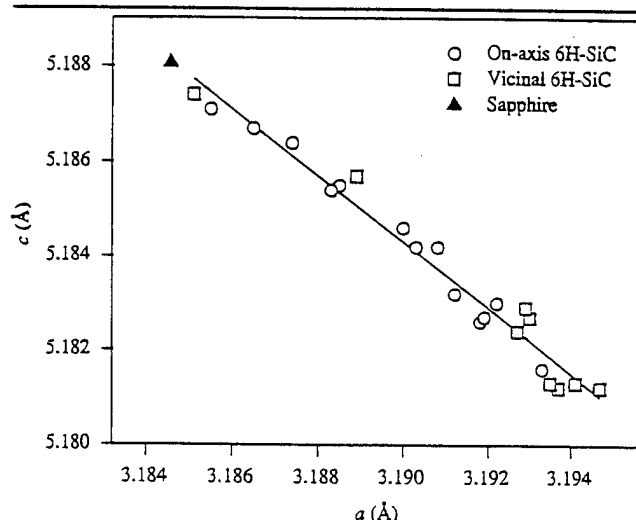


Fig. 4. PL at 4.2K of three sets of GaN films (a, b, c) grown concurrently on vicinal (off-axis) and on-axis SiC. The off-axis tilt of sample c is $\sim 2^\circ$, which is lower than a tilt of $3-4^\circ$ that is typical for the vicinal wafers.

values of 3.467,²⁶ 3.469,²⁷ and 3.472 eV.²⁸ The marked dependence of the values of E_{BX} on c indicated that the wide range of energy values reported for the donor-bound exciton in the literature are due primarily to different amounts of strain present in the films. For GaN on sapphire, typical E_{BX} values are between 3.467–3.494 eV, which are predominantly in the energy range indicated for films under compression in this study. Included in Fig. 2 is a data point for a 4.7 μm GaN film grown on sapphire, which indicated that E_{BX} can be predicted for GaN grown on any substrate using values of c and the relationship determined in this study.

For biaxially strained wurtzitic films, the relationship between the lattice parameters c and a is given by the strain ratio²⁹

$$\epsilon_c/\epsilon_a = (\Delta c/c_0)/(\Delta a/a_0) = -2\nu/(1-\nu), \quad (1)$$

where ν is Poisson's ratio and a_0 and c_0 are the relaxed lattice parameters. For GaN, values of ν which range from 0.372³⁰ to 0.20³¹ have been calculated using anisotropic elastic constants. A recent³² survey of x-ray data available in the literature determined $\nu = 0.23 \pm 0.06$ for samples dominated by biaxial strain. In this study, a and c were measured simultaneously for 22 GaN films on 6H-SiC, including 10 of those shown in Fig. 2. The relationship between a and c is displayed in Fig. 3. Also included is a data point for the 4.2 μm GaN film on sapphire included in Fig. 2. An average strain ratio of $\epsilon_c/\epsilon_a = -0.455$ was determined for this data set using values of 3.1891 and 5.1855 Å for a_0 and c_0 , respectively,²⁸ which resulted in a Poisson's ratio of $\nu = 0.18$. Further analysis showed that remarkably different strain ratios of $\epsilon_c/\epsilon_a = -0.33$, -0.47 , and -0.59 were calculated from the same data using other published values for a_0 and c_0 .^{32,33} This disparity in the strain ratios was due to individual values of c and a that were close to the different values for a_0 and c_0 which resulted in abnormal values in the nominator and/or denominator of Eq. (1) for that sample's strain ratio. A distortion of the average strain ratio for the data set resulted.

Given this wide variation in the calculated strain ratios, two methods were used to obtain a more reasonable estimation of the strain ratio and the resulting Poisson's ratio. The first eliminated those data points (4 total) that had adverse effects on the average strain ratio of the data set. An average strain ratio was then calculated using each of the four sets of published values for a_0 and c_0 .^{28,32,33} and averaged to give a strain ratio $\epsilon_c/\epsilon_a = -0.425$. The corresponding Poisson's ratio was $\nu = 0.18$. The second method fit a line to the data in Fig. 4, and then used the experimentally determined values of c to calculate values of a that fit the line. The strain ratio for each point was then calculated using values of $c_0 = 5.1850$ and $a_0 = 3.1891$, where the latter value was determined from the line fit to the data in Fig. 4. The average strain ratio using this method was $\epsilon_c/\epsilon_a = -0.446 \pm .03$, which resulted in a Poisson's ratio of $\nu = 0.18 \pm .02$. The two calculated values of Poisson's ratio were identical, and they compared favorably with values determined from x-ray data ($0.23 \pm .06$)³² and anisotropic elastic constants (0.20 ,³¹ 0.24 ,³⁴ and 0.26)³⁵.

The shift of E_{BX} as a function of the biaxial film stress ($\Delta E_{\text{BX}}/\Delta \sigma_a$) can be estimated from the data in Fig. 2 using the relationship²⁹

$$\sigma_a = Y/(1-\nu)\epsilon_a = -Y\epsilon_c/2\nu, \quad (2)$$

where Y is the Young's modulus (290 ± 20 GPa).³² The first step was to calculate $\Delta E_{\text{BX}}/\Delta \epsilon_c$ from the data in Fig. 2, where relaxed values of $E_{\text{BX}0} = 3.469$ eV and $c_0 = 5.1855$ Å were assumed. A linear regression of the data yielded $\Delta E_{\text{BX}}/\Delta \epsilon_c = 18.1$ eV. Using this expression, and the previously determined Poisson's ratio of $\nu = 0.18$, a value of $dE_{\text{BX}}/d\sigma_a = 23$ meV/GPa was calculated. This result is lower than that reported previously for hydrostatic pressure experiments (39 ³⁶ and 40 ³⁷ meV/GPa), but it compared favorably to results

for GaN films where biaxial stress was assumed $27^{32,38}$ meV/GPa). However, the similarity of the value given in Ref. 38 with that determined in this research may be a coincidence given that the authors assumed the wrong relationship between stress and strain. It should be noted that uncertainties in Poisson's ratio and Young's Modulus can have a dramatic effect on these calculations.

The role of SiC off-axis tilt on GaN film stress was investigated using films grown concurrently on vicinal and on-axis SiC(0001) wafers. Previous analysis in this laboratory of 1.4 μm GaN/AlN films deposited simultaneously on vicinal and on-axis 6H-SiC(0001) substrates showed the microstructural quality of the GaN and AlN layers on the on-axis substrate to be superior.⁷ Moreover, double crystal x-ray curve (DCXRC) measurements showed a full width at half maximum (FWHM) of 58 arc-sec for the on-axis film, compared to 151 arc-sec for the vicinal film. Plan view TEM measurements showed a lower dislocation density for the GaN film on the on-axis SiC, and the AlN buffer layer was of high microstructural quality. The bound exciton energy of the vicinal film was shifted to a lower energy relative to the on-axis film, with $\Delta E_{\text{BX}} = 3$ meV.

The PL spectra of the bound exciton emission from three separate GaN film sets grown concurrently on off- and on-axis SiC are displayed in Fig. 4, where the film thickness was $\leq 0.6 \mu\text{m}$ for all of the samples. In each case, the BX emission on the vicinal wafers was shifted to lower energies, with ΔE_{BX} as large as 17 meV. A related shift in the lattice parameter c was

observed, with Δc as great as 0.0072\AA . Thus, the GaN films grown on vicinal SiC were compressively strained compared to those grown on on-axis SiC. The disparity in E_{BX} and c values persisted as the film thickness increased. However, ΔE_{BX} decreased, and E_{BX} for both types of films shifted to energies commonly associated with GaN on 6H-SiC(0001) ($E_{\text{BX}} \leq 3.469 \text{ eV}$). It should be noted that the values of c for the underlying vicinal and on-axis 6H-SiC were identical at the AlN/SiC interface, which indicated that the phenomena discussed is not due to differences in the lattice constants of the substrates.

To understand these results, it is necessary to examine the defect microstructures of GaN films

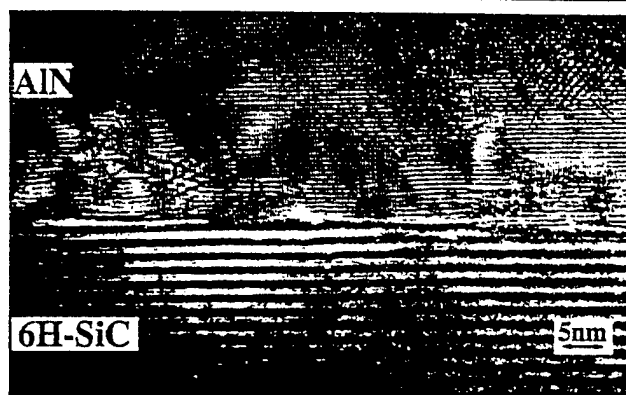


Fig. 5. HR micrograph from an AlN/6H-SiC vicinal interface reveals that the strain at the interface is due to the numerous domain boundaries (denoted by D and the arrows) formed when neighboring grains coalesce during the growth process.

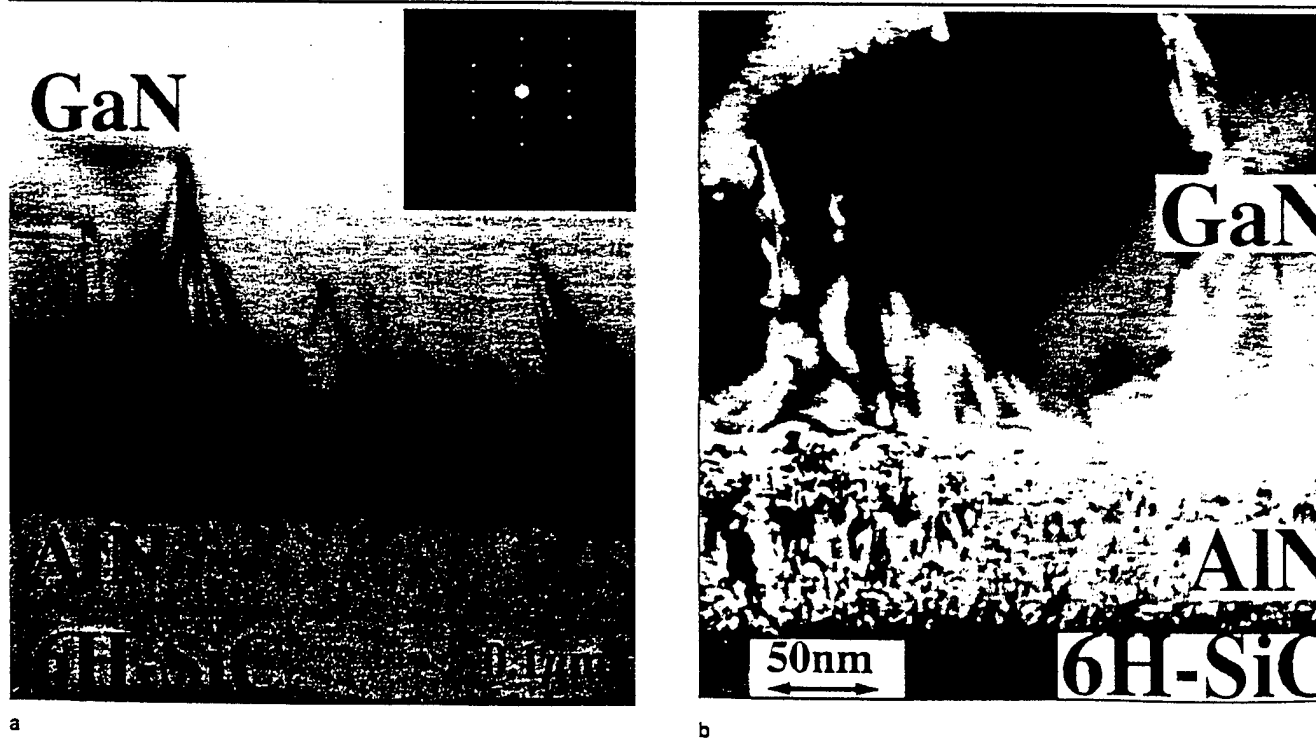


Fig. 6. Low magnification TEM micrographs of a GaN/AlN/vicinal 6H-SiC(0001) heterostructure: (a) the AlN film exhibits domain type of growth with characteristic domain boundaries. Plan view of the GaN film reveals a dislocation density of $\sim 10^{10}$ – $10^{11}/\text{cm}^2$ comprised mostly of threading dislocations and threading segments. (b) The nonuniform contrast in the AlN film is due to the overlapping stress fields at the AlN/6H-SiC and GaN/AlN interfaces from the lattice parameters and coefficients of thermal expansion.

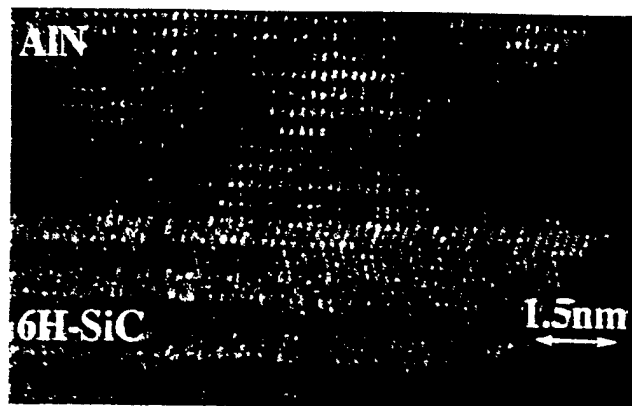


Fig. 7. HRTEM micrograph from AlN on on-axis 6H-SiC(0001). There are no domains and associated domain boundaries as observed in the off-axis films shown in Fig. 5.



Fig. 8. TEM micrograph from the GaN/AlN/on-axis 6H-SiC(0001) heterostructure in $[11\bar{2}0]$ orientation showing the considerably improved quality of the GaN/AlN and AlN/SiC interfaces relative to those achieved with the vicinal substrate (see Fig. 6a). Note also the reduction of the defect density in comparison with the structure grown on the off-axis SiC substrate.

grown on an AlN buffer on 6H-SiC(0001) substrates. The primary defects in the AlN buffer layers grown on the off-axis SiC substrates were domains and their associated domain boundaries, as shown by HRTEM in Fig. 5 and lower magnification TEM in Figs. 6a and 6b. Recent studies³⁹ show that the steps on the vicinal surface provide sites for the growth of inversion domains, which are separated by inversion domain boundaries (IDBs). These defects introduce a marked amount of strain in the AlN buffer layer grown on off-axis SiC substrate. There is also a high density of threading dislocations in the buffer layer.

By comparison, the crystal quality of AlN films grown on on-axis SiC substrate is of improved crystalline quality, as shown by HRTEM in Fig. 7 and TEM in Fig. 8. Most significantly, there is a reduced density of inversion domain boundaries due to the reduction in the density of SiC steps. The primary defects are stacking faults parallel to the AlN/SiC interface and associated partial dislocations. Threading dislocations running from the top to the bottom of the film are also present.

The crystal quality of the GaN is directly influenced by the AlN buffer. The inferior quality of the AlN

buffer layer grown on vicinal SiC results in a high dislocation density ($\sim 10^9$ – $10^{10}/\text{cm}^2$) at the interface, as determined from plan-view TEM analysis by counting the number of dislocations per unit area. The dislocation density decreases markedly about two hundred angstroms away from the GaN/AlN interface. The predominant defects are threading dislocations and threading segments that persist throughout the film. In addition, stacking faults and dislocation loops are observed close to the interface. Finally, domain boundaries that originate at the GaN/AlN interface are also visible. It should be noted though that recent work has shown that the formation of domains can also be associated with nonstoichiometry or contamination of the AlN surface.⁴⁰

The improved quality of the AlN buffer layers on the on-axis SiC carries over into the GaN, as displayed in Fig. 8. A dislocation density in the order of $\sim 10^8/\text{cm}^2$ in the GaN layer was observed in plan-view TEM near the GaN/AlN interface. Most notably there are no planar defects such as stacking faults or domain boundaries in the GaN. The dominant defect in the on-axis GaN films are edge type dislocations with burgers vectors $\mathbf{b} = 1/3\langle 11\bar{2}0 \rangle$ and $\mathbf{b} = 1/3\langle 1\bar{1}00 \rangle$. These are the misfit dislocations which form at the GaN/AlN interface. This TEM analysis, as well as that of Chien et al.⁴¹ on North Carolina State University samples, reveal that the lattice mismatch stress in GaN films grown on the on-axis SiC substrate is accommodated mostly by misfit dislocations. However, our PL, XRD, and TEM studies suggest that these defects do not provide full stress relief.

In order to further assess the residual strain in the GaN films, HRTEM studies were performed at the GaN/AlN interface of the on-axis SiC in the $[11\bar{2}0]$ orientation, as shown in Fig. 9. It can be seen that the interface is epitaxial and free of domains, threading dislocations and low angle grain boundaries. Using HRTEM, it is possible to calculate the residual strain at the interface for the planes that are perpendicular to the interface and parallel to each other. Ning et al.⁵ used this method to calculate the misfit at the GaN/sapphire interface, where they found a $\sim 1\%$ residual strain in the GaN film.

To determine the residual strain in the GaN films grown in the present research, the average lattice mismatch was calculated along the GaN/AlN interface from HRTEM micrographs in $[11\bar{2}0]$ GaN orientation, by counting the number of $(1\bar{1}00)$ GaN and AlN planes along $[1\bar{1}00]$ direction that was bounded on each end by commensurate GaN and AlN planes. The experimental mismatch was assessed to be 0.9% lower than the theoretical misfit value of 2.5% for GaN and AlN. The experimental mismatch is equal to $N_{\text{GaN}} - N_{\text{AlN}}/N_{\text{AlN}}$, where N is the number of $(1\bar{1}00)$ planes perpendicular to the interface (Fig. 9). This calculation was repeated at ~ 20 different locations along the interface, with the average results presented here. Thus there is a 0.9% residual compressive strain in the on-axis GaN film. This result supports the data from our PL and XRD studies

presented earlier.

Additional evidence for the existence of residual compressive strain in the GaN films is the TEM contrast exhibited by the GaN films at distances of 50–80 Å from the interface with AlN. As can be seen in Fig. 9, the contrast reveals traces of rounded peaks and grooves, which are typical for films that are under compression.^{42,43} Such near surface undulations are formed during heteroepitaxial growth by migration of the atoms deposited on the surface under the strain induced chemical potential gradients. From the same figure it can be seen that at the grooves, the interplanar distances are smaller than at areas close to the peaks. This shows that there is a complementary compression at the areas close to the peaks.

Thus, our HRTEM studies reveal the stress due to lattice mismatch is not fully relieved at the GaN/AlN for films grown on on-axis SiC. This results in a residual compressive stress that counteracts the tensile stress due to thermal mismatch. If this compressive stress is stronger, then the GaN films should be in compression. This explains why the thin ($t \leq 0.6 \mu\text{m}$) GaN films grown on-axis films are in compression, while those grown concurrently on vicinal SiC wafers are in tension, with a maximum $\Delta c = 0.0072 \text{ \AA}$. As thickness increases ($t \geq 1 \mu\text{m}$), this compressive stress lessens; and at greater thicknesses ($t \geq 4 \mu\text{m}$), cracking may occur in the GaN to relieve thermal mismatch stress.

SUMMARY

Compressive strain in GaN films grown on AlN/6H-SiC(0001) is reported for the first time. Residual biaxial strains determined in the films was due both to mismatches in thermal expansion coefficients and lattice parameters. A linear dependence due to this strain was determined between E_{bx} and c for 22 GaN films grown on AlN/6H-SiC, and expressed by $E_{\text{bx}} = (-14.912 + 3.545 \cdot c) \text{ eV}$. Poisson's ratio for GaN was determined to be $\nu = 0.18$ from values of c and a for 22 GaN films. The shift of E_{bx} with biaxial film stress was estimated to be 23 meV/GPa. A marked variation in E_{bx} and c was observed for GaN films grown concurrently on AlN buffers and vicinal and on-axis SiC wafers. This variation was greatest for films $\leq 0.6 \mu\text{m}$ thick, where a maximum shift of $\Delta E_{\text{bx}} = 17 \text{ meV}$ and $\Delta c = 0.0072 \text{ \AA}$ was observed, and the samples on the on-axis SiC were in compression.

Related TEM results showed a higher density of steps on the vicinal SiC wafers. These steps acted as formation sites for inversion domain boundaries. Threading dislocation densities of $\sim 10^{10}/\text{cm}^2$ and $\sim 10^8/\text{cm}^2$ were observed for GaN on AlN grown vicinal and on-axis SiC, respectively. The on-axis SiC substrate did not contain sufficient steps for defect formation to fully relieve the lattice mismatch via defect formation at the GaN/AlN and AlN/SiC interfaces at the growth temperature. This resulted in residual compressive stresses that counteracts the tensile stresses that formed upon cooling due to the mismatch in thermal expansion coefficients. A 0.9% residual compressive

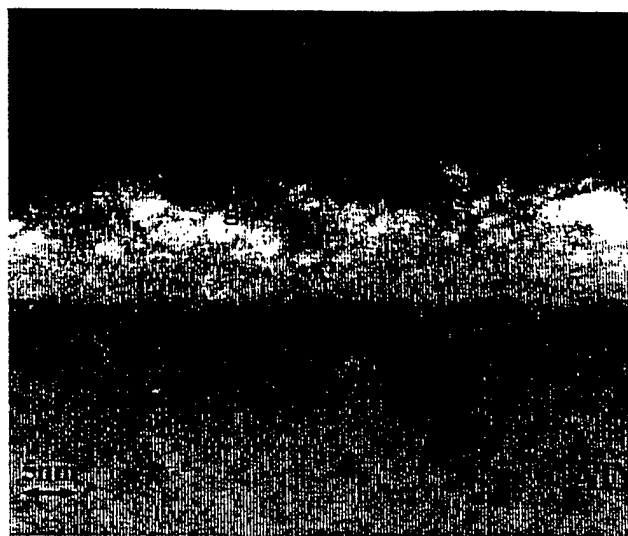


Fig. 9. HRTEM micrograph from GaN/AlN interface of GaN/AlN 6H-SiC on-axis heterostructure. Note the extra-half planes in GaN films which are the misfit dislocations (MD) generated to relieve the misfit strain at that interface. The peaks and grooves are denoted by P and D.

strain at the GaN/AlN interface was calculated by comparing the average experimental lattice mismatch at the interface (1.6%) observed via HRTEM with that theoretically predicted for GaN/AlN (2.5%). It is proposed that this strain was accommodated elastically and resulted in biaxially compressive stresses in the films.

ACKNOWLEDGMENTS

The authors acknowledge the support of the U.S. Office of Naval Research via contract #N00014-92-J-1477, Cree Research, Inc. for the SiC wafers, and Barbara Goldenberg of Honeywell, Inc. for the sample of GaN on sapphire. W. Perry acknowledges Dr. S.K. Streiffer of North Carolina State University and Drs. Jaime Freitas and Evan Glaser of the Naval Research Laboratory for helpful discussions.

REFERENCES

1. H. Amano, K. Hiramatsu and I. Akasaki, *Jpn. J. Appl. Phys.* 27, L1484 (1988).
2. T. Detchprohm, K. Hiramatsu, K. Itoh and I. Akasaki, *Jpn. J. Appl. Phys.* 31, (10B) L1454 (1992).
3. K. Hiramatsu, T. Detchprohm and I. Akasaki, *Jpn. J. Appl. Phys.* 32, 1528 (1993).
4. I.A. Buyanova, J.P. Bergman, B. Monemar, H. Amano and I. Akasaki, *Appl. Phys. Lett.* 69, 1255 (1996).
5. X.J. Ning, F.R. Cein, P. Pirouz, J.W. Yang and M.A. Khan, *J. Mater. Res.* 11, 580 (1996).
6. T.W. Weeks, M.D. Bremser, K.S. Ailey, E. Carlson, W.G. Perry and R.F. Davis, *Appl. Phys. Lett.* 67, 401 (1995).
7. T.W. Weeks, M.D. Bremser, K.S. Ailey, E. Carlson, W.G. Perry, E.L. Piner, N.A. El-Masry and R.F. Davis, *J. Mater. Res.* 11, 1011 (1996).
8. S. Tanaka, PhD dissertation, North Carolina State University, 1993.
9. W. Li and W. Ni, *Appl. Phys. Lett.* 68, 2705 (1996).
10. S. Krishnakutty, R.M. Kolbas, M.A. Khan, J.N. Kunzia, J.M. Van Hove and D.T. Olson, *J. Electron. Mater.* 21, 609 (1992).
11. J.W. Orton, *Semicond. Sci. Technol.* 11, 1026 (1996).
12. B. Monemar, J.P. Bergman, I.A. Buyanova, H. Amano, I.

- Akasaki, K. Hiramatsu, N. Sawaki and T. Detchprohm, presented at the Topical Workshop on III-V Nitrides, Nagoya, Japan (1995).
13. C. Merz, M. Kunzer, U. Kaufmann, I. Akasaki and H. Amano, submitted to *Phys. Rev. B*, 1995.
14. P. Boguslawski, E. Briggs, T.A. White, M.G. Wensell and J. Bernholc, *Mater. Res. Soc. Symp. Proc.* 339, (Pittsburgh, PA: Mater. Res. Soc., 1994), p. 693.
15. J. Neugebauer and C.G. Van de Walle, *Phys. Rev. B* 50, 8067 (1994).
16. P. Boguslawski, E. Briggs and J. Bernholc, *Phys. Rev. B* 51, 17255 (1995).
17. W. Shan, R.J. Hauenstein, A.J. Fisher, J.J. Song, W.G. Perry, M.D. Bremser, R.F. Davis and B.G. Goldenberg, submitted to *Phys. Rev. B*.
18. D. Volm, K. Oetinger, T. Streibl, D. Kovalev, M. Ben-Chorin, J. Diener, B.K. Meyer, J. Majewski, L. Eckey, A. Hoffman, H. Amano, I. Akasaki, K. Hiramatsu and T. Detchprohm, *Phys. Rev. B* 53, 16543 (1995).
19. L. Eckey, J.C. Holst, P. Maxim, R. Heitz, A. Hoffmann, I. Broser, B.K. Meyer, C. Wetzol, E.N. Mokhoco and P.G. Baranov, *Appl. Phys. Lett.* 68, 415 (1996).
20. P.F. Fewster and N.L. Andrew, *J. Appl. Cryst.* 28, 451 (1995).
21. J.C. Braveman and R. Sinclair, *J. Electron Microsc. Technique* 1, 53, (1984).
22. G.M. Ma and S. Chevaharoencul, *MCNC Technical report* TR90-33 (1990).
23. W. Shan, B.D. Little, A.J. Fischer, J.J. Song, B. Goldenberg, W.G. Perry, M.D. Bremser and R.F. Davis, to be submitted.
24. C.M. Balkas, C. Basceri and R.F. Davis, *Powder Diffraction* 10, 266 (1995).
25. E. Burnstein, *Phys. Rev.* 93, 632 (1954).
26. A. Gassmann, T. Suski, N. Newman, C. Kisielowski, E. Jones, E.R. Weber, A. Liliental-Weber, M.D. Rubin, H.I. Heleva, I. Grzegory, M. Bockowski, J. Jun and S. Porowski, *J. Appl. Phys.* 80, 2195 (1996).
27. B. Monemar, *Phys. Rev. B* 10, 676 (1974).
28. K. Pakula, A. Wyszomolek, K.P. Korona, J.M. Baranowski, R. Stepniowski, I. Grzegory, M. Bockowski, J. Jun, S. Krukowski, M. Wroblewski and S. Porowski, *Solid State Commun.* 97, 919 (1996).
29. K.N. Tu, J.W. Mayer and L.C. Feldman, *Electronic Thin Film Science*, (New York: Macmillan, 1992) p. 84.
30. V.A. Savastenko and A.U. Sheleg, *Phys. Status Solidi A* 48, 135 (1978).
31. T. Azuhata, T. Sota, K. Suzuki, *J. Phys.: Condens. Matter* 8, 3111 (1996).
32. C. Kisielowski, J. Krüger, S. Rumimov, T. Suski, J.W. Ager III, E. Jones, Z. Liliental-Weber, M. Rubin, E.R. Weber, M.D. Bremser and R.F. Davis, to be submitted to *Phys. Rev. B*, 1996.
33. *Landolt-Börnstein*, ed. O. Madelung (New York: Springer, 1982), Vol. 17.
34. K. Kim, W.R.L. Lambrecht, and B. Segall, *Phys. Rev. B* 50, 150 (1994).
35. A. Polian, M. Grimsdich and I. Grzegory, *J. Appl. Phys.* 79, 3343 (1996).
36. W. Shan, T.J. Schmidt, R.J. Hauenstien, J.J. Song and B. Goldenberg, *Appl. Phys. Lett.* 66, 3492 (1995).
37. P. Perlin, I. Gorczyca, N.E. Christensen, I. Grzegory, H. Teisseyre and T. Suski, *Phys. Rev. B* 45, 13307 (1992).
38. W. Rieger, T. Metzger, H. Angerer, R. Dimitrov, O. Ambacher and M. Stutzmann, *Appl. Phys. Lett.* 68, 970 (1995).
39. P. Pirouz et al., Nitride Workshop on Wide Bandgap Nitrides, St. Louis, (1996).
40. A. Westwood, R. Youngman, M. McCartney, A. Cormack and M. Notic, *J. Mater. Res.* 10, 1270 (1995).
41. F. Chien, X. Jing, P. Pirouz, M.D. Bremser and R.F. Davis, *Appl. Phys. Lett.* 68, 2678 (1996).
42. C. Roland, *MRS Bulletin* 21, 27 (1996).
43. A. Cullis, *MRS Bulletin* 21, 21 (1996).

Linear and Nonlinear Optical Investigations of GaN and AlGaIn/GaN Heterostructures

J.J. Song,¹ A.J. Fischer,¹ W. Shan,¹ B. Goldenberg,² and G.E. Bulman³

¹ *Center for Laser and Photonics Research and Department of Physics, Oklahoma State University, Stillwater, OK 74078, USA*

² *Honeywell Technology Center, Plymouth, MN 55441, USA*

³ *Cree Research, Inc. Durham, North Carolina, 27713, USA*

Abstract. We present the results of a series of studies on the optical properties of GaN and AlGaIn/GaN heterostructures using a variety of spectroscopic techniques. Strain effects were found to have a strong influence in determining the energies of excitonic transitions. The observations of spectral features associated with the transitions involving the ground and excited exciton states make it possible to directly estimate binding energy for the excitons in GaN. Optical pumping experiments were performed on AlGaIn/GaN separate confinement heterostructures (SCH) grown on sapphire by MBE and on SiC by MOCVD. The threshold pumping powers were found to be an order of magnitude lower than that for regular GaN epilayers. Nonlinear four-wave-mixing experiments were carried out in both femtosecond and picosecond regimes to study the intensity and time response of scattering efficiency, as well as the pump-induced nonlinear refractive index change.

1. Introduction

Extensive studies on the properties of wide bandgap semiconductor materials for the applications of light emitting devices operating in blue and ultraviolet (UV) spectral regions have been undertaken for years. GaN based wide band-gap III-V nitride systems have recently attracted much attention as the most promising material for such device applications.[1] We have performed a variety of spectroscopic techniques to study optical transition processes in GaN and AlGaIn/GaN heterostructures. The work reported here will focus on several subjects including the study of excitonic transitions in GaN and nonlinear four-wave-mixing, as well as optical pumping study on the stimulated emission and lasing in AlGaIn/GaN separate confinement heterostructures (SCH).

2. Experimental details

The GaN samples used in this work were nominally undoped single-crystal films grown by metalorganic chemical vapor deposition (MOCVD) on (0001) 6H-SiC or basal-plane sapphire substrates. The AlGaIn/GaN separate confinement heterostructures (SCH) were grown either on (0001) sapphire substrates by a modified reactive MBE or on 6H-SiC by MOCVD. The SCH structures typically have ~100 Å thick GaN active layer, symmetrically surrounded by a lower mole fraction AlGaIn waveguide layer, and followed by a higher AlGaIn cladding layer. Photoluminescence, reflection, and photomodulation spectroscopy were performed to study excitonic transitions. Optically pumped stimulated emission and lasing phenomena were studied using a frequency-tunable dye laser pumped by the second harmonic laser beam (532 nm) of a pulsed Nd:YAG laser with ~10 ns pulse width and 10 Hz repetition rate. The output of the dye laser was then frequency-doubled to achieve a near UV pumping wavelength. Nonlinear four-

wave-mixing experiments were performed using the second harmonic of a self-mode-locked Ti:Sapphire laser (100 fs) or 13-picosecond (ps) pulses at 532 nm from a mode-locked Q-switch Nd:YAG laser.

3. Results and Discussions

3.1. Strain effects on excitonic transitions

A number of investigations on the optical properties of GaN have revealed that there is a significant amount of variation in the literature about the positions of various excitonic transitions.[2-9] Fig.1 plots the excitonic transition energies measured from the GaN samples used in this work as a function of relative in-plane (biaxial) strain. The strain was determined by X-ray rocking curve measurements. The systematically observed differences in exciton transition energies can be attributed to the effects of residual strain in the epilayers due to the mismatch of lattice parameters and

coefficients of thermal expansion between GaN and the substrate material. By comparing these observed exciton transition energies to the values obtained from virtually strain-free bulk GaN, one can infer that the overall effects of residual strain generated in GaN on sapphire is compressive, which results in an increased band gap, while that induced in GaN on SiC is tensile, which leads to a decrease in measured exciton transition energies. Therefore, the results presented here lead to the conclusion that strain can shift the transition energies either up or down depending on whether the GaN layer is in tension or compression. Furthermore, the strain induced by thermal-expansion mismatch in GaN based epitaxial layers has the prevailing influence on the energy variations of exciton transitions, since lattice-mismatch induced strain is of the opposite sign and hence would have the opposite effect on the variation of the GaN band gap from that observed.

The observed strain shifts in excitonic transition energies permit a direct estimate of the deformation potentials, including both hydrostatic and uniaxial components for wurtzite GaN. With linear fits to the whole set of data shown in Fig.1 using a least-squares fit, and taking into account the facts that the strain caused total energy shift relative to the excitonic transition energy is very small and the elastic properties of GaN are of quasi-cubic nature, the uniaxial deformation potentials can be derived to be $b_1 = -5.3$ eV and $b_2 = 2.7$ eV, and the hydrostatic deformation components to be $a_1 = -6.5$ eV and $a_2 = -11.8$ eV.[10]

3.2. Exciton binding energy

We note that some GaN samples exhibit a set of weak but resolvable spectral features in the spectral region on the higher-energy side of the main A- and B-transitions in the reflection spectra. Shown in Fig.2 is a photorefectance (PR) spectrum from a 7.2- μ m GaN/sapphire sample. While the spectral features A, B, and C can be unmistakably identified to be associated with intrinsic free-exciton transitions, the nature of the *a* and *b*-features is not immediately clear. In order to determine the energy positions associated with the various observed optical transitions and identify those unknown spectral features, the PR spectral features are fitted to the functional form:[11] $\Delta R/R = \text{Re}[\sum_j \{C_j e^{i\theta_j} (E - E_j + i\Gamma_j)^{-2}\}]$, where C_j and θ_j are the amplitude and

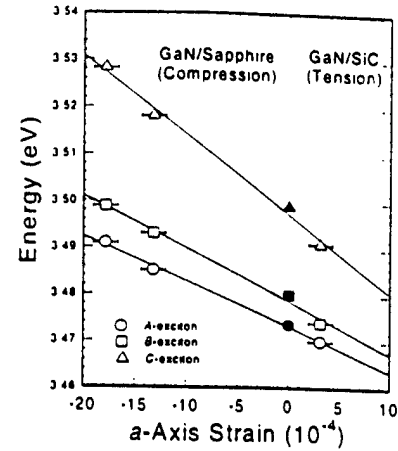


Fig.1. Measured excitonic transition energies as a function of relative in-plane (biaxial) strain. The exciton energies of strain-free GaN were included for reference (dark points).

phase of the line shape, and E_j and Γ_j are the energy and the empirical broadening parameter of the transitions, respectively. The solid line in the figure is the best least-squares fit to the experimental data. The best fits result in an energy separation of 0.008 eV between the a - and b -features, which is almost identical to the A - B separation, and a 0.016 eV difference for both A - a and B - b separations within experimental error ($\leq 0.001 \text{ eV}$). Similar properties could be also observed in the other GaN samples. These observations indicate that the a - and b -features are indeed associated with A - and B -exciton transitions. Therefore, we attribute a and b to the $n=2$ excited states ($2s$) of the excitons. A straightforward estimate of the binding energy from the separation between the $n=1$ and $n=2$ exciton states using simple hydrogenic model $E_n = -E_b/n^2$ with n as an integer and E_b as the binding energy yields $E_b = 0.021 \pm 0.001 \text{ eV}$ for A - and B -excitons. The binding energy for the C -exciton can also be derived using the same approach. A $3.7\text{-}\mu\text{m}$ GaN/SiC exhibiting a much stronger C -exciton transition signal in the PR spectrum allows us to obtain a 0.0172 eV energy separation with the $1s$ and $2s$ states of the C -exciton, which corresponds to a binding energy of $\sim 0.023 \text{ eV}$.

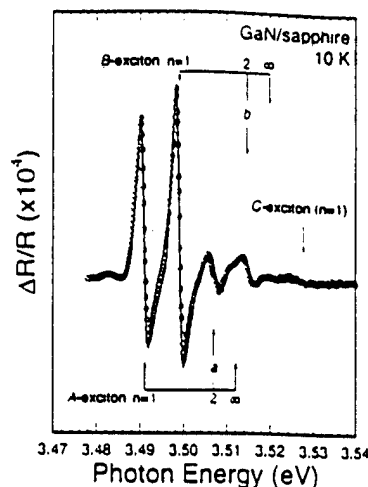


Fig.2. 10-K PR spectrum of a GaN/sapphire sample. The solid line is the best fit to the data. The identifications of various features are given by the notations.

3.3. Optically pumped stimulated emission and laser action in AlGaIn/GaN SCH

A comparative study of optically pumped stimulated emission and laser action in uniform GaN epilayers and AlGaIn/GaN SCH samples was performed. Fig.3 shows the emission intensity against the pumping power density taken from an SCH sample grown on an SiC substrate. The AlGaIn/GaN SCH samples exhibited threshold pumping powers as low as 65 kW/cm^2 at room temperature under the excitation of a frequency-tunable nanosecond laser system in a side-pumping configuration. This represents more than an order of magnitude reduction over uniform GaN epilayer samples (800 kW/cm^2). [12] Such substantial decreases in the threshold values observed in SCH samples can be attributed to the carrier confinement and waveguiding effects.

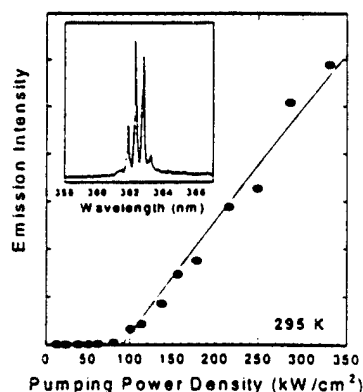


Fig.3. Lasing emission intensity vs. pumping power density of an SCH structure on SiC at 295 K. The inset shows the Fabry-Perot cavity modes.

3.4. Nonlinear four-wave mixing

Using picosecond laser pulses at 532 nm with the photon energy below the band gap of GaN, we performed nonlinear four-wave-mixing (FWM) experiments using a boxcar geometry. Strong wave-mixing signals up to 7th order could be observed with the naked eye as shown in Fig.4. By delaying the arrival of the probe pulses relative to the pump pulses, the response of the nonlinear optical changes such as scattering efficiency in the GaN sample was

studied. The scattering efficiency is defined as the ratio of the intensity of scattered to the transmitted probe beam. At zero delay, a maximum scattering efficiency of 4×10^{-5} was obtained. It corresponds to an index change, $\Delta n(0)$, of 1.2×10^{-3} . This change can be related to the pump beam intensity through an effective nonlinear refractive coefficient, n_2 , defined as $\Delta n(0) = n_2 I_0$ [13]. Using the pump-beam irradiance of 1.2 GW/cm^2 , a value of $1 \times 10^{-3} \text{ cm}^2/\text{GW}$ was derived for the effective nonlinear refractive index n_2 .

We have also observed quantum beats in GaN by performing degenerate fs-FWM experiments. When the laser was tuned to the spectral region at the A- and B-exciton resonance around 3.5 eV, a coherent superposition of the excited A-exciton component with the B-exciton referred to as quantum beats [14] was observed. The beat period of 560 fs, $T_{\text{beat}} = h/(E_B - E_A)$, corresponds exactly to the A-B exciton energy separation in this sample of 7.3 meV.

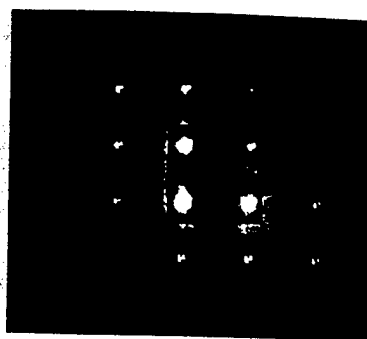


Fig.4. Image of the ps-FWM signals showing three attenuated pump and probe beams and higher order nonlinear diffracted signal spots.

4. Conclusions

Some recent results of linear and nonlinear optical investigations of the properties of GaN and AlGaIn/GaN heterostructures have been presented. The results of studying strain effects clearly indicate that GaN epilayers grown on SiC exhibit basal tensile strain, while those on sapphire substrates are under biaxial compression. Based on these results, the values of the four principal deformation potentials of wurtzite GaN have been determined. The observations of spectral structures of exciton transitions associated with the ground state and excited states of A-, B-, and C-excitons in GaN epitaxial layers enabled us to accurately determine the transition energies and make a straightforward estimate of the binding energy for the excitons. Substantial decreases in the threshold values for lasing were observed in AlGaIn/GaN SCH samples due to the carrier confinement and waveguiding effects. Some interesting phenomena related to the nonlinear optical properties of GaN were also studied in the femtosecond and picosecond regimes by FWM experiments. The value of effective nonlinear refractive index at 532 nm for GaN was derived from ps-FWM results, and the quantum beats resulting from a coherent superposition of exciton wavefunctions were observed by fs-FWM.

5. References

- [1] Strite, S. and H. Morkoç, 1992, *J. Vac. Sci. Technol.* B10, 1237, and references therein.
- [2] Dingle, R. and M. Ilegeme, 1971, *Solid State Commun.* 9, 175.
- [3] Dingle, R. *et al.* 1971, *Phys. Rev.* B4, 1211.
- [4] Monemar, B. 1974, *Phys. Rev.* B10, 676.
- [5] Shan, W. *et al.* 1995, *Appl. Phys. Lett.* 66, 985.
- [6] Gil, B. *et al.* 1995, *Phys. Rev.* B52, R17028.
- [7] Smith, M. *et al.* 1996, *J. Appl. Phys.* 76, 7001.
- [8] Chen, G.D. *et al.* 1996, *Appl. Phys. Lett.* 68, 2784.
- [9] Shan, W. *et al.* 1996, *Appl. Phys. Lett.* 69, 740.
- [10] Shan, W. *et al.* 1996, to be published in *Phys. Rev.* B54, scheduled issue date: Nov. 15.
- [11] Aspnes, D.E. 1980, in *Optical Properties of Solids*, ed. M. Balkanski (North-Holland, Amsterdam).
- [12] Yang, X.H. *et al.* 1995, *Appl. Phys. Lett.* 66, 1.
- [13] Song, J.J. *et al.* 1996, in *Physics and Simulation of Optoelectronic Devices IV*, ed. W.W. Chow and M. Osinski, SPIE Proceedings Series Vol.2693, 86.
- [14] Shen, Y.R. 1984, *Principles of Nonlinear Optics*, (John Wiley and Sons, New York).

Binding energy for the intrinsic excitons in wurtzite GaN

W. Shan, B. D. Little, A. J. Fischer, and J. J. Song

Center for Laser and Photonics Research and Department of Physics, Oklahoma State University, Stillwater, Oklahoma 74078

B. Goldenberg

Honeywell Technology Center, Plymouth, Minnesota 55441

W. G. Perry, M. D. Bremser, and R. F. Davis

Department of Materials Science and Engineering, North Carolina State University, Raleigh, North Carolina 27695

(Received 19 August 1996; revised manuscript received 27 September 1996)

We present the results of an experimental study on the binding energy for intrinsic free excitons in wurtzite GaN. High-quality single-crystal GaN films grown by metalorganic chemical vapor deposition were used in this study. Various excitonic transitions in GaN were studied using reflectance measurements. The observation of a series of spectral features associated with the transitions involving the ground and excited exciton states allows us to make a straightforward estimate of exciton binding energy using the hydrogenic model. Our results yield a binding energy $E_b = 0.021 \pm 0.001$ eV for the *A* and *B* excitons, and 0.023 ± 0.001 eV for the *C* exciton in wurtzite GaN within the framework of the effective mass approximation. [S0163-1829(96)11948-2]

In recent years, much effort has been devoted to the study of wide-band-gap semiconductor materials and their multilayer heterostructures for optoelectronic device applications, such as laser diodes and light-emitting diodes operating in the ultraviolet-blue-green range. Currently, GaN is among the most extensively studied materials. It is known that GaN has a wurtzite structure in natural form, and has a wide direct band gap of ~ 3.42 eV at room temperature (300 K), which provides efficient radiative recombination and makes GaN very attractive to the short-wavelength optical applications in the blue and ultraviolet wavelength range.¹ The outstanding thermal and chemical stability of the wide-band-gap nitrides also allows GaN-based electronic and optoelectronic devices to operate at high temperatures and in hostile environments.^{2,3}

So far, there have been numerous studies reporting the evidence of fine structures observed in the energy region near the band edge of GaN using various optical measurements.⁴⁻¹³ In spite of these detailed studies, the description of the band structure and exciton energy levels in GaN has remained in a state of confusion. In this report we present the results of an experimental study of optical transitions associated with the ground and excited exciton states in wurtzite GaN single-crystal epilayers using conventional reflection and photomodulated reflectance (PR) measurements at low temperatures. In particular, the unambiguous observation of sharp derivativelike PR spectral features related to the $1s$ and $2s$ states of *A*-, *B*-, and *C*-exciton transitions, as well as the fundamental band-to-band ($\Gamma_V^9 - \Gamma_C^7$) transition, allows a precise determination of the energy positions for those transitions, making it possible to directly estimate the binding energy for the excitons using the hydrogenic model. In addition, the longitudinal-transverse splitting and phenomenological damping parameter of the polaritons associated with *A* and *B* excitons were estimated by taking into account the spatial dispersion of the dielectric function of GaN.

The GaN samples used in this work were nominally undoped single-crystal films grown by metalorganic chemical vapor deposition on (0001) sapphire and 6H-SiC substrates. AlN buffer layers were deposited on the substrates at about 775 °C before the growth of the GaN epilayers. The GaN layers were deposited at 1040 °C directly on the AlN buffers. The thickness of the GaN layers ranged from 2.5 to 7.2 μm . The samples were attached to the cold finger of a closed-cycle refrigerator and cooled down to the desired temperatures for optical measurements. For conventional reflection measurements, quasimonochromatic light from a xenon lamp dispersed by a $\frac{1}{2}$ -M monochromator was focused on the samples at near-normal incidence, and the reflection signals were detected using a lock-in amplification system. A chopped HeCd laser beam was used to provide optical modulation when the photomodulation measurements were performed.

Results of conventional reflection measurements taken from two samples of GaN on sapphire with epilayer thicknesses of 2.5 and 7.2 μm at 10 K are shown in Fig. 1. The reflection spectra exhibit three spectral resonances corresponding to intrinsic free-exciton transitions labeled by *A*, *B*, and *C* with the vertical arrows. The excitons referred to as the *A*, *B*, and *C* excitons are related to the $\Gamma_9^V - \Gamma_7^C$, $\Gamma_7^V(\text{upper band}) - \Gamma_7^C$ and $\Gamma_7^V(\text{lower band}) - \Gamma_7^C$ interband transitions in GaN, respectively. The *C*-exciton signature appeared weak in the spectra because the transition process, strictly speaking, is theoretically forbidden for the wave vector of the incident light along the *c* axis ($\mathbf{k} \parallel c$) and the polarization perpendicular to the axis ($\mathbf{E} \perp c$).^{12,14} Of most interest, there is a set of weak but resolvable spectral features marked by *a* and *b* in the spectral region on the higher-energy side of the main *A* and *B* transitions in both reflection spectra. While the spectral features *A*, *B*, and *C* can be unmistakably identified to be associated with intrinsic free-exciton transitions in the spectra,^{7,13} the nature of the *a* and

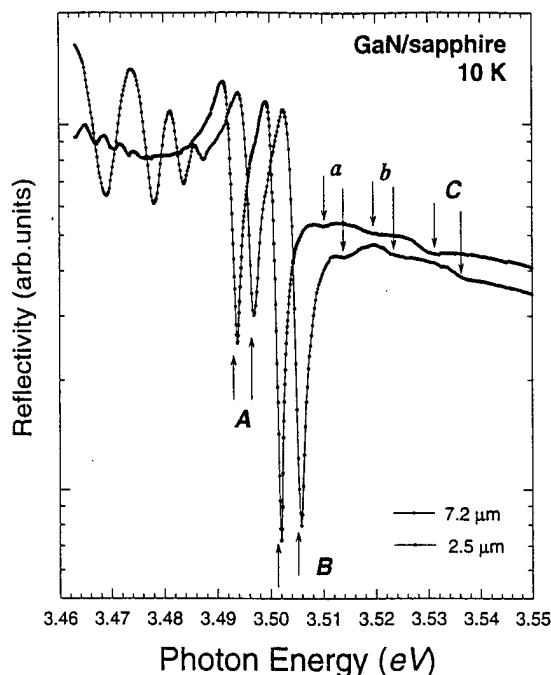


FIG. 1. Reflection spectra taken from a 2.5- μm and a 7.2- μm GaN sample at 10 K. The weak spectral structures on the reflection curves are indicated by the vertical arrows. The difference in the energy positions of A-, B-, and C-exciton resonances between two samples are caused by built-in residual strain.

b features in Fig. 1 is not immediately clear. We found that the energy separation between the *a* and *b* features is very close to the separation of the A- and B-exciton transitions. The individual distance between the A exciton and the *a* feature as well as the B exciton and the *b* feature was also found to be about the same. Similar properties were observed in the exciton spectrum of CdS by Thomas and Hopfield, which led to the determination of the binding energy for A and B excitons in the material by attributing the corresponding spectral features to $n=2$ excited exciton states based on their polarization properties.¹⁴ However, it is very difficult to use a polarization-dependent approach in this work because of the very limited thickness of the samples used and the poor signal-to-noise ratio of the *a* and *b* features in the reflection spectra. Fortunately, photomodulation spectroscopy is an alternative approach capable of detecting weak signals so as to accurately determine their transition energies and make a positive identification for the nature of the transitions. As illustrated in Fig. 2, where photomodulated reflectance (PR) spectra taken from a sample of GaN on sapphire and a sample of GaN on SiC are given, the PR spectra not only consist of a series of sharp structures corresponding to most of the observed spectral features in the reflection spectra, but also exhibit, more strikingly, a pronounced enhancement of the barely observed weak spectral structures on the reflection curves such as the *a* and *b* features.

The difference between conventional reflection and photorefectance is that the former is a straightforward reflectivity measurement without additional optical modulation, and the latter is a differential method utilizing modulation of the built-in electric field through photoinjected carriers by a periodically modulated light beam, such as the chopped laser beam used in this work. The change in reflectivity, $\Delta R/R$,

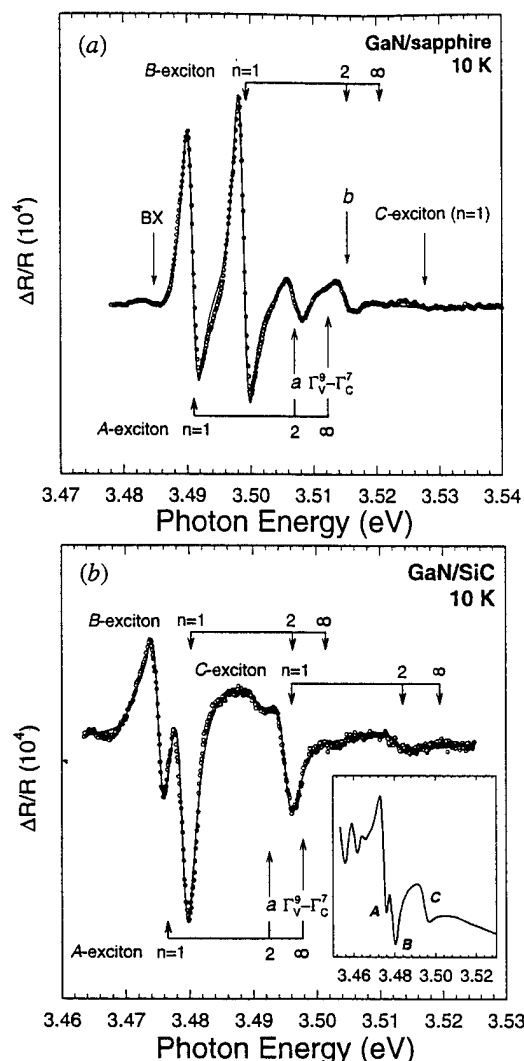


FIG. 2. 10-K PR spectrum taken from the 7.2- μm GaN/sapphire (a) and a 3.7- μm GaN/SiC (b). Open circles are experimental data, and solid lines represent the best result of the least-squares fit to the data. The identifications of the various spectral features are given by the notations.

due to the modulation may be expressed as¹⁵

$$\Delta R/R = a \Delta \epsilon_1 + b \Delta \epsilon_2, \quad (1)$$

where *a* and *b* are referred to as Seraphin coefficients and are related to the unperturbed dielectric function $\epsilon = \epsilon_1 + i\epsilon_2$, while $\Delta \epsilon_1$ and $\Delta \epsilon_2$ are the changes in the real and the imaginary parts of the modulated dielectric function, respectively.¹⁵ The differential changes in the reflectivity appear as sharp derivativelike line shapes in the modulated reflectance spectrum, corresponding to specific transitions in the Brillouin zone. As clearly demonstrated by Fig. 2, the weak spectral structures such as *a* and *b* could be barely observed from the conventional reflection measurement, but were greatly enhanced in the PR spectra.

In order to determine the energy positions associated with the various observed optical transitions and identify those unknown spectral features, the PR spectral features are fitted to the functional form¹⁶⁻¹⁸

$$\Delta R/R = \text{Re} \left[\sum_j \{ C_j e^{i\theta_j} (E - E_j + i\Gamma_j)^{-n} \} \right], \quad (2)$$

where C_j and θ_j are the amplitude and phase of the line shape, and E_j and Γ_j are the energy and the empirical broadening parameter of the transitions, respectively. The exponent n is a characteristic parameter which depends on the type of critical point and the order of the derivative. The values of $n=5/2$ and $n=2$, which correspond to three-dimensional interband and excitonic transitions, respectively,^{16,19} are generally used to fit the derivativelike spectral structures. We found that the line positions and widths of the PR spectral features could only be fit using $n=2$ due to their excitonic nature. The solid lines in Fig. 2 are the best least-squares fits to the experimental data using Eq. (2). The small deviation between the fit and the experimental data on the higher-energy side of the main PR spectral features suggests that the A - and B -exciton profiles at 10 K are both inhomogeneously and homogeneously broadened. The energy positions for the A -, B -, and C -exciton transitions in the GaN/sapphire sample shown in Fig. 2(a) are 3.491, 3.499, and 3.528 eV, respectively. These values are higher than those obtained from virtually strain-free bulk GaN reported in Refs. 4–6 due to the effects of residual strain caused by the mismatch of lattice parameters and thermal expansion coefficients between the GaN epilayer and the substrate.^{8,13,20} The best fits result in an energy separation of 0.008 eV between the a and b features, which is almost identical to the A - B separation, and a 0.016-eV difference for both A - a and B - b separations within experimental error (≤ 0.001 eV). Similar properties could also be observed in the other GaN samples: while the absolute energy position for the main A - and B -exciton transitions varies from sample to sample slightly due to the influence of residual strain, the energy differences of the A - a and B - b features were found to be ~ 0.016 eV for all the samples, and the energy separation between the a and b features was found to closely follow that between the main A - and B -exciton features at lower energies for each individual sample. These observations indicate that the a and b features are indeed associated with A - and B -exciton transitions. Therefore, we attribute a and b to the $n=2$ excited states ($2s$) of the excitons. Such identifications permit a direct estimate of the binding energy for A and B excitons from the separation between the $n=1$ and $n=2$ states for excitons assuming the hydrogenic model based on the effective mass approximation is applicable. According to Elliott's theory,²¹ exciton energy levels are given as

$$E_n = -E_b/n^2, \quad (3)$$

where n is an integer and E_b is the binding energy. From the results presented above, we obtain a binding energy of $E_b \approx 0.021 \pm 0.001$ eV for A and B excitons. This can be further manifested by the result of theoretical fitting to the extra spectral structure in the portion of the PR spectrum between the a and b features. We found that it is necessary to introduce one more oscillator with a third-derivative line shape to improve the fit to the experimental data. The good agreement between the theoretical fit and the observed spectrum indicates a spectral feature corresponding to a band-to-band transition at 3.512 eV. The approximate 0.021-eV energy separation from this band-to-band signature to the transition position of the $n=1$ state of the A exciton is consistent with the estimated binding energy for the exciton. Therefore, it

originates from the $\Gamma_V^9-\Gamma_C^7$ transition, as denoted in Fig. 2(a), which corresponds to the $n=\infty$ state for the excitonic transition.

The binding energy for the C exciton can also be derived from the theoretical fitting to the PR spectrum taken from a 3.7- μm GaN sample grown on SiC as shown in Fig. 2(b) using the same approach. This sample exhibits a much stronger C -exciton transition signal in the reflection spectrum, as shown in the inset of the figure, compared to the samples of GaN on sapphire. The energy positions for the A -, B -, and C -exciton transitions in this sample are 3.470, 3.474, and 3.491 eV, respectively. In addition to the derivativelike spectral features arising from the transitions associated with the $n=1$ exciton states of the A , B , and C excitons, the spectral features related to the transitions involving the $n=2$ exciton states of the A and C excitons could be clearly observed in the PR spectrum. The best fit yields a 0.0172-eV energy separation between the $1s$ and $2s$ states of the C exciton, which corresponds to a binding energy of ~ 0.023 eV, and retains a ~ 0.016 -eV difference between the A exciton ($n=1$) and a feature as indicated in the figure.

It has to be pointed out that the exciton binding energies given above are estimated under the assumption of an isotropic reduced spherical mass for the excitons in GaN. In reality, wurtzite GaN is a hexagonal crystal with axial symmetry: the effective-mass equation for hydrogenic states should, in principle, be modified because the reduced effective mass as well as the dielectric constant is actually anisotropic. Nevertheless, the results presented here are in good agreement with the theoretical values obtained by variational calculations²² (20.3 meV) and perturbation theory²³ (19.8 meV) based on the hydrogenic model. In addition, a reduced effective exciton mass μ can be derived from our results using the relation

$$E_b = e^4 \mu / (2(4\pi\hbar\epsilon)^2) = 13.60 \mu / \epsilon^2 \text{ eV}, \quad (4)$$

with the low-frequency dielectric constant of $\epsilon = 9.5$,²⁴ to be $\mu \approx 0.15m_0$. The obtained value is consistent with the value of $\sim 0.16m_0$ estimated using an effective mass of $0.2m_0$ for the electrons and $0.8m_0$ for the holes in wurtzite GaN.²⁴ Therefore, the simple hydrogen series of Eq. (3) is still a valid approach for the determination of the binding energy for excitons in GaN.

It is known that excitons can interact strongly with photons to form a mixed state referred to as a polariton in direct-gap materials due to spatial dispersion of the dielectric constant.^{25,26} It is interesting to estimate the longitudinal-transverse splitting energies and phenomenological damping parameters of the polaritons associated with A and B excitons with the consideration of spatial dispersion (i.e., the wave-vector dependence) of the dielectric function. The wave-vector-dependent dielectric function is given by^{26,27}

$$\epsilon(\omega, k) = \epsilon_\infty \{ 1 + (\omega_L^2 - \omega_T^2) / (\omega_T^2 - \omega^2 + \beta k^2 - i\omega\Gamma) \}. \quad (5)$$

Where ϵ_∞ is a frequency- and wave-vector-independent background dielectric constant, ω_T and ω_L are the transverse and longitudinal resonance frequencies at $k=0$, and Γ is the phenomenological damping constant. The spatial dispersion is described by $\beta k^2 = (\hbar\omega_T/M)k^2$ with M as the effective exciton mass.²⁷ Figure 3 shows a comparison of the theoretic-

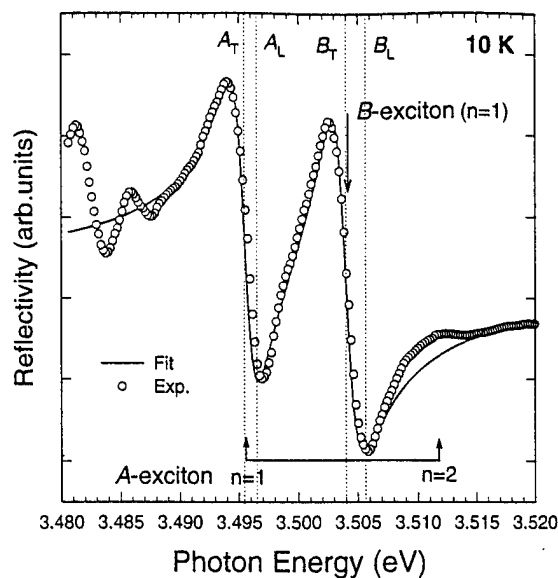


FIG. 3. Comparison of a theoretical fit taking into account spatial dispersion of the dielectric function to the 10-K reflection spectrum of 2.5- μm GaN/sapphire (klc and Elc).

cal fit using Eq. (5) to the experimental spectrum taken from the 2.5- μm GaN/sapphire sample. The dotted lines in the figure indicate the energy positions of transverse and longitudinal branches of the A and B excitons. The fitting results suggest that the energy position of the transverse excitons ($\hbar\omega_T$) is an appropriate reference point for the determination of exciton binding energy within the experimental uncer-

tainty. The best fits to the reflection spectra taken from various samples used in this work yield a longitudinal-transverse splitting $\Delta_{LT}(=\omega_L-\omega_T)\sim 0.001$ eV and a damping constant $\Gamma\sim 0.00275/\hbar$ eV for A-excitonic polaritons, and $\Delta_{LT}\sim 0.0015$ eV and $\Gamma\sim 0.003/\hbar$ eV for B-excitonic polaritons. However, these obtained values should be regarded as the lower limit for Δ_{LT} since the influence of possible mixing of A- and B-exciton states and exchange coupling due to the small energy separation was not taken into account using the simple model described by Eq. (5).

In summary, we have studied the excitonic transitions in high-quality GaN epitaxial films with the emphasis on estimating the binding energy for the intrinsic excitons in GaN. Strong, sharp derivativelike spectral structures of exciton transitions associated with the ground state and excited states of A, B, and C excitons in GaN epitaxial layers observed in photoreflectance spectra enabled us to accurately determine the transition energies and make positive identifications for those structures. Within the framework of the effective-mass approximation, we were able to make a straightforward estimate of the binding energy for these intrinsic excitons. With consideration of the spatial dispersion of the dielectric function, the longitudinal-transverse splittings and the phenomenological damping constants of A- and B-excitonic polaritons in GaN were also estimated by theoretical fitting to the conventional reflection spectra.

We are pleased to acknowledge helpful discussions with Professor X. C. Xie. This work at OSU was supported by AFOSR, DARPA, ONR, and ARO. The work at NCSU was supported by ONR under Contract No. N00014-92-J-1477.

- ¹J. I. Pankove, in *Diamond, Silicon Carbide and Related Wide Bandgap Semiconductors*, edited by J. T. Glass, R. F. Messier, and N. Fujimori, MRS Symposia Proceedings No. 1652 (Materials Research Society, Pittsburgh, 1990), p. 515, and references therein.
- ²S. Strite and H. Morkoç, *J. Vac. Sci. Technol. B* **10**, 1237 (1992), and references therein.
- ³H. Morkoç, S. Strite, G. B. Gao, M. E. Lin, B. Sverdlov, and M. Burns, *J. Appl. Phys.* **76**, 1363 (1994).
- ⁴R. Dingle and M. Illegeme, *Solid State Commun.* **9**, 175 (1971).
- ⁵R. Dingle, D. D. Sell, S. E. Stokowski, and M. Illegems, *Phys. Rev. B* **4**, 1211 (1971).
- ⁶B. Monemar, *Phys. Rev. B* **10**, 676 (1974).
- ⁷W. Shan, T. J. Schmidt, X. H. Yang, S. J. Hwang, J. J. Song, and B. Goldenberg, *Appl. Phys. Lett.* **66**, 985 (1995).
- ⁸B. Gil, O. Briot, and R.-L. Aulombard, *Phys. Rev. B* **52**, R17028 (1995).
- ⁹M. Smith, G. D. Chen, J. Y. Lin, H. X. Jiang, M. Asif Khan, C. J. Sun, Q. Chen, and J. W. Yang, *J. Appl. Phys.* **76**, 7001 (1996).
- ¹⁰G. D. Chen, M. Smith, J. Y. Lin, and H. X. Jiang, S. H. Wei, M. Asif Kahn, and C. J. Sun, *Appl. Phys. Lett.* **68**, 2784 (1996).
- ¹¹D. C. Reynolds, D. C. Look, W. Kim, O. Aktas, A. Botchkarev, A. Salvador, H. Morkoç, and D. N. Talwar, *J. Appl. Phys.* **80**, 594 (1996).
- ¹²S. Chichibu, A. Shikanai, T. Azuhata, T. Sota, A. Kuramata, K. Horino, and S. Nakamura, *Appl. Phys. Lett.* **68**, 3766 (1996).
- ¹³W. Shan, A. J. Fischer, J. J. Song, G. E. Bulman, H. S. Kong, M. T. Leonard, W. G. Perry, M. D. Bremser, and R. F. Davis, *Appl. Phys. Lett.* **69**, 740 (1996).
- ¹⁴D. G. Thomas and J. J. Hopfield, *Phys. Rev.* **116**, 573 (1959).
- ¹⁵D. E. Aspnes, in *Optical Properties of Solids*, edited by M. Balkanski (North-Holland, Amsterdam, 1980), Chap. 4 A.
- ¹⁶V. B. Sandomirskii, *Fiz. Tverd. Tela* **6**, 324 (1964) [*Sov. Phys. Solid State* **6**, 261 (1964)].
- ¹⁷O. J. Glembocki and B. V. Shanabrook, *Superlatt. Microstruct.* **3**, 235 (1987).
- ¹⁸F. H. Pollak and O. J. Glembocki, *SPIE Proc.* **946**, 2 (1988).
- ¹⁹H. Shen, S. C. Shen, F. H. Pollak, and R. N. Sacks, *Phys. Rev. B* **36**, 3487 (1987).
- ²⁰W. Shan, R. J. Hauenstein, A. J. Fischer, J. J. Song, W. G. Perry, M. D. Bremser, R. F. Davis, and B. Goldenberg, *Phys. Rev. B* **54**, 13460 (1996).
- ²¹R. J. Elliott, *Phys. Rev.* **108**, 1384 (1957).
- ²²G. Mahler and U. Schröder, *Phys. Status Solidi B* **61**, 629 (1974).
- ²³S. Xu and X. C. Xie (unpublished).
- ²⁴*Semiconductors, Physics of Group IV Elements and III-V Compounds*, edited by K. H. Hellwege and O. Madelung, Landolt-Börnstein (Springer-Verlag, Berlin, 1982), p. 178, and references therein.
- ²⁵S. I. Pekar, *Zh. Eksp. Teor. Fiz.* **33**, 1022 (1957) [*Sov. Phys. JETP* **6**, 785 (1958)].
- ²⁶J. J. Hopfield and D. G. Thomas, *Phys. Rev.* **132**, 563 (1963).
- ²⁷J. Lagois, *Phys. Rev. B* **23**, 5511 (1985).

Optical transitions in $\text{In}_x\text{Ga}_{1-x}\text{N}$ alloys grown by metalorganic chemical vapor deposition

W. Shan,^{a)} B. D. Little, and J. J. Song

Center for Laser Research and Department of Physics, Oklahoma State University,
Stillwater, Oklahoma 74078

Z. C. Feng, M. Schurman, and R. A. Stall

EMCORE Corporation, Somerst, New Jersey 08873

(Received 22 July 1996; accepted for publication 20 September 1996)

We present the results of optical studies of $\text{In}_x\text{Ga}_{1-x}\text{N}$ alloys ($0 < x < 0.2$) grown by metalorganic chemical vapor deposition on top of thick GaN epitaxial layers with sapphire as substrates. Photoluminescence (PL) and photorefectance measurements were performed at various temperatures to determine the band gap and its variation as a function of temperature for samples with different indium concentrations. Carrier recombination dynamics in the alloy samples were studied using time-resolved luminescence spectroscopy. While the measured decay time for the alloy near-band-edge PL emissions was observed to be generally around a few hundred picoseconds at 10 K, it was found that the decay time decreased rapidly as the sample temperatures increased. This indicates a strong influence of temperature on the processes of trapping and recombination of excited carriers at impurities and defects in the InGaN alloys. © 1996 American Institute of Physics. [S0003-6951(96)04748-1]

The quest for light emitting devices operating in blue and ultraviolet (UV) spectral regions has led to extensive studies on the properties of wide band-gap semiconductor materials for years. GaN based wide band-gap III-V nitride systems have recently attracted much attention as the most promising material for such device applications.¹⁻³ Among these, the $\text{In}_x\text{Ga}_{1-x}\text{N}$ alloy system is of particular importance because its direct band gap covers a wide spectral range from UV (~ 365 nm for GaN band gap) to red (~ 650 nm for InN band gap).^{4,5} In fact, recently commercialized superbright high-efficiency blue light emitting diodes and demonstrated current-injection laser diodes are all based on GaN/ $\text{In}_x\text{Ga}_{1-x}\text{N}$ heterostructures using $\text{In}_x\text{Ga}_{1-x}\text{N}$ layers as the active light emitting medium.^{6,7} In this report, we present the results of a study of the optical properties of $\text{In}_x\text{Ga}_{1-x}\text{N}$ alloys ($0 < x < 0.2$) grown on top of thick GaN epilayers by metalorganic chemical vapor deposition (MOCVD). Photoluminescence (PL) measurements were performed to assess the optical properties of samples with different alloy compositions. Photomodulation spectroscopy was used to determine the energy gap of the samples and to examine the effect of temperature on the band gap. Transient luminescence measurements were carried out to study photoluminescence decay processes in the alloy samples.

The InGaN alloy samples used in this work were nominally undoped single-crystal epilayers grown by MOCVD. Before the depositions of alloys, thick GaN layers were grown on sapphire substrates at a temperature of $\sim 1050^\circ\text{C}$ with 20-nm GaN buffers. The alloy layers were deposited at a temperature around 800°C . The thicknesses of the $\text{In}_x\text{Ga}_{1-x}\text{N}$ epitaxial layers were typically around a few thousand angstroms. Optical measurements were carried out on the InGaN samples over a temperature range from 10

K up to room temperature (295 K). Samples were mounted onto the cold finger of a closed cycle refrigerator and cooled down to desired temperatures for the measurements. Photoluminescence spectra were measured using an experimental setup consisting of a HeCd laser as the excitation source and a 1-M double-grating monochromator connected to a photon-counting system. For photomodulation reflectivity measurements, quasimonochromatic light dispersed by a 1/2-M monochromator from a xenon lamp and a chopped HeCd laser modulating beam were focused on the samples and the reflected signals were detected by an UV-enhanced photomultiplier tube connected to a lock-in amplification and data acquisition system. For transient luminescence measurements, a frequency-doubled pulsed dye laser synchronously pumped by a frequency-doubled mode-locked Nd:YAG laser was used as the primary excitation source (2 ps, 76 MHz). The luminescence signals were dispersed by a 1/4 M monochromator and detected by a synchroscan streak camera with a temporal resolution of 2 ps. The overall time resolution of the system is less than 15 ps.

10-K photoluminescence (PL) and photorelectance (PR) spectra of an $\text{In}_{0.14}\text{Ga}_{0.86}\text{N}$ sample are shown in Fig. 1. The PL spectrum (lower curve) exhibits two dominant spectral features: a sharp, strong emission line at higher energy arising from the near-band-edge excitonic transitions in GaN, and a relatively broad strong luminescence structure related to the alloy. The weak spectral structures observed between them were mainly luminescence signatures involving donor-acceptor-pair transitions in the GaN layer. The spectral feature with derivativelike line shapes on the lower-energy side of the PR spectrum (upper curve) corresponds to the optical transition associated with the alloy band gap, and the differential spectral structures at high energy are free-exciton transitions from the edges of different valence bands to that of the conduction band of wurtzite GaN. Photorelectance is a spectroscopic method utilizing modulation of the built-in

^{a)}Electronic mail: wshan@osuunx.ucc.okstate.edu

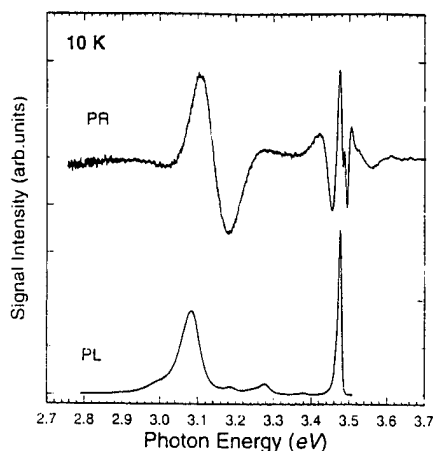


FIG. 1. PR (upper curve) and PL (lower curve) spectra of a $\text{In}_{0.14}\text{Ga}_{0.86}\text{N}$ sample at 10 K, are shown for comparison.

electric field in the samples. While a PR spectrum exhibits sharp derivativelike structures on a featureless background due to the optical modulation, the nature of the derivative is not immediately clear. Therefore, it is necessary to fit the PR curve to different line-shape functional forms^{8,9} in order to determine the energy positions associated with the optical transitions. We found that using a third derivative Gaussian line-shape functional form which is appropriate for describing band-to-band transitions^{10,11} results in a much better fit to the line positions and widths of the PR spectra than using a Lorentzian functional form.^{12,13} This suggests that the optical transition observed at even the lowest temperature is of the nature of band-to-band transition rather than excitonic transition, presumably because of the strong inhomogeneous broadening due to alloying effects. The best fits to the 10-K PR spectral features yield an energy of 3.143 eV for the transition in $\text{In}_{0.14}\text{Ga}_{0.86}\text{N}$, indicating a large Stokes shift (~ 60 meV) between the PL peak position and the actual band-to-band transition energy.

With increasing temperature, the PL signal from the alloy layer quickly lost its intensity and spectral signature due to the increasingly enhanced nonradiative recombination processes and thermal broadening of the emission structures, whereas PR spectral structures associated with the InGaN band gap could be well resolved up to room temperature for all alloy samples used. Figure 2 shows the shift of optical transition energy as a function of temperature for the $\text{In}_{0.14}\text{Ga}_{0.86}\text{N}$ sample. The solid line in the figure represents the best fit to the Varshni empirical equation¹⁴

$$E_0(T) = E_0(0) - \alpha T^2 / (\beta + T), \quad (1)$$

where $E_0(0)$ is the transition energy at 0 K, and α and β are constants referred to as Varshni thermal coefficients. The parameters obtained from the best fit for the sample are given in the figure. The better spectral resolution of PR spectroscopy compared to PL measurement enables us to determine the actual energy gaps for the InGaN alloy samples used in this work. In Fig. 3, we plot the measured energy gaps of various samples at 10 and 295 K against their alloy compositions, with 10-K PL results for comparison. Within the alloy composition range studied in this work, the PR results are in reasonably good agreement with the theoretical pre-

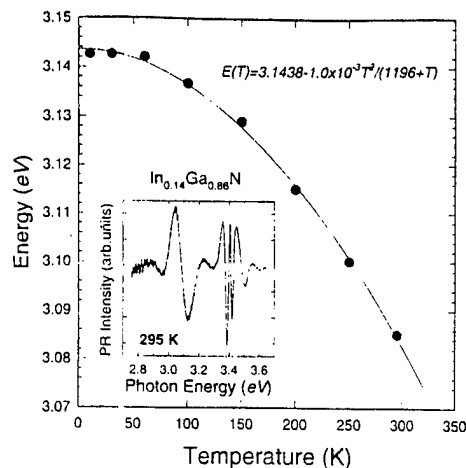


FIG. 2. Temperature dependence of interband transitions energy of the $\text{In}_{0.14}\text{Ga}_{0.86}\text{N}$ sample. The solid curve represents least-squares fits to the experimental data using Varshni empirical equation. The inset shows a room-temperature PR curve of the sample.

diction for the dependence of the $\text{In}_x\text{Ga}_{1-x}\text{N}$ band gap on In concentration including the bowing effect: $E(x) = 3.5 - 2.63x + 1.02x^2$ eV.¹⁵ These measured values suggest that the uncertainty in determination of the alloy concentrations by x-ray measurements is $\sim 1\%$. On the other hand, the scattered PL data, as indicated by the figure, are apparently not a reliable way to map energy gap evolution for the alloy system because the PL signals are most likely associated with impurities and the effects of alloy disorder broadening.

We have also performed time-resolved PL measurements to study carrier recombination dynamics in the $\text{In}_x\text{Ga}_{1-x}\text{N}$ samples. Figure 4 shows the temporal evolution of spectrally integrated luminescence associated with an $\text{In}_{0.08}\text{Ga}_{0.92}\text{N}$ sample as selected temperatures. The time evolution of the luminescence is dominated by exponential decay with a measured effective lifetime around 340 ps at 10 K. The temporal profile of the luminescence gradually evolved into an increasingly nonexponential decay with a drastic decrease of the effective lifetime for the main decay

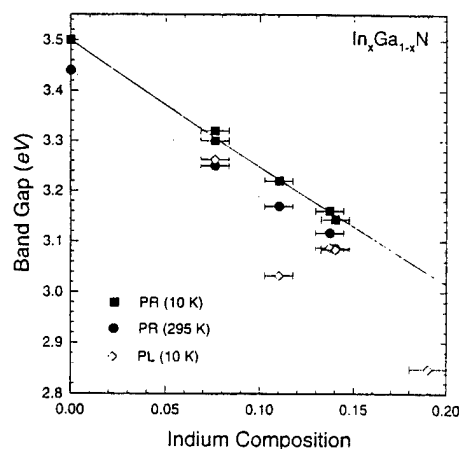


FIG. 3. Energy gaps of various samples measured by PR at 10 K and 295 K vs their alloy compositions. 10-K PL results are shown for comparison. The solid line is the theoretical prediction for the dependence of the $\text{In}_x\text{Ga}_{1-x}\text{N}$ band gap on In concentration. The dotted line is that for room temperature (295 K) data.

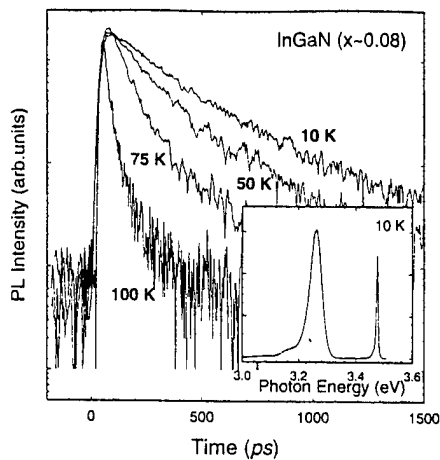


FIG. 4. Temporal variation of the alloy PL peak for an $\text{In}_{0.08}\text{Ga}_{0.92}\text{N}$ sample at selected temperatures. The inset shows the 10-K PL spectrum over a broad spectral range.

process as the sample temperature increased. At temperatures around 150 K, the deduced lifetime for the PL decay has already reached the limit of our instrumental resolution of 15 ps. Similar results were obtained for all samples used in this work: the measured decay time for near-band-edge PL emissions was generally around a few hundred picoseconds at 10 K, and it decreased rapidly as sample temperatures increased. The measured decay time was examined as a function of energy positions of the 10-K PL peak shown in the inset of Fig. 4. The reason for doing so is to verify whether the PL structure resulted from recombination of localized excitons or emission directly involving impurity states and alloy potential fluctuations.^{16,17} If the PL emission originated from localized excitons in the InGaN alloys, the lifetime is predicted to follow the so-called power-law dependence,¹⁸ i.e., $\tau \propto E_{BX}^{3/2}$, where E_{BX} is the exciton localization energy. That means the measured lifetimes increase with increasing exciton localization energy which corresponds to a decrease in electron-hole wave function overlap. Our experimental results did not exhibit such a three-halves dependence of measured effective lifetime upon the energy position, suggesting impurity states and alloy potential fluctuations are most likely responsible for the alloy PL signals.

Although the radiative recombination processes involved in PL emissions in the InGaN samples are not of excitonic nature as mentioned previously it is still worthy to make a comparison of the results obtained in this work with the excitonic emission decay processes observed in pure GaN.¹⁹ While the measured effective lifetime for PL decay in InGaN samples was found to be an order of magnitude longer than that in GaN, the dependence of the PL decay process on the temperature in InGaN alloys is much stronger than that in GaN.²⁰ Such a strong temperature influence suggests that although recombination from carriers bound to extrinsic states such as defects or impurities can be very efficient at low temperatures, the measured decay time is still determined by detailed decay kinetics in the alloy samples. The observed decrease of the PL decay time along with the increasingly nonexponential transient characteristics with temperature indicates that incrementally stronger nonradiative relaxations occur as the temperature increases, resulting in

continued faster decay of the photogenerated carrier population. The decrease of PL in both intensity and observed effective lifetime with temperature suggests that nonradiative processes including trapping and recombination at energy levels associated with impurities and defect centers at or near the midgap (Shockley-Read-Hall recombination), surface recombination, and Auger recombination prevail in the InGaN alloys at relatively high temperatures. It is well known that the lifetime of photogenerated carriers is strongly dependence on the sample quality for semiconductor alloy systems.¹⁷ The observations reported here indicate that the impurities and defects incorporated during the InGaN epitaxial growth generate PL quenching centers in the layers which adversely affect the carrier radiative recombination.

In conclusion, we have studied optical transition processes in $\text{In}_x\text{Ga}_{1-x}\text{N}$ alloys using a few different approaches including both conventional and time-resolved PL measurements as well as PR spectroscopy. The highly sensitive PR spectroscopy allows us to unambiguously determine the band gap energy for the alloy samples within the alloy composition range ($0 < x < 0.2$) studied. We found that the low-temperature PL emission from alloy layers are primarily recombinations directly involving impurity states and alloy potential fluctuations. Strong dependence of PL decay on temperature observed in the various alloy samples indicates that the trapping and recombination of photogenerated carriers at impurities and defect centers are dominant channels in determining the carrier population decay process.

This work at OSU was supported by AFOSR, ARO, DARPA, and ONR.

- ¹S. Strite and H. Morkoç, *J. Vac. Sci. Technol. B* **10**, 1237 (1992), and references therein.
- ²J. I. Pankove, *Mater. Res. Soc. Symp. Proc.* **162**, 515 (1990), and references therein.
- ³H. Morkoç, S. Strite, G. B. Gao, M. E. Lin, B. Sverdlov, and M. Burns, *J. Appl. Phys.* **76**, 1363 (1994).
- ⁴K. Osamura, S. Naka, and Y. Murakami, *J. Appl. Phys.* **46**, 3432 (1975).
- ⁵See, for example, S. Nakamura, T. Mukai, and M. Senoh, *J. Appl. Phys.* **76**, 8189 (1994).
- ⁶S. Nakamura, M. Senoh, S. Nagahama, N. Iwasa, T. Yamada, T. Matsushita, H. Kiyoku, and Y. Sugimoto, *Jpn. J. Appl. Phys.* **35**, L74 (1996).
- ⁷S. Nakamura, M. Senoh, S. Nagahama, N. Iwasa, Y. Yamada, T. Matsushita, H. Kiyoku, and Y. Sugimoto, *Appl. Phys. Lett.* **68**, 2105 (1996).
- ⁸D. E. Aspnes, in *Optical Properties of Solids*, edited by M. Balkanski (North-Holland, Amsterdam, 1980), Chap. 4A.
- ⁹F. H. Pollak and O. J. Glembocki, *Proc. SPIE* **946**, 2 (1988).
- ¹⁰O. J. Glembocki and B. V. Shanabrook, *Superlattices Microstruct.* **5**, 235 (1987).
- ¹¹H. Shen, S. H. Pan, F. H. Pollak, M. Dutta, and T. R. AuCoin, *Phys. Rev. B* **36**, 9384 (1987).
- ¹²O. J. Glembocki and B. V. Shanabrook, in *Semiconductors and Semimetals*, edited by D. G. Semler and C. L. Little (Academic, New York, 1992), Vol. 36, Chap. 4.
- ¹³F. H. Pollak and H. Shen, *Mater. Sci. Eng. R* **10**, 275 (1993).
- ¹⁴Y. P. Varshni, *Physica* **34**, 149 (1967).
- ¹⁵A. F. Wright and J. S. Nelson, *Appl. Phys. Lett.* **66**, 3051 (1995).
- ¹⁶M. Voos, R. F. Leheny, and J. Shah, in *Optical Properties of Solids*, edited by M. Balkanski (North-Holland, Amsterdam, 1980), Chap. 6.
- ¹⁷L. Pavesi and M. Guzzi, *J. Appl. Phys.* **75**, 4779 (1994).
- ¹⁸E. I. Rashba and G. E. Gurgenishvili, *Sov. Phys. Solid State* **4**, 759 (1962).
- ¹⁹W. Shan, X. E. Xie, J. J. Song, and B. Goldenberg, *Appl. Phys. Lett.* **67**, 2512 (1995).
- ²⁰J. J. Song, W. Shan, T. Schmidt, X. H. Yang, A. Fischer, S. J. Hwang, B. Taheri, B. Goldenberg, R. Horning, A. Salvador, W. Kim, Ö. Aktas, A. Botchkarev, and H. Morkoç, *Proc. SPIE* **86** (1996).

Optical studies of GaN and GaN/AlGaIn heterostructures on SiC substrates

W. Shan,^{a)} A. J. Fischer, and J. J. Song

Center for Laser Research and Department of Physics, Oklahoma State University, Stillwater, Oklahoma 74078

G. E. Bulman, H. S. Kong, and M. T. Leonard

Cree Research, Inc., Durham, North Carolina 27713

W. G. Perry, M. D. Bremser, and R. F. Davis

Department of Materials Science and Engineering, North Carolina State University, Raleigh, North Carolina 27695

(Received 22 April 1996; accepted for publication 29 May 1996)

We present the results of spectroscopic studies on GaN based epitaxial materials on SiC substrates by metalorganic chemical vapor deposition. A variety of techniques has been used to study the optical properties of GaN epilayers and GaN/AlGaIn heterostructures. Sharp spectral structures associated with the intrinsic free excitons were observed by photoluminescence and reflectance measurements from GaN based materials grown on SiC substrates. The residual strain was found to have a strong influence in determining the energies of exciton transitions. Picosecond relaxation studies of exciton decay dynamics suggest that an AlGaIn cladding layer with a small mole fraction of AlN can be relatively effective in enhancing the radiative recombination rate for excitons by reducing the density of dislocations and suppressing surface recombination velocity in the GaN active layer for the GaN/AlGaIn heterostructure samples. © 1996 American Institute of Physics. [S0003-6951(96)04532-9]

GaN based wide band-gap III-V nitride semiconductors have been extensively studied for their device applications, such as high-power amplifiers, UV, blue, green, and yellow light-emitting diodes (LED's), and short-wavelength laser diodes.¹⁻³ Observation of optically pumped stimulated emission in GaN epilayers has led to increased interest in the development of efficient nitride UV-visible light emitters.^{4,5} In fact, superbright high-efficiency blue LED's have recently been commercialized and current-injection laser diodes based on nitride heterostructures have been reported by the Nichia group.^{6,7} So far, the majority of research activities, including the assessment of material properties and the development of devices, has concentrated on nitrides grown on sapphire substrates, although its lattice parameter and coefficient of thermal expansion are significantly different from that of any III nitrides. An alternative substrate material for III-nitride epitaxial growth is SiC. It has many advantages over sapphire in terms of nitride epitaxy deposition and device fabrication: close match of lattice parameters and coefficient of thermal expansion to that of III nitrides; higher thermal conductivity of SiC offers greater power handling and improved reliability; and both *n*- and *p*-type electrical conductivity can be achieved allowing vertical device structure. In this report, we present the results of optical studies of the properties of GaN epilayers and GaN/AlGaIn heterostructures grown by metalorganic chemical vapor deposition (MOCVD) on 6H-SiC (0001) substrates. The effects of strain on the exciton transitions in the GaN epitaxial materials on SiC were examined and compared with those observed in the GaN epilayer on sapphire samples. The dynamics of photoexcited excess carriers in the region of near-band-edge excitonic emissions were investigated by transient luminescence spectroscopy in the picosecond regime.

Samples used in this study were all nominally undoped single-crystal films grown on (0001) 6H-SiC substrates by MOCVD. AlN buffers were deposited on the substrates before the growth of GaN. GaN layers were deposited at 1050 °C directly on the AlN buffers. The GaN/AlGaIn heterostructures used in this work included both double heterostructure (DH) samples and separate confinement heterostructure (SCH) samples. The DH and SCH structures were deposited on GaN epilayers with the thickness typically around three microns. The particular DH structure under discussion has an ~800 Å thick GaN active layer, surrounded by a few thousand Å Al_{0.1}Ga_{0.9}N cladding layers. The SCH structure consists of a 100 Å thick GaN quantum well, with an Al_xGa_{1-x}N cladding layer and a lower mole fraction Al_xGa_{1-x}N waveguide layer symmetrically locating on each side. The nominal Al compositions are 11% and 6%, respectively. Conventional photoluminescence (PL) spectra were measured with either a cw HeCd laser (325 nm) or a frequency-doubled Ar⁺ laser (244 nm) as the excitation source and a 1-M double-grating monochromator connected to a photon-counting system. For reflectance measurements, the quasimonochromatic light dispersed by a $\frac{1}{2}$ -M monochromator from a xenon lamp was focused on the sample, and the reflectance signals were detected using a lock-in amplification system. Time-resolved photoluminescence (TRPL) measurements were performed using a frequency tunable pulsed laser (2 ps pulse duration, 76 MHz) as an excitation source and a streak camera (2 ps resolution), in conjunction with a $\frac{1}{4}$ -M monochromator as a detection system.

The GaN based samples studied in this work exhibit strong near-band-edge exciton luminescence. Results of PL spectroscopy from a 3.7-μm GaN epilayer sample are shown in Fig. 1 at selected temperatures. The intensity of the strongest emission line marked by BX in Fig. 1 was found to decrease much faster than that labeled FX as the temperature

^{a)}Electronic mail: wshan@osuunx.ucc.okstate.edu

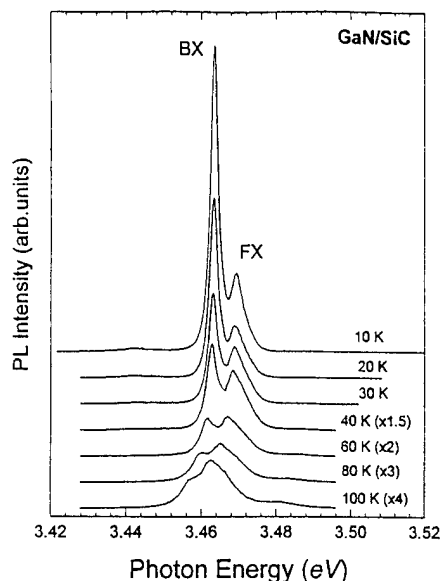


FIG. 1. Near-band-edge exciton luminescence spectra taken from a 3.7- μ m GaN epilayer on SiC at selected temperatures.

increased. It became hardly resolvable at the temperatures higher than 100 K (not shown). Such variations of the luminescence intensity as a function of temperature indicate that the emission line can be attributed to the radiative recombination of excitons bound to neutral donors. The second strongest luminescence structure, together with the weak emission feature on the higher energy side, can be assigned to intrinsic free-exciton emissions. Figure 2 shows a reflectance spectrum taken from the sample at 10 K. Three exciton resonances associated with the transitions referred to as the A, B, and C exciton transitions^{8,9} between the bottom of the conduction band (Γ_7^C) and three topmost valence band edges ($\Gamma_9^V + \Gamma_7^V + \Gamma_7^V$) are indicated by vertical arrows. The energy positions of these transitions are 3.470, 3.474, and 3.491 eV, respectively. We note that the values of the transition energies obtained here are lower than those reported in the literature,⁹⁻¹¹ for example, 3.485, 3.493, and 3.518 eV, for GaN on sapphire substrates.¹⁰ Such discrepancy can be at-

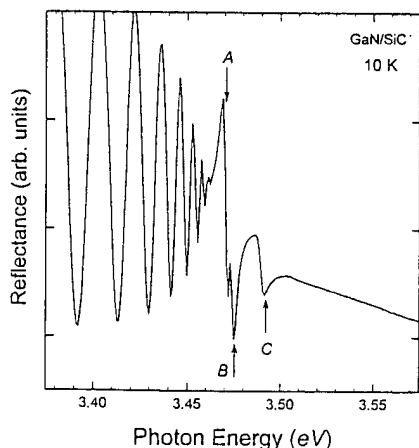


FIG. 2. Reflectance spectrum of the exciton transition region of the MOCVD GaN/SiC sample at 10 K. The oscillatory structures at lower energy are interference effects caused by the heterointerface.

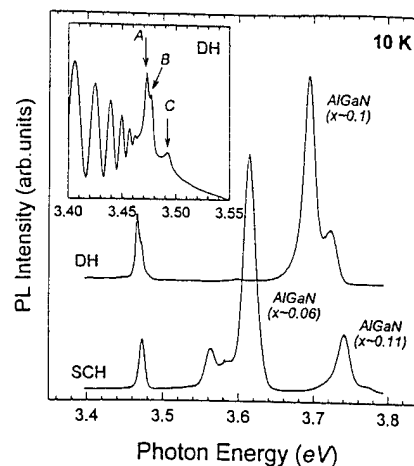


FIG. 3. 10-K PL spectra of a DH and a SCH sample grown on SiC. The inset illustrates the exciton transition signatures of the GaN active layer in the DH sample measured by reflectance spectroscopy.

tributed to the effects of residual strain in the epilayers due to the mismatch of lattice parameters and coefficients of thermal expansion between GaN and the substrate materials.^{11,12} Because of the inevitable occurrence of strain relaxation by the formation of a large density of dislocations, it is generally difficult to separate the strain effects caused by lattice-parameter mismatch from the ones involving thermal-expansion mismatch so as to exactly determine their influences on the optical properties of GaN epitaxial layers. However, by comparing the observed exciton transition energies in GaN epilayers deposited on sapphire and SiC to the values (3.4751, 3.4815, and 3.503 eV) obtained from virtually strain-free bulk GaN reported in Ref. 9, one can infer that the overall effects of residual strain generated in GaN on sapphire is compressive, which results in an increased band gap, while the stress induced in GaN on SiC is tensile, which leads to a decrease in measured exciton transition energies. Therefore, we conclude that residual strain induced by thermal-expansion mismatch in GaN based epitaxial layers has the prevailing influence on the energy variations of exciton transitions, since lattice-mismatch induced strain has a completely opposite effect on the variation of the GaN band gap.

Figure 3 shows the 10 K PL spectra of the DH and SCH samples. The inset highlights the signatures of intrinsic free exciton transitions observed by reflectance measurements from the GaN active layer of the DH structure. The emission peaks at the energy position around 3.47 eV in the PL spectra are exciton luminescence from the GaN active layers in these two heterostructures. The peak position of the SCH GaN active layer was found to be ~ 10 meV higher than that of the DH GaN layer. The blue shift might be due to quantum confinement effects. By using the envelope function approximation approach,¹³ the lowest confinement energy can be readily calculated, with electron the effective mass $m^* \sim 0.2m_0$ and the hole effective mass $m^* \sim 0.8m_0$,¹⁴ to be ~ 10 meV for electrons and ~ 3 meV for holes in a 100-Å single GaN quantum well with $\text{Al}_{0.06}\text{Ga}_{0.94}\text{N}$ barriers. This estimation is consistent with the experimental observation. The strong and relatively broad emission structures at higher

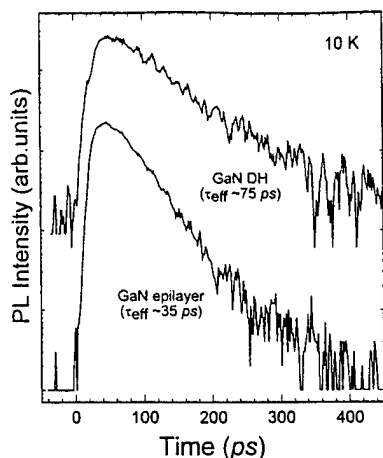


FIG. 4. Comparison of PL decay of exciton emissions in the GaN DH sample and an epilayer sample. The curves are vertically displaced for clarity.

energies are luminescence associated with AlGaIn layers as labeled in the figure. The doublet spectral feature related to AlGaIn alloys in the DH sample presumably arises from a small alloy concentration difference between two AlGaIn cladding layers. If this is the case, the observed energy separation of ~ 25 meV suggests that slightly less than a 1% alloy concentration fluctuation occurred during the preparation of DH structure by MOCVD growth. However, the rather complicated spectral structure on the lower energy side of the main emission peak exhibited by the alloy waveguiding layers in the SCH sample cannot be simply assigned to the deviation in Al compositions between the two layers. This is an issue requiring further study.

We have also performed time-resolved PL measurements to study the dynamics of exciton luminescence in the GaN active layer of the DH structure. In order to avoid generating carriers in the AlGaIn cladding layers and to prevent the profound effects of carrier diffusion from barrier layers into the active layer, the photon energy of the picosecond pulsed laser was tuned to very closely to the band gap of GaN with an excitation wavelength at ~ 345 nm. Figure 4 presents the time evolution of bound-exciton emission observed in the GaN/AlGaIn DH sample, where a typical PL time-decay curve from a GaN epitaxial film taken under the same experimental conditions is also given for comparison. Both samples were deposited on SiC substrates under similar growth conditions except that the DH structure was deposited on top of one of them. As shown in the figure, the measured decay time for the bound exciton emission in the DH sample was found to be (~ 75 ps) twice as longer as that in the GaN epilayer (~ 35 ps). Recent exciton dynamic studies have revealed that the capture of excitons and trapping of carriers by nonradiative centers at defects and impurities play a major role in the recombination processes responsible for the exciton population decay in GaN samples.¹⁵ However, it is unclear whether or not dislocations behave like nonradiative recombination centers. The results presented here suggest that dislocations most likely involve the nonradiative recombination processes. The increase in the exciton PL decay time observed in the DH sample indicates that the density of nonradiative recombination centers in the GaN active

layer of the DH sample is smaller than that of the bare GaN epilayer. The AlGaIn cladding layers could be a factor in the enhancement of the radiative recombination rate by reducing the density of dislocations in the GaN active layer, since it is known that a heterostructure system with built-in strain can significantly reduce the density of defects such as dislocations.¹⁶ In addition, the deposition of a cladding layer on top of the GaN active layer could have passivated the surface states resulting in a reduction in the nonradiative recombination velocity of the photoexcited carriers on the bare surface and in its vicinity.

In conclusion, strong, sharp spectral structures associated with exciton transitions in GaN epitaxial layers and GaN/AlGaIn heterostructures grown on 6H-SiC substrates by MOCVD were observed in photoluminescence and reflectance spectra. The observation of exciton transitions with lower energies in the epitaxial GaN based materials grown on SiC compared to that on sapphire substrates suggests that the GaN based epilayers on SiC substrates are subject to tensile strain, while those on sapphire substrates are under compression. The residual strain induced by lattice-parameter and thermal-expansion mismatch plays an important role in determining the exciton transition energies. In addition, our picosecond relaxation study of exciton decay dynamics suggests that for the GaN/AlGaIn heterostructure samples, an AlGaIn cladding layer with a small mole fraction AlN can be relatively effective in enhancing the radiative recombination rate for excitons as a result of reducing the density of dislocations and suppressing surface recombination velocity in the GaN active layer.

This work at OSU was supported by AFOSR, DARPA, ONR, and ARO. The work at CREE was supported by DARPA under Contract No. MDA972-95-C-0016. The work at NCSU was supported by ONR under Contract No. N00014-92-J-1477.

- ¹ J. I. Pankove, Mater. Res. Soc. Symp. Proc. **162**, 515 (1990), and references therein.
- ² S. Strite and H. Morkoç, J. Vac. Sci. Technol. B **10**, 1237 (1992), and references therein.
- ³ H. Morkoç, S. Strite, G. B. Gao, M. E. Lin, B. Sverdlov, and M. Burns, J. Appl. Phys. **76**, 1363 (1994).
- ⁴ X. H. Yang, T. Schmidt, W. Shan, J. J. Song, and B. Goldenberg, Appl. Phys. Lett. **66**, 1 (1995).
- ⁵ A. S. Zubrilov, V. I. Nikovlaev, V. A. Dmitriev, K. G. Irvine, J. A. Edmond, and C. H. Carter, Jr., Inst. Phys. Conf. Ser. **141**, 525 (1995).
- ⁶ S. Nakamura, M. Senoh, S. Nagahama, N. Iwasa, T. Yamada, T. Matsushita, H. Kiyoku, and Y. Sugimoto, Jpn. J. Appl. Phys. **35**, L74 (1996).
- ⁷ S. Nakamura, M. Senoh, S. Nagahama, N. Iwasa, T. Yamada, T. Matsushita, H. Kiyoku, and Y. Sugimoto, Appl. Phys. Lett. **68**, 2105 (1996).
- ⁸ R. Dingle and M. Illegeme, Solid State Commun. **9**, 175 (1971).
- ⁹ B. Monemar, Phys. Rev. B **10**, 676 (1974).
- ¹⁰ W. Shan, T. J. Schmidt, X. H. Yang, S. J. Hwang, J. J. Song, and B. Goldenberg, Appl. Phys. Lett. **66**, 985 (1995).
- ¹¹ B. Gil, O. Briot, and R.-L. Aulombard, Phys. Rev. B **52**, R17028 (1995).
- ¹² W. Rieger, T. Metzger, H. Angerer, R. Dimitrov, O. Ambacher, and M. Stutzmann, Appl. Phys. Lett. **68**, 970 (1996).
- ¹³ G. Bastard, Phys. Rev. B **25**, 7584 (1982).
- ¹⁴ Landolt-Bornstein, edited by O. Madelung, New Series, Group 3, Vol. 17a (Springer, Berlin, 1982).
- ¹⁵ W. Shan, X. C. Xie, J. J. Song, and B. Goldenberg, Appl. Phys. Lett. **67**, 2512 (1995).
- ¹⁶ Z. Liliental-Weber, H. Sohn, and J. Washburn, in *Semiconductors and Semimetals*, edited by E. R. Weber (Academic, Boston, 1993), Vol. 38, Chap. 9.

Optical Properties of Mg-GaN, GaN/AlGa_N SCH structures, and GaN on ZnO Substrates

H. Morkoç*, W. Kim, Ö. Aktas, A. Salvador, and A. Botchkarev, University of Illinois, Coordinated Science Laboratory and Materials Research Laboratory, 104 South Goodwin Avenue, Urbana, IL 61801

D. C. Reynolds, and D. C. Look, University Research Center, Wright State University, Dayton Ohio 45435

M. Smith, G. D. Chen, J. Y. Lin, and H. X. Jiang, Department of Physics, Kansas State University, Manhattan, Kansas 66506-2601

T.J. Schmidt, X.H. Yang, W. Shan, and J.J. Song, Dept. of Physics, Oklahoma State University, Stillwater, OK 74078-0444

B. Goldenberg, Honeywell Technology Center, 4B75, 1201 State Highway 55 Plymouth MN 55441-4799

C. W. Litton and K. Evans, Electronic Research Directorate, WL/ELR, Building 620 Wright Patterson AFB, OH 45433

Abstract

GaN films and GaN/AlGa_N heterostructures have been grown by MBE. GaN films doped with varying levels of Mg indicate effective mass acceptor at low doping concentrations, as determined from strong photoluminescence emission at about 380 nm. As the Mg concentration is increased the photoluminescence emission line red shifts considerably, indicating the formation of Mg-related or induced complexes whose lifetimes are relatively short. GaN/AlGa_N separate confinement heterostructures grown on sapphire show strong near ultraviolet stimulated emission at room temperature in a side-pumping configuration. The pumping threshold for stimulated emission at room temperature was found to be ~90 kW/cm². Initial GaN films grown on ZnO substrates show the A exciton in low temperature photoluminescence. ZnO is being considered for nitride growth because of its stacking order and close lattice match.

* On sabbatical leave at Wright Laboratory on a University Resident Research Program funded by AFOSR.

Introduction

Unlike Si and GaAs technologies, devices based on group-III nitrides are capable of operating at high temperatures and hostile environments as well as emitters and detectors for wavelengths shorter than green^{1,2,3,4}. Most notable of the group-III nitrides are AlN, GaN, InN and their alloys, which are all wide bandgap semiconductors. They crystallize in both wurtzite and zincblende polytypes, the former being the more stable phase. Wurtzitic GaN, AlN and InN have direct room temperature bandgaps of 3.4, 6.2, and 1.9 eV, respectively. The group-III nitrides thus formed span a continuous range of direct bandgap energies throughout much of the visible spectrum well into the ultraviolet wavelengths. This is one of the reasons fueling the recent interest in GaN, AlN, InN, and their tertiary alloys for short wavelength optoelectronic device applications. These optoelectronic devices, especially emitters such as the light emitting diodes (LEDs) and lasers, can be active in the yellow, green, blue, and ultraviolet (uv) wavelengths.⁵ LEDs have expanded remarkably not only in terms of the range of wavelengths of emission available, but also brightness^{6,7,8}. These LEDs have proved to be reliable and have applications, for example, in displays, lighting, indicator lights, advertisement, traffic signs and traffic signals, possibly light sources for accelerated photosynthesis, and medicine for diagnosis and treatment^{9,10,11,12,13,14,15}. As for coherent sources, they are crucial for high density optical read and write technologies. Because the diffraction limited optical storage density increases roughly quadratically as the probe laser wavelength is reduced, nitride based coherent sources at wavelengths down to uv are attracting a good deal of attention.

Many of the difficulties besetting nitrides have recently been overcome or are about to be overcome. Despite disappointing results early on, p-type conductivity has been achieved for GaN, AlN, and some of their alloys. On the metal contact front, specific contact resistivities have steadily dropped to below $10^{-7} \Omega\text{cm}^{-2}$. While the recent developments in GaN and related compounds have been truly breathtaking, further progress in this material system hinges on the reduction of defects which is closely tied to substrates. Ultimately, substrates with close lattice match and stacking order match to GaN or InGaN, most likely native substrates, may be necessary to achieve the potential performance. In this article we will discuss our recent effort in the growth and characterization of GaN and GaN/AlGaIn heterostructures.

Experimental

The structures were grown by Reactive MBE. The chamber pressure was kept at 2.5×10^{-5} Torr during film growth, and the substrate temperature was varied between 610 and 820 °C, which was monitored by a pyrometer focused on the surface of the growing film. Sapphire substrates were degreased with organic solvents, and etched in a hot solution of H_2SO_4 and H_3PO_4 ($\text{H}_2\text{SO}_4 : \text{H}_3\text{PO}_4 = 3 : 1$) for about 20 mins. They were then rinsed with deionized (DI) water and dried by blowing filtered nitrogen. Nitridation was performed by exposing sapphire substrates to a nitrogen flux for 5-15 mins. at 800 °C. Prior to the GaN growth, about 650 Å of AlN was grown on sapphire at a growth temperature of 800 °C. Note that this growth is decidedly different from that with the low temperature buffer layers employed in the MOCVD process.

Separate Confinement Heterostructures

The GaN/AlGaIn separate confinement heterostructure has a 600 Å thick AlN layer, directly grown on sapphire, followed by a GaN buffer layer, an AlGaIn cladding layer, a low mole fraction AlGaIn waveguide layer, a 70 Å thick GaN quantum well which is capped by a low mole fraction AlGaIn waveguide and an AlGaIn cladding layer. The quantum well was doped with Si to a level of $5 \times 10^{17} \text{ cm}^{-3}$. Samples having a size of $3 \times 1 \text{ mm}^2$ were cut and mounted on a sapphire heat sink, which were then attached to copper sample holders for optical pumping experiments.¹⁶ Under low-excitation, the room temperature spectra exhibit a relatively weak and broad emission feature with the peak position around 365 nm, and the emission intensity linearly increases with the excitation power density. As the excitation power density increases, a sharp narrow emission feature appears on the higher energy side of the spontaneous emission peak. The position of the maximum of this newly emerged emission feature is at ~361.5 nm. Its emission intensity increases super linearly with the excitation power. This new emission structure becomes the dominant feature as the pumping power density is further increased. Spectral narrowing, super linear increase in intensity with the excitation power density, as well as the complete suppression of the broad emission background, are characteristics of stimulated emission.

The onset of the steep rise of the emission intensity marks the threshold for stimulated emission. The pumping threshold for stimulated emission was determined to be $\sim 90 \text{ kW/cm}^2$ for our GaN/AlGaIn SCH sample. The measured threshold value is approximately one order of magnitude less than our previously reported value for the GaN bulk-like films grown by metalorganic chemical vapor deposition.¹⁷ Generally, the threshold value can be affected by parameters which are dependent on the pumping source and quality of the sample and the facets. The specimens were just small pieces simply cut off from the large GaN/AlGaIn SCH wafer with no attempt to finesse the cut surfaces. Difficulties of forming high quality facets in sapphire are well known. This provides the basis for our optimism that the pumping power threshold for stimulated emission lasing in GaN can be lowered substantially with improved facets, possibly brought about by employing other substrates such as ZnO and spinel which are much more amenable to cleaved facet formation.

Mg Doped GaN

As in any wide bandgap semiconductor, p type doping in GaN and related materials is rather complex. In GaN for example, while the effective mass like acceptor is about 200 meV from the valence band, Mg doped GaN exhibits emission at centers which are about 0.5 eV above valence band when the Mg concentration exceeds a certain level. In optical spectra, two broad emission bands of about 290 (dominant for $T < 150$ K) and 550 meV (dominant for $T > 150$ K) below the band gap appear. Typical continuous-wave (CW) PL spectrum of p-type GaN layers at 10 K is dominated by a band at about 3.21 eV which nearly disappears for $T > 150$ K. As the temperature is increased above 150 K, a weak emission band at ~2.95 eV appears. Moreover, the peak position of the lower energy emission red shifts considerably as the Mg doping level is increased. At room temperature, the peak position of this lower energy emission band can be varied from 430 to about 700 nm.

In order to explore the physical origin of the observed emission lines, their dynamical behaviors have been studied.¹⁸ At low temperatures, PL decay is non exponential, but can be approximated by two exponential decay. The typical lifetime of the fast component which contributes 90 percent of the PL signal is about 0.6 ns, and the slow component is about 5.0 ns. In the temperature region $T < 150$ K where the 3.21 eV emission band dominates, the recombination lifetime decreases progressively from 0.6 to 0.3 ns as temperature increases from 10 to 140 K. This behavior can be accounted for by an increased nonradiative recombination rate at higher temperatures, caused by the nonradiative carrier transfer to the lower energy recombination channels. This is consistent with the observation of the thermal quenching of the 3.21 eV emission line and the subsequent increase in the emission intensity of the lower energy band at 2.95 eV with temperature.

In the higher temperature region ($T > 150$ K) where the lower energy emission band (~2.95 eV at $T < 150$ K) dominates, the fast decay component contributes nearly 95 percent of the PL signal and consequently the decay kinetics of PL are nearly single exponential. The temperature dependence of the recombination lifetime of the lower energy emission band indicates an increase with temperature reaching 0.3 at room temperature. This is due to the carrier transfer from the 3.21 eV recombination channel as discussed above.

The observed sub nanosecond PL recombination lifetimes suggest that the band- edge emissions in Mg-doped p-GaN result predominantly from the conduction band-to-impurity recombination, involving substitutional shallow Mg acceptors at low temperatures ($T < 150$ K) and Mg related deep level centers at high temperatures ($T > 150$ K). In such a context, the quenching of the 3.21 eV emission line is due to either thermal ionization of shallow neutral Mg acceptors or hole transfer from the shallow to the deep impurities as temperature increases.

GaN on ZnO

Lattice and thermal expansion mismatch between nitride films and the most frequently used substrates (SiC, sapphire) are often cited as one of the major causes of the observed extended and point defects. Inversion domain boundaries (IDB) and double positioning boundaries (DPB), have been identified as defects spreading into the bulk GaN layers^{19,20, 21}, the former, being well known in III-V on Si (100) epitaxy,²² arise from an inversion transformation of a binary compound. If special care were taken to initiate growth with only one species, such as As, then IDB's would not form. However substrates invariably contain steps, and with single-species initiation the lattice inverts across each single step on Si (100) and produces an IDB. One solution for avoiding IDB's on Si (100), is by making double-stepped substrates. In the case of DPB's there is an equal probability of nucleating two different FCC stacking sequences (ABC and ACB), a topic treated recently by Sverdlov et al.²³ who also suggested that ZnO would be a better substrate to GaN and related materials because of its stacking match to nitrides under discussion.

Attempts have already been made to take advantage of the relatively small lattice mismatch between ZnO and GaN in that there have been several preliminary reports of GaN growth on ZnO and InGaN on ZnO with crystalline quality of InGaN to be superior when grown on the well matched ZnO substrate²⁴. ZnO substrates also would allow for the growth of lattice matched or coherently strained heterostructures for optoelectronic and electronic devices²⁵. In this paper we report on the optical emission and reflection properties of GaN grown on vicinal c plane ZnO substrates.

We have utilized ZnO substrates prepared by Litton industries by the hydrothermal method. The GaN layers were then grown at substrate temperatures of about 650 °C with a growth rate of 1 $\mu\text{m}/\text{hour}$. The optical transitions from the sample were studied by photoluminescence (PL) and optical reflection. The PL was excited with a He-Cd laser. The reflection source was a Xenon lamp. The reflection was measured at approximately 15° off normal incidence. The details of the measurement apparatus can be found elsewhere²⁶.

The PL spectra for the GaN samples show that the ground state exciton transition associated with the A band appears dominant. The exciton associated with the B-band is not seen in emission; however, it can be seen in reflection. In this experiment we did classical reflection; however, it is off normal incidence by approximately 15° as noted before. The minimum in the A reflection peak is shifted to the higher energy from the A emission peaks by approximately 7 meV. Although the work is its embryonic stage and high quality substrates are lacking, clean luminescence emission with only the A exciton present is very exciting. The observed energies of A and B excitons, the latter in reflection only, provide us with necessary information to deduce the sign and extent of strain in the film. Following a procedure employed previously^{27,28}, we calculate at $T=4\text{ K}$, the strain induced energy shift, ΔE , for GaN/ZnO is -3.8 meV while that for GaN/(6H SiC) is -6.7 meV, and for GaN/(a - Al_2O_3) is +9.3 meV. This should yield a difference of 13 meV in GaN grown on Sapphire and ZnO in the band gap energy. This compares with the observed 8 meV. This discrepancy may be due to several factors including the strain variation from sample to sample grown on sapphire substrates. What is certain is that more research is necessary before conclusive remarks can be made.

Conclusions

We have briefly described stimulated emission in GaN/AlGaIn separate confinement heterostructures, discussed the nature of Mg related transitions in lightly and heavily doped GaN, and preliminary growth experiments on ZnO substrates. Investigation of Mg doped GaN show an optical shallow level at 290 meV above the valence band for lightly doped samples. When the Mg concentration is increased past about 10^{19} cm^{-3} level, Mg-related complexes form deeper in the band, the width of which depends on concentration, form and dominate the high temperature luminescence. The transition to this complex is presently used in some commercial LEDs for producing blue light.

Acknowledgments.

The research at the university of Illinois is funded by grants from ONR, AFOSR and BMDO. We thank Mr. M. Yoder and Drs. G. L. Witt, K. Wu and J. Johnson for their interest and support. H. M. acknowledges Dr. G. McCoy at Wright Laboratory for his support.

References:

1. See, for example, See *Transactions of the First International High Temperature Electronics Conference*, June 10-20, Albuquerque, New Mexico, U.S.A., 1991.
2. H. Morkoç, S. Strite, G.B. Gao, M.E. Lin, B. Sverdlov, and M. Burns, *J. Appl. Phys. Rev.* **76**, 1363-1398 (1994). S. Strite and H. Morkoç, "GaN, AlN and InN: A Review," *J. Vac. Sci. & Technol. B*, Vol. 10(4), pp. 1237-1266, 1992.
3. See, for example, D. Zook, and B. Goldenberg, in *Proceedings of International Conference on Silicon Carbide and Related Materials*, Nov. 1-3, 1993, Washington, DC, U.S.A., Eds. M.G.

- Spencer, R.P. Davaty, J.A. Edmond, M.A. Khan, R. Kaplan, and M. Rahman, *Institute of Physics Conference Series*, Number 137, 1994.
4. M.E. Lin, S. Strite, and H. Morkoç, in *The Encyclopedia of Advanced Materials*, Eds. D. Bloor, M.C. Fleming, R.I. Brook, S. Mahajan, Senior Ed. R.W. Cahn, pp. 79-86, Pergamon Press, 1994.
 5. S. Nakamura, M. Senoh, N. Isawa, and S. Nagahama, *Jpn. J. Appl. Phys.* **34**, Part 2, No. 10B, Oct 15 (1995) issue (in press); (c) S. Nakamura, M. Senoh, N. Isawa, and S. Nagahama, *Jpn. J. Appl. Phys.* **34**, Part 2, No. 7A, L795 (1995); (d) S. Nakamura, M. Senoh, N. Isawa, and S. Nagahama, *Jpn. J. Appl. Phys.* **34**, Part 2, No. 7A, L797 (1995).
 6. I. Akasaki and H. Amano, *Mater. Res. Soc. Fall Meeting*, Boston, MA, U.S.A., 1991.
 7. S. Nakamura, Technical Digest of the IEEE Electron Devices Meeting, pp. 567-570, Dec. 11-14, 1994, San Francisco, CA, U.S.A.
 8. D.B. Eason, Z. Yu, W.C. Hughes, W.H. Roland, C. Boney, J.W. Cook, Jr., J.F. Schetzina, G. Cantwell, and W.C. Harsh, *Appl. Phys. Lett.* **65**, 115 (1995).
 9. M.E. Hoemecke, R.J. Bula, T.W. Tibbits, *HortScience* **27**, 427 (1992).
 10. K. Werner, *IEEE Spectrum* **31**, 30 (1994).
 11. M. G. Crawford, *IEEE Circuits & Devices Mag.* **8**, 24 (1992).
 12. R. Engelmann, *IEEE LEOS News Lett.* **8**, 6 (1994).
 13. H. Morkoç and S.N. Mohammad, *Science* **267**, 51 (1995).
 14. R. Engelmann, 3rd Progress Report to DOE Contract No. DE-AC01-89-CE23821, 17 June, 1994.
 15. See, for example, (a) S. Nakamura, *Research Concerning InGaN High-Brightness Blue LEDs* (published in Japanese), Corporate Report, 1994; (b) S. Nakamura, M. Senoh, N. Isawa, and S. Nagahama, *Jpn. J. Appl. Phys.* **34**, Part 2, No. 10B, Oct 15 (1995) issue (in press); (c) S. Nakamura, M. Senoh, N. Isawa, and S. Nagahama, *Jpn. J. Appl. Phys.* **34**, Part 2, No. 7A, L795 (1995); (d) S. Nakamura, M. Senoh, N. Isawa, and S. Nagahama, *Jpn. J. Appl. Phys.* **34**, Part 2, No. 7A, L797 (1995).
 16. T. J. Schmidt, X. H. Yang, W. Shan, J. J. Song, A. Salvador, W. Kim, Ö. Aktas, A. Botchkarev, and H. Morkoç, *Appl. Phys. Lett.*, pending.
 17. X.H. Yang, T. Schmidt, W. Shan, J.J. Song, and B. Goldenberg, *Appl. Phys. Lett.* **66**, 1(1995).
 18. M. Smith, G. D. Chen, J. Y. Lin, H. X. Jiang, A. Salvador, W. Kim, Ö. Aktas, A. Botchkarev, H. Morkoç, and B. Goldenberg, *Appl. Phys. Lett.*, pending.
 19. Z. Sitar, M. J. Paisley, B. Yan, R. F. Davis, *Mat. Res. Soc. Symp. Proc.* **162**, 537 (1990).
 20. S. N. Basu, T. Lei, T. D. Moustakas, *J. Mat. Res.* **9**, 2370 (1994).
 21. D. Smith, D. Chandrasekhar, B. N. Sverdlov, A. E. Botchkarev, and H. Morkoç, 2nd Workshop on GaN and Related Compounds in St. Louis, October 1994 (unpublished); *Appl. Phys. Lett.*, in press.
 22. S. Iyer, H. Morkoç, H. Zabel, and N. Otsuka, *Comments Cond. Mat. Phys* **15**, 1 (1989).
 23. G. M. Martin, S. V. Sverdlov and D. J. Smith, *Appl. Phys. Lett.* October 2, 1995.
 24. S. N. Mohammad and H. Morkoç, *Progress in Quantum Electronics*, in press.
 25. S. N. Mohammad, A. Salvador, and H. Morkoç, *Proc. IEEE* in press, October 1995.
 26. D. C. Reynolds and D. C. Look, W. Kim, Ö. Aktas, A. Botchkarev, A. Salvador, H. Morkoç, and D. N. Talwar, *Appl. Phys. Lett.*, pending.
 27. A. Salvador, G. Liu, W. Kim, Ö. Aktas, A. Botchkarev and H. Morkoç, *Appl. Phys. Lett.*, pending.
 28. H. Amano, K. Hiramatsu and I. Akasaki, *Jpn. J. Appl. Phys.* **27**, L1384 (1988).

Reprinted from

JOURNAL OF **CRYSTAL GROWTH**

Journal of Crystal Growth 164 (1996) 159–166

Growth of GaN by gas-source molecular beam epitaxy by ammonia
and by plasma generated nitrogen radicals

W.S. Wong ^a, N.Y. Li ^a, H.K. Dong ^a, F. Deng ^a, S.S. Lau ^a, C.W. Tu ^{a,*}, J. Hays ^b, S.
Bidnyk ^b, J.J. Song ^b

^a Department of Electrical and Computer Engineering, UCSD, La Jolla, California, USA

^b Department of Physics, Oklahoma State University, Stillwater, Oklahoma, USA



ELSEVIER

Journal of Crystal Growth

EDITORIAL BOARD

M. SCHIEBER (Principal Editor)
Dept. Mater. Sci., School Appl. Sci. & Technol.
Hebrew University, Jerusalem 91904, Israel
Telefax: +972-2-666 804

R. KERN
CRM-C, CNRS, Campus Luminy, Case 913
F-13288 Marseille Cedex 9, France
Telefax: +33-91-418 916

R.S. FEIGELSON
Ctr. Materials Res., 105 McCullough Bldg.
Stanford Univ., Stanford, CA 94305-4045, USA
Telefax: +1-415-723 3044

T. NISHINAGA
Dept. Electron. Eng., Univ. of Tokyo
7-3-1, Hongo, Bunkyo-ku, Tokyo 113, Japan
Telefax: +81-3-5684-3974

D.T.J. HURLE
H.H. Wills Phys. Lab., Univ. Bristol
Tyndall Avenue
Bristol BS8 1TL, UK

G.B. STRINGFELLOW
Dept. Mater. Sci., 304 EMRO, Univ. of Utah
Salt Lake City, UT 84112, USA
Telefax: +1-801-581 4816

ASSOCIATE EDITORS

A. BARONNET (*Industrial, Biological, Molecular Crystals*)
CRM-C, CNRS, Campus Luminy, Case 913
F-13288 Marseille Cedex 9, France
Telefax: +33-91-418 916

K.W. BENZ (*Microgravity, Electronic Materials*)
Kristallographisches Inst., Universität
Hebelstr. 25, D-79104 Freiburg, Germany
Telefax: +49-761-203 4369

A.A. CHERNOV (*Kinetics of Crystallization*)
Inst. Crystallography, Acad. of Sciences
Leninskii Pros., Moscow 117333, Russian Fed.
Telefax: +7-095-135 1011

A.Y. CHO (*Molecular Beam Epitaxy*)
Room 1C-323, AT&T Bell Laboratories
Murray Hill, NJ 07974-2070, USA
Telefax: +1-908-582 2043

B. COCKAYNE (*IOCG News*)
School of Metallurgy and Mater.
Univ. Birmingham, P.O. Box 363, Edgbaston, Birmingham
B15 2TT, UK
Telefax: +44-121-471-2207

S.R. CORIELL (*Theory*)
A153 Mater. Natl. Inst. of Standards & Technol.
Gaithersburg, MD 20899-0001, USA

D. ELWELL (*Priority Communications, Superconductivity*)
Hughes Aircraft Company
P.O. Box H, M/S A2408, 500 Superior Avenue
New Port Beach, CA 92658-8908, USA
Telefax: +1-714-759 2868

M.E. GLICKSMAN (*Solidification*)
School of Eng., Mater. Eng. Dept., Rensselaer Polytechnic
Inst., Troy, NY 12180-3590, USA
Telefax: +1-518-276 8554

M.A.G. HALLIWELL (*X-ray Diffraction*)
Philips Analytical X-ray, Lelyweg 1
7602 EA Almelo, The Netherlands

T. HIBIYA (*Oxides, Melts Thermophysical Properties, Microgravity*)
Fundamental Res. Labs., NEC CORPORATION
34, Miyukigaoka, Tsukuba 305, Japan
Telefax: +81-298-566 136

H. KOMATSU (*Proteins Molecular Crystallization, Growth from Solutions*)
Inst. Mater. Res., Tohoku Univ.
Katahira 2-1-1, Sendai 980, Japan
Telefax: +81-22-215 2011

T.F. KUECH (*Thin Films and Electronic and Optical Devices*)
Dept. Chem. Eng., Univ. Wisconsin-Madison
Madison, WI 53706, USA
Telefax: +1-608-265 3782

A. McPHERSON (*Protein Growth*)
Dept. Biochemistry, Univ. of California
Riverside, CA 92521, USA
Telefax: +1-909-787 3790

P.A. MORRIS HOTSENPILLER (*Electrooptical Crystals, Book Reviews*)
E.I. du Pont de Nemours & Co., Exp. Station
Wilmington, DE 19888-0358, USA
Telefax: +1-302-695 3375

J.B. MULLIN (*Semiconductors*)
EMC, "The Hoo", Brookhill Road
West Malvern, Worcs., WR14 4DL, UK
Telefax: +44-1684-575 591

K. NAKAJIMA (*Liquid and Vapor Phase Epitaxy*)
ULSI Mater. Lab., Fujitsu Labs. Ltd.
Morinosato-Wakamiya 10-1, Atsugi 243-01, Japan
Telefax: +81-462-48 3473

H. OHNO (*Epitaxy*)
Research Inst. of Electrical Commun.
Tohoku Univ., Sendai 980 77, Japan
Telefax: +81-22-217 5553

K. PLOOG (*Molecular Beam Epitaxy*)
Paul-Drude-Inst. für Festkörperelektronik
Hausvogteiplatz 5-7, D-10117 Berlin, Germany
Telefax: +49-30-203 77201

F. ROSENBERGER (*Protein Crystallization, Fluid Dynamics*)
Center for Microgravity and Materials Research
Univ. Alabama, Huntsville, AL 35899, USA
Telefax: +1-205-895 6791

R.W. ROUSSEAU (*Solution Growth, Industrial Crystallization*)
School of Chem. Eng., Georgia Inst. of Technol.
Atlanta, GA 30332-0100, USA
Telefax: +1-404-894 2866

K. SATO (*Biocrystallization and Organic Crystals*)
Fac. Appl. Biol. Sci., Hiroshima Univ.
Higashi-Hiroshima 724, Japan
Telefax: +81-824-227 062

L.F. SCHNEEMEYER (*Superconductivity, Oxides, Novel Materials*)
Room 1A-363, AT&T Bell Labs.
Murray Hill, NJ 07974-2070, USA
Telefax: +1-908-582 2521

D.W. SHAW (*Semiconductors, Epitaxy, Devices*)
Texas Instruments Inc., P.O. Box 655936, MS 147
Dallas, TX 75265, USA
Telefax: +1-214-995 7785

I. SUNAGAWA (*Morphology and Minerals*)
3-54-2 Kashiwa-cho, Tachikawa-shi
Tokyo 190, Japan
Telefax: +81-425-35 3637

G. VAN TENDELOO (*Electron Microscopy, Fullerenes, Superconductivity*)
University of Antwerp, RUCA
Groenenborgerlaan 171, B-2020 Antwerp, Belgium
Telefax: +32-3-2180 217

A.F. WITT (*Semiconductor Crystals*)
Dept. of Metall. & Mater. Sci., Massachusetts
Inst. of Technol., Cambridge, MA 02139, USA
Telefax: +1-617-253 5827

A. ZANGWILL (*Theory (Epitaxy)*)
School of Physics, Georgia Inst. of Technol.
Atlanta, GA 30332, USA
Telefax: +1-404-894 9958

Scope of the Journal

Experimental and theoretical contributions are invited in the following fields: Theory of nucleation and growth, molecular kinetics and transport phenomena, crystallization in viscous media such as polymers and glasses. Crystal growth of metals, minerals, semiconductors, magnetics, inorganic, organic and biological substances in bulk or as thin films. Apparatus, instrumentation and techniques for crystal growth, and purification methods. Characterization of single crystals by physical and chemical methods.

Abstracted/Indexed in:

Aluminium Industry Abstracts; Chemical Abstracts; Current Contents; Physical, Chemical and Earth Sciences; Ei Compendex Plus; Engineered Materials Abstracts; Engineering Index; INSPEC; Metals Abstracts; Physics Briefs.

Subscription Information 1996

Volumes 158-169 of Journal of Crystal Growth (ISSN 0022-0248) are scheduled for publication. (Frequency: semimonthly.) Prices are available from the publishers upon request. Subscriptions are accepted on a prepaid basis only. Issues are sent by SAL (Surface Air Lifted) mail wherever this service is available. Airmail rates are available upon request. Please address all enquiries regarding orders and subscriptions to:

Elsevier Science B.V., Order Fulfillment Department
P.O. Box 211, 1000 AE Amsterdam, The Netherlands
Tel: +31 20 485 3642; Fax: +31 20 485 3598

Claims for issues not received should be made within six months of our publication (mailing) date.

US mailing notice - Journal of Crystal Growth (ISSN 0022-0248) is published semimonthly by Elsevier Science B.V., Molenwerf 1, P.O. Box 211, 1000 AE Amsterdam, The Netherlands. Annual subscription price in the USA is US \$6535 (valid in North, Central and South America only), including air speed delivery. Second class postage paid at Jamaica NY 11431. US postmasters: Send address changes to Journal of Crystal Growth, Publications Expediting, Inc., 200 Meacham Avenue, Elmont NY 11003. Airfreight and mailing in the USA by Publications Expediting.

Ⓢ The paper used in this publication meets the requirements of ANSI/NISO Z39.48-1992 (Permanence of Paper).

PRINTED IN THE NETHERLANDS

North-Holland, an imprint of Elsevier Science



ELSEVIER

Journal of Crystal Growth 164 (1996) 159–166

JOURNAL OF
CRYSTAL
GROWTH

Growth of GaN by gas-source molecular beam epitaxy by ammonia and by plasma generated nitrogen radicals

W.S. Wong^a, N.Y. Li^a, H.K. Dong^a, F. Deng^a, S.S. Lau^a, C.W. Tu^{a,*}, J. Hays^b, S. Bidnyk^b, J.J. Song^b

^a Department of Electrical and Computer Engineering, UCSD, La Jolla, California, USA

^b Department of Physics, Oklahoma State University, Stillwater, Oklahoma, USA

Abstract

We will present a comparison between GaN grown on *c*- and *r*-plane sapphire by gas-source molecular beam epitaxy (GSMBE) using solid source elemental Ga with uncracked ammonia (NH₃). Improved GaN film quality was found for samples grown at substrate temperatures above 700°C with optimized temperatures at 780°C. GaN deposited on a low-temperature (~350°C) GaN buffer layer grown using an rf-plasma radical beam source exhibited poor photoluminescence (PL) intensity and carrier mobility while SEM analysis showed smooth GaN surface morphologies. GaN deposited on an ammonia-grown low-temperature (~550°C) GaN or AlN buffer were found to have improved PL intensity and line widths, GaN surface morphology and carrier mobility. X-ray rocking curve (XRC) data showed that the GaN crystal quality improved as a function of increasing substrate growth temperature independent of buffer layer implementation.

1. Introduction

Successfully improving the crystal quality of GaN films grown on sapphire substrates by the use of a thin buffer layer has been reported in the literature [1,2]. Amano et al. [3,4] reported that GaN grown on sapphire substrates employing an AlN buffer showed an increase in the carrier mobility by a factor of 10 along with narrower X-ray rocking curve line widths. The band-gap photoluminescence (PL) of the GaN films showed two orders of magnitude increase in the intensity compared to GaN grown directly on sapphire. As a result of their findings, low-temperature AlN buffer layers have been employed extensively in the growth of high-quality GaN films.

Nakamura et al. [5] have shown that GaN films grown over a low-temperature GaN buffer layer by metalorganic vapor phase epitaxy have superior quality compared to films grown on AlN buffers. The quality of these GaN films demonstrated for the first time that high-quality GaN films using a GaN buffer could be used to make blue light-emitting diodes. In another study, Kuznia et al. [6] have compared the effect of both AlN and GaN buffer layers and showed that the two buffers gave comparable results with the GaN grown on AlN buffer layers being slightly better.

In GaN growth by gas-source molecular beam epitaxy (GSMBE), Sitar et al. [7] have characterized the initial growth of GaN and AlN grown by using an electron cyclotron resonance (ECR) plasma to generate active nitrogen. Due to possible ion damage from an ECR plasma source [8], the use of rf-plasma

* Corresponding author. Fax: +1 619 534 0415; E-mail: ctu@ucsd.edu.

generated nitrogen radicals as a N source for GSMBE growth of GaN has been demonstrated by Hoke et al. [9]. Powell et al. [10] have shown that uncracked ammonia (NH_3) can be used to successfully grow high-quality GaN films by (GSMBE) without the use of a low-temperature buffer. Their results indicated that the GaN film quality was strongly dependent on the substrate growth temperature.

In this paper, we will report the results obtained from GaN thin films grown by GSMBE, on sapphire substrates, using ammonia as the N source. We will examine the effect of different low-temperature GaN buffer layers grown using an rf-generated nitrogen plasma source or ammonia on bulk GaN films and also present results for GaN grown on AlN buffers.

2. Experimental parameters

The growth of all bulk GaN epilayers was done using elemental solid source Ga and ammonia gas as the nitrogen source. Growth rates for the bulk GaN were set at 3200 \AA/h with a process pressure of $6 \times 10^{-5} \text{ Torr}$ for the optimized ammonia flow. NH_3 was fed directly into the growth chamber without any pre-cracking and was activated thermally at the heated substrate surface. The GaN films were all grown on sapphire substrates using either the *c*-plane (0001) or the *r*-plane (01 $\bar{1}$ 2) orientation. The substrate temperature for the bulk GaN growth was varied between 600 and 800°C.

The deposition of the GaN buffer layers was done

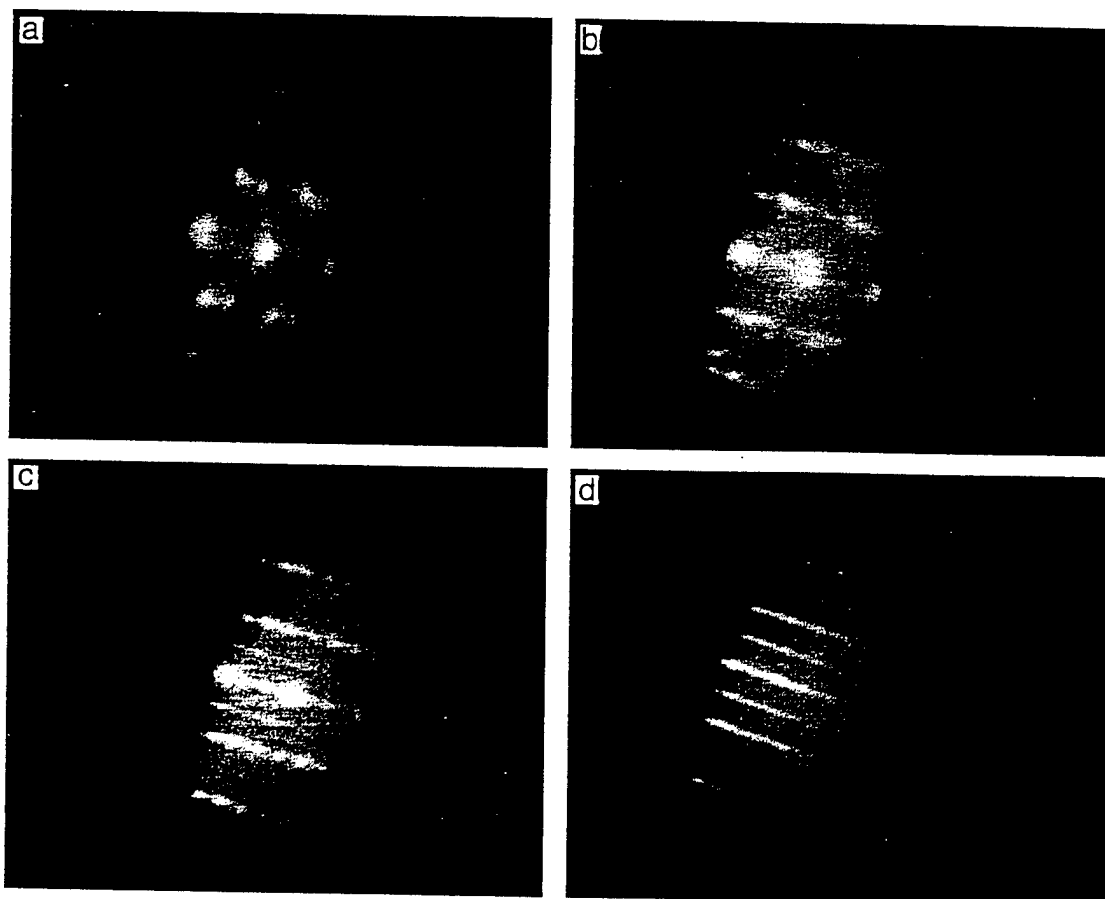


Fig. 1. In situ RHEED characterization of GaN grown on a low-temperature GaN buffer. (a) 200 Å thick GaN at 325°C, $[2\bar{1}\bar{1}0]$ direction. (b) 200 Å thick GaN at 700°C, $[2\bar{1}\bar{1}0]$ direction. (c) 550 Å thick GaN at 700°C, $[2\bar{1}\bar{1}0]$ direction. (d) 5000 Å thick GaN at 700°C, $[2\bar{1}\bar{1}0]$ direction.

using either an rf plasma source or ammonia gas as the N source. For the case of the rf-plasma-grown GaN buffers, a commercially manufactured free-radical beam source from Oxford Applied Research was used to generate the active nitrogen plasma. The N_2 flow into the rf radical source was set to maintain a process pressure in the growth chamber of 1×10^{-4} Torr with the rf input power setpoint at 400 W. The buffer layer growth temperature was 325°C with a GaN growth rate of 600 Å/h.

Both GaN and AlN were used for the ammonia-grown low-temperature buffers. The growth parameters were the same as for the bulk GaN growth with the exception that the GaN buffer growth temperature was increased to 550°C. The thickness of all the GaN buffer layers was nominally 200 Å.

Low-temperature AlN buffer layers were examined by varying the AlN buffer growth parameters. Using ammonia for the N source, the buffers were all grown on *c*-plane oriented sapphire substrates. Three AlN buffer layer growth conditions were examined and are identified as:

AlN(1): GaN grown on a 250 Å thick AlN buffer at 550°C.

AlN(2): GaN grown on a 500 Å thick AlN buffer at 550°C.

AlN(3): GaN grown on a 250 Å thick AlN buffer at 600°C.

Characterization of the GaN films was performed by scanning electron microscopy (SEM), reflection high-energy electron diffraction (RHEED), four-crystal X-ray rocking curve (XRC) and Hall effect measurements.

3. Results and discussion

GaN grown on *c*- and *r*-plane sapphire employing a low-temperature GaN buffer displayed a very distinct streaky in situ RHEED pattern at substrate temperatures of 700°C. Fig. 1a is an image of the RHEED pattern for the 200 Å GaN buffer layer grown using the rf plasma source at 325°C on *c*-plane sapphire. The pattern is spotty, indicating a rough 3D surface. By increasing the temperature to 700°C, the RHEED pattern of the buffer surface has changed to a more streaky formation (Fig. 1b), which may be indicative of GaN nucleation sites beginning to coa-

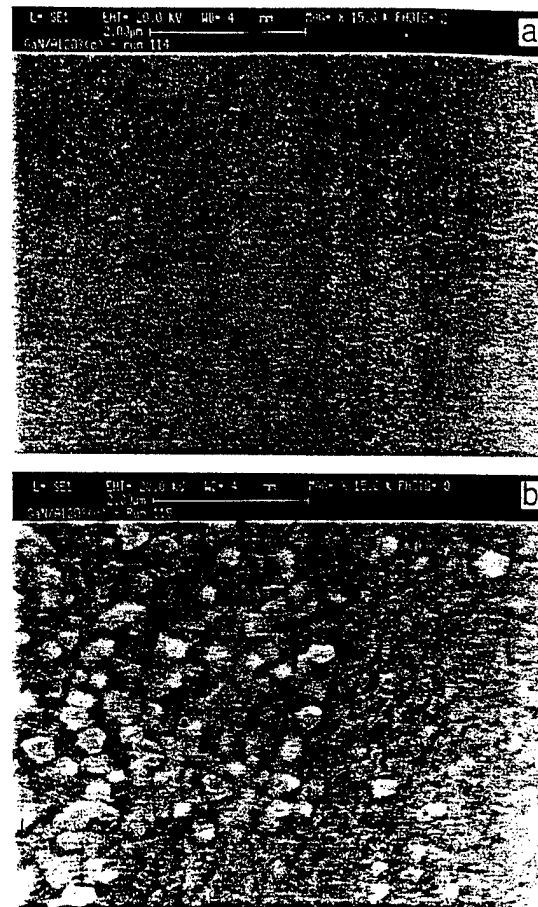
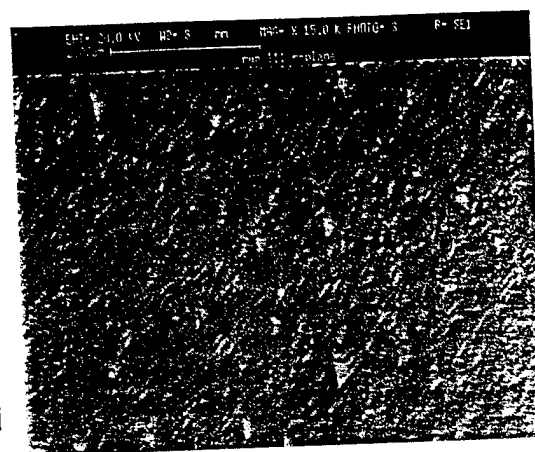
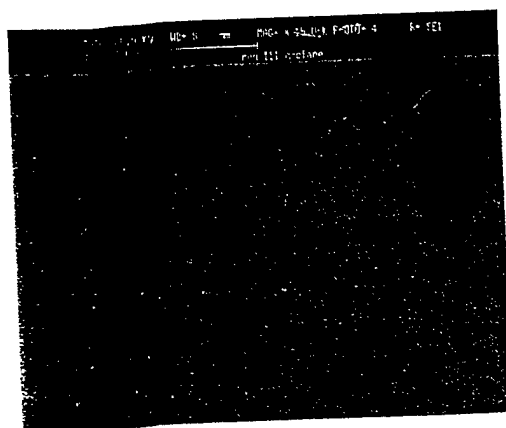


Fig. 2. Effect of low-temperature GaN buffer layers on GaN surface morphology. (a) GaN grown on a low-temperature GaN buffer. (b) GaN grown without a low-temperature buffer.

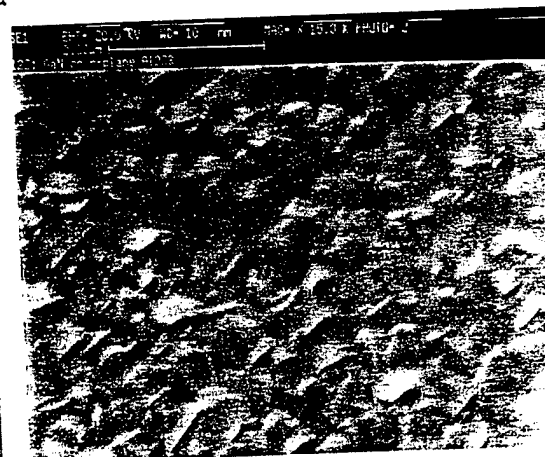
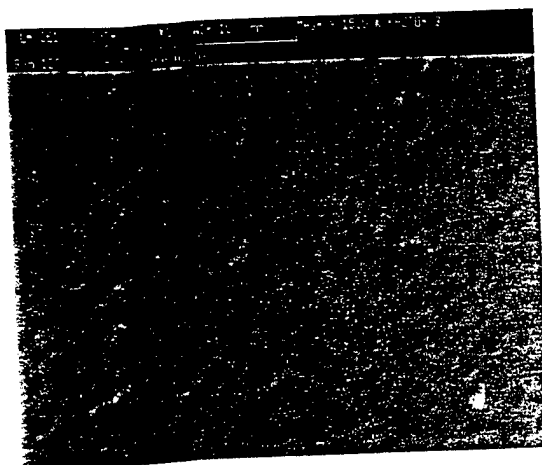
lesce to form a single crystal. The transformation results in the formation of the GaN template for the bulk GaN growth [11].

After 550 Å of GaN growth using ammonia as the N source, the RHEED diffraction pattern showed formation of second-order diffraction lines and increased streakiness (Fig. 1c) indicating a reconstructed GaN surface. After 5000 Å of GaN deposition, the RHEED pattern is shown to be very streaky with a $2 \times$ pattern (Fig. 1d) indicating an atomically smooth reconstructed GaN surface.

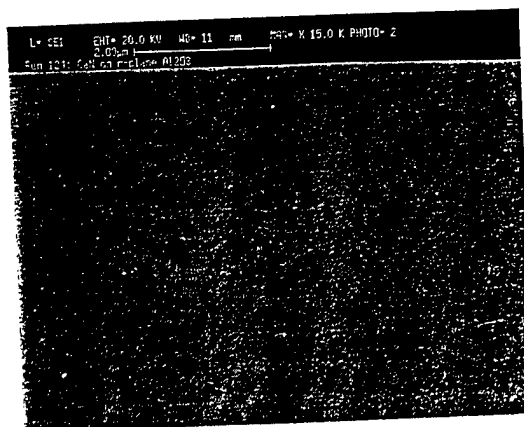
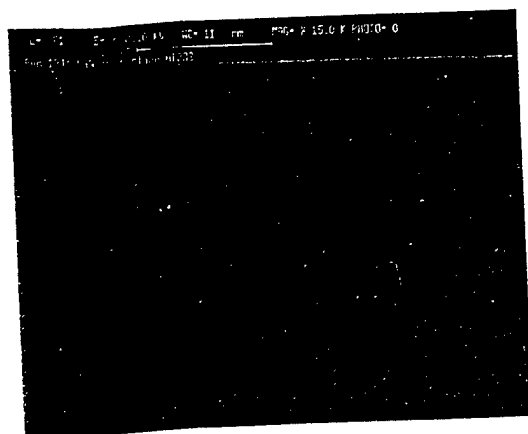
Fig. 2a shows an SEM micrograph for a 6400 Å thick GaN film grown at 700°C on a low-temperature GaN buffer (grown using the plasma source) on



a



b



c

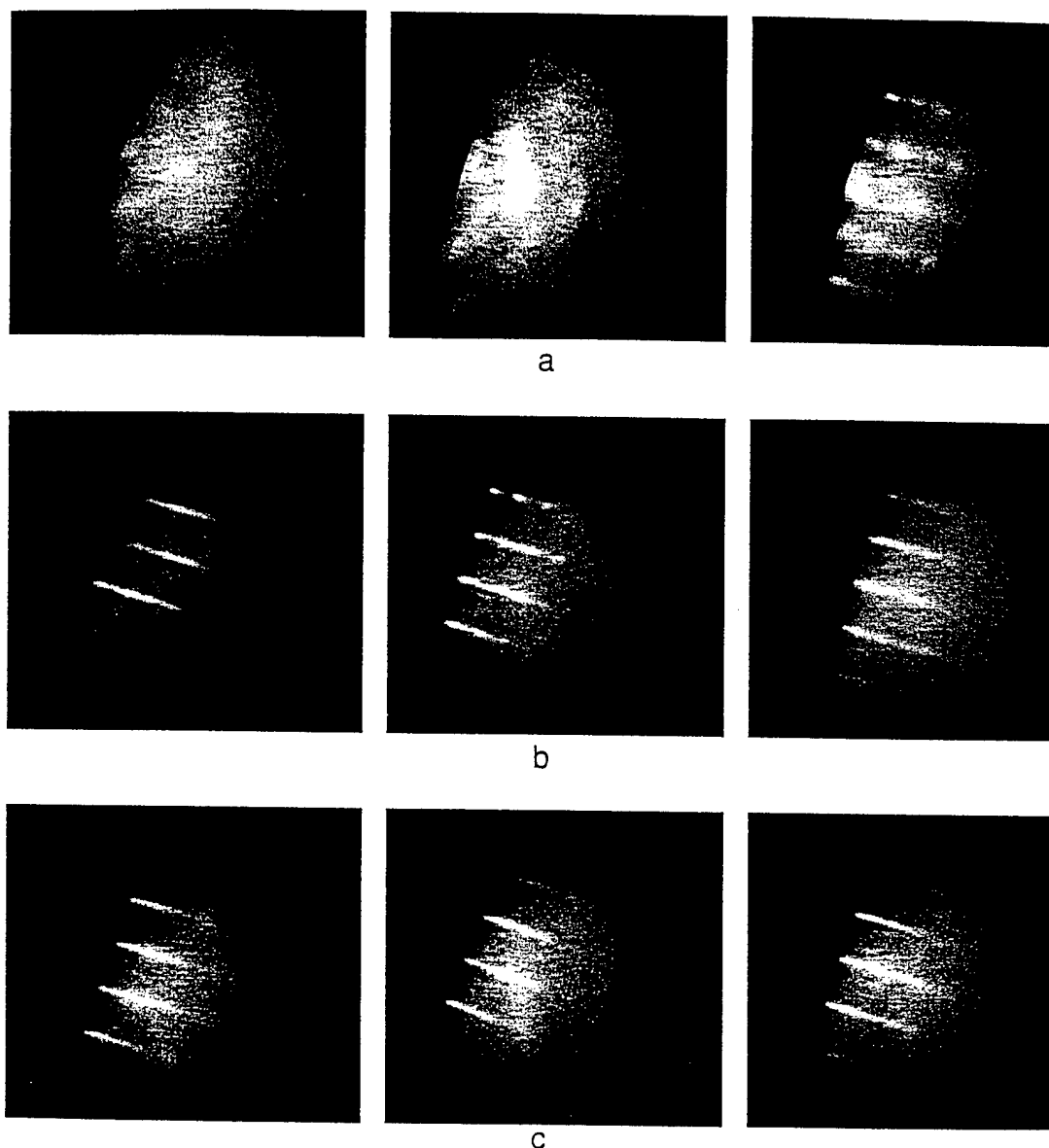


Fig. 4. In situ RHEED characterization of GaN grown on AlN buffer layers. Left: AlN(1); middle: AlN(2); right: AlN(3). (a) RHEED image of AlN buffer at 780°C, $[2\bar{1}\bar{1}0]$ direction. (b) RHEED image of 1600 Å thick GaN at 780°C, $[2\bar{1}\bar{1}0]$ direction. (c) RHEED image of 6400 Å thick GaN at 780°C, $[2\bar{1}\bar{1}0]$ direction.

c-plane sapphire. Fig. 2b shows the surface morphology of GaN grown directly on *c*-plane sapphire. The micrograph clearly shows that an improved surface

morphology is obtained when GaN is grown on a GaN buffer layer.

Fig. 3a and 3b compares the GaN surface mor-

Fig. 3. Substrate orientation effects on GaN surface morphology. Left: *c*-plane sapphire substrate. Right: *r*-plane sapphire substrate. (a) GaN grown at 635°C on a plasma-grown buffer. (b) GaN deposited at 780°C on a plasma-grown buffer. (c) GaN deposited at 780°C on an ammonia-grown buffer.

phology grown on *c*- and *r*-plane sapphire, at a growth temperature of 625 and 780°C. The samples grown on *c*-plane sapphire have a much smoother surface morphology compared to GaN on *r*-plane sapphire. The difference between the surface roughness of GaN on *c*- and *r*-plane sapphire is much less compared to GaN on plasma-grown buffers (Fig. 3c). The low-temperature ammonia-grown GaN buffer has reduced the bulk GaN surface roughness for *r*-plane sapphire substrates compared to the GaN on plasma-grown buffers.

These results would indicate that the low-temperature GaN buffer layer is acting as a template for the bulk GaN growth on *c*-plane sapphire [6]. The template provides nucleation sites for the bulk GaN epilayer to begin forming and, as a consequence, the surface morphology is smoother. The same effect is seen for GaN on *r*-plane sapphire substrates when ammonia-grown GaN buffer layers were used.

For GaN grown on AlN buffers, the initial RHEED images for the AlN buffers showed an amorphous surface with no distinct diffraction pattern for AlN(1) and AlN(2). By raising the substrate temperature to 780°C, the RHEED patterns changed for the cases of AlN(1) and AlN(2) (Fig. 4). AlN(1) was beginning to show some indications of a streaky pattern, which would indicate that "islands" of AlN were beginning to coalesce to form the buffer template. AlN(2) formed a polycrystalline surface indicated by ring-like RHEED diffraction patterns. AlN(3) did not show much change from its initial temperature, which would indicate that the AlN surface as deposited at 600°C had already reached a thermal equilibrium.

The RHEED analysis for AlN(3) gave the best RHEED pattern throughout the growth, which would indicate that the GaN surface morphology should be the best of the three experimental conditions, with AlN(2) being the poorest. By examining the GaN surface morphology with SEM, it was seen that AlN(3) displayed the best surface morphology compared to the other two conditions while AlN(2) was the poorest as predicted by the RHEED analysis (Fig. 5).

An examination of the XRC data displayed a trend in crystallinity with substrate growth temperature. GaN (~6400 Å thick) grown with a low-temperature plasma GaN buffer (~200 Å thick) on *c*-plane sapphire at a growth temperature of 700°C

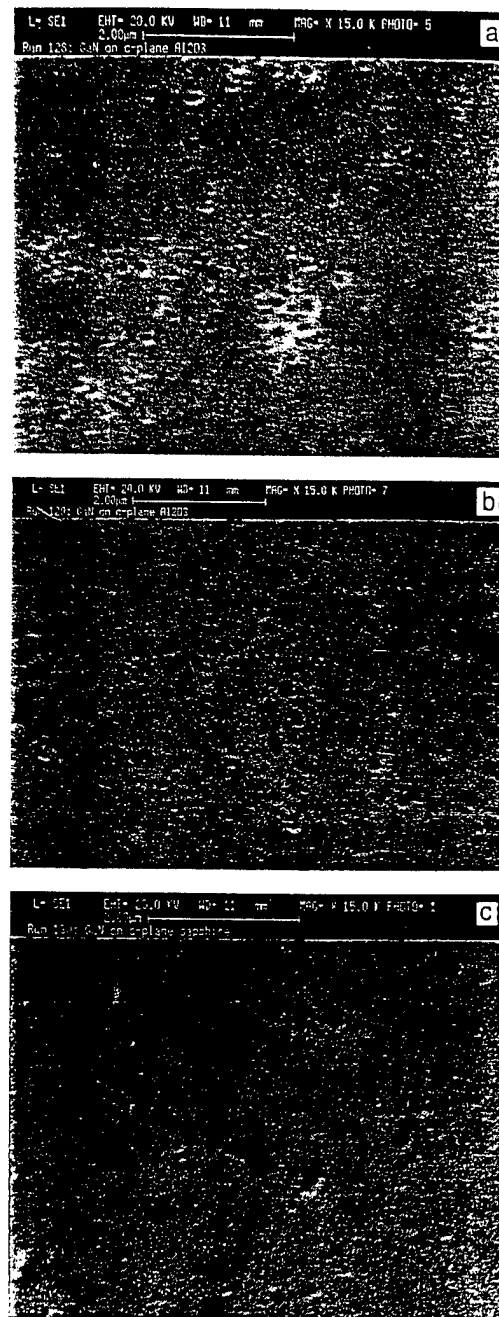


Fig. 5. AlN buffer layer effects on GaN surface morphology. (a) GaN surface morphology for AlN(1). (b) GaN surface morphology for AlN(2). (c) GaN surface morphology for AlN(3).

resulted in a GaN peak full-width at half-maximum (FWHM) of 60 arc min. GaN grown on *c*-plane sapphire at a substrate temperature of 725°C im-

improved the XRC FWHM to 44 arc min indicating improved crystallinity in the film. At a growth temperature of 780°C, the XRC FWHM narrowed to 34 arc min. The same trend is also seen with GaN grown directly on *c*-plane sapphire (Fig. 6). Data points at a growth temperature of 780°C also show that GaN on ammonia-grown GaN or AlN buffers have comparable XRC line widths.

The same trend in electron carrier mobility and concentration was not seen. Hall effect measurements for samples grown on a 200 Å low-temperature GaN plasma-grown buffer layer had relatively poor electrical measurements regardless of the growth temperature. The typical electron mobility was approximately 1–6 cm²/V·s with the carrier concentration between 5×10^{18} and 5×10^{19} cm⁻³ while GaN on ammonia-grown GaN or AlN buffers showed improved electron mobility in the range of 50–60 cm²/V·s with electron concentration comparable to that of GaN on plasma-grown buffers. The degraded mobility would indicate that a compensating effect was introduced by the plasma-grown GaN buffer.

PL line spectra (measured at 10 K using a He–Cd laser with a 325 nm wavelength) for GaN grown with and without a low-temperature buffer is shown in Fig. 7. The data show that the highest quality GaN films were obtained by implementing an ammonia-grown low-temperature GaN buffer, which showed the highest intensity and narrowest line width compared to the other buffer conditions. Bulk GaN grown on a GaN buffer using the rf plasma source showed the poorest PL results. The PL data give more evi-

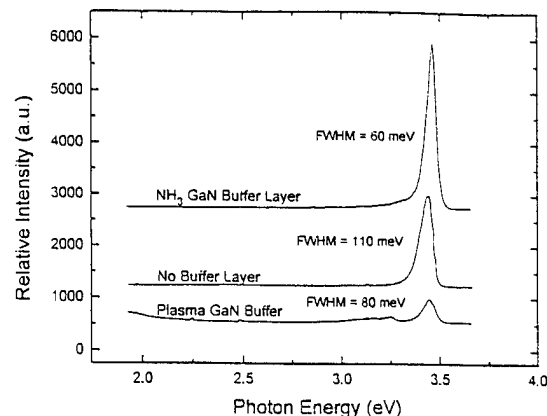


Fig. 7. 10 K PL results for GaN on ammonia-grown GaN buffer, no buffer and plasma-grown GaN buffer.

dence that the thin GaN low-temperature buffer grown using the rf plasma source degrades the bulk GaN film quality compared to the other buffer conditions.

4. Conclusions

Surface morphology was seen to improve when a low-temperature GaN or AlN buffer layer was used to grow bulk GaN. GaN grown on *r*-plane sapphire substrates were typically more featured. When a low-temperature GaN buffer was grown using ammonia as the N source, improvements were seen for GaN surface morphology on *r*-plane sapphire substrates when compared to GaN on plasma-grown GaN buffers. RHEED in situ analysis showed a correlation to GaN surface morphology and different AlN buffer growth parameters.

XRC and PL results, along with transport measurements, showed that improved GaN films were obtained for GaN on ammonia-grown GaN or AlN low-temperature buffers. Samples grown using a GaN plasma buffer were found to have poorer film quality compared to the no buffer and ammonia-grown buffer samples.

Acknowledgements

The authors would like to acknowledge the Rockwell International Science Center and the California MICRO program for their funding and support.

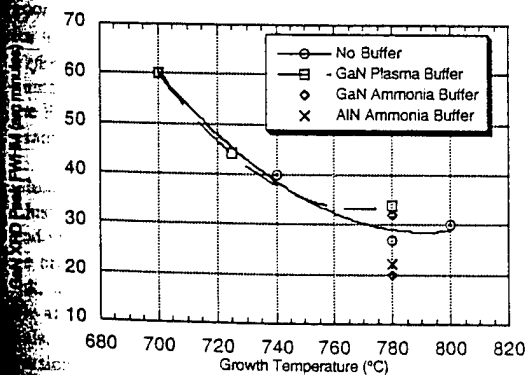


Fig. 6. XRC line width vs. growth temperature. 6400 Å thick GaN grown on 200 Å buffer layer. Plasma-grown GaN buffer deposited at 325°C. Ammonia-grown buffers deposited at 550°C.

References

- [1] S. Nakamura, Jpn. J. Appl. Phys. 30 (1991) L1705.
- [2] M.A. Khan, J.N. Kuznia and D.T. Olsen, J. Appl. Phys. 73 (1993) 3108.
- [3] H. Amano, N. Sawaki, I. Akasaki and Y. Toyoda, Appl. Phys. Lett. 48 (1986) 353.
- [4] H. Amano, I. Akasaki, K. Hiramatsu, N. Koide and N. Sawaki, Thin Solid Films 163 (1988) 415.
- [5] S. Nakamura, T. Mukai and M. Senoh, Jpn. J. Appl. Phys. 30 (1991) L1998.
- [6] J.N. Kuznia, M.A. Khan, D.T. Olsen, R. Kaplan and J. Freitas, J. Appl. Phys. 73 (1993) 4700.
- [7] Z. Sitar, L.L. Smith and R.F. Davis, J. Crystal Growth 141 (1994) 11.
- [8] H. Morkoç, S. Strite, G.B. Gao, M.E. Lin, B. Sverdlov and M. Burns, J. Appl. Phys. 76 (1994) 1363.
- [9] W.E. Hoke, P.J. Lemonias and D.G. Weir, J. Crystal Growth 111 (1991) 1024.
- [10] R.C. Powell, N.E. Lee, Y.W. Kim and J.E. Greene, J. Appl. Phys. 73 (1993) 189.
- [11] A.E. Wickenden, D.K. Wickenden, T.J. Kistenmacher, S.A. Ecelberger and T.O. Poehler, Mater. Res. Soc. Symp. Proc. 280 (1993) 355.

Journal of Crystal Growth

Instructions to Authors (short version)

Submission of papers

Manuscripts (one original + two copies), should be sent to a member of the Editorial Board or preferably to an appropriate subject Associate Editor. Priority communications should be sent to D. Elwell. News or announcements should be submitted through the Principal Editor; a duplicate should be sent directly to Elsevier Science B.V., address given below.

Original material. Submission of a manuscript implies it is not being simultaneously considered for publication elsewhere and that the authors have obtained the necessary authority for publication.

Types of contributions

Original research papers, Letters to the Editors and Priority communications are welcome. They should contain an Abstract (of up to 200 words) and a Conclusions section, which particularly in the case of theoretical papers translates the results into terms readily accessible to most readers.

As a guideline: *experimental papers* should not be longer than 16 double-spaced typed pages, and 8 figures + tables; for *theoretical papers* a maximum of 20 pages and 10 figures + tables is suggested.

Letters and *Priority communications* should not be longer than 5 double-spaced typed pages, and 3 figures + tables. They will be given priority in both the refereeing and production processes. The faster production schedule may preclude sending proofs of Letters and Priority communications to authors.

Manuscript preparation

Contributions may be written in English, French or German. They should have an abstract in English. The paper copies of the text should be prepared with double line spacing and wide margins, on numbered sheets.

Structure. Please adhere to the following order of presentation: Article title, Author(s), Affiliation(s), Abstract, PACS codes and keywords, Main text, Acknowledgements, Appendices, References, Figure captions, Tables.

Corresponding author. The name, complete postal address, telephone and fax numbers and the e-mail address of the corresponding author should be given on the first page of the manuscript.

PACS codes/keywords. Please supply one or more relevant PACS-1996 classification codes and 1-6 keywords of your own choice for indexing purposes.

References. References to other work should be consecutively numbered in the text using square brackets and listed by number in the Reference list. Please refer to the more detailed instructions for examples.

Illustrations

Illustrations should also be submitted in triplicate: one master set and two sets of copies. The *line drawings* in the master set should be original laser printer or plotter output or drawn in black india ink, with careful lettering, large enough (3-5 mm) to remain legible after reduction for printing. The *photographs* should be originals, with somewhat more contrast than is required in the printed version. They should be unmounted unless part of a composite figure. Any scale markers should be inserted on the photograph itself, not drawn below it.

Colour plates. Figures may be published in colour, if this is judged essential by the Editor. The Publisher and the author will each bear part of the extra costs involved. Further information is available from the Publisher.

After acceptance

Important. When page proofs of the accepted manuscripts are made and sent out to authors, this is in order to check that no undetected errors have arisen in the typesetting (or file conversion) process. At the proof stage only printer's errors may be corrected. No changes in, or additions to, the edited manuscript will be accepted.

Notification. The authors will receive the final answer of acceptance or rejection from the Office of the Principal Editor and will be invited to supply an electronic version of the accepted text, if this is not already available.

Copyright transfer. In the course of the production process you will be asked to transfer the copyright of the article to the Publisher. This transfer will ensure the widest possible dissemination of information.

Electronic manuscripts

The Publisher welcomes the receipt of an electronic version of your accepted manuscript. If there is not already a copy of this (on diskette) with the journal editor at the time the manuscript is being refereed, you will be asked to send a file with the text of the accepted manuscript directly to the Publisher by e-mail or on diskette (allowed formats 3.5" or 5.25" MS-DOS, or 3.5" Macintosh) to the address given below. (When e-mailing a non-ASCII word-processor file, you should encode it, e.g. with UUENCODE or BinHex, so as to retain all formatting codes.) The name and version of the word-processing program and the type of operating system should always be indicated. Please note that no deviations from the version accepted by the Editor of the journal are permissible without the prior and explicit approval by the Editor. Such changes should be clearly indicated on an accompanying printout of the file.

Author benefits

No page charges. Publishing in Journal of Crystal Growth is free.

Free offprints. The corresponding author will receive 50 offprints free of charge. An offprint order form will be supplied by the Publisher for ordering any additional paid offprints.

Discount. Contributors to Elsevier Science journals are entitled to a 30% discount on all Elsevier Science books.

Further information (after acceptance)

Elsevier Science B.V., J. Crystal Growth
Issue Management Physics
and Materials Science
P.O. Box 2759, 1000 CT Amsterdam
The Netherlands
Fax: +31 20 485 2319/+31 20 485 2704
E-mail: matsci-de-f@elsevier.nl

Molecular beam epitaxial growth of Eu-doped CaF_2 and BaF_2 on Si

X. M. Fang, T. Chatterjee, and P. J. McCann

School of Electrical Engineering and Laboratory for Electronic Properties of Materials,
University of Oklahoma, Norman, Oklahoma 73019

W. K. Liu and M. B. Santos

Department of Physics and Astronomy and Laboratory for Electronic Properties of Materials,
University of Oklahoma, Norman, Oklahoma 73019

W. Shan and J. J. Song

Department of Physics and Center for Laser Research, Oklahoma State University, Stillwater,
Oklahoma 74078

(Received 18 September 1995; accepted 22 January 1996)

The growth of Eu-doped CaF_2 and BaF_2 thin films on Si(100), (110), and (111) substrates has been realized by molecular beam epitaxy using elemental Eu evaporation. Very bright blue emissions from Eu-doped CaF_2 and yellow emissions from Eu-doped BaF_2 were obtained in the wavelength range of 400–850 nm at 10 K. Depending on the Si substrate orientation, the zero-phonon line of Eu^{2+} in the CaF_2 thin films was shifted by different amounts relative to that of bulk CaF_2 due to residual strain in these epilayers. © 1996 American Vacuum Society.

I. INTRODUCTION

Increasing interest in the incorporation of rare-earth (RE) elements in epitaxial thin films of alkaline-earth fluorides is motivated by potential applications in light emitters and solid state microcavity lasers. Growth of these materials on Si substrates offers potential compatibility with Si-based technology. Nd- and Er-doped CaF_2 films grown on Si substrates by molecular beam epitaxy (MBE) have exhibited strong photoluminescence at 1.04 and 1.54 μm , respectively.^{1–3} Recently, we have demonstrated that Eu can be incorporated into epitaxial CaF_2 films grown on Si(100) by MBE and that Eu doping as high as 4.05 at. % does not significantly degrade the surface morphology.⁴

In this article, we present results on the MBE growth of Eu-doped CaF_2 and BaF_2 on Si(100), (110) and (111) substrates using elemental Eu evaporation. Reflection high-energy electron diffraction (RHEED) and photoluminescence (PL) measurements were performed to characterize these structures. We demonstrate that very bright blue emissions from Eu-doped CaF_2 and yellow emissions from Eu-doped BaF_2 can be obtained in the wavelength range of 400–850 nm. Since BaF_2 can be readily grown on CaF_2 , two-color (blue and yellow) light emitters may possibly be developed from Eu-doped stacked $\text{BaF}_2/\text{CaF}_2$ films on Si.

II. EXPERIMENT

Growth of Eu-doped CaF_2 and BaF_2 on Si was carried out in an Intevac Modular GEN II MBE system with a background pressure of $\sim 10^{-10}$ Torr throughout deposition. The 3-in.-diameter *p*-type Si substrates (Silicon Sense, Inc.) were cleaned using the Shiraki method.⁵ The passivating oxide formed during the *ex situ* cleaning procedure was thermally desorbed in the growth chamber after several minutes at $\sim 1100^\circ\text{C}$. High purity polycrystalline CaF_2 and BaF_2 were evaporated from graphite-coated PBN crucibles at typical growth rates of 20 Å/min and 19 Å/min for CaF_2 and BaF_2

cell temperatures of 1300 and 1180 $^\circ\text{C}$, respectively. An elemental source of Eu was evaporated from a separate low-temperature effusion cell heated to 300–400 $^\circ\text{C}$ to give beam equivalent pressures of 3.5×10^{-10} – 1.9×10^{-8} Torr.

Smooth Eu-doped CaF_2 films on Si(100) were obtained by growing a 400 Å CaF_2 buffer, a 3600 Å Eu-doped CaF_2 layer and a 200 Å CaF_2 top layer at 580 $^\circ\text{C}$ followed by *in situ* annealing at 1100 $^\circ\text{C}$ for a few minutes. For the growth of Eu-doped CaF_2 films on Si(110), a 20 Å CaF_2 and a 7800 Å Eu-doped CaF_2 layer were deposited at 840 $^\circ\text{C}$. These $\text{CaF}_2/\text{Si}(110)$ films always exhibit a ridged and grooved surface morphology.⁶ Eu-doped $\text{CaF}_2/\text{Si}(111)$ films were obtained by depositing a 4100 Å CaF_2 buffer and a 600 Å Eu-doped CaF_2 layer at 700 $^\circ\text{C}$. Eu-doped BaF_2 films were grown on Si(100) substrates using a two-stage growth method.⁷ The first stage was deposition of 600 Å of CaF_2 and 570 Å of BaF_2 at 580 $^\circ\text{C}$. The second stage was rapid thermal annealing at 820 $^\circ\text{C}$ followed by the deposition of a 4600 Å Eu-doped BaF_2 layer at 750 $^\circ\text{C}$.

Figure 1 shows the RHEED patterns recorded during the growth of CaF_2 and BaF_2 on Si(100) with Eu concentrations of ~ 4.05 and ~ 0.93 at. %, respectively. The Eu concentrations were determined in a way described in Ref. 4. A well-defined Si(100)-two-domain (2×1) pattern appears after oxide desorption [Fig. 1(a)]. Diffraction spots, indicative of three-dimensional island growth, were observed after the growth of the Eu-doped CaF_2 layer [Fig. 1(b)]. No apparent change in the surface structure of the CaF_2 matrix due to Eu incorporation is detected through comparison of the RHEED patterns of the Eu-doped CaF_2 layer with those of the undoped CaF_2 buffer. However, surface degradation is visible under optical microscopy when Eu concentration exceeds ~ 7.48 at. % even though the RHEED patterns remain unchanged. Precipitation of Eu at high doping levels may be responsible for the surface degradation. The effect of *in situ* annealing is evident by comparing the RHEED patterns

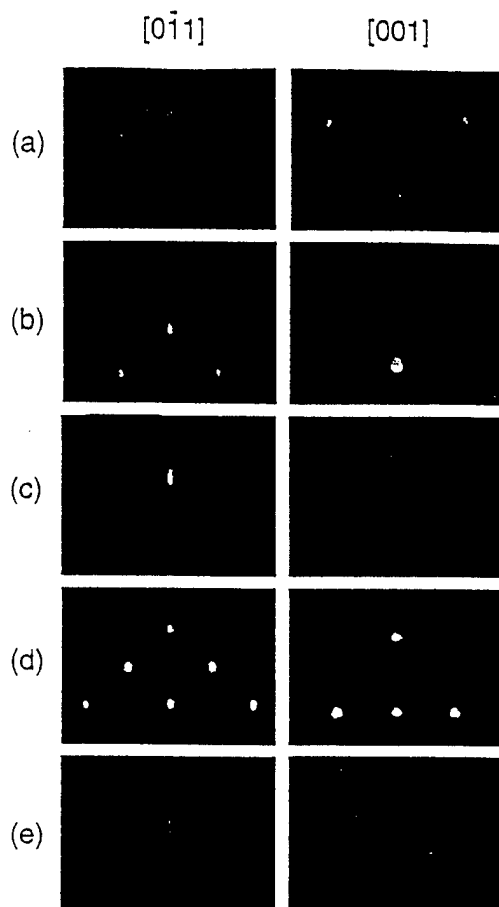


FIG. 1. RHEED patterns along the $[0\bar{1}1]$ and $[001]$ azimuths recorded after: (a) desorption of oxide from Si(100) substrate; (b) deposition of a 3600 Å Eu-doped CaF₂ layer; (c) *in situ* annealing at 1100 °C for 2 min; (d) deposition of a 570 Å BaF₂ layer; (e) second-stage growth of 4600 Å Eu-doped BaF₂ layer.

shown in Figs. 1(b) and 1(c). Diffraction spots were replaced by sharp diffraction streaks accompanied by Kikuchi lines immediately after the substrate temperature was raised to 1100 °C, signifying the smoothing of the CaF₂ surface. While *in situ* annealing improves the growth morphology by smoothing out the $\{111\}$ facets on the surface, it does not seem to alleviate the morphological features due to Eu precipitation. Following the deposition of BaF₂ at 580 °C, a spotty RHEED pattern with off-angle lines and arrow-head features was observed [Fig. 1(d)], indicating island epitaxy at this stage. Dramatic improvement in the growth morphology was achieved after *in situ* annealing and the second-stage growth. Diffraction streaks emerged in the RHEED patterns [Fig. 1(e)] and no change due to the incorporation of Eu in the BaF₂ lattice was observed.

Figure 2 shows the PL spectra of three Eu-doped CaF₂ films grown on Si(100), (110) and (111). A sharp zero-phonon line (ZPL) near 413 nm accompanies a broad vibronic sideband peaking at about 422 nm in each spectrum. The ZPLs shown in Fig. 2 arise from the electronic transition from the lowest lying $^7F_0(4f^65d)$ level of Eu²⁺ to the $^8S_{7/2}(4f^7)$ ground state. The peaks between the vibronic

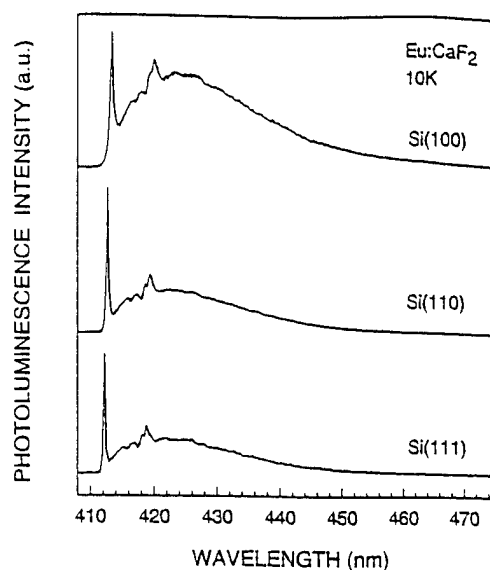


FIG. 2. Photoluminescence spectra of Eu-doped CaF₂ films grown on: (a) Si(100), ~0.77 at. % Eu; (b) Si(110), ~4.32 at. % Eu; and (c) Si(111), ~0.32 at. % Eu. The spectra were taken at 10 K. Note the relative shifts in energy position of the zero-phonon lines.

sideband maxima and the ZPLs are associated with the density of states maxima of various optical and acoustic phonons. No emission indicative of a $^5D_0 \rightarrow ^7F_J$ transition of Eu³⁺ was observed in the entire scanned range of 400–667 nm.

It was noticed that the ZPLs in Fig. 2 were shifted by different amounts relative to bulk CaF₂. The ZPL positions and shifts are listed in Table I. The energy shifts in the ZPLs can be attributed to the residual thermal-induced tensile strain in the CaF₂ layers because of the higher thermal expansion coefficient of CaF₂ ($19 \times 10^{-6}/\text{deg}$) relative to Si ($2.5 \times 10^{-6}/\text{deg}$). Since the CaF₂ layers in our case are much thicker than the critical thickness for growth on Si (~10 nm),⁸ most of the compressive strain in the CaF₂ layers due to the larger lattice constant of CaF₂ compared with Si substrate would be relieved at the growth temperature.

It has been demonstrated that Eu²⁺ incorporated into CaF₂ films grown on Si(111) substrates can be used as a sensitive probe of elastic strain in the grown layers.^{8,9} It is known that with uniaxial stress along $\{100\}$ or $\{110\}$, the ZPL of Eu²⁺ in bulk CaF₂ crystals is split into a doublet and that with uniaxial stress along $\{111\}$, the ZPL is not split but only shifted to longer wavelengths.¹⁰ In general, the in-plane

TABLE I. Energy shift of zero-phonon lines (ΔE) and estimated strain (ϵ_{\parallel}) obtained from the CaF₂ films grown on Si substrates with different orientations.

Substrate orientation	ZPL position (nm) ^a	ΔE (cm ⁻¹)	ϵ_{\parallel} (%)
(100)	413.4	-22	0.83
(110)	412.7	19	0.24
(111)	412.2	48	0.38

^aZero-phonon line (ZPL) of Eu²⁺ in bulk CaF₂ is at 413.01 nm.

strain, induced by the lattice-mismatched epitaxial growth, can be decomposed into uniaxial and hydrostatic contributions. Assuming that CaF₂ films heteroepitaxially grown on

(100)-, (110)-, and (111)-oriented substrates are under planar tensile strain, the relationship between in-plane strain $e_{||}$ and energy shift ΔE of the ZPL can be expressed as follows:^{10,11}

$$\begin{aligned} (100) \quad e_{||} &= a \Delta E \text{ (cm}^{-1}\text{)}, \quad a = -\frac{C_{11}}{2(A+2B)(C_{11}+2C_{12})(C_{11}-2C_{12})} = -3.79 \times 10^{-4}, \\ (110) \quad e_{||} &= b \Delta E \text{ (cm}^{-1}\text{)}, \quad b = -\frac{C_{11}+2C_{12}+4C_{44}}{(A+B)(C_{11}+2C_{12})(C_{11}+2C_{12}+12C_{44})} = 1.31 \times 10^{-4}, \\ (111) \quad e_{||} &= c \Delta E \text{ (cm}^{-1}\text{)}, \quad c = -\frac{C_{11}+2C_{12}+4C_{44}}{12A(C_{11}+2C_{12})C_{44}} = 7.94 \times 10^{-5}, \end{aligned}$$

where C_{ij} are the elastic constants of CaF₂, $A = -0.45 \text{ cm}^{-1} \text{ kg}^{-1} \text{ mm}^{-2}$ and $B = 0.28 \text{ cm}^{-1} \text{ kg}^{-1} \text{ mm}^{-2}$.¹⁰ Using the above expressions, we can estimate the in-plane strain for the Eu-doped CaF₂ layers. The results are listed in Table I. The strains obtained for the CaF₂ layers grown on Si(111) and (110) are close to the one ($\sim 0.3\%$) measured at liquid helium temperature for films not under stress at room temperature.⁹ This suggests that these CaF₂ films may have undergone almost complete relaxation at room temperature, probably through the glide of dislocations on available $\{100\}$ slip planes.¹² Due to the lack of such gliding planes, strain relief is less effective in CaF₂/Si(100) films, resulting in a larger strain value.

The dependences of the integrated emission intensities of both the vibronic sideband and the ZPL on Eu concentration for Eu-doped CaF₂/Si(100) films are shown in Fig. 3. The intensity of the vibronic sideband increases as the Eu concentration increases. At relatively low concentrations, the intensity of the ZPL also increases with Eu concentration. When the Eu concentration exceeds $\sim 1.64 \text{ at. \%}$, however, a

noticeable decline in the PL intensity is observed similar to those reported for Nd-doped CaF₂/Si films.¹³ Such emission quenching seems to be characteristic of rare-earth-doped CaF₂ epilayers on Si and may be attributed to nonuniform distribution of rare-earth ions during growth caused by dislocations and other crystal defects.

Very bright and broad "yellow" emission was obtained from epitaxial BaF₂ films grown on Si(100) with Eu concentration of $\sim 0.93 \text{ at. \%}$ (Fig. 4). As a comparison, a PL spectrum from a Eu-doped CaF₂ film on Si(100) is also shown in Fig. 4. The structureless feature in the emission spectra of Eu²⁺ in BaF₂ compared with the ones in CaF₂ has been attributed to the static Jahn-Teller effect.¹⁴ As shown in Fig. 4, the emissions of Eu²⁺ in CaF₂ and BaF₂ cover a broad wavelength range from 400 nm to 850 nm. Since BaF₂ can be readily grown on CaF₂, two-color (blue and yellow) light emitters may possibly be developed from Eu-doped stacked BaF₂/CaF₂ films on Si.

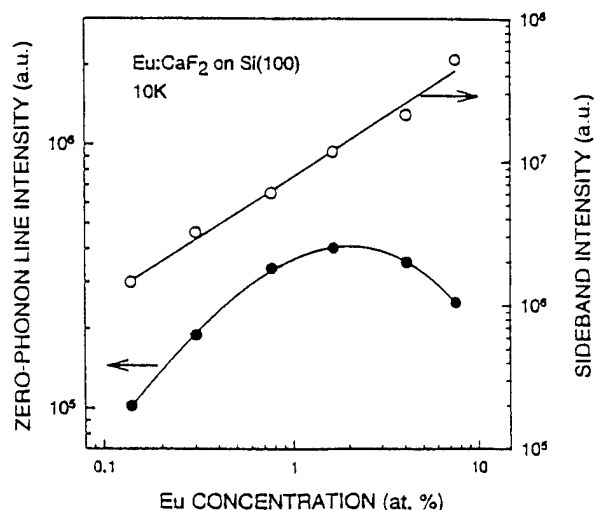


FIG. 3. Dependence of the integrated emission intensities of vibronic sideband and zero-phonon line on Eu concentration for Eu-doped CaF₂/Si(100) films.

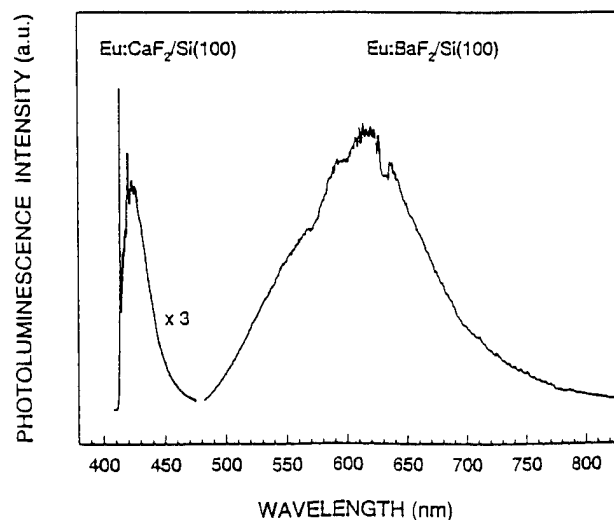


FIG. 4. Photoluminescence spectrum taken at 10 K showing strong yellow emissions from a Eu-doped BaF₂ film on Si(100) with a Eu concentration of $\sim 0.93 \text{ at. \%}$. A photoluminescence spectrum from a Eu-doped CaF₂ film on Si(100) with a Eu concentration of $\sim 0.77 \text{ at. \%}$ is given as a comparison.

III. CONCLUSION

In summary, the growth of Eu-doped CaF_2 thin films on Si with different orientations and Eu-doped BaF_2 layers on Si(100) have been achieved by MBE using an elemental Eu source. Smooth surface morphology is obtained for Eu-doped CaF_2 and BaF_2 on Si(100) using *in situ* annealing and two-stage growth techniques. Very bright blue to violet luminescence in Eu-doped CaF_2 films and yellow luminescence in Eu-doped BaF_2 layers have been observed. Energy shifts in the ZPL for three differently oriented CaF_2 layers have been used to estimate the in-plane thermal strain in the epilayers.

ACKNOWLEDGMENTS

The authors thank John Furneaux and Matthew Johnson for helpful discussions, and Joel Young for technical support with the MBE laboratory. This work was partially supported by the National Science Foundation through Grant No. OSR-9108771.

- ¹L. E. Bausá, R. Legros, and A. Muñoz-Yagüe, *Appl. Phys. Lett.* **59**, 152 (1991).
- ²C. C. Cho, W. M. Duncan, T. H. Lin, and S. K. Fan, *Appl. Phys. Lett.* **61**, 1757 (1992).
- ³E. Daran, R. Legros, A. Muñoz-Yagüe, C. Fontaine, and L. E. Bausá, *J. Appl. Phys.* **76**, 270 (1994).
- ⁴X. M. Fang, T. Chatterjee, P. J. McCann, W. K. Liu, M. B. Santos, W. Shan, and J. J. Song, *Appl. Phys. Lett.* **67**, 1891 (1995).
- ⁵A. Ishizaka and Y. Shiraki, *J. Electrochem. Soc.* **133**, 666 (1986).
- ⁶W. K. Liu, X. M. Fang, and P. J. McCann, *Appl. Phys. Lett.* **67**, 1695 (1995).
- ⁷X. M. Fang, P. J. McCann, and W. K. Liu, *Thin Solid Films* (in press).
- ⁸N. S. Sokolov, N. L. Yakovlev, and J. Almeida, *Solid State Commun.* **76**, 883 (1990).
- ⁹N. S. Sokolov, E. Virgilio, S. V. Gastev, S. V. Novikov, and N. L. Yakovlev, *Sov. Phys. Solid States* **31**, 216 (1989).
- ¹⁰A. A. Kaplyanskii and A. K. Przhevuskii, *Opt. Spectrosc.* **19**, 331 (1965).
- ¹¹R. People and S. A. Jackson, in *Semiconductors and Semimetals*, edited by T. P. Pearsall (Academic, Boston, 1990), Vol. 32.
- ¹²S. Blunier, H. Zogg, C. Maissen, A. N. Tiwari, R. M. Overney, H. Haefke, P. A. Buffat, and G. Kostorz, *Phys. Rev. Lett.* **68**, 3599 (1992).
- ¹³L. E. Bausá, C. Fontaine, E. Daran, and A. Muñoz-Yagüe, *J. Appl. Phys.* **72**, 499 (1992).
- ¹⁴S. A. Kazanskii and E. G. Reut, *Opt. Spectrosc.* **68**, 477 (1990).

PROCEEDINGS REPRINT



SPIE—The International Society for Optical Engineering

Reprinted from

Physics and Simulation of Optoelectronic Devices IV

29 January–2 February 1996
San Jose, California



Volume 2693

©1996 by the Society of Photo-Optical Instrumentation Engineers
Box 10, Bellingham, Washington 98227 USA. Telephone 360/676-3290.

Optical studies of epitaxial GaN based materials

J.J. Song, W. Shan, T. Schmidt, X.H. Yang, A. Fischer, S.J. Hwang, and B. Taheri
*Center for Laser Research and Department of Physics, Oklahoma State University
Stillwater, OK 74078*

B. Goldenberg and R. Horning
Honeywell Technology Center, Plymouth, MN 55441

A. Salvador, W. Kim, Ö. Aktas, A. Botchkarev, and H. Morkoç
Coordinated Science Laboratory, University of Illinois, Urbana, IL 61801

ABSTRACT

A variety of spectroscopic techniques has been used to study the optical properties of epitaxial GaN based materials grown by metalorganic chemical vapor deposition and molecular beam epitaxy. The emphasis was on the issues vital to device applications such as stimulated emission and laser action, as well as carrier relaxation dynamics. Sharp exciton structures were observed by optical absorption measurements above 300 K, providing direct evidence of the formation of excitons in GaN at temperatures higher than room temperature. Using a picosecond streak camera, the time decay of free and bound exciton emissions was studied. By optical pumping, stimulated emission and lasing were investigated over a wide temperature range up to 420 K. In addition, the optical nonlinearity of GaN was studied using wave mixing techniques.

1. INTRODUCTION

GaN based wide band-gap III-V nitride semiconductors currently attract much attention for their applications in electronic and optoelectronic devices, such as high power-high efficiency amplifiers, UV, blue, green, and yellow LED's, and in short-wavelength laser diodes.¹⁻³ With rapid progress in nitride epitaxial growth technology, high quality nitrides single crystal epilayers can now be grown on such substrates as sapphire and SiC. Recent demonstration of superbright high-efficient blue LED's, the development of the blue laser diode based on nitride heterostructures by the Nichia group^{4,5} and the observation of optically pumped stimulated emission in GaN epilayers by a few groups^{6,7} have led to increased interest in the development of efficient nitride UV-visible light emitters.

Although assessment of the properties and potential applications of nitrides is actively pursued to accelerate device fabrication, some vital issues directly related to optoelectronic device applications such as optically pumped stimulated emission and lasing, carrier dynamics, and optical nonlinearities have not been fully explored. In this report, we present the results of optical studies on the properties of GaN based epitaxial materials grown by metalorganic chemical vapor deposition (MOCVD) and molecular beam epitaxy (MBE) on sapphire substrates. Strong, sharp spectral structures associated with excitons in GaN based materials were observed in all samples used in this work by photoluminescence (PL) and

optical absorption measurements. Optically pumped stimulated emission and lasing phenomena in GaN epitaxial layers and GaN/AlGaIn heterostructures were investigated using high-power pulsed lasers. Stimulated emissions exhibiting longitudinal cavity modes were observed over a wide temperature range from 10 up to 420 K. The dynamics of photoexcited excess carriers in high quality GaN samples were investigated by transient luminescence spectroscopy in the picosecond regime using a streak camera in the region of near band-edge excitonic emissions. The nonlinear optical properties of GaN epitaxial layers were studied using degenerate four-wave mixing experiments. The nonlinear refractive coefficient of GaN was derived by examining the third order scattering efficiency.

2. EXPERIMENTAL DETAILS

The GaN samples used in this study were all nominally undoped single-crystal films grown on (0001) sapphire substrates by MOCVD. Thin AlN buffers of ~ 50 nm were deposited on sapphire substrates at 775°C before the growth of GaN. GaN layers were deposited at 1040°C directly on the AlN buffers. The GaN/AlGaIn separate confinement heterostructures used in this work were grown on (0001) sapphire substrates by a modified reactive MBE at a substrate temperature near 800°C. The particular structure under discussion has a 600 Å thick AlN layer, directly grown on sapphire, followed by a GaN buffer layer, an AlGaIn cladding layer, a lower mole fraction AlGaIn waveguide layer, a 70 Å thick GaN quantum well, which is capped by a low mole fraction AlGaIn waveguide, and an AlGaIn cladding layer. The quantum well was doped with Si to a level of $5 \times 10^{17} \text{cm}^{-3}$.

Various optical measurements were carried out on the samples. Conventional photoluminescence (PL) spectra were measured with a cw HeCd laser (325 nm) as an excitation source and a 1-M double-grating monochromator connected to a photon-counting system. For optical absorption measurements, the quasi-monochromatic light dispersed by a $\frac{1}{2}$ -M monochromator from a halogen tungsten lamp was focused on the sample, and the transmission signals were detected using a lock-in amplifier system. Time-resolved photoluminescence (TRPL) measurements were performed using a frequency tunable pulsed laser (2 ps pulse duration, 82MHz) as an excitation source and a streak camera (2 ps resolution), in conjunction with a $\frac{1}{4}$ -M monochromator as a detection system. Stimulated emission and lasing experiments were carried out employing side-pumping geometry. A frequency-doubled pulsed Nd:YAG laser (532 nm) with a repetition rate of 10 Hz was used to pump a dye laser as a primary optical pumping source (10 ns). The output photon energy of the dye laser was then frequency doubled into UV wavelengths to photopump the GaN samples. The wave mixing experiments were performed using frequency doubled laser pulses (532 nm, 13 ps) from a mode-locked Q-switched Nd:YAG laser (10 Hz) in a forward propagating boxcar geometry.

3. RESULTS AND DISCUSSIONS

3.1 Exciton structures

The GaN samples studied in this work exhibit strong near-band-edge exciton luminescence. PL spectra taken from the samples are shown in Fig. 1. The strongest emission line marked by BX in the figure has a full width at half maximum (FWHM) of less than 1.0 meV at 10 K. The second one, labeled FX, shows a FWHM of less than 1.5 meV. The intensity of the BX peak was found to decrease much

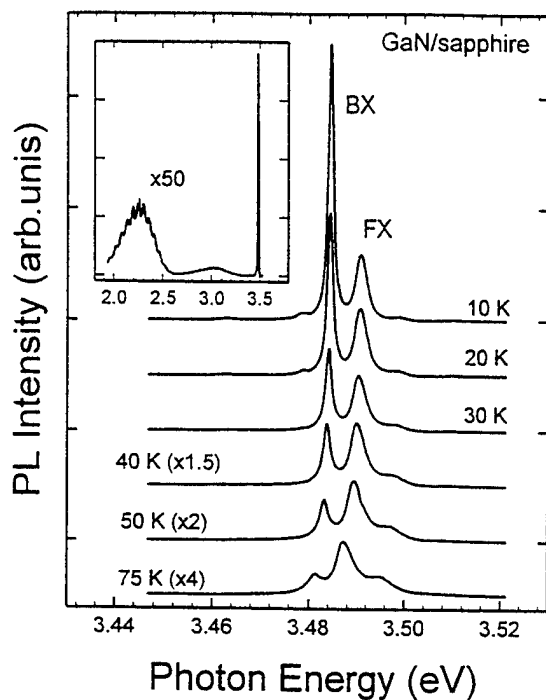


Fig. 1. Exciton luminescence spectra of a GaN sample taken at different temperatures. The inset shows the 10 K PL spectrum over a broad spectral range.

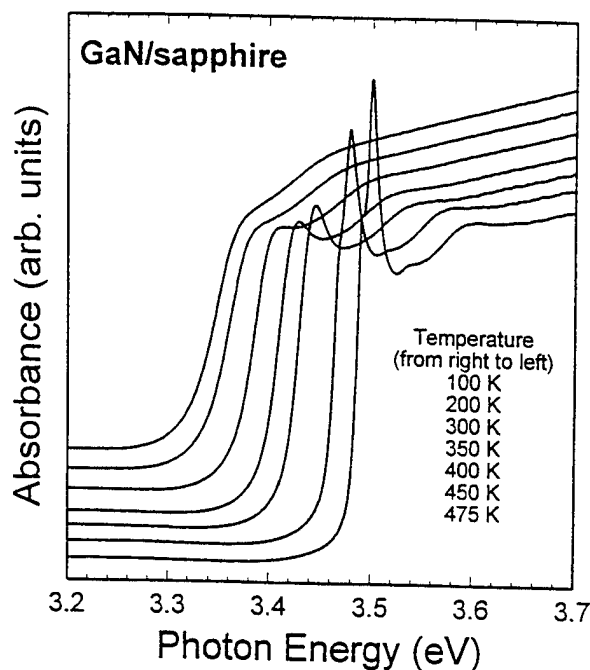


Fig. 2. Absorption spectra of a GaN epitaxial layer in the vicinity of fundamental absorption edge at different temperatures. The curves are vertically displaced for clarity.

faster than that of the FX as the temperature increased. It became hardly resolvable when the temperature was raised to above 100 K (not shown). Such variations of the luminescence intensity as a function of temperature indicate that the emission line can be attributed to the radiative recombination of excitons bound to neutral donors. The second strongest luminescence line, together with the weak emission feature on the higher energy side, can be assigned to intrinsic free-exciton emissions. The inset shows a broad range of the typical PL spectrum taken at 10 K. The broadband yellow emission and a weak emission band in the blue spectral region were observed.

Optical absorption measurements were performed on the GaN over a wide temperature range. The results for a thin GaN epitaxial layer in the vicinity of band edge at various temperatures are shown in Fig. 2. Sharp absorption peaks on the lower-energy side of the fundamental absorption edge are observed and are associated with the formation of excitons. Fine spectral features arising from the 1s state of the intrinsic free excitons associated with the split-off band edges of wurtzite GaN can be well resolved at low temperatures. The excitonic absorption resonance can be clearly observed well above room temperature up to higher than 400 K. Such clear observations of the excitonic absorption resonance above room temperature provide the direct evidence of the formation of excitons in GaN at temperatures higher than room temperature and indicate that the free exciton associated with the fundamental band gap of GaN has a substantially large binding energy. However, the complicated fundamental band edges of wurtzite GaN make it rather difficult to derive exciton binding energy unambiguously from the absorption spectra.

We also note that a weak absorption spectral feature is clearly visible in the energy region of

about 100 *meV* above the excitonic resonance. This is a real absorption structure though it is weaker and broader than the main absorption structures. It was also observed in photoreflectance, photoconductivity and photoluminescence excitation spectra taken from GaN epitaxial samples with various layer thicknesses grown on either sapphire or SiC substrates. Its temperature dependence is found to follow the main absorption edge, reminiscent of the transition from the third valence band (spin-orbit split-off band) to the conduction band in zinc-blende semiconductors. Unfortunately, there are few theoretical band structure calculations for wurtzite GaN detailing the band lineups in the vicinity of fundamental band gap for comparison. The identification of this transition requires further study.

3.2 Relaxation dynamics of free excitons and bound excitons

The temporal evolution of spectrally integrated exciton luminescence for both free-exciton (FX) and bound-exciton (BX) emissions observed in a GaN sample at 10 K is shown in Fig. 3. The overall time resolution of the experimental system used for conducting the measurements is less than 15 *ps*. The intrinsic free-exciton (FX) luminescence lines in these samples can be spectrally well resolved from that of excitons bound to neutral donors, as shown in the inset in the figure. That allows an unambiguous determination of the PL decay time for both intrinsic free excitons and neutral-donor bound excitons. The lifetime of the PL decay at 10 K was found to be typically about 35 ± 5 *ps* for free excitons and 45-55 *ps* for bound excitons, varying from sample to sample used in this work. The measured decay time is much shorter than the value estimated by theoretical considerations regarding the radiative lifetime of an excited state in a semiconductor, where the radiative lifetime of bound excitons in GaN is expected to be on the order of several hundreds of picoseconds and that of free excitons in the nanosecond domain.⁸

The discrepancy between the measured values of PL decay times and the theoretical estimated ones can be attributed to nonradiative relaxation processes in competition with the radiative channel. The measured PL decay time only yields an effective lifetime (τ_{eff}) for free excitons and bound excitons. It is related to both the radiative (τ_R) and nonradiative (τ_{NR}) lifetimes with the decay rate expressed as

$$1/\tau_{\text{eff}} = 1/\tau_R + 1/\tau_{\text{NR}} \quad (1)$$

In this equation, we have assumed that the nonradiative decay is exponential so that a lifetime can be defined, and that the carriers in the levels which undergo recombination are at thermal equilibrium. When the nonradiative decay rate is larger, the measured decay time is characteristic for the nonradiative processes in accordance with Eq.(1).

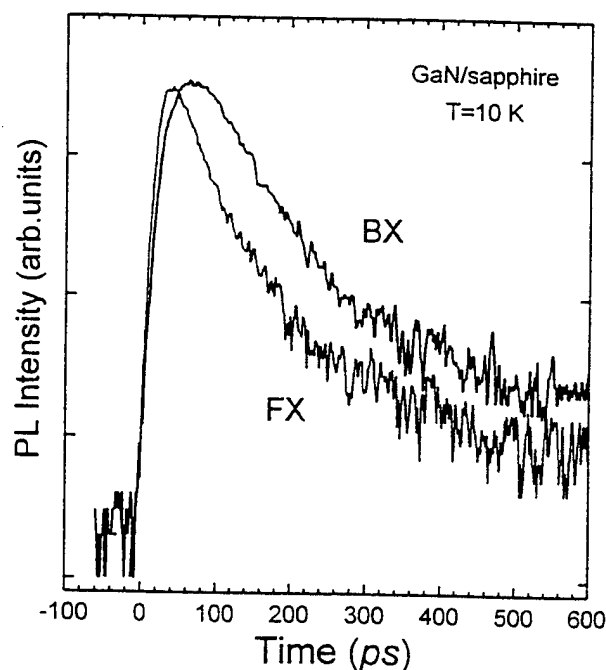


Fig. 3. Temporal evolution of spectrally integrated PL for both intrinsic free-exciton and bound-exciton emissions in a GaN sample at 10 K.

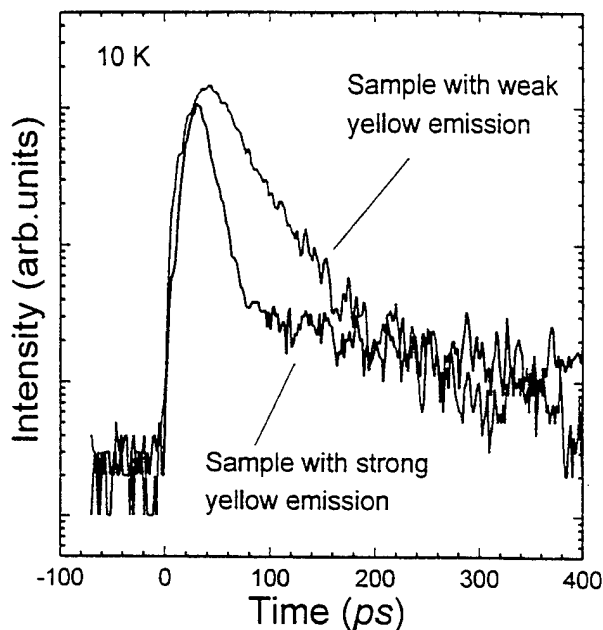


Fig. 4. Comparison of the time decay of free-exciton emission between two GaN samples with the relative intensity ratio of 100:1 for the broadband yellow emission under the same excitation conditions.

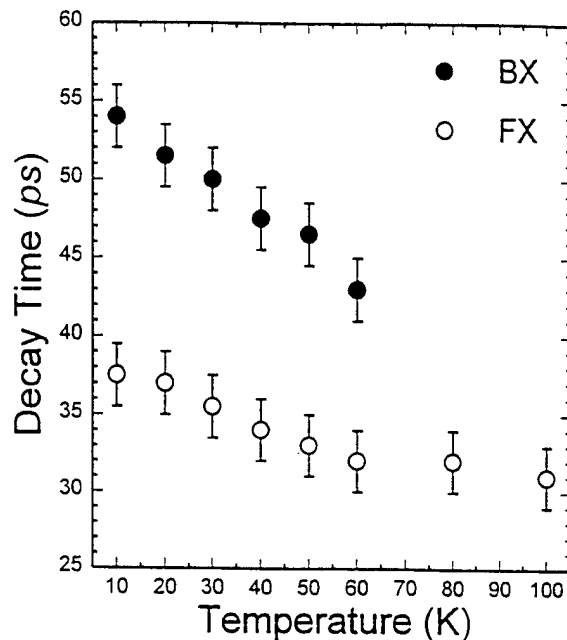


Fig. 5. The measured decay times for free-exciton emission and bound-exciton emission as a function of temperature.

This situation is typical for recombination from intrinsic states of semiconductors.⁹ The nonradiative processes, such as multiphonon emission, capture by deep centers, Auger effect, *etc.*, give rise to fast relaxation of the excited carriers down to lower states from which they decay radiatively or relax nonradiatively. As a result, the measured PL decay time for a given excited state is an effective lifetime and usually much shorter than a radiative one. The slow rise of bound-exciton luminescence intensity compared to that of the free-exciton PL shown in Fig. 3 is an indicator of such nonradiative relaxation processes for free excitons arriving at the bound exciton energy. Therefore, the capture of excitons and trapping of carriers by such nonradiative centers at defects and impurities must play a major role in the recombination processes responsible for the exciton population decay in the GaN samples studied in this work. In fact, the measured PL decay time was found to be directly related to the intensity of broadband emissions lying in the GaN band gap. The broad emission structure referred to as yellow emission in the literature is believed to be associated with the optical transitions between the energy levels involving impurity and/or defect states. The intensity of yellow emission is proportional to the density of some particular defects or impurities present in samples. We found that the stronger the yellow emission, the shorter the PL decay time in a GaN sample. Fig. 4 compares free-exciton PL decay between two samples with the relative intensity ratio of 100:1 for the yellow emission under identical excitation conditions. The deduced lifetime of free-exciton emission in the sample with stronger yellow emission is only 15 ps (which is the limit of our instrumental resolution). Therefore, the fast decay behavior of the intensity indicates that the capture of excitons and trapping of carriers at defects and impurities through nonradiative combinations dominate the decay of the exciton population. The process of capture, therefore, must depend on the density of defects and impurities in the GaN samples.

The influence of nonradiative recombination on the measured decay time of exciton luminescence

can be further manifested by the effects of sample temperature. It is known that for a radiative recombination dominant system, an increase in the radiative lifetime with temperature is expected for the free excitons^{10,11} since their average kinetic energy is increased. The thermal redistribution results in a decreasing number of the excitons close enough to the Brillouin-zone center for radiative recombination. Also the lifetime is expected to be independent of temperature for bound excitons, and only the emission intensity is expected to decrease because of thermal ionization of the bound excitons. However, the bound-exciton PL decay time was found to decrease with increasing temperature before the emission thermally quenched, and the free-exciton PL decay time measured from the majority of samples used in this work exhibited a slow decrease with temperature, as shown in Fig. 5. Although recombination from excitons bound to extrinsic states such as defects or impurities can often be very efficient at low temperatures as demonstrated by Fig. 1, the measured decay time is still determined by detailed decay kinetics. The observed decrease of PL decay time with temperature for the bound excitons in the GaN samples indicates that incrementally stronger nonradiative relaxations occur as the temperature increases, resulting in continued faster decay of the exciton population. The decrease of free-exciton PL in both intensity and decay time with temperature suggests that the nonradiative processes of capture of free excitons at defects or impurities prevail in the competition with the thermally enhanced exciton-exciton and exciton-phonon scatterings.

3.3 Optically pumped stimulated emission and lasing

With a carefully designed optical pumping scheme, optically pumped stimulated emission and laser actions were achieved in the GaN samples with bar-like shape under both picosecond and nanosecond laser excitations. The laser actions could be observed over a broad temperature range from 10 K up to 400 K. All samples exhibit, more or less, longitudinal lasing modes in their emission spectra. Fig. 6 plots the emission intensity against the pumping power density. The observations of superlinear increase in intensity with the excitation power density, together with the spectral narrowing and the complete suppression of the broad emission background, are typical characteristics of the occurrence of stimulated emission. The onset of the superlinear increase in emission intensity is defined as the lasing threshold. The threshold was found to be weakly dependent on temperature. Our results yield a factor of less than two for the increase in the threshold, from $\sim 500 \text{ kW/cm}^2$ at 10 K to $\sim 800 \text{ kW/cm}^2$ at room temperature (295 K).

Generally, the threshold value can be affected by parameters that are dependent on the pumping source and sample. For a given optical

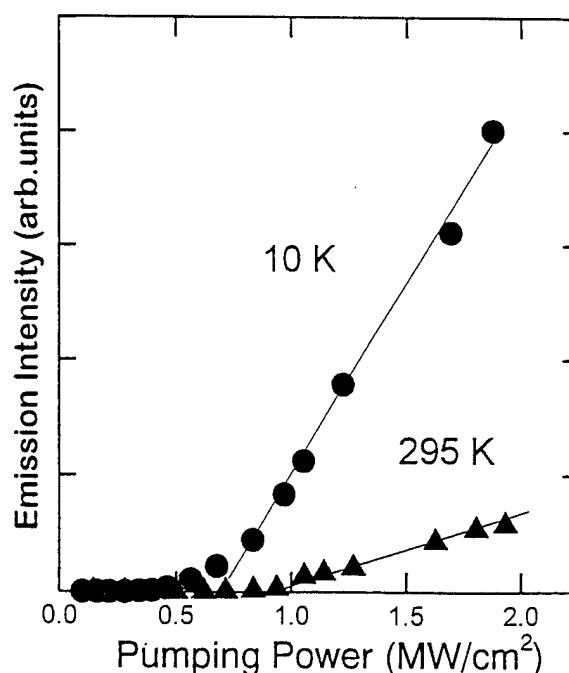


Fig. 6. Measured emission output vs. Pumping power density at 10 K and room temperature (295 K). The onset of the superlinear increase in emission intensity is defined as the lasing threshold.

pumping source, the most important influence on the threshold is from the sample itself with the threshold varying from sample to sample. This can be classified into two groups: one is associated with material properties, such as impurities, crystallinity, and defects; the other is related to the sample preparation, such as laser cavity length and the quality of sample edge facets. We expect that the value of the pumping power threshold for lasing in GaN can be lowered substantially by better preparing the sample facet edges, for example, with reflective coating. With the crystalline quality further improved and better designed laser structures for carrier confinement and waveguiding, such as double heterostructures or quantum well structures being used, the lasing threshold is also expected to be significantly lowered.

The specimens used in this optical pumping experiment were bar-like pieces merely cut off rather than cleaved from the large GaN wafer due to the well-known difficulties of forming high quality facets in sapphire. However, with attempts to finesse the cut surfaces, as shown in Fig. 7, we did observe some substantial improvements in terms of Fabry-Perot cavity mode fringes. Fig. 8 shows a comparison of three lasing spectra taken under almost the same pumping conditions from three specimens subjected to different treatments and demonstrates the progressive improvement of the quality of observed mode fringes. The spectrum exhibited line-width narrowing and mode fringes enhancing, after the specimen's facet edges were fine polished. When a set of external mirrored cavity was imposed to the samples, the mode quality was much improved. In addition, the emission intensity was found to increase by a factor of two.

We have also performed optical gain measurements using the approach of monitoring the emission intensity at fixed power levels by varying the length of the excitation beam on an as-cut sample. Fig. 9 plots the emission intensity as a function of excitation length at selected pumping power levels. The measured gain values are also given in the figure, which are within the range of recently published theoretical calculation results.^{12,13}

The significant reduction of room-temperature threshold has been recently observed in MBE GaN/AlGaIn separate confinement heterostructure (SCH) samples. The pumping threshold for stimulated emission was determined to be $\sim 90 \text{ kW/cm}^2$, approximately one order of magnitude less than the value

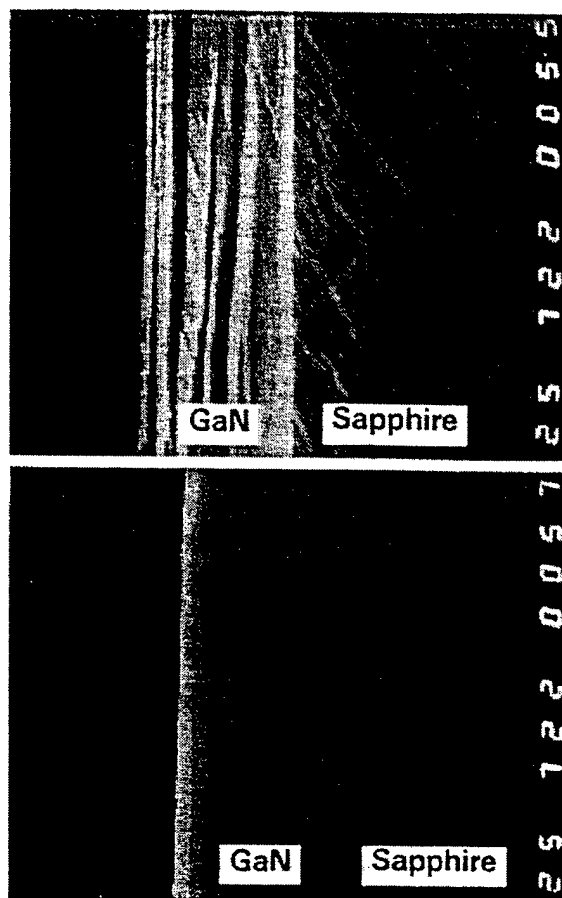


Fig. 7. Images of the surface morphology of GaN layers: cutting facet without polishing (upper portion) and fine polished facet (lower portion). The photographs were taken by SEM.

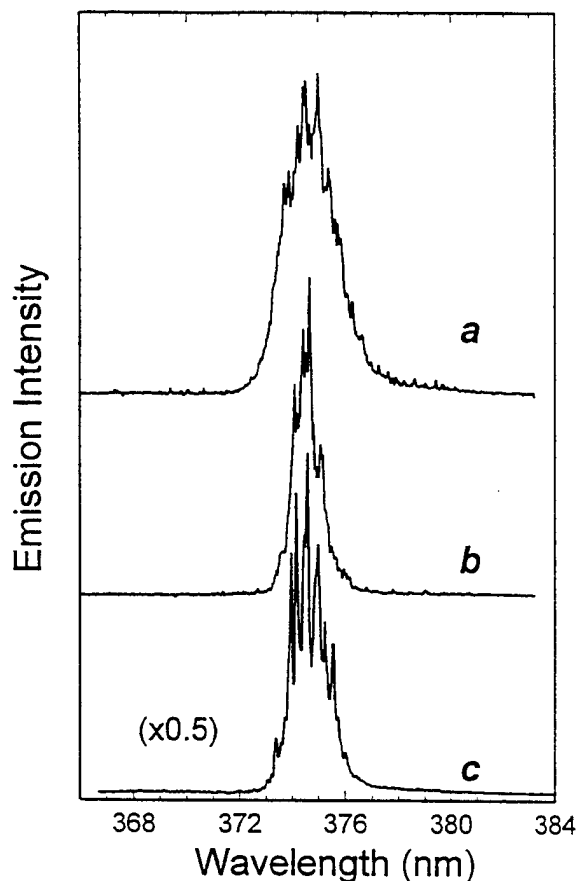


Fig. 8. Comparison of lasing spectra taken at 295 K under almost the same excitation conditions from three samples subjected to progressive treatments: (a) simply cut from wafer; (b) facet surface fine polished; (c) external mirror cavity imposed.

reported elsewhere.¹⁴ It should be noted here that the specimens used in this optical pumping experiment were small pieces simply cut off from the large GaN/AlGaIn SCH wafer with no attempt to finesse the cut surfaces. This provides a basis for our optimism that the pumping power threshold for stimulated emission and lasing in these samples can be further reduced with improved facets.

3.4 Picosecond degenerate four-wave mixing at 532 nm

The degenerate wave mixing experiments were performed using frequency-doubled pulses from a mode-locked, Q-switched Nd:YAG laser operating with a repetition rate of 10 Hz. The 532 nm pulse (13 ps) has a quasi-Gaussian spatial and temporal profile. The second harmonic output of the laser was equally split in energy into two pump beams and one probe beam. These beams were spatially and temporally recombined in the samples in a forward propagating boxcar geometry.¹⁵ The two pump beams were σ -polarized, while the probe beam was π -polarized in order to increase the signal-to-noise ratio and minimize interactions between the pump and probe beams. An energy meter preceded by a polarizer was used to detect the π -polarized diffracted signal. At the front surface of the sample, the two pump beams

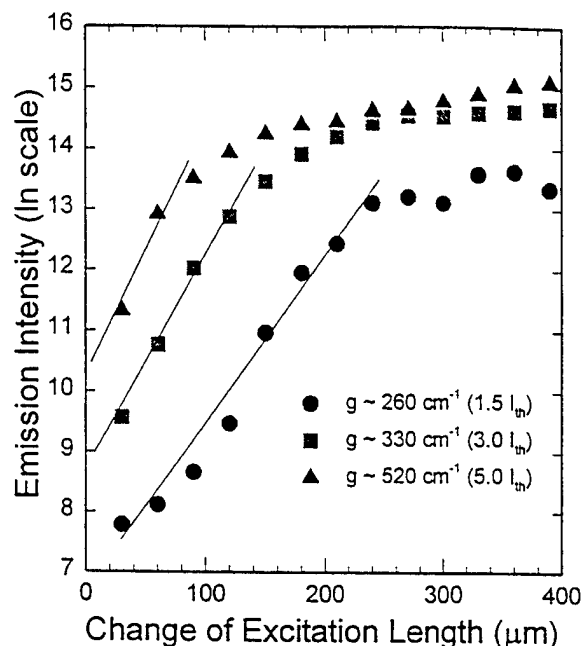


Fig. 9. The variation of emission intensity with the excitation beam length on an as-cut sample surface at selected pumping power levels at 295 K. The estimated optical gain values for the GaN sample are given in the figure. The pumping threshold $I_{th} = 800 \text{ kW/cm}^2$.

for the GaN epitaxial bulk given above even though the SCH sample edges were not cut parallel to each other. The substantial decrease in the stimulated emission threshold can be attributed to the carrier confinement and waveguiding effects of the SCH structure. Detailed discussions of the results will be

have a small crossing angle (2θ). The probe was incident on the interference region at a small angle with respect to the plane of the pump beams. In such a wave-mixing geometry, the pump beams set up an interference pattern in their overlap region with fringe spacing $\Lambda = \lambda/2\sin\theta$, where λ is the wavelength of the beams in free space. Intensity dependence causes the index of refraction in the light regions of the interference pattern to differ from that in the dark region. The overlap region, therefore, behaves as an index grating with spacing of Λ . An incident probe beam will be diffracted from this grating in the directions satisfied by the phase matching conditions. Fig. 10 shows a photograph of the diffracted signals together with the three attenuated incident beams when they are temporally overlapped in a thick GaN sample. The picture was taken at room temperature with the pump beam focal spot of $\sim 500 \mu m$ and the probe beam of $\sim 400 \mu m$ and total incident irradiance of 1.7 GW/cm^2 . The clearly visible patterned spots are diffracted higher order wave-mixing signals in the phase-matching directions. The strong diffracted signals in this wide band-gap material are consistent with the elegant band charge model, which predicts higher nonlinearities as the material becomes more polar.¹⁶⁻¹⁸

By delaying the arrival of the probe pulses relative to the pump pulses, the response of the nonlinear optical changes such as scattering efficiency in the GaN sample was studied. The scattering efficiency is defined as the ratio of the intensity of scattered to the transmitted probe beam. Scattering efficiency for an index grating can be expressed as:¹⁵

$$\eta(t) = I_{\text{scattered}} / I_{\text{transmitted}} = \sin^2\{k\Delta n(t)l/2\} = \{k\Delta n(t)l/2\}^2, \quad (2)$$

where k is the wave vector of the probe beam, $\Delta n(t)$ is the time dependent index change and l is the sample thickness. Fig. 11 illustrates the change of scattering efficiency as a function of the time delay of the probe beam. The non-exponential temporal evolution of the scattering efficiency is primarily caused

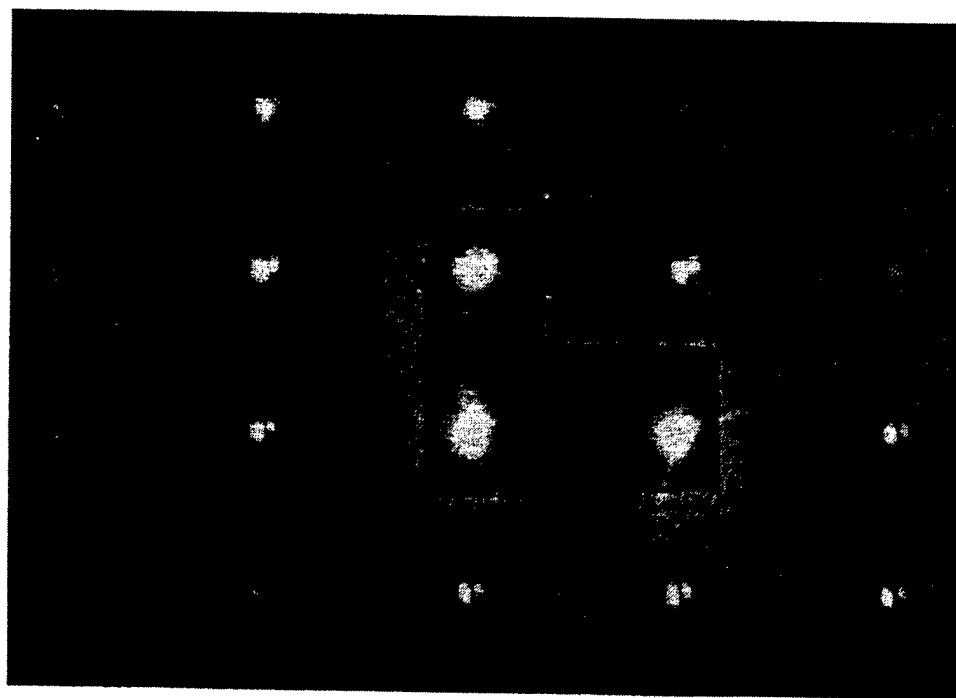


Fig. 10. Photograph of the wave mixing signals showing three attenuated pump and probe beams and higher order nonlinear diffracted signal spots. The laser photon energy (2.33 eV) is well below the room-temperature GaN band gap (3.42 eV).

by the decay of the pump-induced refractive index grating due to the combined effects of both recombination and diffusion of excited carriers. At zero delay, a maximum scattering efficiency of 4×10^{-5} was obtained. It corresponds to an index change, $\Delta n(0)$, of 1.2×10^{-3} . This change can be related to the pump beam intensity through an effective nonlinear refractive coefficient, n_2 , defined as

$$\Delta n(0) = n_2 I_0. \quad (3)$$

Provided the pump-beam irradiance of 1.2 GW/cm^2 , a value of $1 \times 10^{-3} \text{ cm}^2/\text{GW}$ was derived for the effective nonlinear refractive index n_2 from Eq.(3). Compared to the value of other wide band-gap semiconductor materials, for instance, $6.7 \times 10^{-5} \text{ cm}^2/\text{GW}$ for ZnSe,¹⁹ it is more than an order of magnitude higher, indicating the large optical nonlinearities for GaN.

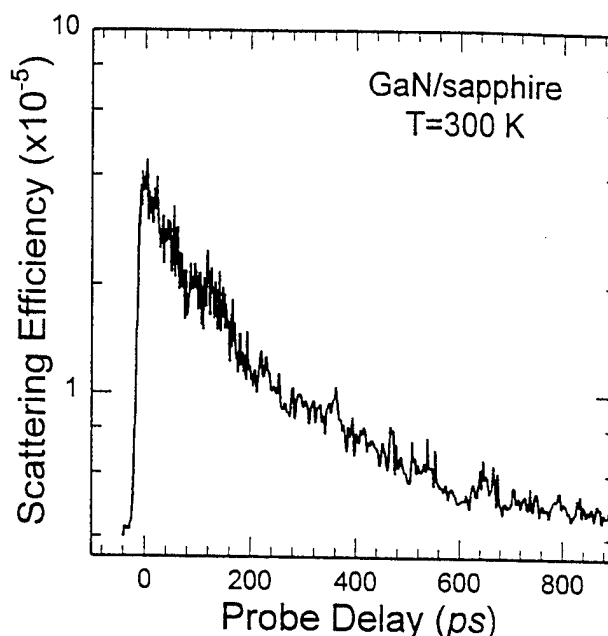


Fig. 11. Scattering efficiency measured as a function of the time delay of probe pulse. A maximum refractive index change can be derived from the result at zero delay.

4. CONCLUSIONS

Strong, sharp spectral structures associated with excitons in epitaxial GaN based materials were observed in photoluminescence and optical absorption spectra over a wide temperature range. In particular, the observation of sharp absorption peaks at the lower energy side of the absorption edge above room temperature provided direct evidence of the formation of excitons in GaN at high temperatures ($> 300 \text{ K}$). The relaxation dynamics of photoexcited carriers in GaN were studied by examining the radiative decay of exciton emissions using time-resolved photoluminescence spectroscopy. We found that the capture of excitons and trapping of carriers at defects and/or impurities through nonradiative relaxation processes dominate the decay of exciton population, resulting in a very short decay time for both free-exciton and bound-exciton emissions. The capture process depends on the density of impurities and defects in the GaN samples. Optically pumped stimulated emission and lasing phenomena in GaN and AlGaIn/GaN heterostructures were investigated using high-power pulsed lasers. Stimulated emission and laser action were observed over a wide temperature range from 10 K to $\sim 420 \text{ K}$. The pumping power threshold for lasing was estimated as $\sim 500 \text{ kW/cm}^2$ at 10 K to $\sim 800 \text{ kW/cm}^2$ at 295 K for bulk GaN epitaxial samples. The MBE grown GaN/AlGaIn SCH samples were found to exhibit stimulated emission threshold pumping powers as low as 90 kW/cm^2 at room temperature. This represents an order of magnitude reduction over the bulk GaN. The results suggest that the carrier confinement and waveguiding effects of the SCH samples give rise to a substantial decrease in the stimulated emission threshold. In addition, we found that the lasing mode quality can be substantially improved by finessing the cut facet edges of GaN on sapphire substrates. Strong high order nonlinear diffraction signals of

degenerate four-wave mixing were found in GaN epitaxial layers in three-beam forward propagating boxcar geometry. The nonlinear refractive index at 532 nm was determined for GaN by the measurement of maximum absolute scattering efficiency using picosecond wave mixing technique.

5. ACKNOWLEDGMENTS

This work at OSU was supported by AFOSR, ARPA, ONR and ARO. The work at UIUC was supported by grants from ONR, AFOSR, and BMDO. H.M. is funded by a university president research program funded by AFOSR. B.G. is pleased to acknowledge the technical assistance of Maurice Hitchell.

6. REFERENCES

1. S. Strite and H. Morkoç, J. Vac. Sci. Technol. **B10**, 1237(1992), and references therein.
2. J.I. Pankove, Mater. Res. Soc. Symp. Proc. **162**, 515(1990), and references therein.
3. H. Morkoç, S. Strite, G.B. Gao, M.E. Lin, B. Sverdlov, and M. Burns, J. Appl. Phys. **76**, 1363(1994).
4. See, for example, S. Nakamura, J. Vac. Sci. Technol. **A13**, 705(1995).
5. S. Nakamura, M. Senoh, S. Nagahama, N. Iwasa, T. Yamada, T. Matsushita, H. Kiyoku, and Y. Sugimoto, Jpn. J. Appl. Phys. **35**, part.2, Jan. 15 (1996).
6. X.H. Yang, T. Schmidt, W. Shan, J.J. Song, and B. Goldenberg, Appl. Phys. Lett. **66**, 1(1995).
7. A.S. Zubrilov, V.I. Nikovlaev, V.A. Dmitriev, K.G. Irvine, J.A. Edmond, and C.H. Carter, Jr., Inst. Phys. Conf. Ser. No.141, 525(1995).
8. W. Shan, X.C. Xie, J.J. Song, and B. Goldenberg, Appl. Phys. Lett. **67**, 2512(1995).
9. M. Voos, R.F. Leheny, and J. Shah, in *Optical Properties of Solids*, edited by M. Balkanski, (North-Holland, Amsterdam, 1980), Chapter 6, p.336.
10. J. Feldmann, G. Peter, E.O. Göbel, P. Dawson, K. Moore, C. Foxon, and R.J. Elliott, Phys. Rev. Lett. **59**, 2337(1987).
11. G.W. 't Hooft, W.A.J.A. van der Poel, and L.W. Molenkamp, Phys. Rev. **B35**, 8281(1987).
12. W. Fang and S.L. Chuang, Appl. Phys. Lett. **67**, 751(1995).
13. W.W. Chow, A. Knorr, and S.W. Koch, Appl. Phys. Lett. **67**, 754(1995).
14. T.J. Schmidt, X.H. Yang, W. Shan, J.J. Song, A. Salvador, W. Kim, Ö. Aktas, A. Botchkarev, and H. Morkoç, to be published in J. Appl. Phys.
15. H.J. Eichler, P. Gunter, and D.W. Pohl, *Laser-Induced Dynamic Gratings*, (Springer-Verlag, Berlin, 1986), p.47.
16. C.L. Tang and C. Flytzanis, Phys. Rev. **B4**, 2520(1971).
17. B.F. Levine, Phys. Rev. **B7**, 2600(1973).
18. F.W. Scholl and C.L. Tang, Phys. Rev. **B8**, 4607(1973).
19. M. Sheik-Bahae, A.A. Said, T.H. Wei, D.J. Hagan, and E.W. van Stryland, IEEE J. Quantum Electron. **26**, 760(1990).

Picosecond four-wave-mixing in GaN epilayers at 532 nm

Bahman Taheri,^{a)} J. Hays, and J. J. Song

Center for Laser Research and Department of Physics, Oklahoma State University,
Stillwater, Oklahoma 74078

B. Goldenberg

Honeywell Technology Center, Bloomington, Minnesota 55420

(Received 31 July 1995; accepted for publication 20 November 1995)

Pulsed probe degenerate four wave mixing experiments were performed on GaN epilayers using 13 ps pulses at 532 nm. Intensity and time response of the scattering efficiency was studied. Intensity dependence of the observed signal suggests carrier generation by both single and two photon effects. The absolute scattering efficiency was measured and related to pump-induced nonlinear index change. The nonlinear refractive coefficient found was $1 \times 10^{-3} \text{ cm}^2/\text{GW}$ which is greater than an order of magnitude larger than the expected value. Time response of the signal was found to be dictated by carrier lifetimes. Double-exponential decays to trap levels with lifetimes of 100 ps and 1.1 ns are suggested as the dominant recombination processes. © 1996 American Institute of Physics. [S0003-6951(96)03905-4]

Gallium nitride shows great promise as a potential material for blue emitting diodes and lasers. To this end, a number of experiments have been performed to study its physical and optical properties. These include studies of its photoluminescence,^{1,2} photorefectance,³ and lasing properties. The latter have been done for a wide range of temperature using nanosecond⁴⁻¹⁰ and picosecond¹¹ pumping. However, few studies have been performed on the nonlinear optical properties of GaN.¹²⁻¹⁴ These properties are an important aspect of any material to be used for optoelectronics. There have been some studies focusing on the second-order process such as second harmonic generation^{12,13} and the electro-optic effects.¹⁴ To our knowledge, however, third-order effects have not yet been investigated. In this letter, we present the results of pulsed probe degenerate four wave mixing (FWM) experiments in GaN epilayers.

The experiments were performed on a 7 μm GaN sample grown, using MOCVD, on a sapphire substrate with an AlN buffer. The study was done using frequency doubled pulses from a mode-locked, Q-switched Nd:YAG laser operating with a repetition rate of 10 Hz. The 532 nm pulses had a quasi-Gaussian spatial and temporal profile with an e^{-1} of 13 ps. Each pulse was split in three pulses of equal energy which were spatially and temporally recombined in the sample in a forward propagating boxcar geometry.¹⁵ The advantage of this geometry over the conventional counter-propagating technique is that the scattered signals are spatially separated from the input beams. This enhances the signal-to-noise (S/N) ratio and allows direct measurement of the absolute scattering efficiency. The two pump beams were σ polarized while the probe beam was π polarized in order to increase the S/N ratio and minimize interactions between the pump and probe beams. An energy meter preceded by a polarizer was used to detect the π -polarized diffracted signal. At the front surface of the sample, the pump beams had a beam radius of 500 μm and a crossing angle 2θ , of 2° . The

probe was incident on the interference region at an angle of 1.7° with respect to the plane of the pump beams. Its beam radius was slightly smaller at 400 μm . The smaller radius allows the central portion of the interaction region between the pump beams to be monitored. This reduces errors that can occur because of the finite radial extent of the pump beams.

The observed behavior can be qualitatively described as follows. The pump beams set up an interference pattern in the overlap region with fringe spacing $\Lambda = \lambda/2\sin\theta$, where θ is the wavelength of the beams in free space. Intensity dependence of the refractive index causes the index of refraction in the light regions of the interference pattern to differ from that in the dark region. The overlap region, therefore, behaves as an index grating with spacing Λ , which for our geometry is 14 μm . An incident probe beam scatters from this grating in a direction satisfied by the phase matching condition. By delaying the arrival of the probe beam the time response of these nonlinear optical changes can be studied.

Figure 1 shows the scattering efficiency as a function of the probe beam delay. Here, the scattering efficiency is de-

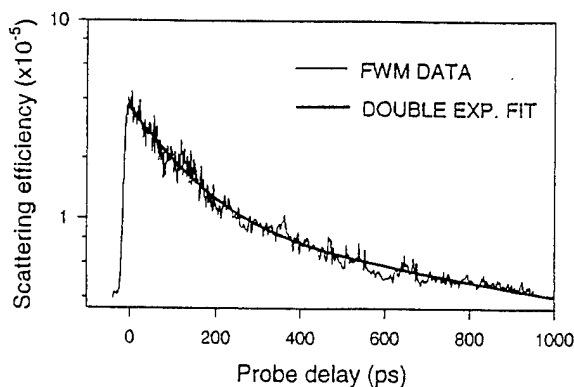


FIG. 1. Scattering efficiency η , as a function of the probe beam arrival delay. η at zero delay is a result of a maximum index change of 1.2×10^{-3} . A double exponential model fit to the time response was used to estimate recombination to trap lifetimes of 100 ± 10 ps and 1 ± 0.2 ns.

^{a)}Electronic mail: bahman@okway.okstate.edu

defined as the ratio of the scattered to the transmitted probe beam. All beams had equal energy resulting in total incident irradiance of 1.7 GW/cm^2 at the sample. Scattering efficiency for an index grating is¹⁵

$$\eta(t) = \frac{I_{\text{scattered}}}{I_{\text{transmitted}}} = \sin^2 \left(\frac{k \Delta n(t) l}{2} \right) = \left(\frac{k \Delta n(t) l}{2} \right)^2, \quad (1)$$

where k is the probe wave vector, $\Delta n(t)$ is the time dependent index change, and l is the sample thickness. At zero delay, a maximum scattering efficiency of 4×10^{-5} corresponds to an index change $\Delta n(0)$, of 1.2×10^{-3} . This change can be related to the pump beam intensity through an effective nonlinear refractive coefficient n_2 . From the definition

$$\Delta n_0 = n_2 I_0, \quad (2)$$

and using pump beam irradiance of 1.2 GW/cm^2 required for this index change, a value of $1 \times 10^{-3} \text{ cm}^2/\text{GW}$ is determined for n_2 . This is much larger than the expected range for semiconductors. For example, ZnSe has a value of $6.7 \times 10^{-5} \text{ cm}^2/\text{GW}$ at 532 nm .¹⁶ Since, at this wavelength, the ratio between the photon and band-gap energies ($E_g/\hbar\omega$) is larger for GaN than ZnSe, a smaller value of n_2 is expected for GaN,¹⁷ in contradiction to the observation. The origin of this enhancement is not known but could be related to presence of defects or impurities in GaN.

A change in the refractive index in undoped semiconductors can be due to (i) bound electrons, (ii) free carriers generated via band-to-band or trap-to-band excitation, or (iii) excited states arising from band-to-trap transitions. In general, all effects are present, however, the lifetimes of the index changes arising from different mechanisms may significantly vary. The lifetimes of bound electronic nonlinearities are shorter than the picosecond pulses used here.¹⁷ Effects arising from bound electrons, therefore, are limited to the autocorrelation time of the three beams. From the magnitude of the scattered signal at longer delays, it can be concluded that bound electronic effects have an insignificant contribution to the observed scattering. Focusing on the band-to-trap transitions, a grating created through this mechanism has a time response associated with trap-to-band recombination lifetimes. These lifetimes are many orders of magnitude longer than the observed time response. Therefore, effects from band-to-trap transitions can also be ignored. Free-carrier generation remains as the primary cause of the index grating. The decay of the signal is, then, due to recombination and/or migration of the excited carriers. For a purely diffusive decay, carriers migrate from the light regions of the grating to the dark regions, washing out the index modulation. The decay rate for such a case is given by:^{15,18}

$$\frac{1}{\tau_D} = \frac{4\pi^2 D}{\Lambda^2}, \quad (3)$$

where D is the diffusion constant. Typical values of D ($1\text{--}10 \text{ cm}^2/\text{s}$),¹⁹ result in recombination lifetimes of, at least, several nanoseconds. The nonlinearity of the semilog plot of scattering efficiency versus probe delay suggests mul-

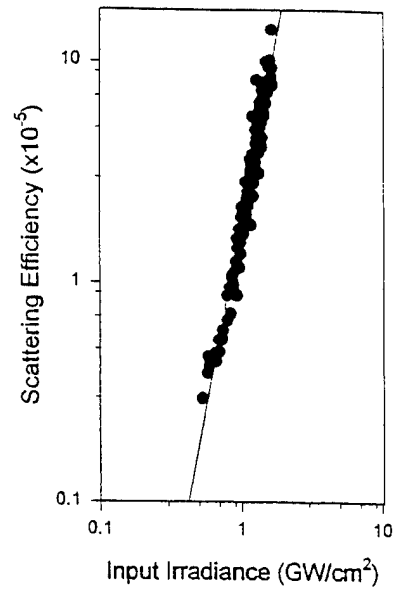


FIG. 2. Dependence of the scattering efficiency as a function of the pump beam irradiance. The slope of the log-log plot represents the order of the process. A value of 3.1 was obtained for the order indicating that both single- and two-photon effects play a significant role.

tipole recombination rates. Assuming two recombination processes, a fit to the decay rate can be obtained with recombination lifetimes of $100 \pm 10 \text{ ps}$ and $1.1 \pm 0.2 \text{ ns}$. The observed time response suggests that diffusion plays an insignificant role in the decay. Recombination, therefore, is the dominant mechanism for grating decay. The observed lifetimes are too small for band-to-band recombination rates in wide-gap semiconductors.²⁰ This suggests that recombination to trap states are the dominant mechanism for the grating decay. These values are consistent with our other observations of recombination lifetimes to trap levels in GaN.²¹

For trap recombination to be the dominant mechanism of grating decay, the number of generated carriers must be less than the number of traps available. In our case, the photon energy of the laser (2.33 eV) is smaller than the band gap of GaN (3.44 eV) restricting direct single photon, band-to-band excitation. Single photon absorption by trapped states or band-to-band transitions through two-photon absorption are the only mechanisms for carrier generation. The latter may take place via an interstitial level, such as a trap, or through virtual states. To determine if band-to-band transitions are the dominant mechanism of carrier generation, the intensity dependence of the scattering efficiency at zero delay was studied. For carrier induced index changes, scattering efficiency is directly related to the carrier concentration N by

$$\eta \propto (\Delta n)^2 = (\sigma N)^2, \quad (4)$$

where σ is the index change per carrier as predicted by Drude model. For single photon generation (trap-to-band), N is related to the pump irradiance, I , whereas for two-photon generation (band-to-band), it is related to I^2 . Therefore, scattering efficiency increases as I^2 for single photon and as I^4 for two-photon effects, respectively. Figure 2 shows the scattering efficiency at zero delay as a function of pump beam irradiance. In the log-log plot shown, the slope gives the order of the process. In this case, scattering efficiency is

found to depend on $I^{3.1}$. Therefore, it can be concluded that both single and two-photon absorption play a significant role in the carrier generation. Since the samples are transparent in the wavelength range of the laser used, relatively low carrier concentrations are obtained from single photon absorption. The importance of both mechanisms on the scattering efficiency suggests that two-photon absorption also leads to relatively small carrier generation. For the small number of carriers generated and the high density of trap sites available in GaN, the primary mechanism of decay is likely to be recombination to traps.

In conclusion, pulsed probe degenerate four wave mixing experiments were performed on GaN epilayers using 13 ps pulses at 532 nm. Time response of the FWM signal suggests the presence of a laser induced grating of generated carriers with a multiexponential decay characteristic. Using a double exponential model, fits with lifetimes of 100 ps and 1.1 ns were obtained for grating decay times. Carrier decays to trap levels are proposed as the primary mechanism for the grating decay. Intensity dependence of the scattering efficiency at zero delay demonstrated that both single- and two-photon effects contribute to carrier generation. Measurement of the maximum absolute scattering efficiency resulted in a value of $1 \times 10^{-3} \text{ cm}^2/\text{GW}$ for the nonlinear refractive coefficient n_2 . This value is more than an order of magnitude larger than expected for this coefficient. This may be due to the presence of traps or impurities in GaN leading to single photon as well as two-photon resonances.

The work at Oklahoma State University has been supported by ARPA, ONR, AFOSR, ARO, and OCAST.

¹H. Okumara, S. Yoshida, and T. Okahisa, *Appl. Phys. Lett.* **64**, 2997 (1994).

- ²J. Baur, K. Maier, M. Kunzer, U. Kaufmann, J. Schneider, H. Amano, I. Akasaki, T. Detchprohm, and K. Hiramatsu, *Appl. Phys. Lett.* **64**, 857 (1994).
- ³W. Shan, T. J. Schmidt, X. H. Yang, S. J. Hwang, J. J. Song, and B. Goldenberg, *Appl. Phys. Lett.* **66**, 985 (1995).
- ⁴R. Dingle, K. L. Shaklee, R. F. Leheny, and R. B. Zetterstrom, *Appl. Phys. Lett.* **19**, 5 (1971).
- ⁵I. M. Catalano, A. Cingolani, M. Ferrara, M. Lugarà, and A. Minafra, *Solid State Commun.* **25**, 349 (1978).
- ⁶R. Cingolani, M. Ferrara, and M. Lugarà, *Solid State Commun.* **60**, 705 (1986).
- ⁷H. Amano, T. Asahi, and I. Akasaki, *Jpn. J. Appl. Phys.* **29**, L205 (1990).
- ⁸M. A. Khan, D. T. Olson, J. M. Van Hove, and J. N. Kuznia, *Appl. Phys. Lett.* **58**, 1515 (1991).
- ⁹X. H. Yang, T. J. Schmidt, W. Shan, J. J. Song, and B. Goldenberg, *Appl. Phys. Lett.* **66**, 1 (1995).
- ¹⁰K. Yung, J. Yee, J. Koo, M. Rubin, N. Newman, and J. Ross, *Appl. Phys. Lett.* **64**, 1135 (1994).
- ¹¹J. Hays, B. Taheri, T. J. Schmidt, X. H. Yang, J. J. Song, and B. Goldenberg (unpublished).
- ¹²J. Chen, Z. H. Levine, and J. W. Wilkins, *Appl. Phys. Lett.* **66**, 1129 (1995).
- ¹³J. Miragliotta, D. K. Wickenden, T. J. Kistenmacher, and W. A. Bryden, *J. Opt. Soc. Am. B* **10**, 1447 (1993).
- ¹⁴S. Gupta, R. K. Jain, and M. A. Khan, in *Proceedings 15th Conference on Lasers and Electro-Optics*, Baltimore, MD, paper CTuO1, May, 1995.
- ¹⁵H. J. Eichler, P. Günter, and D. W. Pohl, *Laser-Induced Dynamic Gratings* (Springer-Verlag, Berlin, 1986), pp. 47–64.
- ¹⁶M. Sheik-Bahae, A. A. Said, T.-H. Wei, D. J. Hagan, and E. W. Van Stryland, *IEEE J. Quantum Electron.* **26**, 760 (1990).
- ¹⁷M. Sheik-Bahae, D. C. Hutchings, D. J. Hagan, and E. W. Van Stryland, *IEEE J. Quantum Electron.* **27**, 1296 (1991).
- ¹⁸M. S. Petrovic, A. Suchocki, R. C. Powell, G. C. Valley, and G. Cantwell, *Phys. Rev. B* **43**, 2228 (1991).
- ¹⁹K. W. Boer, *Survey of Semiconductor Physics* (Van Nostrand Reinhold, New York, 1990), Chap. 43.
- ²⁰K. Seeger, *Semiconductor Physics*, 5th ed. (Springer-Verlag, New York, 1991), p. 396.
- ²¹W. Shan, J. J. Song, and B. Goldenberg (unpublished).

Published without author corrections

Room-temperature stimulated emission in GaN/AlGaIn separate confinement heterostructures grown by molecular beam epitaxy

T. J. Schmidt, X. H. Yang, W. Shan,^{a)} and J. J. Song
*Center for Laser Research and Department of Physics, Oklahoma State University,
Stillwater, Oklahoma 74078*

A. Salvador, W. Kim, Ö. Aktas, A. Botchkarev, and H. Morkoç^{b)}
Coordinated Science Laboratory, University of Illinois at Urbana-Champaign, Urbana, Illinois 61801

(Received 13 November 1995; accepted for publication 29 January 1996)

Strong near-ultraviolet stimulated emission was observed at room temperature in GaN/AlGaIn separate confinement heterostructures (SCH) grown by molecular beam epitaxy (MBE) on sapphire substrates. The MBE grown GaN/AlGaIn SCH samples exhibited stimulated emission threshold pumping powers as low as 90 kW/cm² at room temperature under the excitation of a frequency-tunable nanosecond laser system with a side-pumping configuration. This represents an order of magnitude reduction over bulklike GaN. Our results suggest that the carrier confinement and waveguiding effects of the SCH samples result in a substantial decrease in the stimulated emission threshold. © 1996 American Institute of Physics. [S0003-6951(96)01913-9]

GaN based wide-band-gap group III-V nitride semiconductors have attracted a good deal of attention recently because of their potential applications in electronic and optoelectronic devices, such as high power-high efficiency amplifiers, UV, blue, green, and yellow LEDs, and, as yet to be demonstrated, short wavelength laser diodes.¹⁻³ With rapid progress in nitride epitaxial growth technology, high quality nitride single crystalline epitaxial layers can now be grown on sapphire and SiC substrates. Recent demonstration of superbright high-efficient violet, blue, green, and yellow LEDs based on nitride heterostructures by the Nichia group⁴ and the reports on the observation of optically pumped stimulated emission in GaN epitaxial layers⁵⁻¹⁰ have fueled an intense interest in the development of nitride based UV-visible light emitters. However, pivotal issues pertinent to optical processes in lasers have not been fully explored. In this report, we discuss our investigation of the optically pumped stimulated emission in GaN/AlGaIn separate confinement heterostructures (SCH) at room temperature. The stimulated emission phenomena in the GaN/AlGaIn SCH samples were investigated using a high-power pulsed laser system. Strong near-violet stimulated emissions were achieved at room temperature using a "side pumping" geometry. We observed that the pumping power required for stimulated emission is significantly lowered due to the quantum confinement and waveguiding effects of the SCH structure compared to bulklike epitaxial GaN layers.

The GaN/AlGaIn separate confinement heterostructures used in this work were grown on (0001) sapphire substrates by a modified reactive MBE at a substrate temperature near 800 °C. The particular structure under discussion has a 600 Å thick AlN layer, directly grown on sapphire, followed by a GaN buffer layer, an AlGaIn cladding layer, a lower mole fraction AlGaIn waveguide layer, a 70 Å thick GaN quantum well, which is capped by a low mole fraction AlGaIn waveguide, and an AlGaIn cladding layer. The quantum well was

doped with Si to a level of $5 \times 10^{17} \text{ cm}^{-3}$. Samples having a size of $3 \times 1 \text{ mm}^2$ were cut and mounted on a sapphire heat sink, and then attached to a copper sample holder for optical pumping experiments. The primary optical pumping source of the experimental system consists of a frequency-tunable dye laser pumped by the second harmonic laser beam (532 nm) of a pulsed Nd:YAG laser with $\sim 10 \text{ ns}$ pulse width and 10 Hz repetition rate. The output of the dye laser was then frequency doubled to achieve a near-UV pumping wavelength. The laser beam was focused on the sample surface using a cylindrical lens to form a rectangular excitation spot on the sample for uniform pumping. The excitation intensity of the laser light on the sample was varied continuously using a variable neutral density filter, and the pumping power densities were recorded by a power meter. The emission signal was collected from the edge of the GaN/AlGaIn SCH samples into a 1-M monochromator then detected by either a CCD camera or a photomultiplier tube in conjunction with a boxcar averager.

Figure 1 shows the room-temperature emission spectra of the GaN/AlGaIn SCH samples taken at different excitation power densities. Under the conditions of low-excitation power densities, the observed spectra exhibit a relatively weak and broad emission feature with the peak position around 365 nm, and the emission intensities linearly increase with the excitation power density, showing the typical characteristic of spontaneous emission. As the excitation power density increases, a sharp, narrow emission feature appears on the higher energy side of the spontaneous emission peak. The position of the maximum of this new emission feature is $\sim 361.5 \text{ nm}$. Its emission intensity increases superlinearly with the excitation power. This new emission structure becomes the dominant feature as the pumping power density is further increased. Under the conditions of high-excitation power densities, the output of the emission from the GaN SCH samples was very intense. The observations of spectral narrowing, a superlinear increase in intensity with the exci-

^{a)}Electronic mail: wshan@osuunx.ucc.okstate.edu

^{b)}On sabbatical leave at Wright Laboratories.

This work at OSU was supported by AFOSR, ONR, ARO, and ARPA. The work at UIUC was supported by grants from ONR, AFOSR, and BMDO. H. M. is funded by a University President Research Program funded by AFOSR.

¹J. I. Pankove, Mater. Res. Soc. Symp. Proc. 162, 515 (1990).

²S. Strite and H. Morkoç, J. Vac. Sci. Technol. B 10, 1237 (1992).

³H. Morkoç, S. Strite, G. B. Gao, M. E. Lin, B. Sverdlov, and M. Burns, J. Appl. Phys. 76, 1363 (1994).

⁴S. Nakamura, J. Vac. Sci. Technol. A 13, 705 (1995).

⁵H. Amano, T. Asahi, and I. Akasaki, Jpn. J. Appl. Phys. 29, L205 (1990).

⁶H. Amano, T. Asahi, M. Kito, and I. Akasaki, J. Lumin. 48&49, 389 (1991).

⁷M. A. Khan, D. T. Olson, J. M. Van Hove, and J. N. Kuznia, Appl. Phys. Lett. 58, 1515 (1991).

⁸K. Yung, J. Yee, J. Koo, M. Rubin, N. Newman, and J. Ross, Appl. Phys. Lett. 64, 1135 (1994).

⁹X. H. Tang, T. Schmidt, W. Shan, J. J. Song, and B. Goldenberg, Appl. Phys. Lett. 66, 1 (1995).

¹⁰A. S. Zubrilov, V. I. Nikovlaev, V. A. Dmitriev, K. G. Irvine, J. A. Edmond, and C. H. Carter, Jr., Inst. Phys. Conf. Ser. 141, 525 (1995).

¹¹Landolt-Bornstein, edited by O. Madelung, New Series, Group 3, Vol. 17a (Springer, Berlin, 1982).

¹²D. C. Reynolds, D. C. Look, W. Kim, Ö. Aktas, A. Botchkarev, A. Salvador, H. Morkoç, and D. N. Talwar (unpublished).

Intensity scan and two photon absorption and nonlinear refraction of C_{60} in toluene

Bahman Taheri^{a)}

Center for Laser Research and Department of Physics, Oklahoma State University, Stillwater, Oklahoma 74078

Huimin Liu

Department of Physics, University of Puerto Rico, Mayaguez, Puerto Rico 00680

B. Jassemnejad and D. Appling

Department of Physics, University of Central Oklahoma, Edmond, Oklahoma 73013

Richard C. Powell

Optical Sciences Center, University of Arizona, Tucson, Arizona 85721

J. J. Song

Center for Laser Research and Department of Physics, Oklahoma State University, Stillwater, Oklahoma 74078

(Received 17 April 1995; accepted for publication 2 January 1996)

A single beam technique is introduced to determine the magnitude and sign of third order nonlinear optical coefficients of materials using intensity dependence of the complex refractive index. It is applicable to a large range of materials including those with a low damage threshold such as polymers and absorbing glasses. It is used to determine the two photon absorption and nonlinear refraction coefficients of C_{60} in toluene. Concentration dependence of the nonlinear optical coefficients results in second hyperpolarizabilities of 10^{-31} (esu) for C_{60} . © 1996 American Institute of Physics. [S0003-6951(96)01110-X]

Since its discovery, C_{60} has been the subject of numerous investigations. There have been indications of large optical nonlinearities due to their delocalized, π -conjugated electrons.¹ This makes these materials potentially attractive for optical switching. To this end, experiments using third harmonic generation,² electric field induced second harmonic generation,³ and degenerate four-wave mixing (DFWM) have been carried out on these materials. The latter has been performed with a variety of pump wavelengths using nanosecond,⁴ picosecond,⁵⁻⁸ and femtosecond⁹ laser pulses. The pump-probe studies suggest that the nonlinear optical properties of these materials have an instantaneous response due to their $\chi^{(3)}$, and a long lived component characteristic of excited state population. The instantaneous response, however, has been shown to dominate the nonlinear optical properties during the duration of the pump beams.¹⁰

There is a considerable variation in the reported experimentally obtained numerical values of $\chi^{(3)}$ of these materials in solution. Using DFWM, Blau *et al.*⁵ estimated a relatively large $\chi^{(3)}$ of $\sim 10^{-8}$ (esu). This value was refuted by Kafafi *et al.*⁶ whose measurements resulted in a much smaller value of $\sim 10^{-12}$ (esu). Neither, however, reported any contributions due to toluene. Femtosecond DFWM⁹ and third harmonic generation² experiments have resulted in values of $\sim 10^{-10}$ (esu). More recently, concentration dependence of picosecond degenerate four wave mixing at 532 nm yielded a value of $\sim 10^{-13}$ (esu).⁸ There, the DFWM signal was assumed to arise from the real part of the solution and the imaginary part of the solute. The single beam technique,

namely Z scan,¹¹ can yield both the magnitude and sign of the nonlinear optical coefficients. However, this simple and powerful technique requires movement of the sample across the focal plane of a converging lens which in materials with absorption can result in irreversible damage.¹²

In this study, a simple and reliable single beam technique is introduced to determine the magnitude and the sign of the real and imaginary parts of $\chi^{(3)}$ in materials with a low damage threshold. A pulse of light is passed through a waveplate-polarizer combination followed by a lens. The sample is placed a Rayleigh length z_0 , behind the focal plane of the lens. Transmission through an aperture placed a distance d behind the sample is then monitored as a function of the input pulse energy. Third-order nonlinear optical properties result in changes in the index of refraction n and the absorption coefficient α of the sample. For a spatially radial input beam profile, the material response is equivalent to an intensity dependent absorptive lens with the sign and magnitude of the optical nonlinearity dictating its strength and nature. For lossless medium, lensing from the sample changes the beam divergence at the aperture. Variation in the on-axis irradiance at the aperture plane is indicative of beam divergence and can be monitored using a small radius iris. The intensity dependence of the small aperture transmission can, then, be directly related to the real part of $\chi^{(3)}$. The presence of nonlinear absorption results in an intensity dependent absorption coefficient. The intensity dependence of transmission through the sample can be obtained by fully opening the aperture and collecting the entire beam. In this case, the effects from lensing become minimal so the changes can be related to the imaginary part of $\chi^{(3)}$. Therefore, by performing an open and small aperture transmission experiment,

^{a)}Present address: Liquid Crystal Institute, Kent State University, Kent, OH 44242. Electronic mail: bahman@scorpio.kent.edu

both the sign and magnitude of the complex $\chi^{(3)}$ can be determined.

There are several advantages in performing an intensity scan over the Z-scan technique. First, the sample never crosses the focal plane where it is exposed to large irradiance. The effects due to lensing are minimal at the focal plane, therefore this exposure yields no additional information about material lensing. Second, results from each pulse can be stored to give a continuous range over the input irradiance. This helps isolate third-order effects from higher-order nonlinearities as well as reducing the total exposure time to a few seconds. The latter minimizes nonlinearities due to long exposure times such as thermal lensing. Third, since the only role of the focusing lens is to enhance the effect, thin sample formalism can be easily invoked by a suitable choice in its focal length. Recall that in a thin medium formalism used in current theories, the sample thickness is assumed to be much smaller than the Rayleigh range of the lens.¹³ Z scan using a lens with a focal length that meets this criteria is impractical. Finally, other position dependent parameters affecting the results, namely beam radius, radius of curvature, and sample position, remain fixed. This eases the numerical fittings developed for Z scan, which are also applicable to this case.

To test the applicability of the method presented, single pulses from a mode-locked, Q-switched Nd:YAG laser operating at 10 Hz were frequency doubled to $\lambda=532$ nm with a e^{-1} width of 13 ps. The beam was focused using a 1 m focal length lens preceded by a waveplate-polarizer combination to allow for a continuous change in its energy. Several C_{60} in toluene solutions were filtered and poured into a 2 mm thick cuvette and placed 30 cm behind the focal plane of the lens. The choice of this distance was based on Z-scan experiments showing that greatest lensing effects are observed when the sample is placed at approximately a Rayleigh range from the focal plane. The Rayleigh length (~ 30 cm) of the lens was much larger than the thickness of the cuvette. Therefore the thin lens formalism can be applied to the analysis.¹³ The e^{-2} radius of the beam at the front surface of the cuvette was 320 μm . An aperture was placed in front of the detector to monitor the total and the on-axis transmission of the beam. For each incident pulse, the transmitted energy was stored in a computer as a function of the input energy. Open and small aperture scans were performed on a number of different C_{60} concentrations including pure toluene.

Assuming nonlinear effects within the pulse duration are due to delocalized electrons only,¹⁰ an incident light with a wave vector k will undergo an amplitude I and phase shift $\Delta\phi$ given by:

$$\frac{dI}{dz} = -\alpha I - \beta I^2, \quad \frac{d\Delta\phi}{dz} = -kn_2 I, \quad (1)$$

where α , β , and n_2 are the single photon absorption, two photon absorption, and nonlinear refraction coefficients, respectively. n_2 and β are related to the real and imaginary parts of the third order susceptibility, $\chi^{(3)}$ and molecular second hyperpolarizability γ .¹⁴

In the open aperture experiments, where all of the post-sample energy is collected, propagation effects arising from changes in the phase front can be ignored. Assuming a spa-

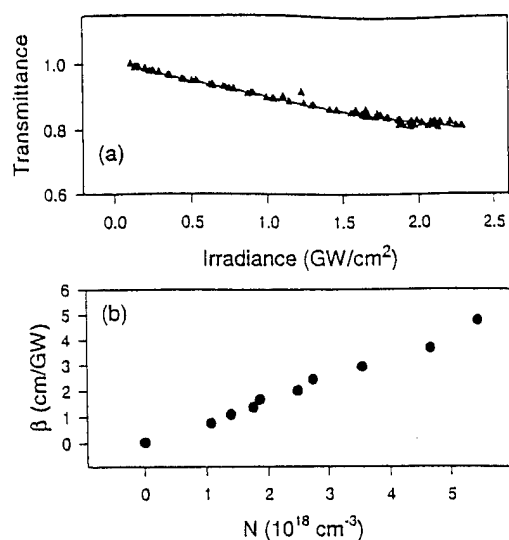


FIG. 1. (a) Typical results obtained for energy transmission through fullerene solution. The solid lines are the corresponding fit. (b) Concentration dependence of the two photon absorption coefficient.

tially and temporally Gaussian incident beam and including single reflection from the front and back surfaces of cuvette, the normalized transmission coefficient T for a sample of thickness L is^{11,15}

$$T(I_0) = \sum_{n=0}^{\infty} \frac{[-\beta(1-R)L_{\text{eff}}]^n}{(n+1)^{3/2}} I_0^n, \quad (2)$$

where $L_{\text{eff}} = [1 - \exp(-\alpha L)]/\alpha$ is the effective sample thickness, R the reflection coefficient, and E_{in} and E_{out} the incident and transmitted energy of the beam, respectively. The value of β can be determined by a numerical fit of the above equation to observed transmission.

Figure 1(a) shows a typical result obtained for the transmittivity of a beam through a fullerene solution. The solid line is a fit to the data using Eq. (2). This was done for a number of different fullerene concentrations. Figure 1(b) summarizes the concentration dependence of two photon absorption coefficient (TPA). A monotonic increase in the TPA coefficient is observed with an increase in the C_{60} concentration. The TPA coefficient per atomic concentration, $N(\text{cm}^{-3})$, is directly related to the imaginary part of the second hyperpolarizability¹⁴ γ'' and is

$$\gamma'' = \frac{\chi_I^{(3)}}{N} = 5.0 \times 10^{-31} (\text{esu}). \quad (3)$$

In the second set of experiments, the radius of the aperture was set at a minimum. Figure 2(a) is a typical result obtained for pure toluene and C_{60} in toluene. The difference in the slope of transmission versus irradiance suggests that the sign of the nonlinearity for pure toluene is opposite to that of C_{60} solution. Increase in the small aperture transmission exhibited by pure toluene indicates that the nonlinearity due to the solvent is self-focusing. In other words, as the intensity is increased the sample behaves more like a focusing lens, recollimating the diverging incident beam. For C_{60} solution, on the other hand, the decrease in the transmission beyond the expected decrease due to TPA suggests a self-defocusing effect. In this case, an increase in the intensity

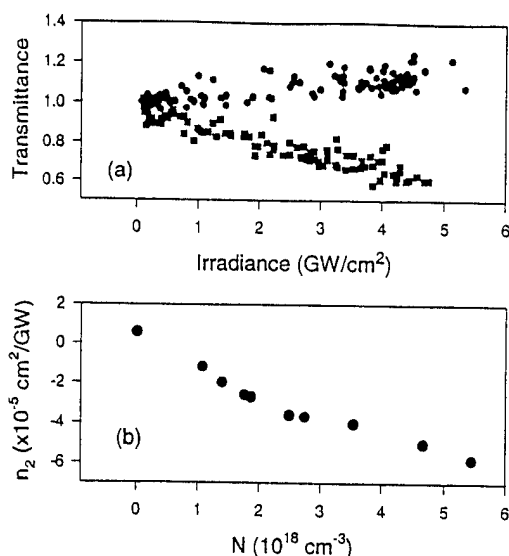


FIG. 2. (a) Typical results for the small aperture experiment for toluene (circle) and fullerene solution (square). The increase in the transmittivity of pure toluene suggests a focusing mechanism in the solvent. (b) Concentration dependence of the nonlinear refractive coefficient n_2 .

results in an increase in the divergence of the incident beam and a subsequent decrease in the on-axis irradiance at the aperture plane. For a thin medium, as is the case here, this behavior can be understood in terms of a nonlinear phase change induced by the material. The magnitude of this change depends on the nonlinear refractive coefficient n_2 , while the nature of lensing (focusing or defocusing) depends on the sign of n_2 . As in the case of Z scan, in the limit of small phase changes, the Gaussian decomposition¹¹ method can be extended to obtain an analytical expression for changes in the normalized transmission. Furthermore, if the closed aperture results are divided by those from open aperture experiments, the resulting transmittivity changes are from, primarily, a refractive effect. The sign and magnitude of n_2 are, then, directly related to the slope of the normalized transmission curve using the Z-scan analysis by:

$$T(I_0) = 1 + \frac{4kg \, dn_2 \, L_{\text{eff}}}{\sqrt{2}(g^2 + 9d^2/d_0^2)d_0} I_0, \quad (4)$$

where

$$g = 1 + da/(a^2 + z_0^2), \quad (5)$$

$$d_0 = \pi\omega^2/\lambda.$$

In the above, z_0 is the Rayleigh range (29 cm), a is the sample position behind the focal plane of the lens (30 cm), d is the distance between the sample and the aperture (144 cm) and ω is the beam radius at the sample.

Figure 2(b) is the result of the concentration dependence of n_2 . The values were obtained using the above analysis,

which required division of the small aperture transmission by the open aperture results. The negative slope to this graph further supports the conclusion that the contribution from C_{60} atoms is self-defocusing. The real part of the second hyperpolarizability of C_{60} molecules γ' is directly related to the slope of n_2 versus concentration and is

$$\gamma' = \frac{\chi_R^{(3)}}{N} = -4.0 \times 10^{-31} \text{ (esu)}.$$

This is in agreement with the values obtained by Ref. 8 using the concentration dependence of our wave mixing signal.

In conclusion, we have presented a simple and sensitive single beam technique to determine the sign and magnitude of third order nonlinear optical coefficients of materials. The technique is based on the intensity dependence of the complex refractive index. In addition to hardened materials, the technique is suited for materials with low damage thresholds such as polymers, absorbing glasses, and biological tissue. The similarity of this technique to Z scan means that it can be easily extended to more sensitive Z-scan derivatives such as EZ scan. Intensity scan measurements were performed on C_{60} solutions in toluene. The results indicate that the nonlinear refraction due to C_{60} has a defocusing effect. This is opposite to the focusing effect of pure toluene and as such care must be taken in experiments utilizing the nonlinear refraction of fullerenes. Values of -10^{-31} (esu) were obtained for the second hyperpolarizability of C_{60} .

This work has been supported by ARPA, ONR, and ARO. The authors wish to thank S. A. Holmstrom for his assistance.

¹ P. N. Parsad and B. A. Reinhardt, *Chem. Mater.* **2**, 660 (1990).

² H. Hoshi, N. Nakamura, T. Nakagawa, S. Suzuki, H. Shiromaru, and Achira, *Jpn. J. Appl. Phys.* **30**, L1397 (1991).

³ Y. Wang and L. T. Cheng, *J. Phys. Chem.* **96**, 1530 (1992).

⁴ R. Vijaya, Y. V. G. S. Murti, G. Sundarajan, C. K. Mathews, and P. Vasudeva Rao, *Opt. Commun.* **94**, 353 (1992).

⁵ W. J. Blau, H. J. Byrne, D. J. Cardin, T. J. Dennis, J. P. Hare, H. W. Kro R. Taylor, and D. R. M. Walton, *Phys. Rev. Lett.* **67**, 1423 (1991).

⁶ Z. H. Kafafi, J. R. Lindle, R. G. S. Pong, F. J. Bartoli, L. J. Lingg, and Milliken, *Chem. Phys. Lett.* **188**, 492 (1992).

⁷ Z. Zhang, D. Wang, P. Ye, Y. Li, P. Wu, and D. Zhu, *Opt. Lett.* **17**, 9 (1992).

⁸ F. J. Aranda, D. V. G. L. N. Rao, J. F. Roach, and P. Tayebati, *J. Appl. Phys.* **73**, 7949 (1993).

⁹ M. J. Rosker, H. O. Marcy, T. Y. Chang, J. T. Khoury, K. Hansen, and L. Whetten, *Chem. Phys. Lett.* **196**, 427 (1992).

¹⁰ H. Liu, B. Taheri, and W. Jia, *Phys. Rev. B* **49**, 10166 (1994).

¹¹ M. Sheik-Bahae, A. A. Said, T. H. Wei, D. J. Hagan, and E. W. Stryland, *IEEE J. Quantum Electron.* **26**, 760 (1990).

¹² P. N. Parsad and D. J. Williams, *Introduction to Nonlinear Optical Effects in Molecules and Polymers* (Wiley, New York, 1991), p. 212.

¹³ D. Weaire, B. S. Wherrett, D. A. B. Miller, and S. D. Smith, *Opt. Lett.* **331** (1974).

¹⁴ Y. R. Shen, *The Principles of Nonlinear Optics* (Wiley, New York, 1984).

¹⁵ B. Taheri, S. A. Holmstrom, R. C. Powell, J. J. Song, A. Munoz, F. Foldvari, and A. Peter, *Opt. Mater.* **3**, 251 (1994).

SPECTROSCOPIC STUDIES OF GaN GROWN BY METALORGANIC CHEMICAL VAPOR DEPOSITION

W. Shan¹, J.J. Song¹, T.J. Schmidt¹, X.H. Yang¹, and B. Goldenberg²

¹Center for Laser Research and Department of Physics, Oklahoma State University, Stillwater, Oklahoma 74078, USA, and ²Honeywell Technology Center, Plymouth, Minnesota 55441, USA

Abstract— The effects of temperature and pressure on the optical interband transitions and the transitions associated with impurity/defect states were studied using a variety of spectroscopic methods, including photoluminescence and photoreflectance, in conjunction with the diamond-anvil pressure-cell technique. Optically pumped, stimulated emission and lasing were also investigated over a wide temperature range up to 420 K.

1. INTRODUCTION

GaN-based III-V nitrides have attracted much attention because of their potential applications in electronic and optoelectronic devices, such as high power-high efficiency amplifiers, UV, blue, green, and yellow LED's and yet to be demonstrated short wavelength laser diodes.[1,2] Although efforts have been devoted to the preparation of high quality crystals and epitaxial films and the general features of the properties of these materials have been known in broad terms, detailed studies on the optical and electrical properties of GaN based nitrides, in particular, some important parameters associated with the electronic structures have not been fully explored. The work reported here will focus on subjects that are important for understanding the electronic structures and optical properties of GaN. The subjects discussed in this report include effects of temperature and pressure on the band gap of GaN, as well as the stimulated emission and lasing phenomena in MOCVD grown GaN samples under high excitation conditions.

2. EXPERIMENTAL

The GaN samples used in this study were all nominally undoped single-crystal films grown on (0001) sapphire substrates by MOCVD. Various

optical measurements were carried out on the GaN samples. Photoluminescence (PL) experiments were conducted using a cw HeCd laser (325 nm) as an excitation source and a 1-M monochromator connected to a photon-counting system to detect and spectrally resolve the emission. The pressure-dependent PL measurements were conducted using a diamond-anvil cell in conjunction with the above system. For reflectance measurements, the quasi-monochromatic light dispersed by a 1/2-M monochromator from a halogen tungsten lamp was focused on the sample, and the reflection signals were detected using a lock-in amplifier system. Optical modulation was provided in the photoreflectance (PR) measurements by the HeCd laser beam. Stimulated emission and lasing experiments were carried out using a "side-pumping" geometry and a pulsed laser as the excitation source. The primary pumping source of the experimental system consisted of a frequency-tunable dye laser pumped by the second harmonic laser beam (532 nm) of a pulsed Nd:YAG laser (~10 ns pulse width and 10 Hz repetition rate). The output of the dye laser was then frequency-doubled to achieve a near UV pumping wavelength.

3. RESULTS AND DISCUSSIONS

The GaN samples studied in this work

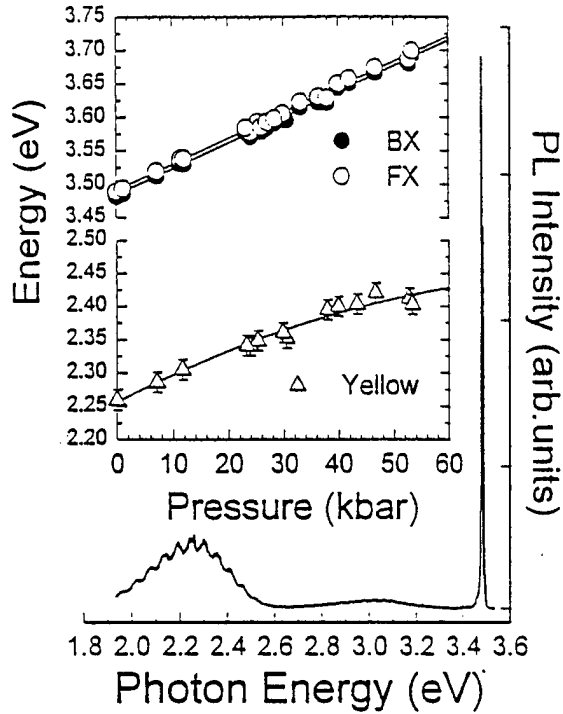


Fig. 1. PL spectrum at 10 K and the shifts of observed emission peaks with pressure.

exhibit strong near-band-edge exciton emissions. Luminescence lines with the full width at half maximum (FWHM) of <1.5 meV for the intrinsic free excitons and of <1.0 meV for the excitons bound to neutral donors were observed in PL spectra taken at 10 K. The PL spectra also consist of a broadband emission structure centered in the yellow spectral region and another much weaker broadband emission structure peaked in the blue spectral region. Low-temperature PL of GaN was measured as a function of applied pressure using the diamond-anvil pressure-cell technique. The exciton emission lines were found to shift almost linearly toward higher energy with increasing pressure, as shown in Fig.1. By examining the pressure dependence of the exciton emission structures, using the quadratic fit equation:[3]

$$E(P) = E(0) + \alpha P + \beta P^2, \quad (1)$$

the pressure coefficient of the direct Γ band gap in GaN was determined to be 3.9 meV/kbar. The value of the hydrostatic deformation potential of the band gap ($a = \partial E / \partial \ln V$) was also deduced from the experimental results to be -9.2 ± 1.2 eV. The broadband emission band in the yellow

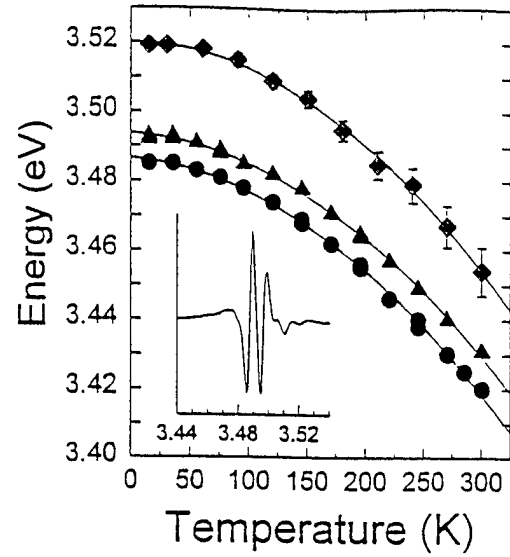


Fig. 2. Temperature dependence of interband transitions between the top-most valence band edges and the bottom of the conduction band edge. The inset shows a typical PR spectrum taken at 10 K.

spectral region showed a similar behavior under applied pressure to that of exciton emissions but with a relatively strong sublinear pressure dependence (4.0 meV/kbar). The result suggests that the yellow emission band most likely involves transitions associated with shallow donors and deep acceptors.

The effects of temperature on the interband transitions in GaN were studied to determine the temperature dependence of the GaN band gap. In order to maintain a good spectral resolution and allow a more precise determination of the transition energies, particularly at high temperatures, PR measurements were employed. The sharp derivative-like PR spectral features allow us to accurately determine the energy values of the optical transitions between the top-most valence band edges and the bottom of the conduction band of GaN. The observed interband transitions in GaN were mapped out as a function of temperature using the empirical Varshni equation:[4]

$$E_0(T) = E_0(0) - \alpha T^2 / (\beta + T), \quad (2)$$

and the Varshni thermal coefficients were determined. The parameters obtained from the best fit are $E_0(0) = 3.486$ eV, $\alpha = 8.32 \times 10^{-4}$ eV/K, and $\beta = 835.6$ K for the $\Gamma_9^V - \Gamma_7^C$ transition, and

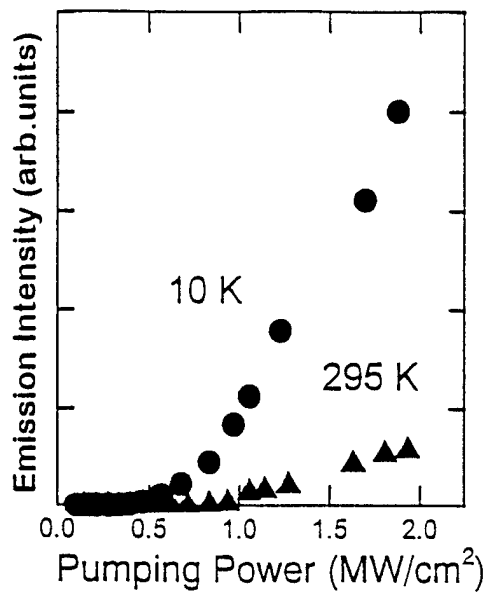


Fig. 3. Emission output vs. pumping power density at 10 K and room temperature (295 K)

$E_0(0)=3.494$ eV, $\alpha=10.9 \times 10^{-4}$ eV/K, and $\beta=1194.7$ K for the $\Gamma_7^V(\text{upper band})-\Gamma_7^C$ transition. Attempts to fit to Eq.(2) the $\Gamma_7^V(\text{lower band})-\Gamma_7^C$ transition energies measured at different temperatures yield $E_0(0)=3.520$ eV, $\alpha=2.92 \times 10^{-3}$ eV/K, and $\beta=3698.9$ K. The room-temperature band gap of GaN (295 K) was found to be 3.420 eV.

We have extended our efforts to the study of the stimulated emission and lasing phenomena in the MOCVD grown GaN. With a carefully designed optical pumping scheme, optically pumped stimulated emission and laser actions were achieved in the GaN samples with bar-like shapes under both picosecond and nanosecond laser excitations. The laser actions could be observed over a broad temperature range from 10 K up to 400 K. All samples exhibit, more or less, longitudinal lasing modes in their emission spectra. Fig.3 plots the emission intensity against the pumping power density. The observations of superlinear increase in intensity with the excitation power density, together with the spectral narrowing and the complete suppression of the broad emission background, are typical characteristics of the occurrence of stimulated emission. The onset of the superlinear increase in emission intensity is defined as the lasing threshold. The threshold was found to be weakly dependent on temperature. Our results yield a

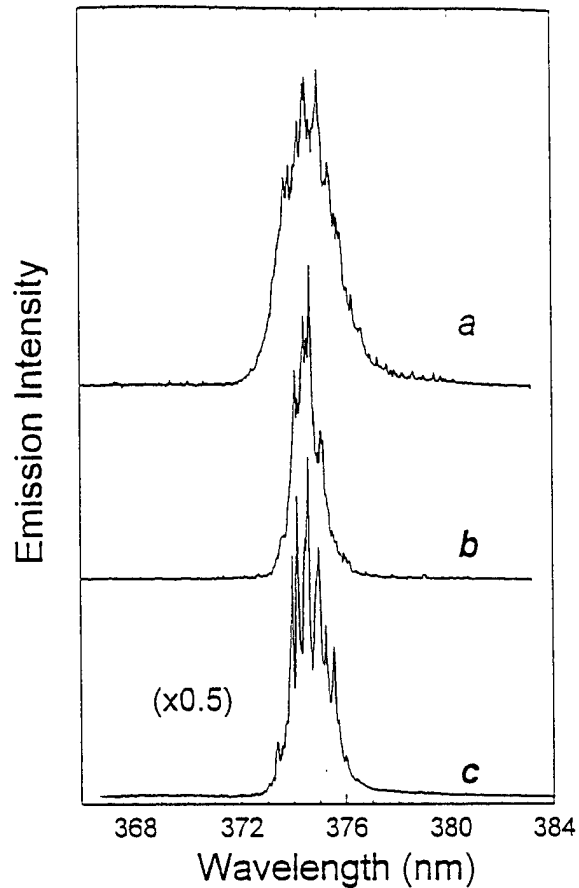


Fig. 4. Comparison of lasing spectra taken at 295 K under almost the same excitation conditions from three samples subjected to progressive treatments: (a) simply cut from wafer; (b) facet surface fine polished; (c) external mirror cavity imposed.

factor of less than two increase in the threshold, from ~ 500 kW/cm² at 10 K to ~ 800 kW/cm² at room temperature (295K). Usually, the threshold value can be affected by parameters, which are dependent on the pumping source and sample. For a given optical pumping source, the most important influence on the threshold is from the sample itself, with the threshold varying from sample to sample. This can be classified into two groups: one is associated with material properties, such as impurities, crystallinity, and defects; the other is related to the sample preparation such as laser cavity length and the quality of sample edge facets. We expect that the value of the pumping power threshold for lasing in GaN can be lowered substantially by better preparing the sample edge facet, with reflective coating, for example. With improved crystalline quality and better designed laser structures for carrier confinement, such as double-heterostructures or quantum well structures, the

lasing threshold is also expected to be significantly lowered. We observe an order of magnitude reduction of the pumping power threshold ($\sim 90 \text{ kW/cm}^2$) at room temperature in GaN/AlGaN separate confinement heterostructures samples. The results will be discussed in elsewhere.[5]

The specimens used in the stimulated emission and lasing studies were bar-like specimens cut from the large as-grown sample wafer. Attempts to finesse the cut facets resulted in substantial improvement in terms of the finesse of the Fabry-Perot cavity mode fringes, as shown in Fig. 4. This figure shows a comparison of three lasing spectra taken under essentially identical pumping conditions for three specimens, each subjected to different edge facet treatment. It demonstrates the progressive improvement in the quality of the observed mode fringes. The spectra exhibit line-width narrowing and enhanced mode fringe finesse for samples whose edge facets have been fine-polished. When these polished facets were mirrored, we noticed a substantial increase in mode quality and a factor of two increase in emission intensity.

Optical gain measurements were also performed by varying the length of the excitation beam on the sample for fixed excitation powers.

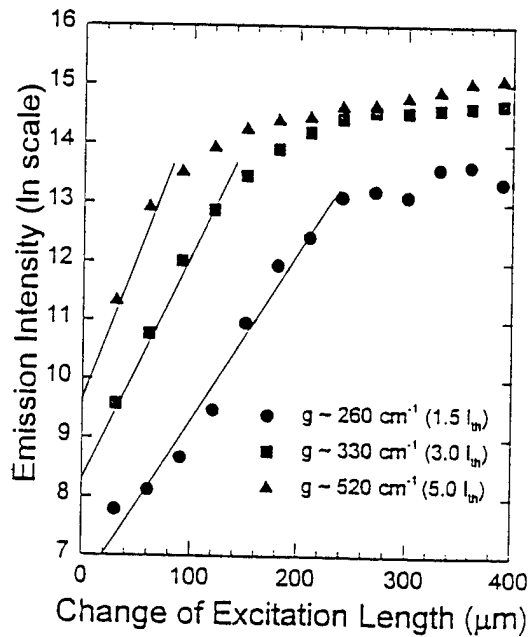


Fig. 5. The change of emission intensity with the excitation beam length on the sample surface at selected pumping power levels at room temperature (295 K). The estimated optical gain values are given. The pumping threshold $I_{th} = 800 \text{ kW/cm}^2$

Fig. 5 plots the emission intensity as a function of excitation length for selected pumping power levels. The measured gain values, which are consistent with the recently reported theoretically calculated results, are also given in the figure[6,7].

4. CONCLUSIONS

We have studied the optical properties of GaN grown on sapphire by MOCVD. The effects of temperature and pressure on the various optical transitions associated with both intrinsic and extrinsic processes in the GaN samples were examined by PL and PR measurements. The variation of the fundamental band gap of GaN was mapped out as a function of temperature. The room-temperature interband transition energy values obtained from these measurements are 3.420 eV for the $\Gamma_9^V - \Gamma_7^C$ transition and 3.428 eV for the $\Gamma_7^V(\text{upper band}) - \Gamma_7^C$ transition. The variation of GaN band gap with pressure was determined to be $\Delta E(P) = 3.9 \times 10^{-3} P - 1.0 \times 10^{-6} P^2 \text{ eV}$. The deformation potential for the direct Γ band was also deduced from the experimental results to be $-9.2 \pm 1.2 \text{ eV}$. Optically pumped stimulated emission and lasing phenomena were investigated using high-power pulsed lasers. Stimulated emission and laser action were observed over a wide temperature range from 10 K to $\sim 420 \text{ K}$. The pumping power threshold for lasing was estimated as $\sim 500 \text{ kW/cm}^2$ at 10 K to $\sim 800 \text{ kW/cm}^2$ at 295K. We found that the lasing mode quality can be substantially improved by finessing the cut edge facets of GaN on sapphire substrates.

REFERENCES

1. S. Strite and H. Morkoc, *J. Vac. Sci. Technol.* B10, 1237(1992).
2. J.I. Pankove, *Mater. Res. Soc. Symp. Proc.* 162, 515(1990).
3. W. Shan, T.J. Schmidt, R.J. Hauenstein, J.J. Song, and B. Goldenberg, *Appl. Phys. Lett.* 66, 3492(1995).
4. Y.P. Varshni, *Physica*, 34, 149(1967).
5. T.J. Schmidt, X.H. Yang, W. Shan, J.J. Song, A. Salvador, W. Kim, Ö. Aktas, A. Botchkarev, and H. Morkoç, submitted to *Appl. Phys. Lett.*
6. W. Fang and S.L. Chuang, *Appl. Phys. Lett.* 67, 751(1995).
7. W.W. Chow, A. Knorr, and S.W. Koch, *Appl. Phys. Lett.* 67, 754(1995).

Optical properties of wurtzite GaN grown by low-pressure metalorganic chemical-vapor deposition

W. Shan,^{a)} T. Schmidt, X. H. Yang, and J. J. Song

Center for Laser Research and Department of Physics, Oklahoma State University, Stillwater, Oklahoma 74078

B. Goldenberg

Honeywell Technology Center, Plymouth, Minnesota 55420

(Received 20 October 1995; accepted for publication 18 December 1995)

We present the results of optical studies on the properties of GaN grown by low-pressure metalorganic chemical-vapor deposition, with emphasis on the issues vital to device applications such as stimulated emission and laser action as well as carrier relaxation dynamics. By optical pumping, stimulated emission and lasing were investigated over a wide temperature range up to 420 K. Using a picosecond streak camera, the free and bound exciton emission decay times were examined. In addition, the effects of temperature and pressure on the optical interband transitions and the transitions associated with impurity/defect states were studied using a variety of spectroscopic methods, including photoluminescence and photoreflectance. The fundamental band gap of GaN was mapped out as a function of temperature using the empirical Varshni relation. The pressure coefficient of the gap was determined using diamond-anvil pressure-cell technique. The hydrostatic deformation potential for the direct Γ band gap was also derived from the experimental results. © 1996 American Institute of Physics. [S0021-8979(96)01907-6]

I. INTRODUCTION

GaN-based wide-band-gap III-V nitride semiconductors currently attract extensive attention for their potential electronic and optoelectronic device applications such as UV-blue light-emitting diodes (LEDs) and laser diodes.¹⁻³ With rapid progress in nitride epitaxial growth technology, high-quality nitride single-crystal epilayers can now be grown on such substrates as sapphire and SiC. Recent demonstration of superbright high-efficient blue LEDs based on nitride heterostructures by the Nichia group⁴ and the reports on observation of optically pumped stimulated emission in GaN epilayers by a few groups^{5,6} have led to much more intense interest in the development of efficient nitride UV-visible light emitters.

Although assessment of the properties and potential applications of nitrides is actively pursued to accelerate the device fabrication, some vital issues directly related to optoelectronic device applications such as optically pumped stimulated emission and lasing, as well as carrier dynamics, have not been widely addressed, and detailed studies on some important parameters associated with the electronic structures have not been fully explored. In this article we present the recent results of our spectroscopic studies on the optical properties of GaN grown by low-pressure metalorganic chemical-vapor deposition (MOCVD). A variety of experimental techniques was employed. The effects of temperature and pressure on the various optical transitions associated with both intrinsic and extrinsic processes in the GaN samples were examined by photoluminescence (PL) and photoreflectance (PR) spectroscopy. The variation of the fundamental band gap of GaN was mapped out as a function of temperature, and the energy value for the band gap of

GaN at room temperature was obtained. The pressure coefficient of the GaN band gap was determined by studying the shift of exciton emission lines in GaN with applied pressure using the diamond-anvil pressure-cell technique. The deformation potential for the direct Γ band of GaN was also deduced from the experimental results. The dynamics of photoexcited excess carriers in high-quality GaN samples were investigated by transient luminescence spectroscopy in the picosecond regime using a streak camera in the region of near-band-edge excitonic emissions. We found that the strong capture of photoexcited carriers in impurities and/or defects through nonradiative recombination processes dominates the decay of carrier population. The capture process depends on the density of impurities and defects in the GaN samples. Optically pumped stimulated emission and lasing phenomena in GaN on sapphire were investigated using high-power pulsed lasers. Stimulated near-violet emissions were achieved with clearly observable longitudinal cavity modes over a wide temperature range from 10 up to 400 K.

II. EXPERIMENTAL DETAILS

The GaN samples used in this study were all nominally undoped epitaxial films grown on (0001) sapphire substrates by low-pressure MOCVD. Thin AlN buffers of ~ 50 nm were deposited on sapphire substrates at 775 °C before the growth of GaN. GaN layers with the thickness of a few microns (μm) were deposited at 1040 °C directly on the AlN buffers. These conditions typically result in high-quality single-crystal GaN layers. Various optical measurements were carried out on the GaN samples over a temperature range typically from 10 K to room temperature (295 K). Samples were mounted onto the cold finger of a closed-cycle refrigerator and cooled to desired temperatures for designated measurements. Conventional photoluminescence spec-

^{a)}Electronic mail: wshan@osuunx.ucc.okstate.edu

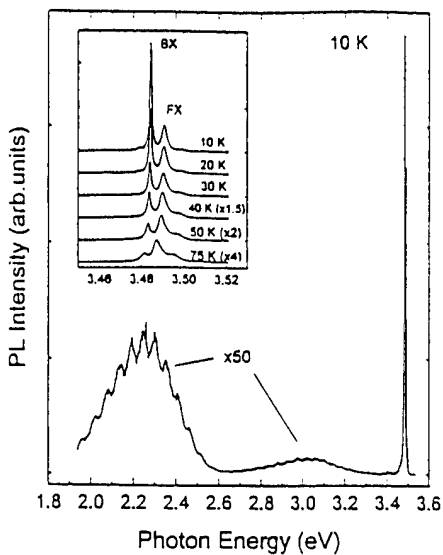


FIG. 1. Photoluminescence spectrum of a MOCVD GaN sample taken at 10 K. The inset shows the exciton luminescence spectra of the sample taken at different temperatures.

tra were measured using an experimental setup consisting of a cw HeCd laser (325 nm) as an excitation source and a 1 m double-grating monochromator connected with a photon-counting system. Time-resolved photoluminescence (TRPL) measurement was performed using a frequency-tunable pulsed laser with 2 ps pulse duration (82 MHz) as an excitation source and a streak camera with 2 ps time resolution in conjunction with a $\frac{1}{4}$ m monochromator as a detection system. Pressure-dependent PL measurement was conducted by using the diamond-anvil pressure-cell technique. For reflectance measurements, quasimonochromatic light dispersed by a $\frac{1}{2}$ m monochromator from a halogen-tungsten lamp was focused on the sample and the reflection signals were detected by a lock-in amplification system. Optical modulation was provided by chopping the HeCd laser beam when the PR measurements were performed. Stimulated emission and lasing experiment were carried out by employing side-pumping geometry. A frequency-doubled pulsed Nd:yttria aluminum garnet (YAG) laser (532 nm) with a repetition rate of 10 Hz was used to pump a dye laser as a primary optical pumping source (10 ns). The output of the dye laser was then frequency doubled into UV wavelengths to pump the GaN samples.

III. RESULTS AND DISCUSSIONS

To illustrate the quality and purity of the GaN epilayer samples used in this work, PL spectra taken from the samples are shown in Fig. 1. All GaN samples exhibit strong, predominant near-band-edge exciton luminescence lines corresponding to the radiative decay of excitons at low temperatures. Figure 1 shows a whole view of the typical PL spectrum taken at 10 K. The broadband yellow emission and a weak emission band in the blue spectral region could be observed. The strongest emission line marked by BX in Fig. 1 has a full width at half-maximum (FWHM) of less than 1.0 meV at 10 K. The second one labeled FX in the figure shows

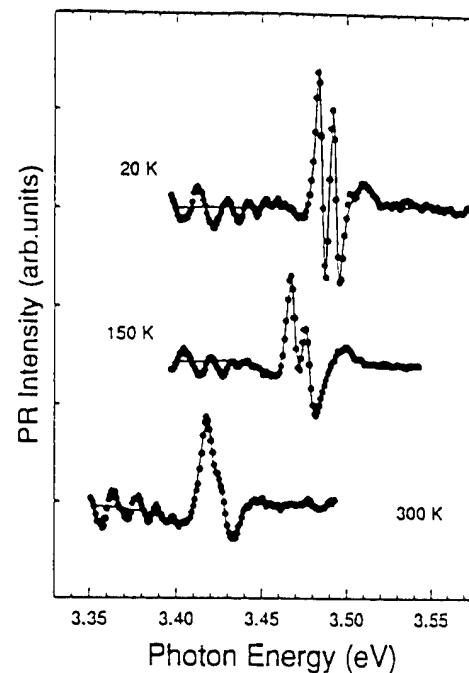


FIG. 2. Photoreflectance spectra of the GaN film at selected temperatures.

a FWHM of less than 1.5 meV, indicating the high quality as well as substantial purity of the samples. The intensity of the BX peak was found to decrease with increasing temperature much faster than that of FX. It became hardly resolvable when the temperature was raised to above 100 K (not shown). Such variations of the luminescence intensity as a function of temperature indicate the emission line can be attributed to the radiative recombination of excitons bound to neutral donors. The second strongest luminescence line, together with the weak emission feature on the higher-energy side, can be assigned to intrinsic free-exciton emissions.

A. Temperature dependence of the interband transitions

The effects of temperature on the energy shift of interband transitions in the GaN samples were examined by both PL and PR measurements. Shown in Fig. 2 are PR spectra measured at different temperatures. The 20 K PR spectrum has three exciton resonances. The excitons referred to as the intrinsic A, B, and C exciton^{7,8} are related to the $\Gamma_9^V - \Gamma_7^C$, $\Gamma_7^V(\text{upper band}) - \Gamma_7^C$, and $\Gamma_7^V(\text{lower band}) - \Gamma_7^C$ interband transitions in wurtzite GaN, respectively. The sharp derivative-like line shapes in PR spectra allow us to accurately determine the transition energies, particularly at high temperatures. The PR spectra were fitted to different line-shape functions. The solid lines in Fig. 2 are the best fits to the experimental data by the Lorentzian line-shape functional form⁹⁻¹¹

$$\Delta R/R = \text{Re}[C e^{i\theta} (E - E_0 + i\Gamma)^{-n}], \quad (1)$$

where C and θ are the amplitude and phase of the line shape, respectively, and E_0 and Γ are the energy and empirical broadening parameter of the transition, respectively. The exponent n is a characteristic parameter which depends on the type of critical point in the Brillouin zone and the order of

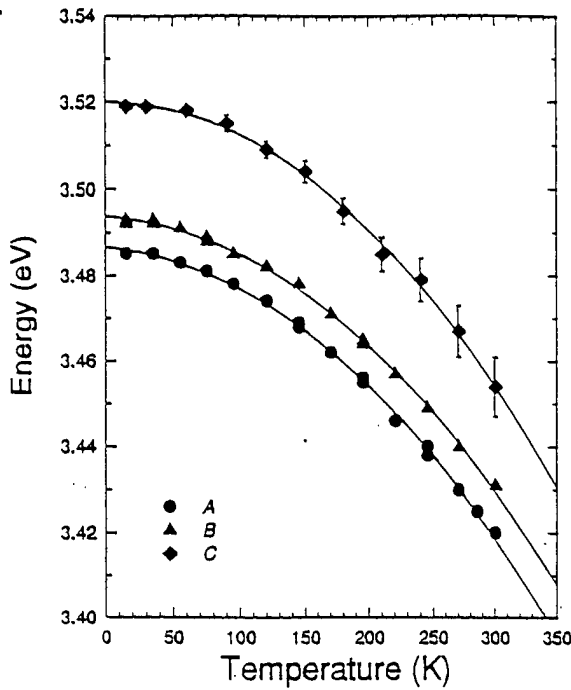


FIG. 3. Temperature dependence of three interband transition energies. $\Gamma_9^V - \Gamma_7^C$ transition: solid circles; $\Gamma_7^V(\text{upper band}) - \Gamma_7^C$ transition: solid triangles; and $\Gamma_7^V(\text{lower band}) - \Gamma_7^C$ transition, solid diamonds. The solid curves are least-squares fits to the experimental data using the Varshni empirical equation.

derivative. Both values of $n=2$ and $n=5/2$, which describe the nature of the interband excitonic transitions and three-dimensional band-to-band transitions, respectively, were used to fit the observed PR spectral structures. We found that using $n=2$ (corresponding to the first derivative line shape) results in a better fit to the line positions and widths of the PR spectra than using $n=5/2$ (the third derivative line shape). This was found to be appropriate even at the highest temperature employed. The best fits to the PR spectral features yield an energy of 3.420 eV for the lowest interband ($\Gamma_9^V - \Gamma_7^C$) transition and an energy of 3.428 eV for the second interband [$\Gamma_7^V(\text{upper band}) - \Gamma_7^C$] transition at room temperature (300 K), respectively.

Figure 3 plots the energies as a function of the temperature of all three observed interband excitonic transitions in the low-pressure MOCVD GaN. The temperature dependence for the interband transitions was deduced by using the Varshni empirical equation,¹²

$$E_0(T) = E_0(0) - \alpha T^2 / (\beta + T), \quad (2)$$

where $E_0(0)$ is the transition energy at 0 K, and α and β are constants referred to as Varshni thermal coefficients. The solid lines in the figure represent the least-squares fit to the experimental data using Eq. (2). The parameters obtained from the best fit are $E_0(0)=3.486$ eV, $\alpha=8.32 \times 10^{-4}$ eV/K, and $\beta=835.6$ K for the $\Gamma_9^V - \Gamma_7^C$ transition, and $E_0(0)=3.494$ eV, $\alpha=10.9 \times 10^{-4}$ eV/K, and $\beta=1194.7$ K for the $\Gamma_7^V(\text{upper band}) - \Gamma_7^C$ transition. Attempts to fit to Eq. (2) the $\Gamma_7^V(\text{lower band}) - \Gamma_7^C$ transition energies measured at different temperatures yield $E_0(0)=3.520$ eV, $\alpha=2.92 \times 10^{-3}$ eV/K, and $\beta=3698.9$ K. The values of α and β for the $\Gamma_7^V(\text{lower band}) - \Gamma_7^C$ transition are somewhat anomalously larger than those for the $\Gamma_9^V - \Gamma_7^C$ and $\Gamma_7^V(\text{upper band}) - \Gamma_7^C$ transitions. This is due primarily to the relatively large uncertainty in determination of the transition energy at high temperatures ($T > 150$ K) caused by a poor signal-to-noise ratio.

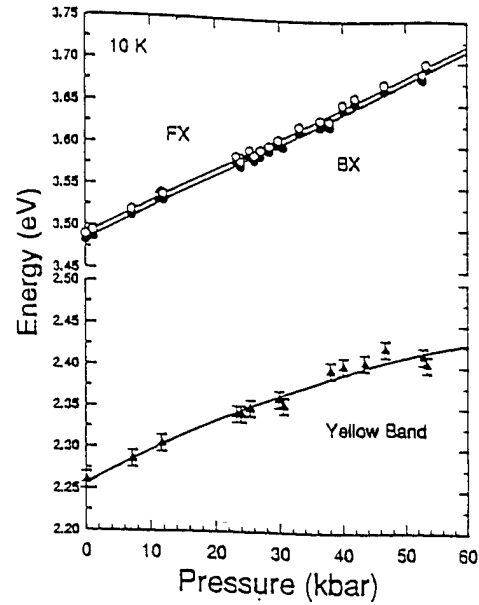


FIG. 4. Dependence of the energy positions on pressure for the various observed PL transitions in the GaN sample.

band) Γ_7^C transition are somewhat anomalously larger than those for the $\Gamma_9^V - \Gamma_7^C$ and $\Gamma_7^V(\text{upper band}) - \Gamma_7^C$ transitions. This is due primarily to the relatively large uncertainty in determination of the transition energy at high temperatures ($T > 150$ K) caused by a poor signal-to-noise ratio.

B. Pressure coefficient and hydrostatic deformation potential for direct Γ band gap

In Fig. 4 we plot the peak energies of exciton emission and yellow emission structures measured by PL using the diamond-anvil cell as a function of pressure. The solid lines in the figure are the least-squares fits to the experimental data using the quadratic-fit function,

$$E(P) = E(0) + \alpha P + \beta P^2. \quad (3)$$

It is known that the emission lines associated with the radiative decay of a free exciton or a shallow bound exciton shift with the host semiconductor band gap under hydrostatic pressure at the same rate. The electron stays in the conduction-band-edge state or in the orbit of shallow donor state associated with the conduction-band edge. The excitonic hole bound in the Coulomb field retains the symmetry of the valence-band edges. Therefore, the change of the intense and sharp BX transition with pressure plotted in the figure provides an unmistakable signature of the direct Γ band-gap dependence for wurtzite GaN. The best fits to the data yield a linear slope of 3.86×10^{-3} eV/kbar with an extremely small sublinear term of -8×10^{-7} eV/kbar². Similar results can be obtained from fitting the FX transition as well ($\alpha=3.9 \times 10^{-3}$ eV/kbar and $\beta=-1.8 \times 10^{-6}$ eV/kbar²).

The application of hydrostatic pressure, inducing a shift of the conduction-band edge relative to the valence-band edge due to a change in the volume, allows a direct estimation of the hydrostatic deformation potential for the direct Γ band gap of wurtzite GaN. The deformation potential is de-

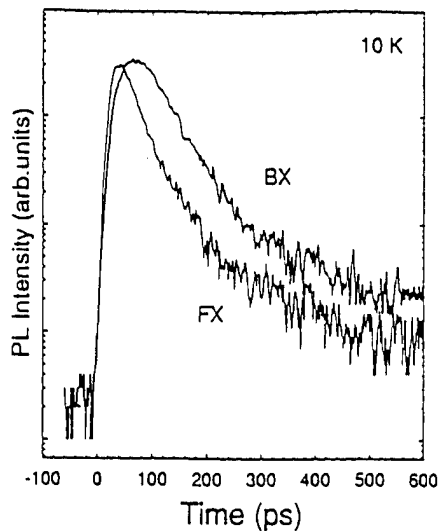


FIG. 5. Temporal variation of spectrally integrated PL for both intrinsic free and bound exciton emissions.

finied as $a = \partial E / \partial \ln V$. The relative volume change caused by applied pressure can be related by the Murnaghan equation of state,¹³

$$P = (B_0/B'_0)[(V_0/V)^{B'_0} - 1], \quad (4)$$

where B_0 is the bulk modulus of the wurtzite GaN, B'_0 is its pressure derivative ($= dB/dP$), V is the volume, and V_0 is the volume at atmospheric pressure. Using recently reported values of $B_0 = 2370 \pm 310$ kbar and $B'_0 = 4.3 \pm 2$,¹⁴ the hydrostatic deformation potentials for the direct Γ band gap of wurtzite GaN could be deduced as $a = -9.2 \pm 1.2$ eV.

The broad yellow emission band maximum was found to shift with pressure at a rate of 4.0×10^{-3} eV/kbar, almost the same as that of exciton emissions, but, it shows a relatively strong sublinear dependence compared to the exciton emissions. The broadband yellow emission spectral structure could be commonly observed in the PL spectra of nominally undoped GaN single crystals regardless of the crystal growth technique. More strikingly, this band was observed in samples implanted with a variety of atomic species.¹⁵ These results have led to the general belief that the broadband emission in the yellow spectral region involves defects. Recent theoretical studies on the electronic structures of impurities and native defects in GaN have suggested that point defects, such as antisites and vacancies, play important roles.¹⁶⁻¹⁹ The pressure dependence of the yellow emission band is consistent with the transitions involving shallow donors and deep acceptors because its pressure dependence follows the GaN band gap. Nevertheless, further theoretical and experimental studies are necessary to investigate the microscopic nature of the broadband yellow emission in GaN.

C. Radiative decay of free excitons and bound excitons

Temporal evolution of spectrally integrated exciton luminescence for both free exciton (FX) and bound exciton (BX) emissions observed in a GaN sample at 10 K is shown in Fig. 5. The overall time resolution of the experimental

system used for conducting the measurements is less than 15 ps. The time evolution for both FX and BX luminescence is dominated by exponential decay. A much weaker long-decay component with an intensity more than two decades smaller compared to the main process could also be observed. The lifetime of the main PL decay was found to be ~ 35 ps for the FX emissions and ~ 55 ps for the BX emissions for the GaN sample at 10 K. It should be pointed out that the measurement of luminescence decay time does not provide a direct measurement of radiative lifetime. The measured PL decay time only yields an effective lifetime τ_{eff} for free excitons and bound excitons. It involves both the radiative τ_R and nonradiative τ_{NR} lifetimes with the decay rate expressed as

$$1/\tau_{\text{eff}} = 1/\tau_R + 1/\tau_{\text{NR}}. \quad (5)$$

The radiative lifetime for an excited state in a semiconductor can be estimated by considerations of optical transition probability. The radiative lifetime τ_R of the excited state can be described by^{20,21}

$$\tau_R = 2\pi\epsilon_0 m_0 c^3 / \tilde{n} e^2 \omega^2 f, \quad (6)$$

where f is the oscillator strength of the optical transition, \tilde{n} is the refractive index, and the other symbols have their usual meanings. By using $\tilde{n} = 2.4$ and $\omega \approx 5.3 \times 10^{15} \text{ s}^{-1}$ for GaN, one can roughly obtain $\tau_R \sim (800/f)$ ps. The radiative lifetime of bound excitons in GaN is expected to be just a little shorter than 1 ns and on the order of several hundreds of picoseconds if we take the upper limit with its oscillator strength as unity ($f \sim 1$). The oscillator strength of free excitons calculated within the effective-mass approximation is given by $f = E_p / \pi \hbar \omega (V/a_x^3)$, where E_p is the Kane matrix element connecting Bloch states in the valence and conduction bands, V is the volume of unit cell, and a_x is the effective Bohr radius of free exciton. Our result yields $f \sim 0.012$ for the free excitons in GaN using $E_p \sim 18$ eV and $a_x \sim 20$ Å. Thus, the calculated value of the radiative lifetime for free excitons in GaN will be in the domain of several tens of nanoseconds.

The discrepancy between the measured values of PL decay time and the theoretical estimated radiative lifetime can be attributed to nonradiative relaxation processes in competition with the radiative channel. In the case where nonradiative decay rate is larger, the measured decay time is characteristic for the nonradiative processes in accordance with Eq. (5). This situation is typical for recombination from intrinsic states of semiconductors. The nonradiative processes such as multiphonon emission, capture by deep centers, Auger effect, etc., give rise to fast relaxation of the excited carriers down to lower states from which they decay radiatively or relax nonradiatively. As a result, the measured PL decay time for a given excited state is an effective lifetime and usually much shorter than a radiative one. This has been observed in a number of semiconductor bulk materials and heterostructures with the measured free exciton PL decay time decreasing progressively as the density of nonradiative recombination centers increased. The slow rise of bound exciton luminescence intensity compared to that of the free exciton PL shown in Fig. 5 is an indicator of such nonradi-

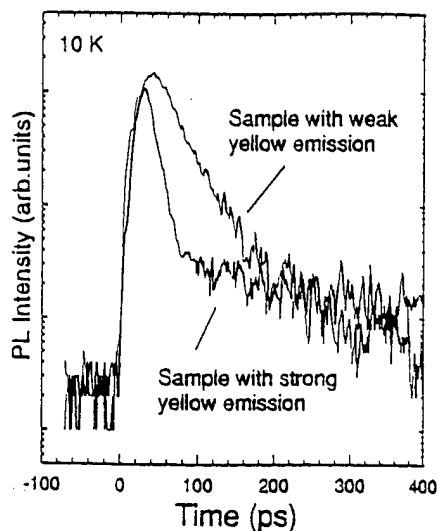


FIG. 6. Comparison of the time decay of free exciton emission between two GaN samples with the relative intensity ratio of 100:1 for the yellow emission under the same excitation conditions.

ative relaxation processes for free excitons arriving at the bound exciton energy. We found that the capture of excitons and trapping of carriers by such nonradiative centers as defects and impurities play a major role in the recombination processes responsible for the exciton population decay in the GaN samples studied in this work. The measured PL decay time was found to be directly related to the intensity of broadband emissions lying in the GaN band gap. The broad emission structure referred to as yellow emission in the literature is believed to be associated with the optical transitions between the energy levels involving impurity and/or defect states. The intensity of yellow emission is proportional to the density of defects and impurities present in samples. We found that the stronger the yellow emission, the shorter the PL decay time in a GaN sample. Shown in Fig. 6 is a comparison of free exciton PL decay between two samples with the relative intensity ratio of 100:1 for the yellow emission under identical excitation conditions. The deduced lifetime of free exciton emission in the sample with stronger yellow emission is only 15 ps (which is the limit of our instrumental resolution). Therefore, the fast decay behavior of the PL intensity indicates that the capture of excitons and trapping of carriers at defects and impurities through nonradiative combinations dominate the decay of exciton population. The process of capture is dependent on the density of defects and impurities in the GaN samples.

D. Optically pumped stimulated emission and lasing

Strong stimulated emission and lasing at near-UV wavelengths could be observed from the GaN samples over a broad temperature range from 10 to over 400 K under the conditions of high-pumping power densities. In Fig. 7 we plot the emission spectra taken at 375 K for pumping power densities below and above the estimated threshold. Under low-excitation conditions, the spectrum is characterized by a very broad spontaneous emission band with the maximum positioning at 376 nm. With increasing pumping power den-

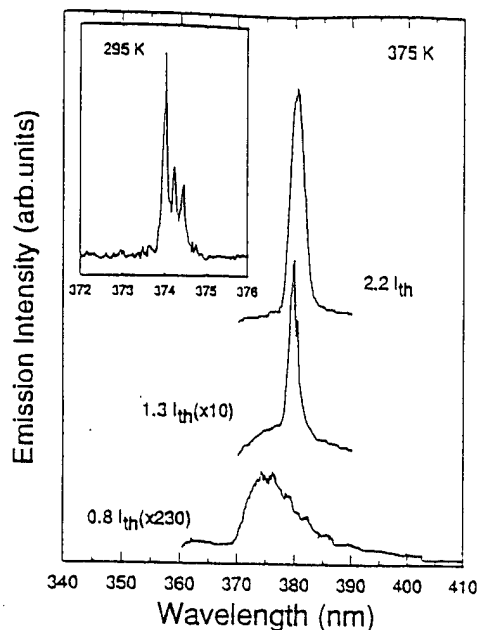


FIG. 7. Emission spectra of GaN at 375 K under different pumping power densities. The inset shows the longitudinal mode fringes.

sities, a second emission feature with a narrower line shape appears on the lower-energy side of the spontaneous emission band and becomes predominant as the pumping power densities are further increased. The emission feature is found to exhibit superlinear increase in intensity and a red shift of peak position as pumping power increases. In addition, the longitudinal cavity modes of lasing in some samples with small cavity lengths could clearly observed with a charge-coupled-device (CCD) camera. An example is given in the inset of Fig. 7, where the resonant cavity length of the sample is about 200 μm thick. The resonant cavity of the samples was prepared just by cutting the large wafer into barlike specimens with a diamond saw since it is almost impossible to cleave GaN grown on (0001) sapphire substrates. The resultant sample edges are far from mirrorlike facets.

The threshold pumping power was estimated to be ~ 500 kW/cm^2 at 10 K and ~ 800 kW/cm^2 at room temperature. Generally, the lasing threshold varies from sample to sample. For a given optical pumping source, the most important influence on the threshold is from the sample itself. This can be classified into two groups: One is associated with material properties, such as impurities, crystallinity, and defects; the other is related to the sample preparation, such as laser cavity length and the quality of sample edge facets. We expect that the value of the pumping power threshold for lasing in GaN can be lowered substantially by better preparing the sample facet edges, for example, with reflective coating. With better designed laser structures, such as double heterostructures, the lasing threshold is also expected to be significantly lowered. Recently, Zubrilov *et al.* reported the observation of multipass stimulated emission with Fabry-Pérot modes from GaN grown on 6H-SiC substrates.⁶ In this case, the interference fringes originated from the microcavities. These cavities were formed by microcracks, which were generated during

the cleaving process. As better lattice-matched substrates become available for epitaxial growth of GaN with better crystallinity, the lasing threshold is expected to be lowered further.

We also note that the threshold is not very sensitive to the change of sample temperature. It is known that high-temperature sensitivity of the lasing threshold usually limits the performance of a laser under high-temperature operation.²² The weak temperature dependence of the lasing threshold suggests that laser operation can be substantially extended to the high-temperature range. Thus, the results reported here imply that GaN-based laser diodes have the potential of operating with a much higher temperature tolerance compared to the conventional semiconductor laser diodes.

IV. CONCLUSIONS

We have employed a variety of experimental techniques to study the optical properties of GaN-grown sapphire by MOCVD. Optically pumped stimulated emission and lasing phenomena in GaN on sapphire were investigated using high-power pulsed lasers. Stimulated near-violet emissions were achieved with clearly observable longitudinal cavity modes over a wide temperature range from 10 up to 400 K. The dynamics of photoexcited excess carriers in high-quality GaN samples were investigated by transient luminescence spectroscopy in the picosecond regime using a streak camera in the region of near-band-edge excitonic emissions. We found that the strong capture of photoexcited carriers in impurities and/or defects through nonradiative recombination processes dominates the decay of carrier population. The capture process depends on the density of impurities and defects in the GaN samples. The effects of temperature and pressure on the various optical transitions associated with both intrinsic and extrinsic processes in the GaN samples were examined by photoluminescence and photoreflectance spectroscopy. The variation of the fundamental band gap of GaN was mapped out as a function of temperature. The room-temperature interband transition energy values obtained from these measurements are 3.420 eV for the Γ_9^V - Γ_7^C transition and 3.428 eV for the Γ_7^V (upper band)- Γ_7^C transition. By fitting the temperature-dependent energy values of the Γ_9^V - Γ_7^C and Γ_7^V (upper band)- Γ_7^C transitions to the Varshni empirical relation, our results yield

$$E_0(T) = 3.486 - 8.32 \times 10^{-4} T^2 / (835.6 + T) \text{ eV}$$

and

$$E_0(T) = 3.494 - 10.9 \times 10^{-4} T^2 / (1194.7 + T) \text{ eV},$$

respectively. The pressure coefficient of the GaN band gap was determined by studying the shift of exciton emission lines in GaN with applied pressure using the diamond-anvil pressure-cell technique. Our results yield the variation of GaN band gap with pressure to be

$$\Delta E(P) = 3.9 \times 10^{-3} P - 1.0 \times 10^{-6} P^2 \text{ eV}.$$

The deformation potential for the direct Γ band was also deduced from the experimental results to be -9.2 ± 1.2 eV.

ACKNOWLEDGMENTS

This work was supported by AFOSR, ARPA, ARO, and ONR. One of the authors (B.G.) is pleased to acknowledge the technical assistance of Maurice Hitchell.

- ¹S. Strite and H. Morkoç, J. Vac. Sci. Technol. B 10, 1237 (1992), and references therein.
- ²J. I. Pankove, Mater. Res. Soc. Symp. Proc. 162, 515 (1990), and references therein.
- ³H. Morkoç, S. Strite, G. B. Gao, M. E. Lin, B. Sverdlov, and M. Burns, J. Appl. Phys. 76, 1363 (1994), and references therein.
- ⁴S. Nakamura, Appl. Phys. Lett. 64, 1687 (1994).
- ⁵X. H. Yang, T. Schmidt, W. Shan, J. J. Song, and B. Goldenberg, Appl. Phys. Lett. 66, 1 (1995).
- ⁶A. S. Zubrilov, V. I. Nikovlaev, V. A. Dmitriev, K. G. Irvine, J. A. Edmond, and C. H. Carter, Jr., Inst. Phys. Conf. Ser. 141, 525 (1995).
- ⁷B. Monemar, Phys. Rev. B 10, 676 (1974).
- ⁸R. Dingle and M. Hegems, Solid State Commun. 9, 175 (1971).
- ⁹D. E. Aspnes, in *Optical Properties of Solids*, edited by M. Balkanski (North-Holland, Amsterdam, 1980), Chap. A.
- ¹⁰F. H. Pollak and O. J. Glembocki, Proc. SPIE 946, 2 (1988).
- ¹¹O. J. Glembocki and B. V. Shanabrook, in *Semiconductors and Semimetals*, edited by D. G. Semler and C. L. Littler (Academic, San Diego, 1992), Chap. 4.
- ¹²Y. P. Varshni, Physica 34, 149 (1967).
- ¹³F. D. Murnaghan, Proc. Nat. Acad. Sci. 30, 244 (1944).
- ¹⁴M. Ueno, M. Yoshida, A. Onodera, O. Shimomura, and K. Takemura, Phys. Rev. B 49, 14 (1994).
- ¹⁵J. I. Pankove and J. A. Hutchby, J. Appl. Phys. 47, 5387 (1976).
- ¹⁶D. W. Jenkins and J. D. Dow, Phys. Rev. B 39, 3317 (1989).
- ¹⁷T. L. Tansley and R. J. Egan, Phys. Rev. B 45, 10 942 (1992); Physica B 185, 190 (1993).
- ¹⁸J. Neugebauer and C. G. Van de Walle, Phys. Rev. B 50, 8067 (1994).
- ¹⁹P. Boguslawski, E. Briggs, and J. Bernholc, Phys. Rev. B 51, 17 255 (1995).
- ²⁰D. L. Dexter, in *Solid State Physics*, edited by F. Seitz and D. Turnbull (Academic, New York, 1958), Vol. 6.
- ²¹G. W. 't Hooft, W. A. J. A. van der Poel, and L. W. Molenkamp, Phys. Rev. B 35, 8281 (1987).
- ²²G. P. Agrawal and N. K. Dutta, in *Semiconductor Lasers* (Van Nostrand Reinhold, New York, 1993), p. 132.

Recent Progress in Optical Studies of Wurtzite GaN Grown by Metalorganic Chemical Vapor Deposition

W. Shan, T. Schmidt, X.H. Yang, and J.J. Song

*Center for Laser Research and Department of Physics, Oklahoma State University,
Stillwater, Oklahoma 74078, USA*

B. Goldenberg

Honeywell Technology Center, Plymouth,, Minnesota 55441, USA

Abstract. We present the recent results of our spectroscopic studies on optical properties of GaN grown by metalorganic chemical vapor deposition, including the issues vital to device applications such as stimulated emission and laser action, as well as carrier relaxation dynamics. By optical pumping, stimulated emission and lasing were investigated over a wide temperature range up to 420 K. Using a picosecond streak camera, free and bound exciton emission decay times were measured. In addition, the effects of pressure on the optical interband transitions and the transitions associated with impurity/defect states were studied using diamond-anvil pressure-cell technique.

1. Introduction

GaN based wide band-gap III-V nitride semiconductors currently attract extensive attention for their potential electronic and optoelectronic device applications such as UV-blue LED's and laser diodes.[1-3] Recent demonstration of superbright high-efficient blue LED's based on nitride heterostructures by the Nichia group and others[4] and the reports on observation of optically pumped stimulated emission in GaN epilayers by a few groups[5,6] have led to much more intense interest in the development of efficient nitride UV-visible light emitters. In this report, we present recent results of our spectroscopic studies on the optical properties of GaN grown by metalorganic chemical vapor deposition (MOCVD).

2. Experimental details

The GaN samples used in this study were all nominally undoped single-crystal films grown on (0001) sapphire substrates by MOCVD. Various optical measurements were carried out on the GaN samples over a temperature range typically from 10 K to room temperature (295 K). Conventional photoluminescence (PL) spectra were measured with a cw HeCd laser (325 nm) as an excitation source and a 1-M double-grating monochromator connected to a photon-counting system. Time-resolved photoluminescence (TRPL) measurements were performed using a frequency tunable pulsed laser (2 ps pulse duration, 82MHz) as an excitation source and

a streak camera (2 ps resolution), in conjunction with a 1/4-M monochromator as a detection system. Pressure-dependent PL measurements were conducted using the diamond-anvil pressure-cell technique. Stimulated emission and lasing experiments were carried out employing side-pumping geometry using a nanosecond pulsed laser (10 Hz) as the optical pumping source.

3. Results and discussions

To illustrate the quality and purity of the GaN epilayer samples used in this work, PL spectra taken from the samples are shown in Fig. 1. All GaN samples exhibit strong, predominant near band-edge exciton luminescence lines corresponding to the radiative decay of excitons at low temperatures. The inset shows a broad range of the typical PL spectrum taken at 10 K. The broadband yellow emission and a weak emission band in the blue spectral

region could be observed. The strongest emission line marked by BX in Fig. 1 has a full width at half maximum (FWHM) of less than 1.0 meV at 10 K. The second one labeled FX in the figure shows a FWHM of less than 1.5 meV, indicating the high quality, as well as substantial purity of the samples. The intensity of the BX peak was found to decrease much faster than that of the FX as the temperature increased. It became hardly resolvable when the temperature was raised to above 100 K (not shown). Such variations of the luminescence intensity as a function of temperature indicate that the emission line can be attributed to the radiative recombination of excitons bound to neutral donors. The second strongest luminescence line, together with the weak emission feature on the higher energy side, can be assigned to intrinsic free-exciton emissions.

3.1 Optically pumped stimulated emission and lasing

Strong stimulated emission and lasing at near-UV wavelengths could be observed from the GaN samples over a broad temperature range from 10 K to ~ 420 K by optical pumping with a tunable nanosecond laser. In Fig. 2 we plot the emission spectra taken at 375 K for pumping power densities below and above the estimated threshold. Under low-excitation conditions, the spectrum is characterized by a very broad spontaneous emission band with the maximum position at 376 nm. With increasing pumping power densities, a new feature with a narrower linewidth appears on the low energy side of the spontaneous emission band and becomes predominant as the pumping power densities are further increased. The emission feature is found to exhibit superlinear increase in intensity and a red shift in the peak position as the pumping power increases. In addition, the longitudinal cavity modes of lasing in some samples

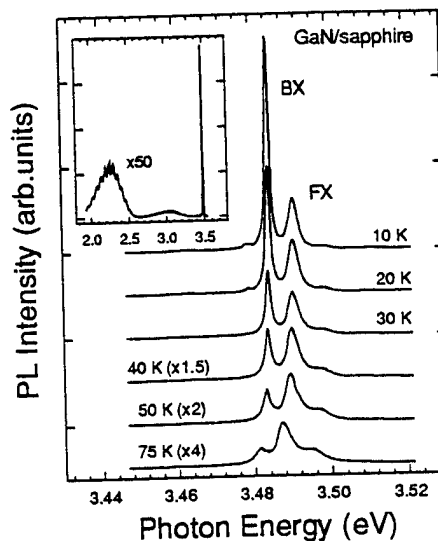


Fig. 1. Exciton luminescence spectra of a MOCVD GaN sample taken at different temperatures. The inset shows the 10 K PL spectrum of the sample over a broad spectral range.

with small cavity lengths could be clearly observed with a CCD camera. An example is given in the inset of Fig. 2, where the resonant cavity length of the sample is about 200 μm thick. The resonant cavity of the samples was prepared just by cutting the large wafer into bar-like specimens with a diamond saw. The resulting sample edges are far from mirror-like facets.

The threshold pumping power was estimated to be $\sim 500 \text{ kW/cm}^2$ at 10 K and $\sim 800 \text{ kW/cm}^2$ at room temperature. Generally, the lasing threshold varies from sample to sample. For a given optical pumping source, the most important influence on the threshold is from the sample itself. This can be classified into two groups: one is associated with material properties, such as impurities, crystallinity, and defects; the other is related to the sample preparation such as the laser cavity length and the quality of sample edge facets. We expect that the lasing threshold in GaN can be lowered substantially by better preparing the sample edge facets, for example, with reflective coating. With better designed laser structures, such as double-heterostructures, the lasing threshold is also expected to be significantly lowered. Recently, Zubrilov *et al.* reported the observation of multipass stimulated emission with Fabry-Perot modes from GaN grown on 6H-SiC substrates.[6] In this case, the interference fringes originated from the microcavities. These cavities were formed by microcracks, which were generated during the cleaving process. As better lattice-matched substrates become available for epitaxial growth of GaN with better crystallinity, the lasing threshold is expected to be lowered further.

We also noted that the threshold is not very sensitive to the change of sample temperature. It is known that high-temperature sensitivity of the lasing threshold usually limits the performance of a laser in high temperature operations.[7] The weak temperature dependence of the lasing threshold suggests that laser operations can be substantially extended to the high temperature range. Thus the results reported here imply that GaN based laser diodes have the potential of operating with a much higher temperature tolerance compared to conventional semiconductor laser diodes.

3.2 Radiative decay of free excitons and bound excitons

The temporal evolution of spectrally integrated exciton luminescence for both free-exciton (FX) and bound-exciton (BX) emissions observed in a GaN sample at 10 K is shown in Fig. 3. The overall time resolution of the experimental system used for conducting the measurements is less than 15 ps. The time evolution for both FX and BX luminescence is dominated by exponential decay. The lifetime of the main PL decay was found to be $\sim 35 \text{ ps}$ for the FX emissions and $\sim 55 \text{ ps}$ for the BX emissions for the GaN sample at 10 K. It should be pointed out that the

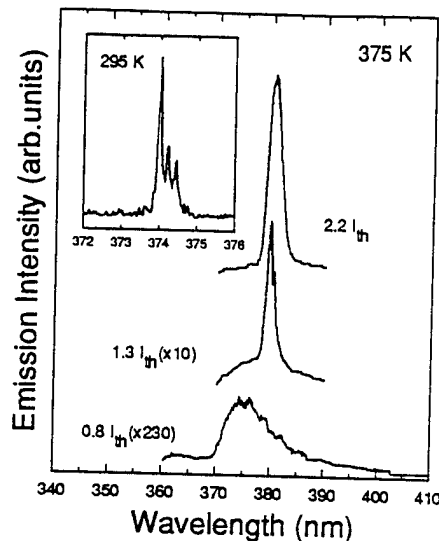


Fig. 2. Emission spectra of GaN at 375 K under different pumping power densities. The inset shows the emission spectrum taken at room temperature (295 K) exhibiting longitudinal mode fringes.

measurement of luminescence decay time does not provide a direct measurement of radiative lifetime and that the measured PL decay time yields only an effective lifetime (τ_{eff}) for free excitons and bound excitons. It involves both the radiative (τ_R) and nonradiative (τ_{NR}) lifetimes with the decay rate expressed as

$$1/\tau_{\text{eff}} = 1/\tau_R + 1/\tau_{\text{NR}}. \quad (1)$$

The radiative lifetime for an excited state in a semiconductor can be estimated by considerations of optical transition probability. The radiative lifetime τ_R of the excited state can be described by:[8,9]

$$\tau_R = 2\pi\epsilon_0 m_0 c^3 / \tilde{n} e^2 \omega^2 f, \quad (2)$$

where f is the oscillator strength of the optical transition, \tilde{n} is the refractive index, and the other symbols have their usual meanings. By using $\tilde{n}=2.4$, and $\omega \approx 5.3 \times 10^{15} \text{ sec}^{-1}$ for GaN, one can roughly obtain $\tau_R \sim (800/f)$ ps. The radiative lifetime of bound excitons in GaN is expected to be just slightly shorter than one nanosecond if we take the upper limit with its oscillator strength as unity ($f \sim 1$). The oscillator strength of free excitons calculated within the effective-mass approximation is given by $f = E_p / \pi \hbar \omega (V/a_x^3)$, where E_p is the Kane matrix element connecting Bloch states in the valence and conduction bands, V is the volume of unit cell, and a_x is the effective Bohr radius of free exciton. Our result yields $f \sim 0.012$ for the free excitons in GaN using $E_p \sim 18$ eV and $a_x \sim 20$ Å. Thus, the calculated value of the radiative lifetime for free excitons in GaN will be in several tens of nanoseconds domain. The discrepancy between the measured values of PL decay time and the theoretical estimated radiative lifetime can be attributed to nonradiative relaxation processes in competition with the radiative channel. In the case where nonradiative decay rate is larger, the measured decay time is characteristic for the nonradiative processes in accordance with Eq.(1). This situation is typical for recombination from intrinsic states of semiconductors. The nonradiative processes such as multiphonon emission captured by deep centers, Auger effect, etc., give rise to fast relaxation of the excited carriers down to lower states from which they decay radiatively or relax nonradiatively. As a result, the measured PL decay time for a given excited state is an effective lifetime and usually much shorter than a radiative one. This has been observed in a number of semiconductor bulk materials and heterostructures with the measured free-exciton PL decay time decreasing progressively as the density of nonradiative recombination centers increased.[9] The slow rise of bound-exciton luminescence intensity compared to that of the free-exciton PL shown in Fig. 3 is one indicator of such nonradiative relaxation processes for the free excitons relaxing to the bound excitons. We found that the capture of excitons and trapping of carriers by such nonradiative centers as defects and impurities play a major role in the recombination processes responsible for the exciton population decay in the GaN samples studied in this work. The measured PL decay time was found to be directly related to the intensity of broadband emissions lying in the GaN band gap. The broad emission structure referred to as yellow emission in the literature is believed to be associated with the optical

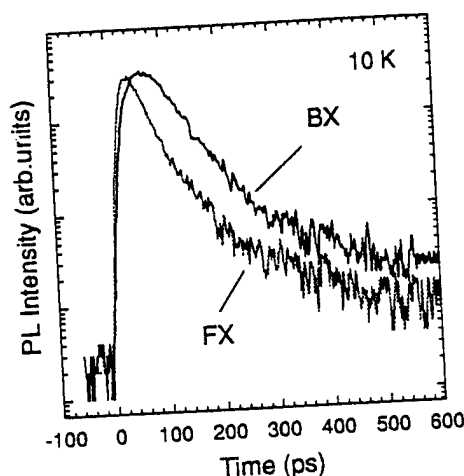


Fig. 3. Temporal variation of spectrally integrated PL for both intrinsic free-exciton and bound-exciton emissions.

transitions between the energy levels involving impurity and/or defect states. The intensity of yellow emission is likely to be proportional to the density of defects and impurities present in samples. We found that the stronger the yellow emission, the shorter the PL decay time in a GaN sample. Fig. 4 shows a comparison of free-exciton PL decays taken from two samples under identical excitation conditions. The yellow emission intensities of the two samples are drastically different, with approximately a 100:1 ratio. The lifetime of free-exciton emission in the sample with stronger yellow emission was deduced to only 15 ps (which is the limit of our instrumental resolution). Therefore, the fast decay behavior of the PL intensity in this sample indicates that the capture of excitons and trapping of carriers at defects and impurities through nonradiative combinations appear to dominate the decay of exciton population. The process of capture is dependent on the density of defects and impurities in the GaN samples.

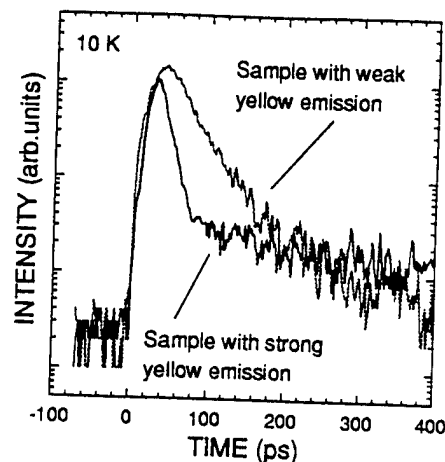


Fig. 4. Comparison of the decay times of free-exciton emission between two GaN samples with the relative intensity ratio of 100:1 for the yellow emission.

3.3 Pressure coefficient and hydrostatic deformation potential for direct Γ band gap

In Fig. 5 we plot the peak energies of exciton emission and yellow emission structures as a function of pressure. The solid lines in the figure are the least-square fits to the experimental data using the quadratic-fit function

$$E(P) = E(0) + \alpha P + \beta P^2. \quad (3)$$

The change of the intense and sharp BX transition with pressure plotted in the figure provides an unmistakable signature of the direct Γ band-gap dependence for wurtzite GaN based on the effective mass approximation. The best fits to the data yield a linear slope of 3.86×10^{-3} eV/kbar with an extremely small sublinear term of -8×10^{-7} eV/kbar². Similar results can be obtained from fitting the FX transition as well ($\alpha = 3.9 \times 10^{-3}$ eV/kbar and $\beta = -1.8 \times 10^{-6}$ eV/kbar²).

The application of hydrostatic pressure allows a direct estimation of the hydrostatic deformation potential for the direct Γ band gap of wurtzite GaN. The deformation potential is defined as $\alpha = \partial E / \partial \ln V$. The hydrostatic deformation potential for the direct Γ band gap of wurtzite GaN could be deduced as $\alpha = 9.2 \pm 1.2$ eV.

The broad yellow emission band maximum was found to shift with pressure at a rate of 4.0×10^{-3} eV/kbar, almost the same as that of exciton emissions. This spectral structure could be commonly observed in the PL spectra of nominally undoped GaN single crystals regardless of the crystal growth techniques. More strikingly, this band was observed in samples implanted with a variety of atomic species.[10] These results have led to the general belief that the broadband emission in the yellow spectral region involves defects. Recent theoretical studies on the electronic structures of impurities and native defects in GaN have suggested that point

defects, such as antisites and vacancies, play important roles.[11-14] The pressure dependence of the yellow emission band, in broad terms, is consistent with the transitions involving shallow donors and deep acceptors. Further theoretical and experimental studies are necessary to investigate the microscopic nature of the broadband yellow emission in GaN.

4. Conclusions

Optically pumped stimulated emission and lasing phenomena in GaN on sapphire were investigated using high-power pulsed lasers. Stimulated near-violet emissions were observed over a wide temperature range from 10 K to ~420 K. The dynamics of photoexcited excess carriers in high quality GaN samples were investigated. This was done using transient luminescence spectroscopy in the picosecond regime using a streak camera in the region of near band-edge excitonic emissions. We found that the strong capture of photoexcited carriers in impurities and/or defects through nonradiative recombination processes dominates the decay of carrier population. The capture process depends on the density of impurities and defects in the GaN samples. The effects of pressure on the various optical transitions associated with both intrinsic and extrinsic processes in the GaN samples were examined by photoluminescence spectroscopy. The pressure coefficient of the GaN band gap was determined by studying the shift of exciton emission lines in GaN with applied pressure. Our results yielded the variation of the GaN band gap with pressure to be $\Delta E(P) = 3.9 \times 10^{-3} P - 1.0 \times 10^{-6} P^2$ eV. The deformation potential for the direct Γ band was also deduced from the experimental results to be -9.2 ± 1.2 eV.

References

- [1] Strite, S. and H. Morkoç, 1992, *J. Vac. Sci. Technol.* **B10**, 1237, and references therein.
- [2] Pankove, J.I. 1990, *Mater. Res. Soc. Symp. Proc.* **162**, 515, and references therein.
- [3] Morkoç, H. *et al.* 1994, *J. Appl. Phys.* **76**, 1363, and references therein.
- [4] See, for example, Nakamura, S. *et al.* 1994, *Appl. Phys. Lett.* **64**, 1687.
- [5] Yang, X.H. *et al.* 1995, *Appl. Phys. Lett.* **66**, 1.
- [6] Zubrilov, A.S. *et al.* 1995, *Inst. Phys. Conf. Ser.* No.141, 525.
- [7] Agrawal, G.P. and N.K. Dutta, 1993, in *Semiconductor Lasers*, (Van Nostrand Reinhold, New York), p.132.
- [8] Dexter, D.L. 1958, in *Solid State Physics*, ed. F. Seitz and D. Turnbull (Academic, New York), Vol.6.
- [9] 't Hooft, G.W. *et al.* 1987, *Phys. Rev.* **B35**, 8281.
- [10] Pankove, J.I. and J.A. Hutchby, 1976, *J. Appl. Phys.* **47**, 5387.
- [11] Jenkins, D.W. and J.D. Dow, 1989, *Phys. Rev.* **B39**, 3317.
- [12] Tansley, T.L. and R.J. Egan, 1992, *Phys. Rev.* **B45**, 10942; 1993, *Physica B* **185**, 190.
- [13] Neugebauer, J. and C.G. Van de Walle, 1994, *Phys. Rev.* **B50**, 8067.
- [14] Boguslawski, P. *et al.* 1995, *Phys. Rev.* **B51**, 17255.

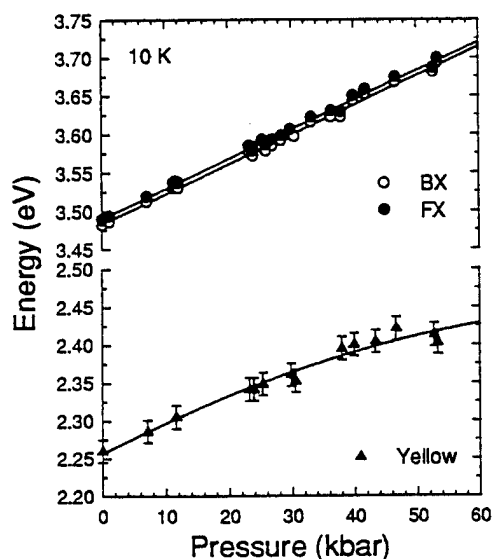


Fig. 5. Dependence of the energy positions on pressure for the various observed PL transitions in the GaN sample.

Strain effects on excitonic transitions in GaN: Deformation potentials

W. Shan, R. J. Hauenstein, A. J. Fischer, and J. J. Song

Center for Laser Research and Department of Physics, Oklahoma State University, Stillwater, Oklahoma 74078

W. G. Perry, M. D. Bremser, and R. F. Davis

Department of Materials Science and Engineering, North Carolina State University, Raleigh, North Carolina 27695

B. Goldenberg

Honeywell Technology Center, Plymouth, Minnesota 55441

(Received 11 July 1996)

We present the results of experimental studies of the strain effects on the excitonic transitions in GaN epitaxial layers on sapphire and SiC substrates, with the emphasis on the determination of deformation potentials for wurtzite GaN. Photoluminescence and reflectance spectroscopies were performed to measure the energy positions of exciton transitions and x-ray-diffraction measurements were conducted to examine the lattice parameters of GaN epitaxial layers grown on different substrates. Residual strain induced by the mismatch of lattice constants and thermal expansion between GaN epitaxial layers and substrates was found to have a strong influence in determining the energies of excitonic transitions. The overall effects of the strain generated in GaN is compressive for GaN grown on sapphire and tensile for GaN on SiC substrate. The uniaxial and hydrostatic deformation potentials of wurtzite GaN were derived from the experimental results. Our results yield the uniaxial deformation potentials $b_1 \approx -5.3$ eV and $b_2 \approx 2.7$ eV, as well as the hydrostatic components $a_1 \approx -6.5$ eV and $a_2 \approx -11.8$ eV. [S0163-1829(96)06843-9]

GaN-based III-V nitride semiconductors currently attract extensive attention for their potential device applications.¹⁻³ It is known that GaN has a wurtzite structure in natural form, and has a wide direct band gap of ~ 3.42 eV at 300 K, which provides efficient radiative recombination. The wavelength of radiation from GaN-based materials can be tuned over a wide range from visible to ultraviolet by alloying or forming heterostructures, such as quantum wells, with other nitrides (AlN and InN). These merits make III-V nitrides very attractive to short-wavelength optical applications such as light emitters and detectors operating in the blue and ultraviolet wavelength range. The outstanding thermal and chemical stability of the wide-band-gap nitrides also allows GaN-based electronic and optoelectronic devices to operate at high temperatures and in hostile environments.

Great efforts have recently been devoted to the preparation of high-quality GaN crystals and epitaxial films, the characterization of GaN crystals and films, and the development of devices using GaN-based materials. In the course of these studies, a number of investigations on the optical properties of GaN have revealed that there is a relatively large difference in the reported values of observed energy positions of excitonic transitions in GaN.⁴⁻¹¹ It is found that the energy positions vary from sample to sample depending on the epitaxial layer thickness, growth techniques and substrate materials. Such discrepancy has been attributed to the effects of residual strain in the epilayers due to the mismatch of lattice parameters and coefficients of thermal expansion between GaN and the substrate materials.^{8,11,12} In this report, we present the results of experimental studies of the strain effects on the excitonic transitions in GaN epitaxial layers on sapphire and SiC substrates. Photoluminescence and reflectance spectroscopies were performed to examine the effects of strain on the exciton transitions in the GaN epitaxial materials on sapphire and SiC substrates. X-ray-diffraction mea-

surements were conducted to measure the lattice parameters of GaN epitaxial layers grown on different substrates. The residual strain built in GaN epitaxial films induced by the mismatch of lattice constants and thermal expansion between GaN epitaxial layers and substrates was found to play an important role in determining the energies of excitonic transitions. The overall effects of the strain generated in GaN is compressive for GaN grown on sapphire and tensile for GaN on SiC substrate. The uniaxial and hydrostatic deformation potentials were derived from the experimental results.

The GaN samples used in this work were nominally undoped single-crystal films grown by metalorganic chemical vapor deposition on (0001) 6H-SiC or basal-plane sapphire substrates. AlN buffer layers were deposited on the substrates at about 775 °C before the growth of the GaN epilayers.¹³ Photoluminescence (PL) measurements were conducted with either a cw HeCd laser (325 nm) or a frequency-doubled Ar⁺ laser (244 nm) as the excitation source and a 1-M double-grating monochromator connected to a photon-counting system. For reflectance measurements, the quasimonochromatic light dispersed by a $\frac{1}{2}$ -M monochromator from a xenon lamp was focused on samples, and the reflectance signals were detected using a lock-in amplification system. To determine the lattice parameters of GaN epitaxial films, four-crystal x-ray rocking curves were measured. Absolute lattice parameter measurements were performed in the triple-axis mode of a Philips high-resolution diffractometer with four-bounce Ge (220) incident beam optics and three-bounce Ge (220) diffracted beam optics. The resolution limit of this configuration is ~ 10 arc sec. The high resolution of the triple-bounce analyzer crystal and the steps taken to eliminate inaccuracies due to the 2θ zero error as well as sample centering account for the limit. The data were collected using $2\theta-\omega$ scans, with corrections made for refraction. The accuracy of lattice parameters measured

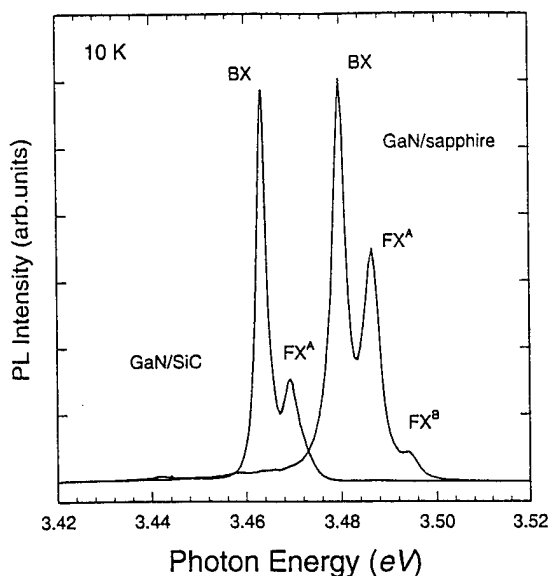


FIG. 1. Near-band-edge exciton luminescence spectra taken from a 3.7- μm GaN epilayer on SiC and a 4.2- μm GaN epilayer on sapphire at 10 K.

using this system is predicted to be better than 0.0002 Å. The high resolution of the triple-bounce analyzer crystal and the steps taken to eliminate inaccuracies due to the 2θ zero error as well as sample centering account for this. The lattice parameter c was measured using the (002) reflection and a was measured using both the (002) and (015) reflections.

The GaN-based samples studied in this work all exhibit strong near-band-edge exciton luminescence. Results of PL measurements from a 3.7- μm GaN epilayer on SiC and a 4.2- μm sample with sapphire substrate are shown in Fig. 1. The intensity of the strongest emission line marked by BX in Fig. 1 was found to decrease much faster than that labeled FX as the temperature increased. It became hardly resolvable at temperatures higher than 100 K. Such variations of the luminescence intensity as a function of temperature indicate that the emission line can be attributed to the radiative recombination of excitons bound to neutral donors.⁷ The second strongest luminescence structure, together with the weak emission feature on the higher-energy side, are a radiative recombination of the intrinsic free exciton. As clearly illustrated by the figure, the values of PL transition energies obtained here from GaN on an SiC substrate are lower than those from GaN on sapphire. The energy positions of the BX peak and FX peak are 3.4634 and 3.4693 eV, respectively, for the GaN/SiC sample, and 3.4790 and 3.4845 eV, respectively, for the GaN/sapphire sample. Figure 2 shows the comparison of the reflectance spectra taken from the same two samples at 10 K. Three exciton resonances associated with the transitions referred to as the A, B, and C exciton transitions⁴⁻⁷ between the bottom of the conduction band (Γ_7^c) and three topmost valence-band edges ($\Gamma_9^v + \Gamma_7^v + \Gamma_7^v$) are indicated by vertical arrows. The energy positions of these transitions are 3.470, 3.474, and 3.491 eV, respectively, for the GaN/SiC sample while the corresponding values, 3.485, 3.493, and 3.518 eV, were obtained for GaN on sapphire. Such systematically observed differences in exciton transition energies have been attributed to the effects of residual strain in the epilayers due to the mismatch of lattice

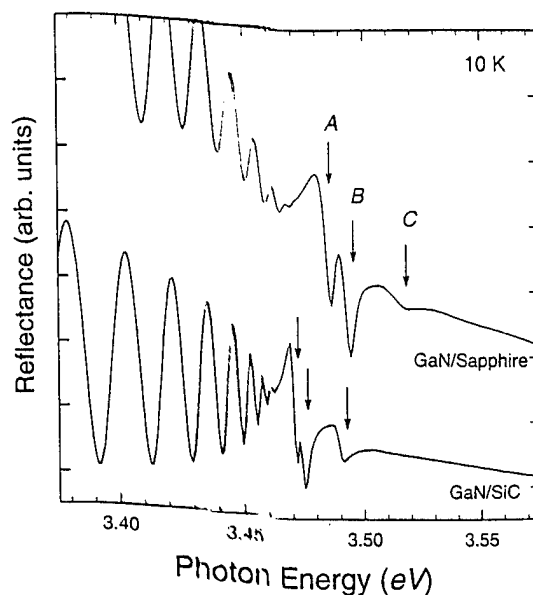


FIG. 2. Reflectance spectra of the exciton transition region of the MOCVD GaN/SiC and GaN/sapphire samples at 10 K. The oscillatory structures at lower energy are interference effects caused by the heterointerface.

parameters and coefficients of thermal expansion between GaN and the substrate materials.^{8,11,12}

Because of the inevitable occurrence of strain relaxation by the formation of a large density of dislocations, it is generally difficult to separate the strain effects caused by lattice-expansion mismatch from the ones involving thermal-influences on the optical properties of GaN epitaxial layers. However, by comparing the observed exciton transition energies in GaN epilayers deposited on sapphire and SiC to the values (3.4751, 3.4815, and 3.503 eV) obtained from virtually strain-free bulk GaN reported in Ref. 6, one can infer that the overall effects of residual strain generated in GaN on sapphire is compressive, which results in an increased band gap, while that induced in GaN on SiC is tensile, which leads to a decrease in measured exciton transition energies. This was further confirmed by x-ray rocking curve measurements. The lattice parameters were determined to be $a=3.1848$ Å and $c=5.1879$ Å for the 4.2- μm GaN on sapphire and $a=3.1900$ Å and $c=5.1840$ Å for the 3.7- μm GaN on SiC, compared to the lattice parameters of $a=3.1891$ Å and $c=5.1855$ Å for strain-free GaN.¹⁴ Therefore, the results presented here lead to the conclusion that residual strain induced by thermal-expansion mismatch in GaN-based epitaxial layers has the prevailing influence on the energy variations of exciton transitions, since lattice-mismatch induced strain is of the opposite sign and hence would have the opposite effect on the variation of GaN band gap from that observed.

The observed strain shifts in excitonic transition energies permit a direct estimate of the deformation potentials, including both hydrostatic and uniaxial components for wurtzite GaN. The strain Hamiltonian of a material having a wurtzite structure is given by Pikus.¹⁵ Under the assumption of a strain-independent and isotropic spin-orbit interaction, the energies of the three free excitons A, B, and C can be described as^{16,17}

$$E_A = E_A(0) + a_1 \epsilon_{zz} + a_2(\epsilon_{xx} + \epsilon_{yy}) + b_1 \epsilon_{zz} + b_2(\epsilon_{xx} + \epsilon_{yy}), \quad (1)$$

$$E_B = E_B(0) + a_1 \epsilon_{zz} + a_2(\epsilon_{xx} + \epsilon_{yy}) + \Delta + [b_1 \epsilon_{zz} + b_2(\epsilon_{xx} + \epsilon_{yy})], \quad (2)$$

$$E_C = E_C(0) + a_1 \epsilon_{zz} + a_2(\epsilon_{xx} + \epsilon_{yy}) + \Delta - [b_1 \epsilon_{zz} + b_2(\epsilon_{xx} + \epsilon_{yy})], \quad (3)$$

where $E_i(0)$ represents strain-free exciton transition energy, a and b are deformation potentials, and the ϵ_{ii} are components of the strain tensor for the GaN film. Since the energy variation given in Eqs. (1)–(3) by a_1 and a_2 is analogous to the hydrostatic shift of a cubic semiconductor, a_1 and a_2 are combined hydrostatic deformation potentials for transitions between the conduction and the valence bands, while b_1 and b_2 are uniaxial deformation potentials characterizing the further splitting of the three topmost valence-band edges for tension or compression along and perpendicular to (0001), respectively. Since the growth direction of our epilayers is the z axis, the strain components are described by

$$\epsilon_{xx} = \epsilon_{yy} = \epsilon_{\parallel} = (a_s - a_0)/a_0, \quad \epsilon_{zz} = \epsilon_{\perp} = (c_s - c_0)/c_0, \quad (4)$$

where a_0 and c_0 are lattice parameters for strain-free bulk GaN, and a_s and c_s are those for the strained GaN epilayer. Under biaxial-stress conditions, the components of ϵ_{xx} , ϵ_{yy} , and ϵ_{zz} are related through the elastic stiffness coefficients as $\epsilon_{\perp} = -2C_{13}/C_{33}\epsilon_{\parallel}$. The coefficients Δ_{\pm} represent the mixing of valence-band orbital states by the spin-orbit interaction and are given by^{16,17}

$$\Delta_{\pm} = \frac{1}{2} \{ 1 \pm [1 + 8(\Delta_3/(\Delta_1 - \Delta_2))^2]^{-1/2} \}, \quad (5)$$

where Δ_1 is the crystal-field splitting of the Γ_9 and Γ_7 orbital states, Δ_2 and Δ_3 are parameters which describe the spin-orbit coupling. In principle, one has to know the values of these three band-structure parameters, in addition to the deformation potentials to predict strain shifts from Eqs. (1)–(3) above. This approach is complicated by the lack of consistent numerical values for the parameters, Δ_i .^{4,8,10,18–20} Fortunately, Eqs. (2) and (3) only require a knowledge of the ratio, $\gamma = \Delta_3/(\Delta_1 - \Delta_2)$, rather than the individual numerical values for these parameters. By plotting the observed excitonic transition energies against the residual strain in Fig. 3, we were able to obtain a value of ~ 0.531 for γ from the slopes of the solid lines in the figure.

The observed shifts in excitonic transition energies relative to the values of strain-free GaN (Refs. 5, 6, and 8) result from an overall effect of strain on the band gap which includes contributions from both hydrostatic and uniaxial components of the stress. To determine the respective values for the uniaxial and hydrostatic potentials of wurtzite GaN, one has to separate their contributions to the energy variations in observed exciton transition energies under strain compared to the strain-free case. By taking the differences between the experimentally obtained values of each individual excitonic transition according to Eqs. (1)–(3), the uniaxial component of strain-induced energy shift of the conduction-band edge relative to the valence-band edges can be readily separated from the total energy shift. With linear fits to the whole set of data listed in Table I using the least-square fitting, our results yield the relationship of the uniaxial deformation potentials b_1 and b_2 :

$$b_1 - C_{33}/C_{13}b_2 = -15.2 \text{ eV}. \quad (6)$$

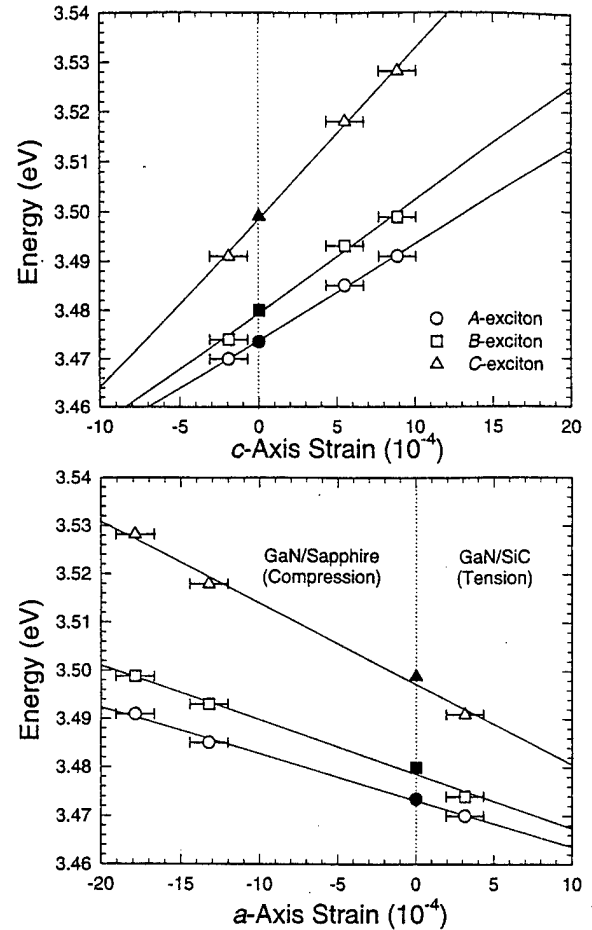


FIG. 3. The measured excitonic transition energies from GaN samples used in this work as a function of relative in-plane (biaxial) strain (lower portion) as well as the relative strain along the c axis (upper portion). The exciton transition energies of strain-free GaN were included in the figure for reference. The solid lines are the best linear fits to the experimental data.

A similar approach allows us to relate the combined hydrostatic deformation potentials a_1 and a_2 to each other as

$$a_1 - C_{33}/C_{13}a_2 = 37.9 \text{ eV}, \quad (7)$$

by subtracting the contribution of uniaxial component of strain from the total-energy shift induced by strain. Based on the facts that the strain-caused total-energy shift relative to the excitonic transition energy is very small and the elastic properties of GaN are of quasicubic nature ($C_{11} \approx C_{33}$),^{21,22} we found that it is appropriate to estimate the numerical val-

TABLE I. Values of measured excitonic transition energies and built-in residual strain for GaN on SiC and sapphire, together with those for strain-free bulk GaN.

	GaN/sapphire		GaN/bulk	GaN/SiC
Thickness (μm)	4.2	7.2	>100 ^a	3.7
A exciton (eV)	3.485	3.491	3.4735 ^a	3.470
B exciton (eV)	3.493	3.499	3.4800 ^a	3.474
C exciton (eV)	3.518	3.528	3.4993 ^a	3.491
ϵ_{\parallel} (10^{-4})	-13.2	-17.9	0	3.1
ϵ_{\perp} (10^{-4})	5.5	8.9	0	-1.9

^aReferences 5, 6, and 8.

ues, within the range of linear dependence on strain, for the uniaxial and hydrostatic deformation potentials using quadratic approximation²³ with $b_1 \approx -2b_2$, and $a_1 - a_2 \approx 2b_2$. The uniaxial deformation potentials are readily estimated to be $b_1 \approx -5.3$ eV and $b_2 \approx 2.7$ eV, using the values $C_{13} = 106$ and $C_{33} = 398$ GPa.²² The uncertainty of the above estimates is $\sim 15\%$, originating primarily from experimental error in the precise determination of lattice parameters. Our numerical values are comparable to the results reported for the materials with similar crystal structures such as CdS and ZnO,^{17,24} as well as recently reported values for GaN.^{8,20} Additionally, the numerical estimates for a_1 and a_2 are readily determined, once the values for b_1 and b_2 are known. Our results yield $a_1 \approx -6.5$ eV and $a_2 \approx -11.8$ eV.

It should be pointed out that the results of deformation potentials calculated using Eqs. (6) and (7) are dependent on the numerical values of the elastic stiffness constants C_{13} and C_{33} , especially for the hydrostatic parameters. For instance, the respective values of a_1 and a_2 could be as large as >20 eV if values, $C_{13} = 158$ and $C_{33} = 267$ GPa,²¹ are used. Fortunately, we were able to make a comparison of the estimated deformation potentials, obtained using variously reported values for C_{13} and C_{33} , with our previous work, in which a value for the "effective hydrostatic deformation potential" a of -9.2 eV for the Γ band gap of GaN was determined.²⁵ The value of a was determined by direct application of hydrostatic pressure. The reason for the term, *effective* hydrostatic deformation potential is that, strictly speaking, it is the stress, but (for the wurtzite structure) not the strain, that is isotropic, so that the terms involving b_1 and b_2 will contribute slightly in Eqs. (1)–(3). Thus, we regard the results of $b_1 \approx -5.3$ eV and $b_2 \approx 2.7$ eV as well as $a_1 \approx -6.5$ eV and $a_2 \approx -11.8$ eV as consistent and more accurate estimates, given the assumptions described above. Fi-

nally, we note that these in principle should represent an upper limit for the deformation potentials since they were evaluated by using the value of the lattice parameters measured at room temperature to fit optical data obtained at 10 K. The built-in residual strain is generally expected to increase with decreasing temperature due to the difference of thermal expansion coefficients between GaN epilayers and substrate materials.

In conclusion, we have studied the effects of residual strain in GaN epitaxial films using spectroscopic methods combined with x-ray-diffraction measurements, with the emphasis on determination of deformation potentials. Strong, sharp spectral structures associated with exciton transitions in GaN epitaxial layers grown on sapphire and 6H-SiC substrates by metal-organic chemical-vapor deposition (MOCVD) were observed in photoluminescence and reflectance spectra. The observation of exciton transitions with lower energies in GaN grown on SiC, and with higher energies for the same transitions for GaN grown on sapphire, in comparison to those obtained from strain-free bulk GaN, suggests that residual strain in GaN epilayers resulting from lattice-parameter and thermal-expansion mismatch plays an important role in determining the precise exciton transition energies. X-ray-diffraction measurements were performed to determine the variations in the lattice parameters of GaN epilayers on SiC and sapphire, respectively. Our results clearly indicate that GaN epilayers grown on SiC exhibit basal tensile strain, while those on sapphire substrates are under biaxial compression. Based on these results, the values of the four principal deformation potentials of wurtzite GaN have been determined.

This work at OSU was supported by AFOSR, DARPA, ONR, and ARO. The work at NCSU was supported by ONR under Contract No. N00014-92-J-1477.

- ¹J. I. Pankove, Mater. Res. Soc. Symp. Proc. **162**, 515 (1990), and references therein.
- ²S. Strite and H. Morkoç, J. Vac. Sci. Technol. B **10**, 1237 (1992), and references therein.
- ³H. Morkoç, S. Strite, G. B. Gao, M. E. Lin, B. Sverdlov, and M. Burns, J. Appl. Phys. **76**, 1363 (1994).
- ⁴R. Dingle and M. Illegeme, Solid State Commun. **9**, 175 (1971).
- ⁵R. Dingle, D. D. Sell, S. E. Stokowski, and M. Illegems, Phys. Rev. B **4**, 1211 (1971).
- ⁶B. Monemar, Phys. Rev. B **10**, 676 (1974).
- ⁷W. Shan, T. J. Schmidt, X. H. Yang, S. J. Hwang, J. J. Song, and B. Goldenberg, Appl. Phys. Lett. **66**, 985 (1995).
- ⁸B. Gil, O. Briot, and R.-L. Aulombard, Phys. Rev. B **52**, R17 028 (1995).
- ⁹M. Smith, G. D. Chen, J. Y. Lin, H. X. Jiang, M. Asif Khan, C. J. Sun, Q. Chen, and J. W. Yang, J. Appl. Phys. **76**, 7001 (1996).
- ¹⁰G. D. Chen, M. Smith, J. Y. Lin, H. X. Jiang, S. H. Wei, M. Asif Khan, and C. J. Sun, Appl. Phys. Lett. **68**, 2784 (1996).
- ¹¹W. Shan, A. J. Fischer, J. J. Song, G. E. Bulman, H. S. Kong, M. T. Leonard, W. G. Perry, M. D. Bremser, and R. F. Davis, Appl. Phys. Lett. **69**, 740 (1996).
- ¹²W. Rieger, T. Metzger, H. Angerer, R. Dimitrov, O. Ambacher, and M. Stutzmann, Appl. Phys. Lett. **68**, 970 (1996).
- ¹³T. W. Weeks, Jr., M. D. Bremser, K. S. Ailey, E. Carlson, W. G. Perry, and R. F. Davis, Appl. Phys. Lett. **67**, 401 (1995).
- ¹⁴C. M. Balkas, C. Basceri, and R. F. Davis, Powder Diffraction **10**, 266 (1995).
- ¹⁵G. Pikus, Zh. Eksp. Teor. Fiz. **41**, 1507 (1961) [Sov. Phys. JETP **14**, 1075 (1962)].
- ¹⁶V. B. Sandomirskii, Sov. Phys. Solid State **6**, 261 (1964).
- ¹⁷A. Gavini and M. Cardona, Phys. Rev. B **1**, 672 (1970).
- ¹⁸M. Suzuki, T. Uenoyama, and A. Yanase, Phys. Rev. B **52**, 8132 (1995).
- ¹⁹Yu. M. Sirenko, J. B. Jeon, K. W. Kim, M. A. Littlejohn, and M. A. Strosio, Phys. Rev. B **53**, 1997 (1996).
- ²⁰S. Chichibu, A. Shikanai, T. Azuhata, T. Sota, A. Kuramata, K. Horino, and S. Nakamura, Appl. Phys. Lett. **68**, 3766 (1996).
- ²¹V. A. Savastenko and A. U. Sheleg, Phys. Status Solidi A **48**, K135 (1978).
- ²²A. Polian, M. Grimsditch, and I. Grzegory, J. Appl. Phys. **79**, 3343 (1996).
- ²³G. L. Bir and G. E. Pikus, in *Symmetry and Strain-Induced Effects in Semiconductors* (Wiley, New York, 1974), Chap. V.
- ²⁴D. W. Langer, R. N. Euwema, K. Era, and T. Koda, Phys. Rev. B **2**, 4005 (1970).
- ²⁵W. Shan, T. J. Schmidt, R. J. Hauenstein, J. J. Song, and B. Goldenberg, Appl. Phys. Lett. **66**, 3492 (1995).

Going beyond the mean-field approximations of alloys and alloy superlattices: a few puzzles solved?

D. S. Kim, H. S. Ko, Y. S. Lim, Y. M. Kim, J. S. Lee, S. J. Rhee, W. S. Kim, S. C. Hong, Y. H. Yee, J. S. Khim, J. M. Jung, S. Huhr, J. H. Lee, J. S. Chang, B. D. Choe, and J. C. Woo

Department of Physics, Seoul National University, Seoul 151-742, Korea

P. H. Song, H. J. Choi, S. H. Jhi, and J. Ihm

Department of Physics and Center for Theoretical Physics, Seoul National University, Seoul 151-742, Korea

E. J. Shin and D. Kim

Spectroscopy Laboratory, Korea Research Institute of Standards and Science, Taejeon 305-606, Korea

D. H. Woo and K. N. Kang

Korea Institute of Science and Technology, Cheongryang, Seoul 136-791, Korea

J. J. Song

*Department of Physics and Center for Laser Research,
Oklahoma State University, Stillwater, Oklahoma 74078*

Received September 14, 1995; revised manuscript received December 5, 1995

We discuss a few examples of cases in which the widely used mean-field approaches to alloys and alloy superlattices may not give complete solutions. These examples include the anomalously large Stokes and anti-Stokes real space-charge transfer over thick alloy barriers and the spatial extent of optical phonons in alloys and alloy superlattices, which have remained unsolved or controversial. We argue, both theoretically and experimentally, that approaches that fully account for inhomogeneities, partial ordering, and disorder effects in the alloys as well as the proper understanding of coupled quantum-mechanical systems do give answers to these important puzzles. © 1996 Optical Society of America

1. INTRODUCTION

Since their conception¹ and subsequent realization, semiconductor superlattices have remained one of the most active areas of condensed-matter physics. Some of the most widely used superlattices have alloys as barriers, or wells, as in GaAs/Al_xGa_{1-x}As, GaAs/GaAs_{1-x}P_x, and In₂Ga_{1-x}As/GaAs, to name a few. The overwhelming majority of experimental results on these alloys and alloy superlattices have been analyzed by the mean-field approach, which has been quite successful in dealing with many important quantities such as band gaps, dispersion relations, and density of states. However, there have remained a few well-known problems for which such an approach might not yield complete results. We present experimental and theoretical investigations of (1) anomalously large real space-charge transfer over thick alloy barriers in GaAs/Al_xGa_{1-x}As, (2) anomalously large anti-Stokes charge transfer at low temperature and low excitation density in GaAs/Al_xGa_{1-x}As, (3) the coherence length of GaAs LO phonons and dynamic transfer of GaAs optical phonons through the Al_xGa_{1-x}As barrier in GaAs/Al_xGa_{1-x}As, and (4) localization properties of optical phonons in Al_xGa_{1-x}As alloy. These problems have

remained unsolved or controversial, and from systematic and extensive experimental and theoretical investigations we contend that inhomogeneities and fluctuations of the atomic arrangement in the alloy are crucial for an understanding of these puzzles.

2. ANOMALOUSLY LARGE REAL SPACE-CHARGE TRANSFER OVER THICK ALLOY BARRIERS: Al_xGa_{1-x}As AS A LEAKY BARRIER

Recently an anomalously large interwell exciton transfer over thick barriers in GaAs/Al_xGa_{1-x}As asymmetric double quantum wells (ADQWs) received attention.² The existence of this unexplained transfer has been observed by many researchers for quite some time, in samples grown by many different groups of researchers. The experimentally deduced transfer coefficient was of the order of 10⁻³, orders of magnitudes larger than the theoretical predictions based on the one-dimensional tunnelling model for the given barrier width (*d*) and the average potential height. The experiments were performed at 2 K, so thermal excitations above the barrier were ruled out. Reabsorption of the narrow-well (NW)

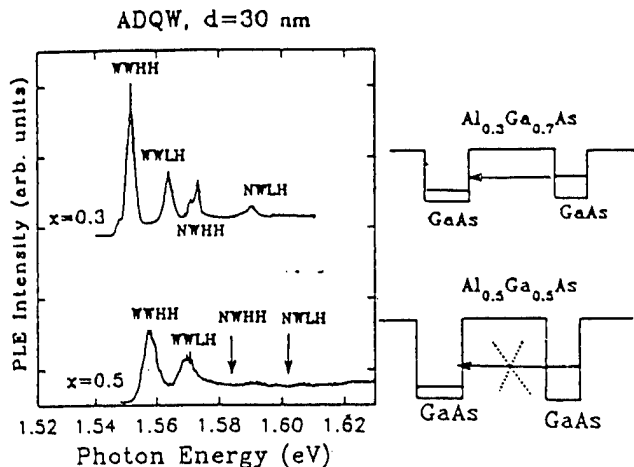


Fig. 1. PLE spectra obtained at 14 K for the GaAs/AlGaAs/GaAs (7.5 nm/30 nm/10 nm) ADQW, with $x = 0.3$ and $x = 0.5$. At the right, schematics of the sample structure are shown, with the unadorned dotted arrow indicating strong transfer and the crossed-out dotted arrow indicating much smaller transfer.

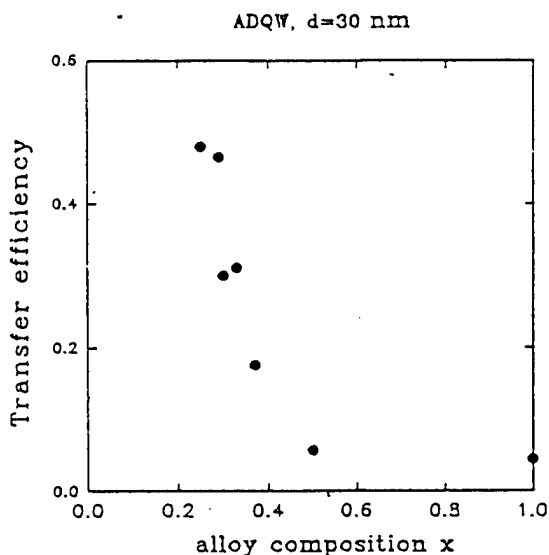


Fig. 2. Transfer efficiency at 14 K defined as the ratio of the areas under the NW HH to the WW HH peaks in the PLE spectra, plotted against x for the GaAs/Al_xGa_{1-x}As/GaAs ADQW (7.5 nm/30 nm/10 nm). The efficiency was averaged over several different spots.

luminescence by the wide-well (WW) dipole-dipole interaction of excitons and polariton effects were proposed as possible explanations for this transfer.²⁻⁶

In this section an extensive study of this mysterious transfer in GaAs/Al_xGa_{1-x}As ADQW's grown by molecular-beam epitaxy is presented. Photoluminescence excitation (PLE) was performed in a series of samples with variable x and barrier thickness d . The most interesting observations that we made are as follows: (1) the strong x dependence of the transfer (Figs. 1 and 2), (2) the drastic reduction in the transfer when the barrier is GaAs or a digital alloy (Fig. 3), and (3) the very weak d dependence of the transfer shown in Fig. 4. Our results demonstrate the importance of the nonuniformity of the alloy potential barrier in charge transfer, as we discuss in detail below.

In Fig. 1, PLE spectra at 14 K obtained with a cw Ti:sapphire laser are shown for two ADQW samples. The photoluminescence (PL) window was at the low-energy side of the WW heavy-hole (HH) exciton peak. The sample parameters are GaAs/Al_{0.3}Ga_{0.7}As/GaAs (7.5 nm/30 nm/10 nm) for the top and GaAs/Al_{0.5}Ga_{0.5}As/GaAs (7.5 nm/30 nm/10 nm) for the bottom. For $x = 0.3$ the NW exciton peaks are pronounced, indicating a strong transfer from the NW to the WW. The height of the NW HH peak is larger than the background as a result of continuum excitation and is comparable with the WW light-hole (LH) exciton peak. The experiments were performed at low excitation density ($\sim 10^8$ cm⁻²), and the PLE spectra are mostly independent of laser intensity. Therefore intensity-dependent nonlinear effects can be immediately ruled out. For $x = 0.5$ in Fig. 1 (bottom trace), there is virtually no sign of the NW peaks, whose positions are indicated by arrows. This absence of NW peaks in the PLE of WW excitons is of course what one would expect from the mean-field approach.

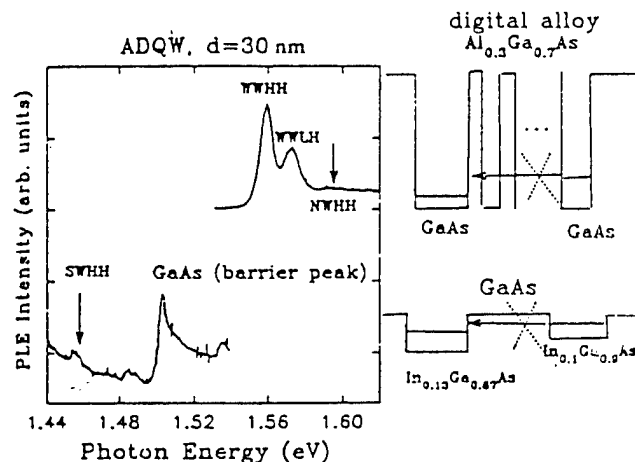


Fig. 3. PLE spectra at 14 K for the GaAs/(GaAs/AlAs; 5ML/2ML digital alloy)/GaAs ADQW (7.5 nm/30 nm/10 nm) (top trace) and for In_{0.1}Ga_{0.9}As/GaAs/In_{0.13}Ga_{0.87}As (10 nm/30 nm/10 nm) ADQW (bottom trace). SWHH denotes the heavy hole of the shallower well (In_{0.1}Ga_{0.9}As).

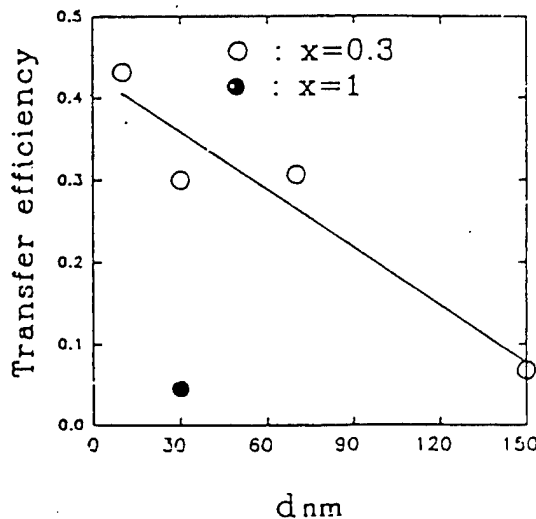


Fig. 4. Transfer efficiency at 14 K for the GaAs/Al_{0.3}Ga_{0.7}As/GaAs ADQW (7.5 nm/10, 30, 70, or 150 nm/10 nm) plotted against d .

When the laser photon energy is at the NW HH, both the NW exciton and the WW continuum are excited. If there were no transfer from the NW to the WW, the resonant excitation of NW excitons would have no effect on the intensity of the WW luminescence; therefore no increase in the luminescence would be expected. In other words, there would be no structure at the NW HH or NW LH positions: there would simply be the flat, WW continuum. In contrast, when there is a strong transfer from the NW to the WW (Fig. 1, top), the amount of electron-hole pairs from the NW that eventually end up in the WW can be estimated in the following simple way: inasmuch as the WW luminescence is enhanced by a factor of 2 when the NW HH is resonantly excited, it can be estimated that nearly half of the electron-hole pairs in the WW originate from the NW. From this and the PLE spectra with the low-energy tail of the NW luminescence as a window we can easily estimate that as much as 30% of the resonantly excited NW excitons eventually end up in the WW. We also can divide the area under the NW HH peak by that of the WW HH peak⁶ and come up with roughly the same number, ~30%. From the known lifetime of resonantly excited excitons⁷ and from the vertical velocities of the first quantized electrons and holes we can estimate that the transfer coefficient is of the order of $\sim 10^{-3}$, at least 10 orders of magnitude greater than the tunneling coefficient over the one-dimensional mean-field barrier.

In Fig. 3, striking examples of the complete failure of the mean-field approach are shown. PLE spectra of a GaAs ADQW with a digital alloy barrier (top trace) and a shallow $\text{In}_x\text{Ga}_{1-x}\text{As}/\text{GaAs}$ ADQW are shown. The digital alloy barrier consists of GaAs/AlAs at a ratio of five monolayers to two monolayers, and d was kept at 30 nm. With these structural parameters the effective alloy concentration is 0.28. For this digital alloy barrier, which is roughly equivalent to 10 nm of AlAs, the mean-field theory would predict a larger, albeit negligible, transfer coefficient than for the 30-nm $\text{Al}_{0.3}\text{Ga}_{0.7}\text{As}$ alloy barrier. Likewise, the exciton transfer of the $\text{InGaAs}/\text{GaAs}$ ADQW should be much larger than the GaAs ADQW with $x = 0.3$ because the wells are much shallower. The absence of NW peaks in the PLE spectra of the digital alloy ADQW, or of the weak shallower-well HH peak in the $\text{In}_x\text{Ga}_{1-x}\text{As}/\text{GaAs}$ ADQW, tells exactly the opposite story. The absence of exciton transfer when the barrier is GaAs or AlAs/GaAs digital alloy strongly suggests that this anomalous transfer is a result of the alloy nature of the barrier. $\text{Al}_x\text{Ga}_{1-x}\text{As}$, being a substitutional alloy, has an intrinsic spatial fluctuation of atomic arrangement. Therefore we contend that a large spatial variation of the alloy potential barrier is responsible for this puzzling phenomenon. Because the order parameter or the size of the fluctuations in alloys is often a strong function of x , this picture is consistent with the observed sharp decrease between $x = 0.3$ and $x = 0.5$.

To investigate the x dependence of the transfer more systematically, we studied many GaAs/ $\text{Al}_x\text{Ga}_{1-x}\text{As}$ ADQW samples with varying x . In Fig. 2 the transfer efficiency that we obtained by normalizing the NW HH peak to the WW HH or to the background is plotted against x . A sharp decrease is observed near $x = 0.3$. From this x dependence, photon reabsorption by the WW can safely

be ruled out, as the barrier region is always transparent at the photon energies used. It is interesting that this critical x is close to the direct-to-indirect crossover ($x \sim 0.35$). With the exciting photon energies well below the threshold for the intervalley transfer, the real space-charge transfer⁸ is not directly relevant. Furthermore, the issues of type II superlattices or the barrier-confined states⁹ do not apply here because of relatively large well thickness. In contrast, a deeper understanding of the direct-to-indirect crossover in $\text{Al}_x\text{Ga}_{1-x}\text{As}$ alloy in terms of order parameters or cluster sizes¹⁰ might prove useful. Finally, note that even for large x there is a significant transfer efficiency of ~5%, which is roughly independent of x . This transfer might be due to photon reabsorption or coherent polariton transfer,³⁻⁵ processes that are thought to be largely independent of x and d .

We note that significant transfer persists up to $d = 30$ nm, which means that the d dependence is much weaker than what the one-dimensional tunneling model would predict. To see this effect more closely, we studied the d dependence of the transfer as a function of d for a fixed $x = 0.3$. In Fig. 4 the d dependence of the normalized transfer efficiency in a GaAs/ $\text{Al}_x\text{Ga}_{1-x}\text{As}$ ADQW is shown for $x = 0.3$ (open circles) along with that for $x = 1$ and $d = 30$ nm (filled circles). The d dependence at $x = 0.3$ is weak, and even at $d = 150$ nm it is still greater than that of $x = 1$ and $d = 30$ nm. The weak dependence on d suggests that the apparent penetration depth is of the order of 100 nm. Because the tunneling coefficient would decrease exponentially with d , with its penetration depth of the order of 1 nm, this dependence is again suggestive of a transfer efficiency that is orders of magnitude larger than the prediction of tunneling. We now discuss model calculations that take into account the effect of the detailed structure of the alloy barrier and the possible clustering of GaAs and AlAs molecules.

In the mean-field approach the barrier height in a GaAs/ $\text{Al}_x\text{Ga}_{1-x}\text{As}$ superlattice is assumed to be constant determined by x . In contrast, recent scanning tunneling microscopic studies of GaAs/ $\text{Al}_x\text{Ga}_{1-x}\text{As}$ quantum wells, AlAs/GaAs superlattices, and $\text{Al}_x\text{Ga}_{1-x}\text{As}$ alloys¹¹ show that there is elongated clustering of Ga-rich and Al-rich regions in the barrier along the growth direction, thus possibly connecting adjacent GaAs wells. This is related to recent theoretical studies of long- and short-range order in the ternary substitutional alloys.^{10,12} We first considered the effect of atomic scale fluctuations on the transmission coefficient. We divided the barrier into small cubes of atomic scale representing GaAs or AlAs molecules and randomly assigned the potential V_0 for AlAs or 0 for GaAs. V_0 is 1.12 eV (0.26 eV) to simulate the band offsets for electrons (holes) [Fig. 5(a)]. We solved the resulting three-dimensional effective mass equation with appropriate boundary conditions to obtain the transmission coefficients. The resulting transmission coefficients are larger than those obtained from the one-dimensional mean-field approach up to a factor of 10 but are still far too small to explain the large transmission coefficient of the order of 10^{-3} deduced from experiments. Essentially, the wavelength of the incoming waves (~ 10 nm, comparable with the well size) is too large for the waves to see the low but narrow potential pathways.

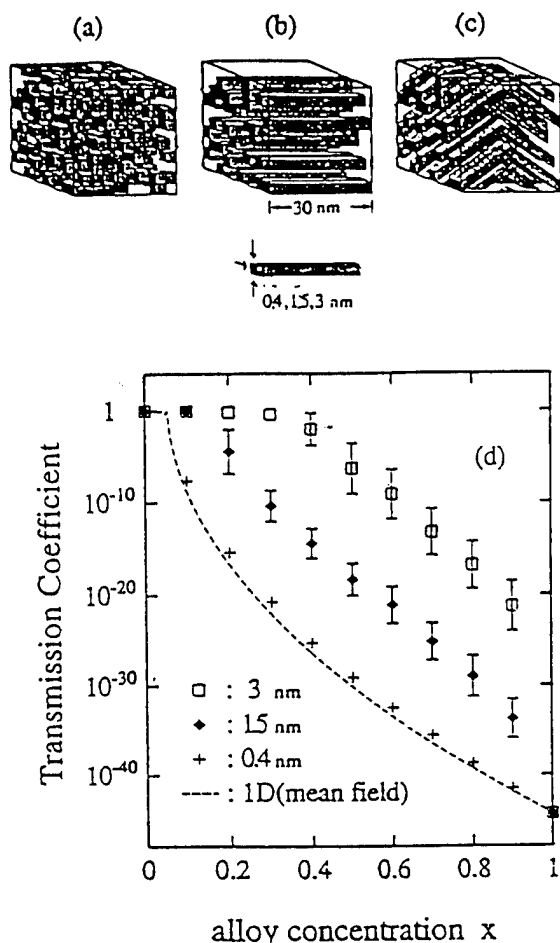


Fig. 5. (a) Schematic of the construction of barriers used in our model calculations, assuming completely random, atomic alloy fluctuations. The shaded squares represent AlAs molecules. (b) Schematic of our model calculations taking into account the clustering and the formation of channels. (c) Same as (b), except for the existence of kinks. (d) Transmission coefficients using barriers described in (b), plotted against x for several grid sizes. The incident wave simulates holes in the narrow well, with an effective mass of $\sim 0.5m_e$ and a wavelength of 15 nm.

We then replaced the cubes in the barrier region with rectangular cylinders (or wires) long enough to connect the two wells, as shown in Fig. 5(b), simulating the possible aligning of GaAs or AlAs roughly along the growth direction in light of recent scanning tunneling microscopy studies.¹¹ We performed the quantum-mechanical calculation for various sizes of rectangles to study the cluster size effect on the transmission coefficients. Furthermore, the possible effect of kinks was considered [Fig. 5(c)] in connection with Ref. 11, where the GaAs quantum wires were shown to zigzag their ways through the barrier. In Fig. 5(d) we plot the transmission coefficients of holes as functions of x for several cluster sizes, using the model of Fig. 5(b). We considered holes rather than electrons because it is generally believed that the transport of excitons is determined mostly by the first quantized holes, whose transport is generally slower than that of electrons because of their larger effective masses. For the grid size of 0.4 nm the results are only slightly larger than the prediction of the mean-field theory, despite the fact that there are many low-potential quantum wires in the barrier. The physics of this low

transmission coefficient is the same as described above: the pathways are much narrower than the wavelength. Increasing the cluster size rapidly enhances the transmission coefficient, so for the cluster size 3 nm, nearly all holes can pass through the barrier for relatively low x . The physics of this huge enhancement in the transmission coefficient is that, for the average cluster size of 3 nm, there is a small fraction of GaAs clusters whose dimensions are larger than 15 nm, which is the wavelength of the holes or electrons. These large clusters permit the ballistic transport of holes or electrons, resulting in large transmission coefficients. The strong x dependence and the weak d dependence can then be explained in this model, albeit somewhat trivially. In addition, the results obtained from the model schematically described in Fig. 5(c) show that the effect of the kink is to decrease the transmission coefficient only slightly without changing the overall trends. Finally, note that our results have only a weak dependence on the specific band offsets used, for the physics is determined essentially by the maximum cluster size.

Our model calculations suggest that the anomalously large transmission coefficient and most features of our experiments could be explained, at least qualitatively, if there were a large enough clustering of GaAs or $\text{Al}_x\text{Ga}_{1-x}\text{As}$ with very low x connecting two GaAs quantum wells in a quantum-wire-like fashion. Although a more realistic approach to the detailed mechanism of clustering and the resulting structure and pattern formation would be much desired, our results imply that the clustering of GaAs in the alloy barrier is a likely source of the greatly enhanced interwell coupling. Finally, even without clustering, quantum wells with completely random substitutional alloy as barriers might have extended states below a certain x .¹³ This type of approach has not yet shown its full potential in semiconductor physics.

To conclude this section, we have experimentally demonstrated that a mysteriously largely transfer of excitons through thick barriers occurs when the barrier is composed of $\text{Al}_x\text{Ga}_{1-x}\text{As}$ alloy. Unlike solid barriers such as GaAs/AlAs digital alloys, $\text{Al}_x\text{Ga}_{1-x}\text{As}$ is essentially leaky, or percolating, especially for $x < 0.4$. There may be regions of low potential in the barrier connecting two adjacent wells, which permit the observed huge charge transfer. Our results show that, beyond the widely used mean-field approach, one needs a three-dimensional approach that considers the detailed nature of the barrier such as clustering to understand the transfer over thick alloy barriers in semiconductor superlattices.

3. ANTI-STOKES LUMINESCENCE AT LOW TEMPERATURE AND EXCITATION DENSITY IN ADQW'S AS A NATURAL CONSEQUENCE OF COUPLED QUANTUM SYSTEMS WITH INTERSITE DEPHASING

From Section 2 it is clear that GaAs quantum wells separated by an $\text{Al}_x\text{Ga}_{1-x}\text{As}$ alloy barrier with $x < 0.4$ are a weakly but reasonably well-coupled system even when the barrier is thick, with the coupling strength or the transmission coefficient per single trial near 10^{-3} . In this section we focus on the emission of anti-Stokes luminescence (ASL) that results from the NW in a GaAs/ $\text{Al}_x\text{Ga}_{1-x}\text{As}$

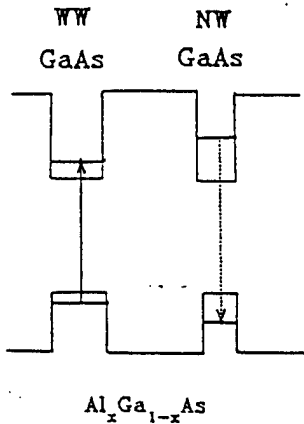


Fig. 6. Schematic of the ASL. When the WW exciton or continuum is excited below the NW HH, blue-shifted luminescence from the NW is observed.

ADQW even when only the WW seems to be initially excited, resonantly at the excitonic level or nonresonantly at the continuum. This phenomenon was observed earlier,² but its origin has remained a complete puzzle, especially because it did not increase with intensity or temperature. Thus intensity-dependent nonlinear effects or temperature-related excitation processes observed in other systems¹⁴ cannot explain it. We studied this ASL from both experimental and theoretical points of view. We found that the intensity of the ASL normalized to the normal Stokes luminescence is of the order of 10^{-3} in samples with significant Stokes charge transfer, again orders of magnitudes larger than the thermal coefficient. Interestingly, this efficiency matches well the transfer coefficient deduced from the Stokes PLE spectra. From a simple, coupled four-level system analysis we show that, indeed, the emission of anti-Stokes luminescence is a general feature of any coupled, spatially separated quantum-mechanical system with dephasing. In addition, it is shown that the ASL efficiency directly gives the coupling constant.

In Fig. 6 a schematic of ASL is given, with the solid and the dashed arrows corresponding, respectively, to

excitation of the WW level without exciting the NW (thus with photon energy below the NW HH) and to the anti-Stokes emission at the NW HH. Figure 7 shows a PLE spectrum at 14 K of a molecular-beam epitaxy-GaAs/ $\text{Al}_x\text{Ga}_{1-x}\text{As}$ /GaAs (10 nm/20 nm/5 nm) ADQW with $x = 0.28$ when the WW continuum is excited (top left-hand curve). Very strong ASL with a normalized efficiency of $\sim 10^{-3}$ is observed. At the bottom of the figure an anti-Stokes PLE spectrum is shown with the photoluminescence window at the peak of the NW HH and excitation energies scanned across the WW excitons and continuum. Well-defined WW HH and LH peaks are visible, as is the WW continuum. Therefore the ASL occurs regardless of whether the WW excitons or the free-carrier continuum is excited.

In the following discussion we propose the interwell dephasing of a coupled quantum system as the mechanism for the ASL. Realizing that the ADQW is essentially a weakly coupled system, we attempt to understand the ASL starting from this point of view. We consider the following simple model, described in Fig. 8. We consider a coupled four-level model, in which the coupling is between electrons in a WW and a NW and between holes in a WW and a NW. With coupling included, the eigenstates of electrons are slightly extended in space, with some small probability amplitudes to be found at the other well:

$$\psi_{\text{WW}} = \psi'_{\text{WW}} + \alpha\psi'_{\text{NW}}, \quad E = E_{\text{WW}}, \quad (3.1)$$

$$\psi_{\text{NW}} = \psi'_{\text{NW}} - \alpha\psi'_{\text{WW}}, \quad E = E_{\text{NW}}(>E_{\text{WW}}), \quad (3.2)$$

where $\alpha \ll 1$ and ψ'_{WW} and ψ'_{NW} are noneigenstate wave functions localized in the WW and the NW, respectively. The eigenstates for holes can be described similarly. We now consider the excitation of the low-energy eigenstates of electrons and holes of the coupled system, as described in Fig. 8(a). The eigenstates have well-defined energy and are mostly localized in the WW but have some small probability amplitudes to be found in the NW. In the absence of scattering the eigenstates, which are coherent superpositions of the localized wave functions, would

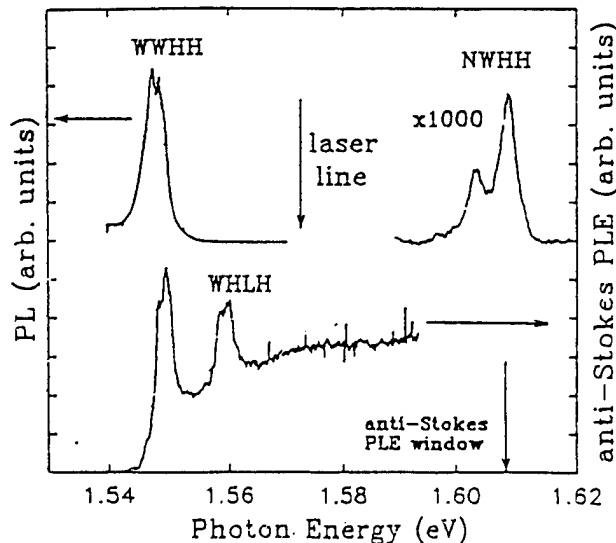


Fig. 7. (Top) PL spectrum at 14 K from an ADQW (5 nm/20 nm/10 nm; $x = 0.28$) when the WW continuum is excited. A well-defined NW HH peak is visible. (Bottom) anti-Stokes PLE spectrum with the window at the peak of the NW HH peak. The arrows indicate the position of the laser line (top) and the anti-Stokes PLE window (bottom). PL, Photoluminescence.

Anomalous anti-Stokes Transfer

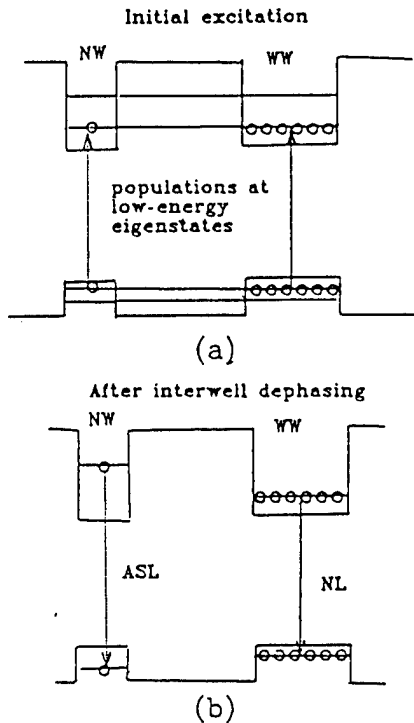


Fig. 8. (a) Schematic of photoexcitation of the spatially coherent eigenstates of electrons and holes that are mostly localized in the WW (thus the lower-energy eigenstates) in the coupled-well picture. (b) Schematic of the dephased wave functions that are not eigenstates but are superpositions of eigenstates with small probability to be found at the higher-energy states and of the resulting ASL.

maintain their spatial coherence between the sites. In realistic situations, however the states would undergo a variety of weak but random scatterings, some of which would destroy the phase relationship between the sites. One commonly describes the effects of these random scatterings by multiplying random phase factors, which would destroy the spatial coherence. Therefore, after a characteristic intersite dephasing time, the system can be described as being in an essentially mixed state in terms of its spatial coherence.

The effect of this intersite dephasing on the energy transfer becomes clear when we consider the dephased electron state $\psi_{d,WW}$ initially at the eigenstate $\psi_{WW} = \psi_{WW} + \alpha\psi_{NW}$: after intersite dephasing the state can now be described as

$$\psi_{d,WW} = \psi_{WW}' \exp(i\theta) + \alpha\psi_{NW}' \exp(i\theta') \\ = \exp(i\theta) \{ \psi_{WW}' + \alpha\psi_{NW}' \exp[i(\theta' - \theta)] \}, \quad (3.3)$$

where θ and θ' are random phases introduced by scatterings at the WW and the NW, respectively. Note that, whereas ψ_{WW} is an eigenstate, the dephased state $\psi_{d,WW}$ described in Eq. (3.3) is not. Expanding the dephased state $\psi_{d,WW}$ with the eigenbases ψ_{WW} and ψ_{NW} , we get, keeping only up to the first order in α ,

$$\psi_{d,WW} = \exp(i\theta) \{ \psi_{WW} + \alpha\psi_{NW} [\exp[i(\theta' - \theta)] - 1] \}. \quad (3.4)$$

In Eq. (3.4) the probability for the dephased state to be found at the initially vacant eigenstate ψ_{NW} is

$4\alpha^2 \sin^2[(\theta - \theta')/2]$. Taking an ensemble average, we arrive at the fraction of electron population transferred to the higher-energy state ψ_{NW} :

$$\text{fraction of population transfer} = 2\alpha^2. \quad (3.5)$$

Therefore an anti-Stokes population transfer to a higher-energy state has occurred purely as a result of dephasing. Furthermore, the fraction of the transferred population is determined only by the coupling strength α and does not depend on temperature or intensity. Similarly, the fraction of the anti-Stokes population of holes can be represented by $2\beta^2$, where β is the coupling constant for holes.

We now consider the photoexcitation of electrons and holes in their respective lower-energy eigenstates that are mostly, but not completely, localized in the WW. Initially, without interwell dephasing, the electrons and the holes would recombine to give luminescence at the excitation energy (resonant luminescence). However, after interwell dephasing, a small fraction of electrons and holes can be found with higher energy and gives rise to ASL, as shown in Fig. 8(b). When the interwell dephasing is much faster than the radiative recombination time, a condition easily satisfied in semiconductors,¹⁵ the normalized intensity of the ASL to the normal luminescence (NL) would be given by

$$\text{normalized ASL intensity} = 2 \min\{\alpha^2, \beta^2\}. \quad (3.6)$$

Equation (3.6) shows that the efficiency of the ASL can be useful as a general tool to determine the coupling strength in weakly coupled systems with fast dephasing.

Finally, we ask, Where does the energy for the anti-Stokes transport come from? Because dephasing causes the anti-Stokes transport, the answer would depend on the dominant scattering process that causes the dephasing. The energy cost of breaking the spatial coherence in our ADQW is of the order of ~ 0.01 meV (the energy separation between the NW HH and the WW exciton or the WW continuum, multiplied by the ASL efficiency) per exciton or electron-hole pair. This energy cost is relatively small compared with the excess energy of the electron-hole pair (as much as 50 meV) of the energy of acoustic phonons, even at low temperatures ($k_B T \sim 0.16$ meV at 2 K), so the energy comes from these heat baths. Furthermore, even at the excitation of a WW HH exciton, which corresponds to the lowest possible excess energy, there is an excess energy of the order of 0.1 meV, purely as a result of photon momentum at the plane of the quantum well.⁷ Thus it is quite likely that, even with excitation of WW HH at zero temperature limit, ASL would be observed, with the energy for the ASL coming essentially from the excess energy of excitons. Experimentally, even at low temperature and low excitation limits, dephasings (interband, intraband, and interwell) of excitons or free carriers in semiconductors owing to acoustic phonons, impurities, other excitons, or carriers are much faster than the radiative recombination

time.¹⁵⁻¹⁷ Therefore observation of ASL at low temperature and low intensity limits in ADQW should arise quite naturally.

To conclude this section, we have proposed a new mechanism, namely, intersite dephasing, as an efficient mechanism of anti-Stokes population transfer at low temperature and intensity limits. The resulting ASL can serve as a general tool to probe weak coupling strengths. We then showed that the main features of the intriguing phenomenon of ASL at low temperature and low density in GaAs ADQW's are entirely consistent with the proposed mechanism of anti-Stokes population transfer.

4. DYNAMICAL SIMULATION OF OPTICAL PHONON TRANSFER IN THE GaAs/Al_xGa_{1-x}As/GaAs SINGLE-BARRIER STRUCTURE

The approximations inherent in mean-field theories of alloys force the state to be infinitely extended in space. For this reason, although mean-field theories of semiconductor alloys and alloy superlattices may give an adequate description of many important quantities such as band gaps, dispersion curves, and density of states, the issue of spatial extent or coherence length is largely unclear. In this section we are concerned specifically with the dynamical transfer and spatial properties of optical phonons in GaAs/Al_xGa_{1-x}As superlattices as a function of x . This is an issue that has not been fully resolved and remains controversial.^{18,19} The problem of spatial properties of optical phonons in GaAs/AlAs is well known: because there is relatively large energy gap between the GaAs and AlAs optical branches, all the optical phonons are expected to be localized within each layer, supported by cw Raman experiments.²⁰ However, when the barrier consists of GaAs alloy, the existence of GaAs-like optical phonons in the alloy makes the energy barrier much smaller, making the transmission of GaAs phonons much easier. Recent picosecond Raman scattering experiments^{18,19} showed that the generation rate of hot Raman-active phonons for $x < \sim 0.3$ shows a saturating behavior, which was attributed to the saturation of transmission coefficient T at a substantial value. Because mean-field theories always produce extended wave functions, a different, more realistic, approach is needed.

To take the random fluctuations and the structural inhomogeneity fully into account, we need to consider a much greater number of atoms than in typical supercell methods. For this purpose we start with the classical time-dependent equation of motion and simulate the propagation of the vibration corresponding to GaAs optical phonons in the GaAs/Al_xGa_{1-x}As/GaAs single-barrier structure consisting of 16 monolayers of GaAs (GaAs I), Al_xGa_{1-x}As alloy of variable x and L_b (barrier thickness) and 16 monolayers of GaAs (GaAs II) in the [001] direction (Fig. 9). One monolayer contains typically 400–1600 atoms. In the alloy barrier region we first consider an atomic scale fluctuation of substitutional alloy by distributing Ga and Al atoms on cation sites at random with the probabilities $1-x$ and x , respectively. Next we investigate the effect of spatial correlation or clustering of alloy by introducing clusters in a cylindrical

shape (Fig. 10). The cation sites in each cylinder will all be occupied by either Ga or Al atoms with the probability $1-x$ or x . The spring constants are set to a constant value, and the difference in atomic species is considered through their mass difference. The initial optical phonon wave is assumed to be in the GaAs I region.

We calculated the energy transmission at the detection layer in the GaAs II region and then defined the transmission coefficient T by normalizing the transmitted energy to the value for $x = 0$. The transmission coefficient for an alloy barrier ($L_b \approx 5.6$ nm) T continues to decrease exponentially as a function of x until $x \sim 0.3$ and remains at a small value above $x \sim 0.3$. The exponential decay of the transmission coefficient for small x shows that the propagating-to-confined transition does not occur in a rigorous sense and indicates incoherent scattering from random scatterers. The small constant T values for larger x are attributed to the fluctuation by acoustic modes as well as by the overlap of localized modes.

Then the question arises of how such a saturating behavior of T would possibly be realized as observed in the generation rate of the Raman-active phonons for $x < \sim 0.3$. We suggest two plausible candidates for the cause of the saturation of the transmission coefficient, namely, the lifetime effect of optical phonons and the clustering effect of atoms. As in tunneling, the transmission coefficient should be multiplied by the number of round trips (i.e., the number of attempted tunnelings) that the optical phonon makes during its lifetime to yield the eventual tunneling coefficient. Because the lifetime of optical phonons in GaAs ranges from 7 to 20 ps, depending on experimental conditions and the assumption of homoge-

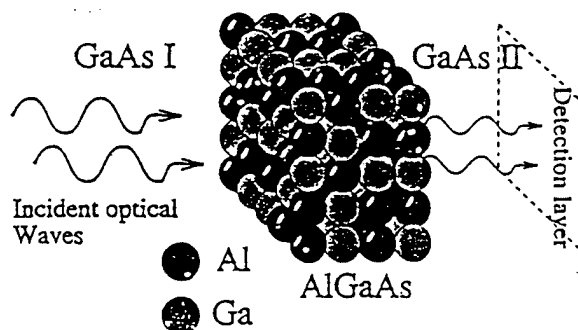


Fig. 9. Schematic of the single-barrier structure in the [001] direction. The darker circles in the barrier region represent Al atoms, and the lighter ones GaAs atoms, on the cation sublattice. We simplified the crystal structure for convenience and do not show atoms in the GaAs regions.

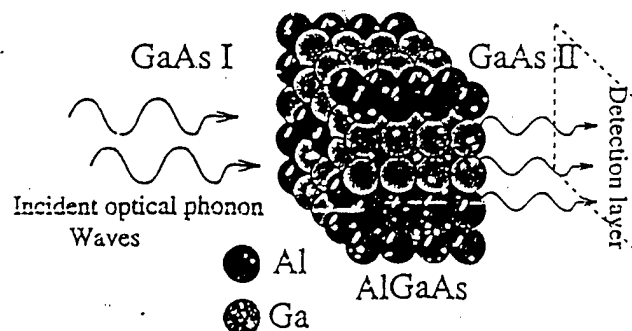


Fig. 10. Schematic of a partially ordered or clustered barrier.

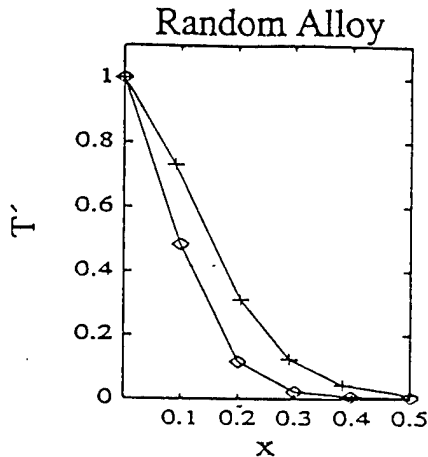


Fig. 11. Modified transmission coefficient T' as a function of x for barrier thicknesses of six (top curve) and ten (bottom curve) monolayers, including the effect of attempted tunneling three times over the phonon lifetime.

neous or inhomogeneous broadening,^{21,22} the total number of attempted tunnelings is one to three during the experimental lifetime in the present geometry.

Regarding the previously calculated T as the coefficient of the equation for the decay of the vibration energy, we obtained the modified transmission coefficient T' during the optical phonon lifetime for the alloy thickness of 6–10 monolayers and then normalized to the value for $x = 0$ as before. The result is plotted in Fig. 11 as a function of x . A noticeable saturation is observed for a thin alloy barrier. However, the transmission coefficient is still small in the case of a thick alloy barrier compared with that in the experiment.

To see the effect of partial order or clustering^{21,22} in the alloy as discussed in Section 2 on optical phonon propagation, we considered the model schematically described in Fig. 10. Results are presented in Fig. 12 for various cluster sizes with a total barrier thickness of 10 monolayers. The notation 111 represents no clustering, whereas 225 represents clustering of two monolayers in the plane of the layer and that of five monolayers in the growth direction. The transmission coefficient surely increases dramatically as the alloy is ordered, because GaAs optical phonons can propagate more easily through the cluster of GaAs than can the completely random alloy barrier. This is essentially the same physics as described in Section 2. The transmission coefficient for the largest cluster (555) is increased as much as several tens of times in comparison with the value for completely random alloy barrier at $x = 0.2$. Although such clustering or partial ordering of GaAs or AlAs in AlGaAs alloy is not yet accepted as a general phenomenon, it is clear that partial ordering or clustering would enhance the transmission of the optical phonon dramatically, even through a thick alloy barrier, in the same qualitative way as the transmission of electrons and holes described in Section 2. We now discuss nonequilibrium Raman scattering experiments on $\text{Al}_x\text{Ga}_{1-x}\text{As}$ alloys and $\text{GaAs}/\text{Al}_x\text{Ga}_{1-x}\text{As}$ quantum wells, in connection with our theoretical results.

It is well known now that a nonequilibrium hot-phonon population probed by Raman scattering can be, when properly analyzed, a sensitive probe of the spatial extent

of the Raman-active LO phonons.^{18,23} This is essentially because the hot-phonon distribution curve generated by the hot-electron relaxation is a strong function of the phonon wave vector and therefore of the spatial extent. Although the details are given elsewhere,²³ once the hot-phonon occupation number properly normalized to that of bulk GaAs under the same experimental conditions is known we can deduce the coherence length of the Raman-active GaAs or GaAs-like LO phonons in $\text{GaAs}/\text{Al}_x\text{Ga}_{1-x}\text{As}$ quantum wells or $\text{Al}_x\text{Ga}_{1-x}\text{As}$ alloy, using the hot-phonon distribution curve.

In Fig. 13(a) the hot-phonon occupation number of GaAs LO phonons for the $\text{GaAs}/\text{Al}_x\text{Ga}_{1-x}\text{As}$ multiple quantum wells observed by picosecond (1.5–70-ps) and cw Raman scattering is shown as a function of x . We took the data under the same irradiation density, using photon energies of 1.9–2.3 eV. We used a number of quantum-well samples (more than 30) with $L_x = 10$ nm and $L_y > 2$ nm, where the hot-phonon occupation number is largely independent of L_y but strongly dependent on x . Using these results, and assuming the phonon wave function $\psi = \exp(iq_0z)\exp(-z^2/\xi^2)$ (where q_0 is the Raman-active wave vector at the backscattering geometry), we deduced the coherence length $\sim \xi$ as a function of x , as shown in Fig. 13(b). In calculating the coherence length we assumed that LO phonons in bulk GaAs have an infinite coherence length and that the hot-electron relaxation that emits the hot phonon is bulklike because of the high excess energy of the electrons above the barrier. These assumptions can be relaxed somewhat without changing the overall results. The strong x dependence near $x = 0.3$ shown in Fig. 13(b) can be interpreted as the localized-to-extended or the confined-to-propagation transition. Because the increasing transmission rate would increase the coherence length, these results are in some qualitative agreement with theoretical results shown in Figs. 11 and 12. However, the experimentally deduced change in the coherence length as a function of x is more abrupt than in the theoretical results. One contributing factor to this discrepancy can be the assumption of bulklike hot-electron relaxation in a quantum well. This

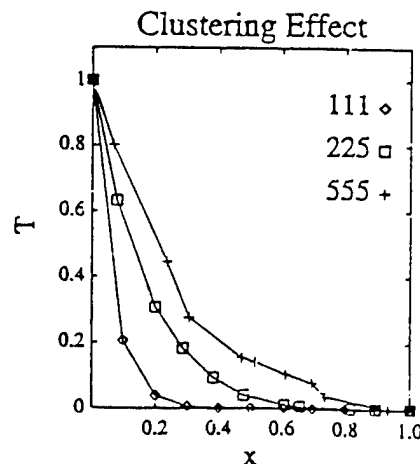


Fig. 12. Transmission coefficient (per single trial) for variable sizes of clusters in the barrier, from an atomically random alloy (111) to an ~ 1.8 -nm (555) cluster, for a barrier thickness of 10 monolayers.

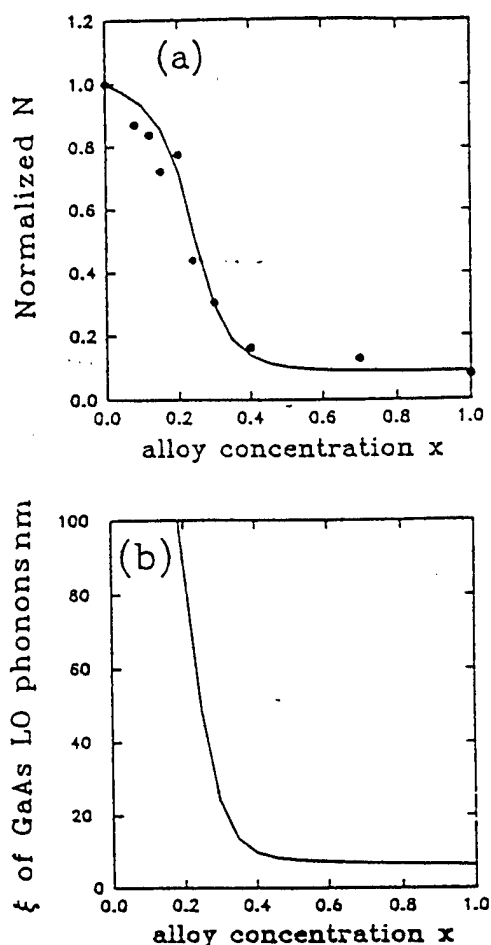


Fig. 13. (a) Normalized (to bulk GaAs under the same irradiation density) hot-phonon occupation number of GaAs LO phonons as a function of x . The curve is an analytical fit. (b) Coherence length as a function of x deduced from the method described in Ref. 19 obtained from the analytical fit of (a).

assumption can make the experimentally deduced coherence length change more abruptly than in more-realistic situations.

In this section we have shown that we have studied the spatial extent and dynamical transfer of optical phonons in GaAs/ $\text{Al}_x\text{Ga}_{1-x}\text{As}$ quantum wells, both theoretically and experimentally. It is clear that whether an optical phonon is spatially localized or extended should be answered carefully, depending on the alloy composition or the barrier width. Furthermore, we have shown theoretically that partial ordering of GaAs or AlAs in the alloy barrier can dramatically enhance the transmission of optical phonons through the barrier.

5. ANDERSON LOCALIZATION STUDY OF OPTICAL PHONONS IN $\text{Al}_x\text{Ga}_{1-x}\text{As}$

Ever since the famous paper by Anderson¹³ the localization transition in disordered systems has been an active area of research. A large amount of research exists for electronic systems, whereas there are relatively few results for phonon systems. For the electronic cases of the Anderson model, the randomness resides only in the on-site energies, and as a result only diagonal disorders exist. However, for a disordered phonon system it

was believed that the introduction of off-diagonal disorder is inevitable irrespective of whether the randomness resides in the masses or in the elastic interactions.^{24,25} Partly because of this incompatibility, the quantitative connection between a disordered phonon system and the Anderson model is at present not well established.

As a related problem, the optical phonon property in $\text{Al}_x\text{Ga}_{1-x}\text{As}$ alloys is an important issue for which some controversies exist. The asymmetric Raman profiles of the GaAs-like branch have been fitted on the assumption of finite (≤ 10 nm) coherence length or spatial extent,²⁶ whereas a recent paper reports that well-defined GaAs-like phonon dispersions exist for all values of x .²⁷ These two results are somewhat contradictory, because a well-defined dispersion relation itself may imply that the spatial correlation function of the phonon is infinite in extent. Needless to say, the word dispersive should be used with caution, because the inherent uncertainty in k (Δk) owing to alloy fluctuation results in line broadening and limits the spatial extent to $\sim 1/\Delta k$. In this sense the implication of the experimental results in support of Baroni *et al.*²⁷ (i.e., the existence of well-defined dispersion) is that the spatial extent is much larger than the lattice constant for $x \leq 0.3$. For larger x the width of the GaAs-like optical branch becomes smaller, whereas the linewidth as well as the asymmetry of the Raman-active optical phonons becomes larger. Therefore the concept of a dispersion relation with well-defined k may not be a useful one in this regime. In contrast, the method of Parayanthal and Pollak²⁶ is limited to only large x (in the case of the GaAs-like mode) for which substantial asymmetries in the line shape exist. Of course any direct use of mean-field methods, e.g., the coherent potential approximation (CPA) and the average T -matrix method, is nonsensical as far as the localization properties are concerned because the approximations inherent in them always imply that we are dealing with extended states.²⁴ We need a more fundamental approach to study the localization property of this alloy system.

In this section we first show that the localization properties of a disordered phonon model can be exactly mapped to those of a generalized Anderson model. A simple model for phonon properties of a ternary alloy system is constructed. It is an isotopically disordered one, i.e., the spring constants are a constant but the masses of one sublattice are random variables. By an appropriate identification of corresponding parameters, our phonon model is exactly mapped to the Anderson model generalized to a diatomic basis lattice. This enables us to study the localization property of the isotopically disordered phonon system by the same method as used for the Anderson model; in the present calculation we use the method introduced by Licciardello and Economou.²⁸ At the expense of some rigor, their method is known to yield qualitatively, and to some extent quantitatively, correct results for localization problems in three-dimensional electronic system without much computational effort.

Our model allows us to study the localization property of phonons in any zinc-blende ternary alloy system. We applied our method to the $\text{Al}_x\text{Ga}_{1-x}\text{As}$ alloys, and the results obtained with our model calculation present a general localization picture that reconciles the two above mentioned seemingly contradictory results. It is shown

that, above $x_c \approx 0.45$, all GaAs-like optical phonon states are localized, which is in agreement with the assumption of Parayanthal and Pollak.²⁶ For $x < x_c$ most states are extended, except for some near the edges of the GaAs-like branch, in which case a dispersion relation may still be a useful description of the eigenstates. Thus in our picture the two seemingly conflicting results mentioned above are reconciled as two limiting cases whose validity depends on whether $x < x_c$ or $x > x_c$.

We consider an alloy of the chemical formula $A_{1-x}B_xC$ on the zinc-blende structure. A cation site of the lattice is randomly occupied by an A or a B atom with probability $(1-x)$ or x , respectively. For simplicity, it is assumed that a displacement from its equilibrium position can be represented by a scalar quantity and that the elastic interactions are restricted only to those with nearest-neighbor sites. No important qualitative features of the system are thereby lost, and extension of our model to the general cases is straightforward. The equations of motion for this system are written as follows:

$$\begin{aligned} M_i \frac{d^2 U_i}{dt^2} &= K \sum_j^i (u_j - U_i), \\ m_i \frac{d^2 u_i}{dt^2} &= K \sum_j^i (U_j - u_i), \end{aligned} \quad (5.1)$$

where M_i (m_i) and U_i (u_i) are the mass and the atomic displacement from the equilibrium position of the atom at the i th cation (anion) site, respectively. The superscript i on the summation denotes that the summation is over only the nearest-neighbor sites of site i . There is no mass randomness on the anion sites, so we can remove the site label from m_i and set them all equal to M_C . A widely used way of treating Eq. (5.1) is as follows. The relations $U_i = \tilde{U}_i \exp(-i\omega t)$ and $u_i = \tilde{u}_i \exp(-i\omega t)$ are inserted into Eq. (5.1), and each equation is divided by the mass. When ω^2 and zK/M_i are identified by E and ϵ_i , respectively, the equations are of the same form as the eigenvalue equations of a tight-binding model for an electronic system. However, this transform has the unfortunate effect that off-diagonal disorder as well as the diagonal disorder in the tight-binding Hamiltonian is generated. We take a different approach; each equation is divided by ω^2 instead of by the mass. Then we get a set of equations as follows:

$$\begin{aligned} (\epsilon_i - E)\tilde{U}_i + V \sum_j^i \tilde{u}_j &= 0, \\ (\epsilon - E)\tilde{u}_i + V \sum_j^i \tilde{U}_j &= 0, \end{aligned} \quad (5.2)$$

where $z = 4$ is the coordination number of diamond lattices and a transformation of parameters $M_i \rightarrow \epsilon_i$, $M_C \rightarrow \epsilon$, $zK/\omega^2 \rightarrow E$, and $K/\omega^2 \rightarrow V$ has been performed. Equations (5.2) have exactly the same form as Anderson model for the electronic problem generalized to the diatomic basis lattice. No off-diagonal disorder is generated by the transform, and the localization of the vibrational state can be determined by the corresponding electronic state of the diatomic Anderson model, in which the on-site energies of one sublattice are randomly distributed according to a binary distribution of the mass of

atom A (M_A) and the mass of atom B (M_B) and those of the other sublattice are a constant (M_C). However, it should be noted that, because the hopping energy V is dependent on E , for two distinct values of E two corresponding Anderson Hamiltonians have hopping energies different from each other.

For a localization property we adopt the criterion introduced by Licciardello and Economou,²⁸ which is based on the fact that the single-particle Green's function shows different analytical behavior depending on whether the eigenstate of energy E is an extended state or a localized one; the imaginary part of the self-energy goes to zero for a localized state, whereas it remains nonzero for the extended state when E approaches the real axis in the complex E plane.²⁹ From a random perturbation series for the self-energy, they obtained the localization function $L(E)$, the numerical value of which determines the nature of the eigenstate of energy E ; for $L(E) \geq 1$ (< 1) the state is an extended (a localized) one.²⁸ A generalization of their result, which is for a monatomic system, to our diatomic one gives the localization function as follows:

$$L(E) = \lim_{M \rightarrow \infty} \left[V^{M+1} \sum (\bar{G}_a)_1^0 (\bar{G}_c)_2^{0,1} \dots (\bar{G}_a)_M^{0,1 \dots M-1} \right]^{1/M}. \quad (5.3)$$

The summation is over all indices $1, 2, \dots, M$, with the restrictions corresponding to all self-avoiding paths of order M starting and ending at the site 0. The quantity $(\bar{G}_{a(c)})_i^{0,1 \dots i-1}$ is defined by

$$\ln(\bar{G}_{a(c)})_i^{0,1 \dots i-1} = \langle \ln |(\bar{G}_{a(c)})_i^{0,1 \dots i-1}| \rangle. \quad (5.4)$$

$(\bar{G}_{a(c)})_i^{0,1 \dots i-1}$ is the diagonal element of the Green's function at site i , which is an anion (a cation) site, for Eqs. (5.2), where the on-site energies of the sites 0, 1, ..., $i-1$ have been set to infinity. The $L(E)$ given by Eq. (5.3) is complicated for practical calculations. In contrast, an estimate $L^*(E)$ is found by the following approximations²⁸:

$$\begin{aligned} L(E) &\approx VK |(\bar{G}_a)_1^0 (\bar{G}_c)_2^{1,2}|^{1/2} \\ &\approx VK |(\bar{G}_a)_1^0 (\bar{G}_a)_2^{1,2}|^{1/2} \equiv L^*(E), \end{aligned} \quad (5.5)$$

where K is the connectivity,²⁹ which is evaluated to be ≈ 2.88 for the diamond lattice. The second approximation, Eq. (5.5), is replacing the Green's functions defined in Eq. (5.4) with those obtained by CPA.²⁸ Note that using the CPA at this step is to estimate the Green's function on which $L(E)$ depends and not to investigate the analytical property of the single-particle Green's function obtained by the CPA.

We need two independent fitting parameters to correct the behaviors of $L^*(\omega)$ at the edges of the branches. For ordered cases, i.e., $x = 0$ or $x = 1$, $L(\omega)$ is equal to 1 at the edges and is larger than (smaller than) 1 inside (outside) the branches. Therefore we multiply a weighting function $w(\omega, x)$ to $L^*(\omega)$. We use, as a weighting function,

$$w(\omega, x) = \left(A \exp \left\{ -\frac{[\omega^2 - z(K/M_C + \eta)/2]^2}{\Delta^2} \right\} + 1 \right)^{-1}, \quad (5.6)$$

where A and Δ are numerical fitting parameters and $\eta = (1 - x)(K/M_A) + x(K/M_B)$.

The results of calculations for $K/M_B = 2.41$ and

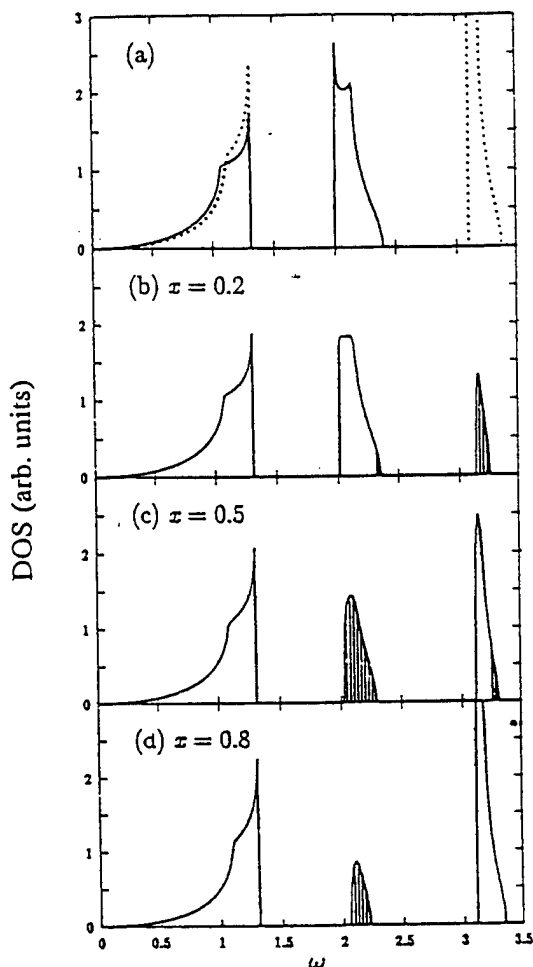


Fig. 14. Phonon density of states (DOS) and localization property with parameters chosen to represent acoustic, GaAs-like and AlAs-like optical branches of $\text{Al}_x\text{Ga}_{1-x}\text{As}$ branches: (a) $x = 0$ (solid curve, pure GaAs) and $x = 1$ (dotted curve, pure AlAs); (b) $x = 0.2$; (c) $x = 0.5$; (d) $x = 0.8$. The hatched areas represent localized eigenstates, and the white areas the extended eigenstates.

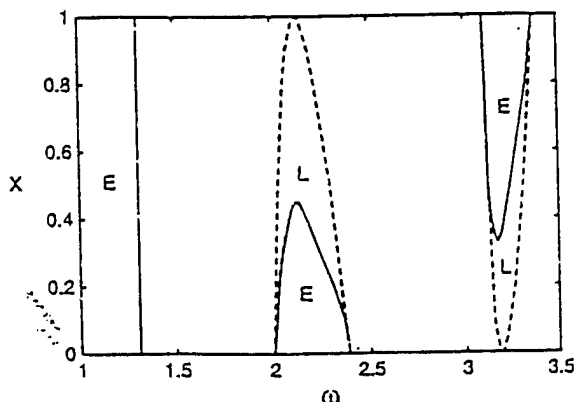


Fig. 15. Phase diagram shown in the ω - x plane. L, region of localized states; E, region of extended eigenstates. The solid curves form the boundaries between these two regimes. The dashed curves represent the trajectories of phonon branches within the coherent potential approximation. For the acoustic branches the dashed curves and the solid curves nearly coincide.

$K/M_C = 0.43$ with K/M_A normalized to 1 are shown in Fig. 14; we have used these numerical values to match the reported experimental data of two optical phonon spectral ranges of GaAs and AlAs.^{30,31} Below, numerical values of ω normalized by $\sqrt{K/M_A}$ are used. For ordered cases, as shown in Fig. 14(a), the density of states (DOS) diverges at the upper edge of the acoustic branch and at the lower edge of the optical branch, which is not typical behavior for a three-dimensional system. This pathological feature is the same as found in fcc lattice when the interactions are restricted only to those with nearest-neighbor sites.³² These singularities induce sharp peaks (widths of which are $\leq 0.02 \approx \delta$) of $L^*(\omega)$ at the edges, which we have neglected by interpolating the values of $L^*(\omega \pm 3\delta)$. In Figs. 14(b)–14(d) the DOS calculated within the CPA as well as the localization properties determined by the numerical value of $w(\omega, x)L^*(\omega)$ is depicted for $x = 0.2, 0.5, 0.8$. The hatched areas represent the regions of localized eigenstates, and the white areas the regions of extended eigenstates. We interpret the states in the frequency range 2.0–2.39 (238–285) cm^{-1} as the GaAs-like optical phonon branch and the ones between 3.1 and 3.37 (370 and 404) cm^{-1} as the AlAs-like optical phonon branch. As x increases, the states of the GaAs-like optical branch localize, because the Al atoms are barriers for these excitations, whereas those of the AlAs-like optical branch localize as $(1 - x)$ increases. A convenient way to see the localization property is furnished by Fig. 15. Restricted to the GaAs-like branch, all phonon excitations localize beyond $x_c \approx 0.45$; as x increases, localization proceeds from the edges, and the boundaries between the extended states and the localized states move inward until they coalesce at x_c .

Variation of x_c over some ranges of the parameters K/M_B and K/M_C is shown in Fig. 16. Within such a range of input parameters, qualitative behaviors of optical phonon branches are not different from those of Figs. 14 and 15, although the numerical value of x_c varies. x_c is a monotonically decreasing (increasing) function of K/M_B (K/M_C). One can explain such behavior intuitively when the variation of gap size between two optical phonon branches of the pure materials is considered; the gap size is given as $(xK/M_B)^{1/2} - [x(1 + K/M_C)]^{1/2}$, which is monotonically increasing (decreasing) with respect to K/M_B (K/M_C). As the gap size increases, the probability that a GaAs-like optical phonon excitation can penetrate the site occupied by an Al ion gets smaller because there is a larger difference between the natural vibrational frequencies of two species. Therefore GaAs-like optical phonon excitation localizes more easily, i.e., yields smaller x_c , at a larger gap size. Of course a behavior such that all phonons of a branch localize as the fraction of corresponding material decreases is a somewhat unique one specific for an optical branch. For the acoustic branch the excitation at sufficiently small ω is always extended because the excitation at $\omega \rightarrow 0$ represents the pure translation of the whole system.

Therefore there is some nontrivial x_c such that, when $x > x_c$, all GaAs-like optical phonons are localized, justifying the method of Parayanthal and Pollak²³ to fit the asymmetric line shape of Raman-active phonons. In contrast, when $x < x_c$, a finite fraction of GaAs-like optical phonons is extended, whereas the states near the

edges of the branch are localized. In the latter case a dispersion relation of form $\omega = \omega(k)$ may be a useful description of the eigenstates. However, the phrase dispersion relation here should be interpreted in a rather different sense from that in an ordered system. When x is different from 0 or 1 there is no true translation symmetric in the alloy. There k is not a good quantum number, and the Fourier transform of an eigenfunction cannot have a perfectly sharp spectrum in reciprocal space. In a disordered system the relation $\omega = \omega(k)$ should be interpreted as follows. An eigenstate of energy ω is a superposition of many different Bloch states whose distribution $P_\omega(k)$ is centered at k but that have some finite linewidth caused by incoherent scattering from the disordered assembly of sites. This linewidth is given as $\sim 1/\xi$ when the eigenstate is localized within an spatial extent ξ . Therefore, in a disordered system, existence of a dispersion relation does not necessarily imply that all eigenstates are extended. One can safely use the terminology of a dispersion relation in a qualitatively same sense as in an ordered system only when a significant fraction of eigenstates of a given branch is extended. We now discuss nonequilibrium Raman scattering experiments and the coherence length of LO phonons in $\text{Al}_x\text{Ga}_{1-x}\text{As}$ alloy.

In Fig. 17(a) the properly normalized (to bulk GaAs) nonequilibrium hot-phonon population of GaAs-like LO phonons for $\text{Al}_x\text{Ga}_{1-x}\text{As}$ alloy observed by picosecond (1.5–70 ps) and cw Raman scattering is shown as a function of x . The occupation numbers were normalized so that the effects of changing band gap, penetration depths, and number of modes with x were taken into account. We took the data under the same irradiation density, using photon energies of 1.9–2.3 eV. The decrease in the hot-phonon occupation number as a function of x can be interpreted as the decrease in the coherence length. Using these results, and assuming that the Raman-active

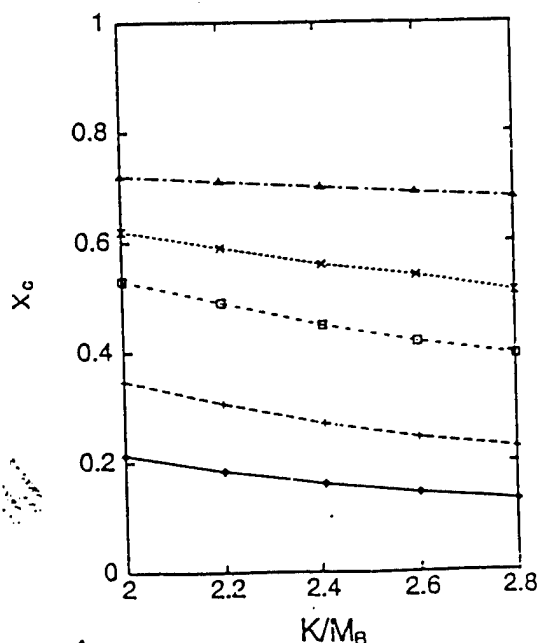


Fig. 16. Variation of x_c as a function of K/M_B and K/M_C . K/M_C is, from top to bottom, 0.6, 0.5, 0.43, 0.3, and 0.2.

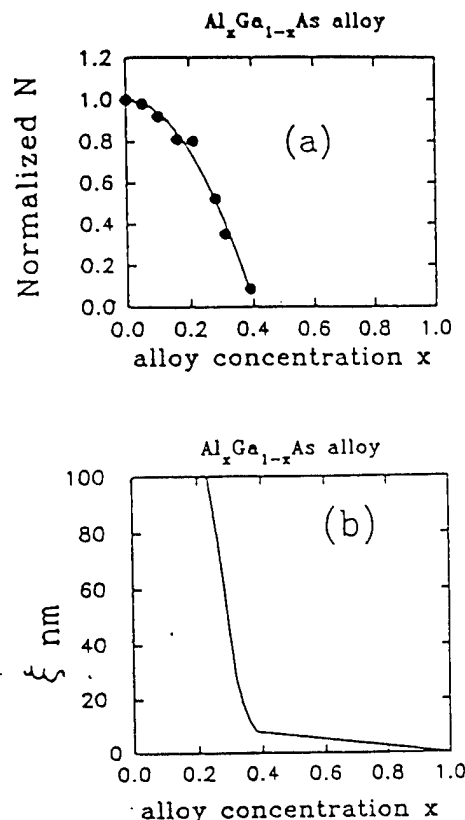


Fig. 17. (a) Normalized (to bulk GaAs under the same irradiation density) hot-phonon occupation number of GaAs-like LO phonons as a function of x . The curve is an analytical fit, and the dependencies of band gap, density of states of GaAs-like LO phonons, and penetration depth were properly corrected. (b) Coherence length as a function of x deduced from the method described in Ref. 22 obtained from the analytical fit of (a).

phonon wave function is $\psi = \exp(iq_0z)\exp(-z^2/\xi^2)$ in the same way as in Section 4, we deduced the coherence length $\sim \xi$ as a function of x , as shown in Fig. 17(b). In calculating the coherence length it was assumed that LO phonons in bulk GaAs have an infinite coherence length. The strong x dependence near $x = 0.3$ shown in Fig. 17(b) is consistent with that in Fig. 16. It is also entirely consistent with the theoretical results presented in Figs. 14 and 15.

In conclusion, we have found that the question of whether GaAs-like optical phonons are spatially extended or localized should be answered depending on x . This conclusion was drawn from the Anderson localization study of optical phonons in $\text{Al}_x\text{Ga}_{1-x}\text{As}$ and from nonequilibrium Raman scattering experiments.

6. SUMMARY

We have solved the puzzles of anomalously large Stokes and anti-Stokes real space-charge transfer in GaAs/ $\text{Al}_x\text{Ga}_{1-x}\text{As}$ ADQWs by going beyond the mean-field approach and by realizing the importance of quantum coupling and dephasing in coupled systems. Thick alloy barriers permit fairly strong coupling between adjacent GaAs layers, with the coupling strength strongly dependent on x and on the degree of inhomogeneity of the barrier. Once we realize that coupling exists, the emission of blue-shifted anti-Stokes luminescence from the

NW when the WW is excited is understood as a natural consequence of dephasing in coupled systems.

In the problem of spatial and dynamical properties of GaAs optical phonons in GaAs/Al_xGa_{1-x}As superlattices we developed a realistic, first-principle dynamical simulation model of GaAs optical phonon transport through an Al_xGa_{1-x}As barrier. The results show strong x dependence of the transmission coefficient and are in qualitative agreement with nonequilibrium Raman scattering investigations. We developed an Anderson localization model of phonon properties in Al_xGa_{1-x}As. We showed that the localization properties strongly depend on x , thus reconciling an ongoing controversy regarding the nature of optical phonons in Al_xGa_{1-x}As. These results are also in good agreement with nonequilibrium Raman investigations.

In both electronic and phonon coupling of two adjacent GaAs layers across the Al_xGa_{1-x}As barrier there is a nontrivial x dependence whose importance is not well appreciated in the mean-field approach. Furthermore, partial ordering in the barrier is shown always to increase the coupling between electrons or phonons across the barrier relative to that when the arrangement of Ga and Al atoms is completely random.

ACKNOWLEDGMENTS

We acknowledge helpful discussions with T. W. Noh, D. Kim, P. Y. Yu, J. Shah, and T. C. Damen. We thank J. M. Kuo for providing one of the samples used in this investigation. This research was partially supported by Korean Science and Engineering Foundation (951-0205-023-2), Ilju Foundation, and Ministry of Education (BSRI 94-2421 and 95-E-4009).

REFERENCES

1. L. Esaki and R. Tsu, "Superlattice and negative differential conductivity in semiconductors," *IBM J. Res. Dev.* **14**, 61 (1970).
2. A. Tomita, J. Shah, D. S. Kim, T. C. Damen, J. M. Kuo, S. Schmitt-Rink, P. Thomas, and R. S. Knox, "Energy transfer between quantum wells by dipole-dipole interaction?" in *Diffraction Optics: Design, Fabrication and Applications*, Vol. 9 of OSA Technical Digest Series (Optical Society of America, Washington, D.C., 1992), p. 116.
3. M. Batsch, T. Meier, P. Thomas, M. Lindberg, S. W. Koch, and J. Shah, "Dipole-dipole coupling of excitons in double quantum wells," *Phys. Rev. B* **48**, 11817 (1993).
4. N. B. An and G. Mahler, "Polaritons in semiconductor multiple quantum well structures with Förster-type interwell coupling," *Phys. Rev. B* **50**, 17256 (1994).
5. D. S. Citrin, "Coherent vertical transport of excitons in multiple quantum wells," *Phys. Rev. B* **51**, 14361 (1995).
6. S. Haacke, N. T. Pilekanos, M. Mariette, M. Zigone, A. P. Heberle, and W. W. Rühle, "Tunneling dynamics in CdTe/(Cd,Zn)Te asymmetric double quantum well structures," *Phys. Rev. B* **47**, 16643 (1993).
7. A. Vinattieri, J. Shah, T. C. Damen, D. S. Kim, L. N. Pfeiffer, M. Z. Maialle, and L. J. Sham, "Exciton dynamics in GaAs quantum wells under resonant excitation," *Phys. Rev. B* **50**, 10868 (1994).
8. J. Feldmann, R. Sattmann, E. O. Göbel, J. Kuhl, J. Hebling, K. Ploog, R. Murahdharan, P. Dawson, and C. T. Fox, "Sub-picosecond real space charge transfer in type II GaAs/AlAs superlattices," *Phys. Rev. Lett.* **62**, 1392 (1989).
9. J. Ihm, "Effects of the layer thickness on the electronic character in GaAs-AlAs superlattices," *Appl. Phys. Lett.* **50**, 1068 (1987).
10. B. Koiller and R. B. Capaz, "Indirect-to-direct crossover in semiconductor alloys: a first order transition?" *Phys. Rev. Lett.* **74**, 769 (1995).
11. A. R. Smith, K. J. Chao, C. K. Shih, Y. C. Shih, and B. G. Streetman, "Cross sectional scanning tunneling microscopy study of GaAs/AlAs short period superlattices: the influence of growth interrupt on the interfacial structure," *Appl. Phys. Lett.* **66**, 478 (1995); M. B. Johnson, U. Maier, H. P. Meier, and H. W. M. Salemink, "Atomic scale view of AlGaAs/GaAs heterostructures with cross sectional scanning tunneling microscopy," *Appl. Phys. Lett.* **63**, 1273 (1993).
12. K. A. Mäder and A. Zunger, "Short and long range order effects on the electronic properties of III-V semiconductor alloys," *Phys. Rev. B* **51**, 10462 (1995).
13. P. W. Anderson, "Absence of diffusion in certain random lattices," *Phys. Rev.* **109**, 1492 (1958).
14. R. Hellmann, A. Euteneuer, S. G. Hense, J. Feldmann, P. Thomas, E. O. Göbel, D. R. Yakovlev, A. Waag, and G. Landwehr, "Low temperature anti-Stokes luminescence mediated by disorder in semiconductor quantum well structures," *Phys. Rev. B* **51**, 18053 (1995).
15. P. Leishang, T. Dekorsy, H. Bakker, H. Kurz, and K. Köhler, "Exceptionally slow dephasing in electronic continuum states in a semiconductor," *Phys. Rev. B* **51**, 18105 (1995).
16. L. Schultheis, J. Kuhl, A. Honold, and C. W. Tu, "Ultrafast phase relaxation of excitons via exciton-exciton collision and exciton-electron collision," *Phys. Rev. Lett.* **57**, 1635 (1986).
17. D. Some and A. V. Nurmikko, "Coherent transient cyclotron emission from photoexcited GaAs," *Phys. Rev. B* **50**, 5783 (1994).
18. D. S. Kim, A. Bouchalkha, J. M. Jacob, J. F. Zhou, J. J. Song, and J. F. Klem, "Confined-to-propagating transition of LO phonons in GaAs/Al_xGa_{1-x}As superlattices observed by picosecond Raman scattering," *Phys. Rev. Lett.* **68**, 1002 (1992); "Reply to comment on 'Confined-to-propagating transition of LO phonons in GaAs/Al_xGa_{1-x}As superlattices observed by picosecond Raman scattering,'" *Phys. Rev. Lett.* **72**, 1572 (1994).
19. G. S. Spencer and J. Menéndez, "Comment on 'Confined-to-propagating transition of LO phonons in GaAs/Al_xGa_{1-x}As superlattices observed by picosecond Raman scattering,'" *Phys. Rev. Lett.* **72**, 1571 (1994).
20. B. Jusserand and M. Cardona, in *Light Scattering in Solids V*, M. Cardona and G. Güntherodt, eds., Vol. 66 of Topics in Applied Physics (Springer-Verlag, Berlin, 1989), p. 40, and references therein.
21. F. Vallee and F. Bogani, "Coherent time-resolved investigation of LO phonon dynamics in GaAs," *Phys. Rev. B* **43**, 12049 (1991).
22. K. T. Tsen and H. Morkoç, "Population relaxation time of nonequilibrium LO phonons and electron-phonon interactions in GaAs-AlGaAs multiple quantum well structure," *Phys. Rev. B* **34**, 4412 (1986).
23. D. S. Kim, A. Bouchalkha, J. M. Jacob, J. J. Song, J. F. Klem, H. Hou, C. W. Tu, and H. Morkoç, "Hot phonon generation in GaAs/Al_xGa_{1-x}As superlattices: observations and implications on the coherence length of LO phonons," *Phys. Rev. B* **51**, 5449 (1995); J. M. Jacob, D. S. Kim, A. Bouchalkha, J. J. Song, J. F. Klem, H. Hou, C. W. Tu, and H. Morkoç, "Spatial characteristics of GaAs, GaAs-like, and AlAs-like LO phonons in GaAs/Al_xGa_{1-x}As superlattices: the strong x dependence," *Solid State Commun.* **91**, 721 (1994).
24. J. M. Ziman, *Models of Disorder* (Cambridge U. Press, Cambridge, 1979), p. 290.
25. H. A. Fertig and T. L. Reinecke, "Localization and diffusion of energy via confined phonon modes in semiconductor superlattices," *Phys. Rev. B* **50**, 7443 (1994).
26. P. Parayanthal and F. H. Pollak, "Raman scattering in alloy semiconductors: spatial correlation model," *Phys. Rev. Lett.* **52**, 1822 (1984).
27. S. Baroni, S. Gironcoli, and P. Giannozzi, "Phonon dispersions in Ga_{1-x}Al_xAs alloys," *Phys. Rev. Lett.* **65**, 84 (1990).
28. D. C. Licciardello and E. N. Economou, "Study of localization in Anderson's model for random lattices," *Phys. Rev. B* **11**, 3697 (1975).

29. C. Domb, "Self-avoiding walks and the Ising and Heisenberg models," J. Phys. C 3, 256 (1970).
30. J. L. T. Waugh and G. Dolling, "Crystal dynamics of gallium arsenide," Phys. Rev. 132, 2410 (1963).
31. H. M. Kagaya and T. Soma, "Interatomic force constants and lattice vibrations of AlP, AlAs and AlSb," Solid State Commun. 48, 785 (1983).
32. T. Morita and T. Horiguchi, "Lattice Green's functions for the cubic lattices in terms of the complete elliptic integral," J. Math. Phys. 12, 981 (1971).

Reprinted from

PHYSICA B

CONDENSED MATTER

Physica B 219 & 220 (1996) 684-686

Spatial and dynamical properties of optical phonons in $\text{Al}_x\text{Ga}_{1-x}\text{As}$ and $\text{GaAs}/\text{Al}_x\text{Ga}_{1-x}\text{As}$ superlattices: Beyond the mean field approach

D.S. Kim^{a,*}, P.H. Song^a, S.H. Jhi^a, Y.S. Lim^a, E.J. Shin^c, Y.H. Yee^a, J.S. Khim^a, J. Ihm^a,
J.H. Lee^a, J.S. Chang^a, D.H. Woo^b, K.N. Kang^b, D. Kim^c, J.J. Song^d

^a Department of Physics, Seoul National University, Seoul 151, South Korea

^b Korea Institute of Science and Technology, Cheongryang, Seoul 136-791, South Korea

^c Optics Laboratory, Korea Research Institute of Standards and Science, Taejeon 305-606, South Korea

^d Center for Laser Research and Department of Physics, Oklahoma State University, Stillwater, OK 74078, USA



ELSEVIER

PHYSICA B

An interdisciplinary journal of research on condensed matter

Editors:

F.R. de Boer, Van der Waals-Zeeman Laboratory, Valckenerstraat 65, 1018 XE Amsterdam, The Netherlands
Telefax: +31-20-699 4800

Z. Fisk, National Magnetic Field Laboratory, 1800 E. Paul Dirac Street, Tallahassee, FL 32306-4005, USA
Telefax: +1-505-665 2992

R. Jochemsen, Kamerlingh Onnes Laboratorium, Rijksuniversiteit Leiden, P.O. Box 9506, 2300 RA Leiden, The Netherlands
Telefax: +31-71-275 404

G.H. Lander, European Institute for Transuranium Elements, P.O. Box 2340, D-76125 Karlsruhe, Germany
Telefax: +49-7247-951 599

Advisory editorial board:

A.O.E. Animalu, Lagos

R. Blinc, Ljubljana

D.F. Brewer, Brighton

R. de Bruyn Ouboter, Leiden

J. Flouquet, Grenoble

A.J. Freeman, Evanston, IL

H. Fujii, Hiroshima

P. Fulde, Stuttgart

C. Haas, Groningen

W. van Haeringen, Eindhoven

A. Janner, Nijmegen

C. Janot, Grenoble

G. Kido, Sendai

M. Krusius, Helsinki

J.J. van Loet, Delft

W. van der Lugt, Groningen

T.V. Ramakrishnan, Bangalore

S.A. Rice, Chicago

T. Satoh, Sendai

V. Sechovsky, Prague

G. Solt, Neuchâtel

F. Steglich, Darmstadt

W.G. Stirling, Keele

M.A. Strzhemechny, Kharkov

G. van Tendeloo, Antwerp

M. Tosi, Pisa

R. Tournier, Grenoble

P. Wachter, Zürich

P.R. Wyder, Grenoble

Aims and scope

Physica B (Condensed Matter) contains papers and review articles in the realm of physics of condensed matter. Both experimental and theoretical contributions are invited, although theoretical papers should preferably be related to experimental results.

Abstracted/indexed in:

Current Contents: Physical, Chemical and Earth Sciences
Aluminium Industry Abstracts, *EI Compendex Plus*,
Engineered Materials Abstracts, *Engineering Index*, *INSPEC*,
Metals Abstracts, *Physics Briefs*

Subscription information

Physica B (ISSN 0921-4526) is published semimonthly except monthly in July, August, September, November, December. For 1996, volumes 215-228 are scheduled for publication. Subscription prices are available upon request from the Publisher. A combined subscription with *Physica A*, *Physica C* and *Physica D* is available at a reduced rate.

US Mailing Notice

Physica B (ISSN 0921-4526) is published semimonthly except monthly in July, August, September, November, December (19 issues) by Elsevier Science, Molenwerf 1, P.O. Box 211, 1000 AE Amsterdam, The Netherlands. The annual subscription price in the USA is US\$ 3686 (valid in North, Central and South America only), including air speed delivery. Second class postage paid at Jamaica, NY 11431.

USA postmasters: Send address changes to *Physica B*, Publications Expediting Inc., 200 Meacham Avenue, Elmont, NY 11003. Airfreight and mailing in the USA by Publications Expediting Inc., 200 Meacham Avenue, Elmont, NY 11003.

Subscriptions are accepted on a prepaid basis only and are entered on a calendar year basis. Issues are sent by surface mail except to the following countries where air delivery via SAL is ensured: Argentina, Australia, Brazil, Canada, China, Hong Kong, India, Israel, Japan, Malaysia, Mexico, New Zealand, Pakistan, Singapore, South Africa, South Korea, Taiwan, Thailand, USA. For all other countries air mail rates are available upon request. Please address all enquiries regarding orders and subscriptions to:

Elsevier Science B.V.
Order Fulfilment Department
P.O. Box 211, 1000 AE Amsterdam
The Netherlands
Telephone: +31-20-485 3642; Telefax: +31-20-485 3598

Claims for issues not received should be made within six months of our publication (mailing) date.

Ⓢ The paper used in this publication meets the requirements of ANSI NISO Z39.48-1992 (Permanence of Paper).



North-Holland

Printed by Elsevier Science

Printed in The Netherlands

Spatial and dynamical properties of optical phonons in $\text{Al}_x\text{Ga}_{1-x}\text{As}$ and $\text{GaAs}/\text{Al}_x\text{Ga}_{1-x}\text{As}$ superlattices: Beyond the mean field approach

D.S. Kim^{a,*}, P.H. Song^a, S.H. Jhi^a, Y.S. Lim^a, E.J. Shin^c, Y.H. Yee^a, J.S. Khim^a, J. Ihm^a, J.H. Lee^a, J.S. Chang^a, D.H. Woo^b, K.N. Kang^b, D. Kim^c, J.J. Song^d

^a Department of Physics, Seoul National University, Seoul 151, South Korea

^b Korea Institute of Science and Technology, Cheongryang, Seoul 136-791, South Korea

^c Optics Laboratory, Korea Research Institute of Standards and Science, Taejeon 305-606, South Korea

^d Center for Laser Research and Department of Physics, Oklahoma State University, Stillwater, OK 74078, USA

Abstract

Spatial and dynamical properties of optical phonons in $\text{Al}_x\text{Ga}_{1-x}\text{As}$ alloys and $\text{GaAs}/\text{Al}_x\text{Ga}_{1-x}\text{As}$ quantum wells are studied. An isotopically disordered harmonic crystal model is developed to study spatial properties of optical phonons in $\text{Al}_x\text{Ga}_{1-x}\text{As}$ alloys. In the $\text{GaAs}/\text{Al}_x\text{Ga}_{1-x}\text{As}$ system, transmission of the GaAs optical phonons through an $\text{Al}_x\text{Ga}_{1-x}\text{As}$ barrier is studied using three-dimensional lattice dynamical model, fully accounting for the random arrangement of Ga and Al atoms in the alloy barrier. In the $\text{Al}_x\text{Ga}_{1-x}\text{As}$ alloy, a localized-to-extended transition is found as a function of x . In $\text{GaAs}/\text{Al}_x\text{Ga}_{1-x}\text{As}$ quantum wells, the transmission coefficient of the GaAs LO phonons through the alloy barrier remains significant below $x < 0.3$. These results are in good qualitative agreement with the experimentally deduced coherence length of LO phonons from nonequilibrium hot phonon populations.

The approximations inherent to mean field theories of alloys always force the state to be infinitely extended in space. For this reason, although mean field theories of semiconductor alloys and alloy superlattices may give adequate description of many important quantities such as band gaps, dispersion curves, and density of states, the issue of spatial extent or coherence length is largely shadowed. In this paper, we are specifically concerned with the spatial extent and dynamical transfer of optical phonons in $\text{Al}_x\text{Ga}_{1-x}\text{As}$ alloys and $\text{GaAs}/\text{Al}_x\text{Ga}_{1-x}\text{As}$ superlattices as a function of x .

For optical phonon properties of $\text{Al}_x\text{Ga}_{1-x}\text{As}$, we constructed a lattice dynamical model using the zinc-blende structure where the cations masses are random variables, taking the values of either M_1 or M_2 ($M_1 < M_2$) simulating the masses of Al and Ga . With the spring constants between atoms assumed to be constant, the masses of cations and anions are adjusted to reproduce the well-known density of states of the optical branches, as shown in Fig. 1(a). This model is then exactly mapped to the Anderson localization model [1] for the electronic system. By the series method introduced by Licciardello and Economou [2], we can easily show that for $x = 0.2$, the entire AlAs branch is localized, whereas the states in the GaAs branch are mostly extended, except for the edge

* Corresponding author.

states (Fig. 1(a)). When the concentration of Al atoms is increased to 0.5 (Fig. 1(b)), the GaAs branch is localized while most of the Al branches are extended (Fig. 2(b)). The x -dependence of spatial characteristics of each branch is shown in Fig. 1(c), where $L(E)$ denotes for the localized (extended) states, showing well-defined localization transition of the GaAs branch around $x \sim 0.4$.

Results shown in Fig. 1(c) can be used to resolve existing controversy concerning the spatial extent of optical phonons in $\text{Al}_x\text{Ga}_{1-x}\text{As}$. Parayanthal and Pollak [3] analyzed the asymmetric line shapes of LO phonons in $\text{Al}_x\text{Ga}_{1-x}\text{As}$ assuming localization length of $< 100 \text{ \AA}$. Baroni et al. [4] theoretically showed that well-defined dispersion relationship exists in $\text{Al}_x\text{Ga}_{1-x}\text{As}$ for all x 's, partially supported by Raman scattering experiments of Jusserand et al. [5]. These two results are somewhat in conflict because the well-defined dispersion may imply that the states are extended in space. Our picture shows that whether a state is extended or not strongly depends

on x , and therefore, both of the two seemingly conflicting results remain valid as two limiting cases whose validity depends on whether $x < x_c$ or $x > x_c$ ($x_c \sim 0.45$).

To investigate the dynamical and spatial properties of GaAs optical phonons in $\text{GaAs}/\text{Al}_x\text{Ga}_{1-x}\text{As}$ quantum wells, we have simulated the propagation of GaAs optical phonons in $\text{GaAs}/\text{Al}_x\text{Ga}_{1-x}\text{As}/\text{GaAs}$ single barrier structure consisting of 16 monolayers of GaAs (GaAs I), 14 monolayers of $\text{Al}_x\text{Ga}_{1-x}\text{As}$, and 16 monolayers of GaAs (GaAs II) (inset of Fig. 2). The spring constants are assumed to be constant, and the atomic masses of Al or Ga atoms are assigned randomly at the cation sites in the barriers. The initial optical phonon wave is assumed to be in the GaAs I region, and the lattice dynamics is solved to calculate the normalized energy transmission at the detection layer in the GaAs II region. The results are plotted in Fig. 2, where the transmission coefficient continues to decrease until $x \sim 0.3$, and remains at a small value above $x \sim 0.3$. The analysis of the transmitted phonon wave function reveals that, for the flat region of $x > 0.3$, the transmitted energy is mostly in the form of acoustic waves. Therefore, $x \sim 0.3$ can be thought of as a transition alloy composition, beyond which virtually no optical phonon waves can transmit through the relatively thick barrier. We now discuss nonequilibrium Raman scattering experiments on $\text{Al}_x\text{Ga}_{1-x}\text{As}$ alloys and $\text{GaAs}/\text{Al}_x\text{Ga}_{1-x}\text{As}$ quantum wells, in connection with our theoretical results.

It is well known now that nonequilibrium hot phonon population probed by Raman scattering can be, when

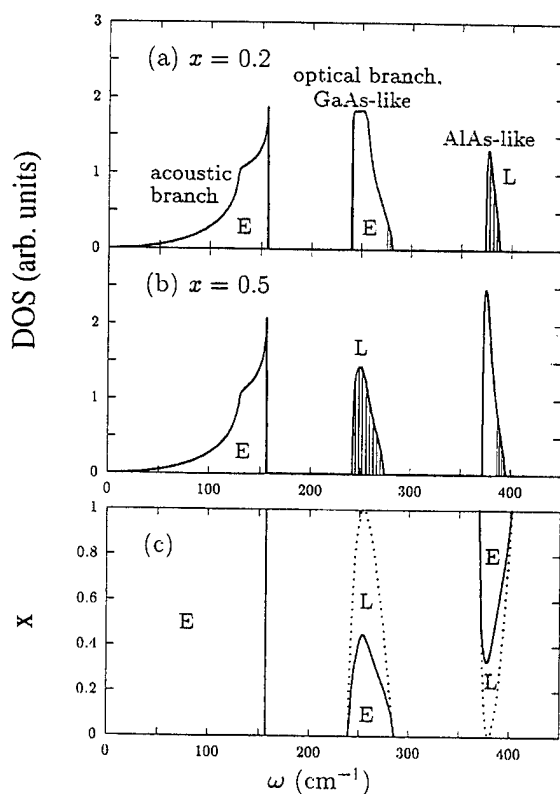


Fig. 1. (a) Phonon density of states obtained by coherent potential approximation for $x = 0.2$. The shaded areas represent localized states under the criterion of Ref. [2]. (b) Same as (a) for $x = 0.5$. (c) The phase diagram of localized (L) and extended (E) states.

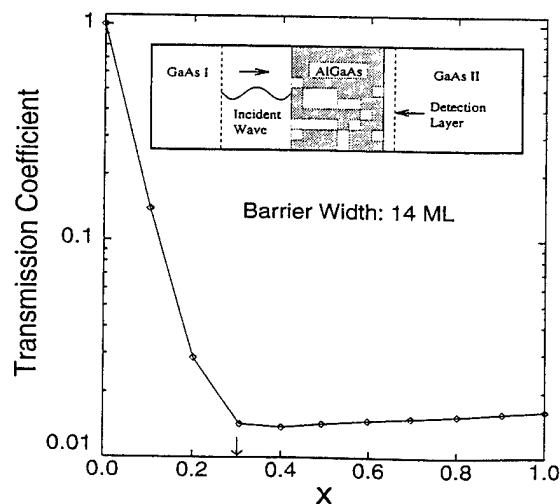


Fig. 2. The transmission coefficient from GaAs (I) to GaAs (II) through the 14 monolayer of $\text{Al}_x\text{Ga}_{1-x}\text{As}$ barrier as a function of x .

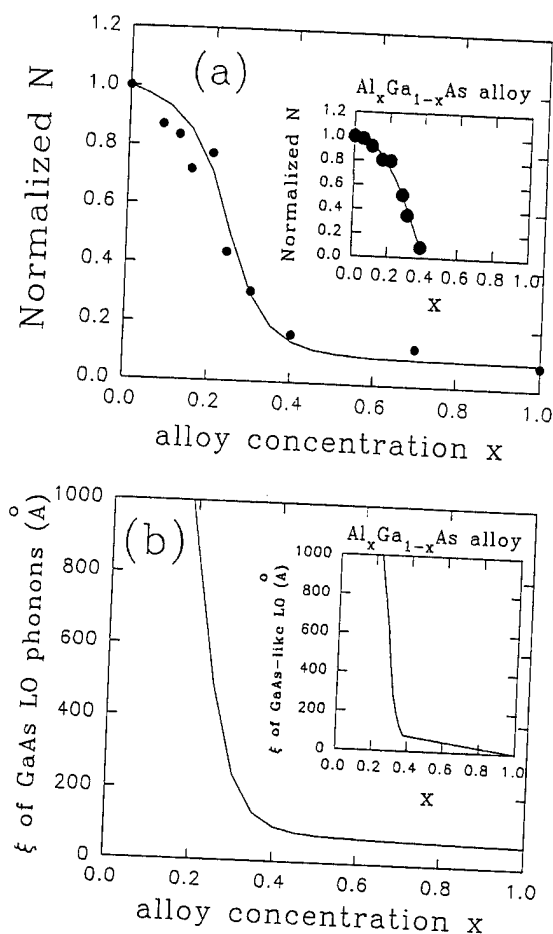


Fig. 3. (a) The normalized (to bulk GaAs under the same experimental conditions) hot phonon occupation number of GaAs/Al_xGa_{1-x}As multiple quantum well as a function of x . The results were averaged over picosecond and cw excitations, in the temperature range 10–300 K. The line is a fit as a guide to the eye. (Inset) The normalized and properly corrected (for the band gap change with x) hot phonon occupation number as a function of x for the Al_xGa_{1-x}As alloys. (b) The coherence length obtained from the solid lines of Fig. 3(a), assuming a coherence length of infinity for the bulk GaAs LO phonon, and a phenomenological wave function $\Psi = \exp(iq_0z) \exp(-z^2/\xi^2)$. (Inset) The same as (b) for the Al_xGa_{1-x}As alloys.

properly analyzed, a sensitive probe of the spatial extent of the Raman active LO phonons [6]. This is essentially because the hot phonon distribution curve generated by the hot electron relaxation is a strong function of the phonon wave vector, and therefore to the spatial extent.

Although the details are given elsewhere [6], once the hot phonon occupation number properly normalized to that of bulk GaAs under the same experimental conditions is known, we can deduce the coherence length of the Raman active GaAs or GaAs-like LO phonons in GaAs/Al_xGa_{1-x}As quantum wells or Al_xGa_{1-x}As alloy.

In Fig. 3(a), the hot phonon occupation number of GaAs LO phonons for the GaAs/Al_xGa_{1-x}As multiple quantum wells observed by picosecond (1.5–70 ps) and cw Raman scattering is shown as a function of x . The data were taken under the same irradiation density using photon energies of 1.9–2.3 eV. We have used a number of quantum wells (over 30) with $L_z = 100$ Å and $L_b > 20$ Å, where the hot phonon occupation number is largely independent of L_b but strongly dependent on x . In the inset, properly corrected hot phonon occupation number of the GaAs-like LO phonons for the Al_xGa_{1-x}As alloy is plotted as a function of x , showing strong x dependence. Using these results, and assuming the phonon wave function $\Psi = \exp(iq_0z) \exp(-z^2/\xi^2)$ (q_0 : Raman active wave vector at the backscattering geometry), we have deduced the coherence length $\sim \xi$ as a function of x , as shown in Fig. 3(b). The strong x -dependence near $x = 0.3$ – 0.4 in both GaAs/Al_xGa_{1-x}As multiple quantum well and Al_xGa_{1-x}As alloy (inset) can be interpreted as the localized-to-extended or the confined-to-propagation transition, in good qualitative agreement with theoretical results of Figs. 1 and 2.

In conclusion, we have studied the spatial extent and dynamical transfer of optical phonons in Al_xGa_{1-x}As alloy and GaAs/Al_xGa_{1-x}As quantum wells, both theoretically and experimentally. It is clear that whether or not an optical phonon is spatially localized or extended should be answered carefully, depending on the alloy composition.

This work was partially supported by Korean Science and Engineering Foundation, Ilju Foundation, and the Ministry of Education.

References

- [1] P.W. Anderson, Phys. Rev. 109 (1958) 1492.
- [2] D.C. Licciardello and E.N. Economou, Phys. Rev. B 11 (1975) 3697.
- [3] P. Parayanthal and F.H. Pollak, Phys. Rev. Lett. 52 (1984) 1822.
- [4] S. Baroni et al., Phys. Rev. Lett. 65 (1990) 84.
- [5] Jusserand et al., Phys. Rev. Lett. 67 (1991) 2803.
- [6] D.S. Kim et al., Phys. Rev. B 51 (1995) 5449; J.M. Jacob et al., Solid. State Commun. 91 (1994) 721.

PHYSICA B

INSTRUCTIONS TO AUTHORS

Submission of papers

Manuscripts (one original + two copies) should be sent to one of the following regular editors:

Prof. Dr. F.R. de Boer, Amsterdam
Dr. Z. Fisk, Tallahassee, FL
Dr. R. Jochemsen, Leiden
Dr. G.H. Lander, Karlsruhe
(Addresses: see p. 2 of cover)

Original material: Submission of a manuscript implies that it is not being simultaneously considered for publication elsewhere and that the authors have obtained the necessary authority for publication.

Refereeing: Authors should supply names of three referees who will, if appropriate, be acknowledged in the printed articles, as in the case of any other colleague who improves the paper with constructive criticism.

Types of contributions

Original research papers and letters to the editor are welcomed. Both should contain an Abstract (of up to 200 words) and a Conclusions section, which, particularly in the case of theoretical papers, translates the results into terms readily accessible to most readers.

Manuscript preparation

All manuscripts should be written in proper English. The paper copies of the text should be prepared with double line spacing and wide margins, on numbered sheets.

Structure: Please adhere to the following order of presentation: Article title, Author(s), Affiliation(s), Abstract, PACS codes and keywords, Main text, Acknowledgements, Appendices, References, Figure captions, Tables.

Corresponding author: The name, complete postal address, telephone and fax numbers and the E-mail address of the corresponding author should be given on the first page of the manuscript.

PACS codes/keywords: Please supply one or more relevant PACS-1995 classification codes and 3 keywords of your own choice for indexing purposes.

References: References to other work should be consecutively numbered in the text using square brackets and listed by number in the Reference list.

Illustrations

Illustrations should also be submitted in triplicate: one master set and two sets of copies. The *line drawings* in the master set should be original laser printer or plotter output or drawn

black india ink, with careful lettering, large enough (3–5 mm) to remain legible after reduction for printing. The *photographs* should be originals, with somewhat more contrast than is required in the printed version. They should be unmounted unless part of a composite figure. Any scale markers should be inserted on the photograph itself, not drawn below it.

Colour plates: Figures may be published in colour, if this is judged essential by the editor. The publisher and the author will each bear part of the extra costs involved. Further information is available from the publisher.

After acceptance

Notification: You will be notified by the Editor of the journal of the acceptance of your article.

Copyright transfer: In the course of the production process you will be asked to transfer the copyright of the article to the publisher. This transfer will ensure the widest possible dissemination of information.

Electronic manuscripts

The publisher welcomes the receipt of an electronic version of your accepted manuscript. If there is not already a copy of this (on diskette) with the journal editor at the time the manuscript is being refereed, you are invited to send a file with the text of the accepted manuscript directly to the Publisher on diskette (allowed formats 3.5" or 5.25" MS-DOS, or 3.5" Macintosh) to the address given below. Please note that no deviations from the version accepted by the Editor of the journal are permissible without the prior and explicit approval of the Editor. Such changes should be clearly indicated on an accompanying printout of the file.

Author benefits

No page charges: Publishing in Physica B is free of charge.

Free offprints: The corresponding author will receive 50 offprints free of charge. An offprint order form will be supplied by the publisher for ordering any additional paid offprints.

Discount: Contributors to Elsevier Science journals are entitled to a 30% discount on all Elsevier Science books.

Further information (after acceptance):

Desk Editor Physica B
Elsevier Science B.V.
P.O. Box 103
1000 AC Amsterdam
The Netherlands
Telefax: +31-20-485 2775
E-mail: w.tukker@elsevier.nl



North-Holland, an imprint of Elsevier Science

1994 PHYSICS and MATERIALS SCIENCE JOURNALS

Applied Surface Science

Volumes 72-81 in 40 issues. Price: US \$ 2114.00 / Dfl. 3910.00

Astroparticle Physics

Volume 2 in 4 issues. Price: US \$ 182.00 / Dfl. 336.00

Computational Materials Science

Volume 2 in 4 issues. Price: US \$ 211.00 / Dfl. 391.00

Computer Physics Communications

Volumes 79-85 in 21 issues. Price: US \$ 2236.00 / Dfl. 4137.00

International Journal of Applied Electromagnetics in Materials

Volume 5 in 4 issues. Price: US \$ 203.00 / Dfl. 376.00

Journal of Crystal Growth

Volumes 135-145 in 44 issues. Price: US \$ 4822.00 / Dfl. 8921.00

Journal of Geometry and Physics

Volumes 13 and 14 in 8 issues. Price: US \$ 358.00 / Dfl. 662.00

Journal of Luminescence

Volumes 59-62 in 24 issues. Price: US \$ 1083.00 / Dfl. 2004.00

Journal of Magnetism and Magnetic Materials

Volumes 126-137 in 36 issues. Price: US \$ 3347.00 / Dfl. 6192.00

Journal of Non-Crystalline Solids

Volumes 162-176 in 45 issues. Price: US \$ 3535.00 / Dfl. 6540.00

Journal of Nuclear Materials

Volumes 206-216 in 33 issues. Price: US \$ 3098.00 / Dfl. 5731.00

Materials Letters

Volumes 19-22 in 24 issues. Price: US \$ 899.00 / Dfl. 1664.00

Nuclear Instruments and Methods in Physics Research - Section A

**Accelerators, Spectrometers, Detectors & Associated
Equipment**

Volumes 337-351 in 45 issues. Price: US \$ 5441.00 / Dfl. 10,065.00

Nuclear Instruments and Methods in Physics Research - Section B

Beam Interactions with Materials and Atoms

Volumes 83-94 in 48 issues. Price: US \$ 4352.00 / Dfl. 8052.00

*Reduced combined 1994 subscription price to Nuclear Instruments
and Methods - A and B: US \$ 9063.00 / Dfl. 16,767.00*

Nuclear Physics A

Volumes 566-580 in 60 issues. Price: US \$ 4792.00 / Dfl. 8865.00

Nuclear Physics B

Volumes 409-432 in 72 issues. Price: US \$ 7537.00 / Dfl. 13,944.00

Nuclear Physics B - Proceedings Supplements

Volumes 34-38 in 15 issues. Price: US \$ 881.00 / Dfl. 1630.00

*Reduced combined 1994 subscription price to
Nuclear Physics A + Nuclear Physics B + NPB-Proceedings
Supplements: US \$ 11,202.00 / Dfl. 20,724.00*

Optical Materials

Volume 3 in 4 issues. Price: US \$ 206.00 / Dfl. 381.00

Optics Communications

Volumes 103-111 in 54 issues. Price: US \$ 2121.00 / Dfl. 3924.00

Physica A - Statistical and Theoretical Physics

Volumes 201-211 in 44 issues. Price: US \$ 2503.00 / Dfl. 4631.00*

Physica B - Condensed Matter Physics

Volumes 192-202 in 44 issues. Price: US \$ 2503.00 / Dfl. 4631.00*

Physica C - Superconductivity

Volumes 219-236 in 72 issues. Price: US \$ 4096.00 / Dfl. 7578.00*

Physica D - Nonlinear Phenomena

Volumes 70-78 in 36 issues. Price: US \$ 2048.00 / Dfl. 3789.00*

**Reduced rates are available for combined subscriptions to Physica;
please contact the publisher for details.*

Physics Letters A

Volumes 185-197 in 78 issues. Price: US \$ 2537.00 / Dfl. 4693.00

Physics Letters B

Volumes 317-340 in 96 issues. Price: US \$ 4683.00 / Dfl. 8664.00

Physics Reports

Volumes 240-251 in 72 issues. Price: US \$ 2342.00 / Dfl. 4332.00

*Reduced combined 1994 subscription price to Physics Letters A,
Physics Letters B + Physics Reports: US \$ 8502.00 / Dfl. 15,729.00*

Solid State Ionics

Volumes 68-76 in 36 issues. Price: US \$ 1805.00 / Dfl. 3339.00

Surface Science

(including Surface Science Letters)

Volumes 296-318 in 69 issues. Price: US \$ 6104.00 / Dfl. 11,293.00

Surface Science Reports

Volume 18-20 in 24 issues. Price: US \$ 618.00 / Dfl. 1143.00

*Reduced combined 1994 subscription price to Surface Science
(including Surface Science Letters), Applied Surface Science and
Surface Science Reports: US \$ 8192.00 / Dfl. 15,156.00*

Ultramicroscopy

Volumes 52-56 in 20 issues. Price: US \$ 1151.00 / Dfl. 2130.00

*Dutch Guilder price(s) quoted applies worldwide, except in the Americas
(North, Central and South America). US Dollar price(s) quoted applies
in the Americas only. Journals are sent by Surface Mail to all countries
except to the following where Air Delivery via SAL mail is ensured at no
extra cost to the subscriber: Argentina, Australia/New Zealand, Brazil,
Hong Kong, India, Israel, Japan, Malaysia, Mexico, Pakistan, P.R.
China, Singapore, S. Africa, S. Korea, Taiwan, Thailand, USA &
Canada. Customers in the European Community should add the
appropriate VAT rate applicable in their country to the price(s).*



ELSEVIER SCIENCE B.V.

P.O. Box 103, 1000 AC Amsterdam, The Netherlands

Elsevier Science Inc., Journal Information Center, PO Box 882,
Madison Square Station, New York, NY 10159, U.S.A.

DYNAMICS OF PHOTOEXCITED CARRIERS IN GaN

J.J. Song¹, W. Shan¹, B. Goldenberg², G.E. Bulman³, and J.A. Edmond³

¹Center for Laser Research and Department of Physics, Oklahoma State University, Stillwater, Oklahoma 74078, USA, ²Honeywell Technology Center, Plymouth, Minnesota 55441, USA, and

³Cree Research Inc, Durham, North Carolina 27713, USA.

Abstract—The dynamics of photoexcited carriers in GaN were studied by examining the radiative decay of exciton emissions using time-resolved photoluminescence spectroscopy. We found that the capture of excitons and trapping of carriers at defects and/or impurities through nonradiative relaxation processes dominate the decay of exciton population, resulting in a very short decay time for both free-exciton and bound-exciton emissions. The capture process depends on the density of impurities and defects in the GaN samples.

1. INTRODUCTION

GaN-based III-V nitride semiconductors have been extensively studied recently for their potential electronic and optoelectronic device applications. Superbright high-efficient blue LED's based on nitride structures have been demonstrated by the Nichia group and others.[1] The observation of optically pumped laser action in GaN with clear resolvable longitudinal lasing modes over a broad temperature range from 10 to 400 K has been recently reported by a few research groups.[2,3] All this progress has led to much more intense interest in the development of efficient nitride UV-visible light emitters. Many aspects of device operation are governed by carrier recombination and relaxation processes, and the understanding of these processes is of fundamental importance to the development of practical electro-luminescence devices.

In this work, we report the results of a study of the dynamics of photoexcited carriers in high quality GaN epitaxial films and double heterostructures by metalorganic chemical vapor deposition. The dynamics of photoexcited carriers were investigated using time-resolved luminescence spectroscopy by

examining the time decay of the intrinsic free-excitons and bound-exciton emissions.

2. EXPERIMENTAL

The GaN samples used in this work were all grown by metalorganic chemical vapor deposition, either on sapphire or on SiC substrates. Time-resolved photoluminescence spectroscopy was performed using a picosecond dye laser and a synchroscan streak camera. The dye laser with the pulse duration of ~ 2 ps was pumped by a frequency-doubled modelocked Nd:YAG laser (82 MHz). The output wavelengths were frequency doubled into UV range using a nonlinear crystal. The luminescence signals were dispersed by a 1/4 M monochromator and detected by the streak camera. The system provides the capabilities of simultaneously measuring photoluminescence intensity, time, and wavelength. The overall time resolution of the system is less than 15 ps.

3. RESULTS AND DISCUSSIONS

Fig. 1 illustrates the time evolution of PL decay for both free-exciton and bound-exciton emissions observed in a GaN sample. The intrinsic free-exciton (FX) luminescence lines

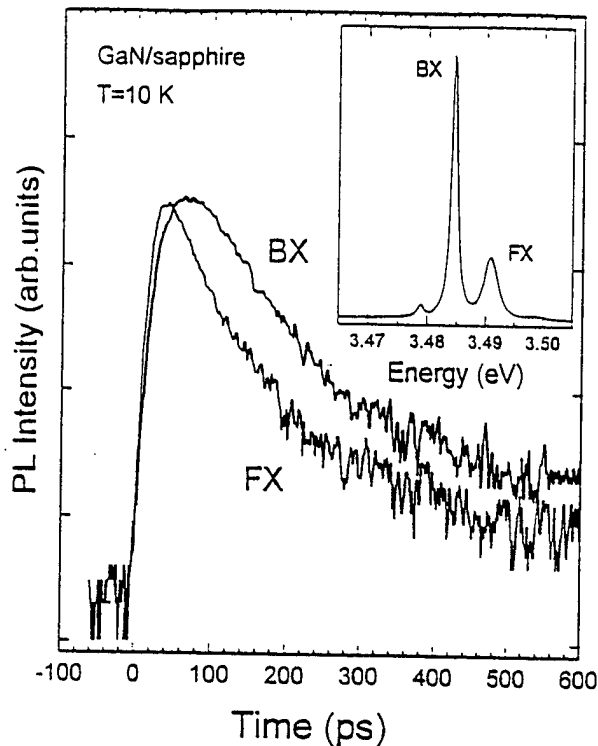


Fig. 1. Time evolution of spectrally integrated PL for both intrinsic free-exciton and bound-exciton emissions. The inset shows the well-resolved time-integrated free-exciton and bound-exciton luminescence structures.

in these samples can be spectrally well resolved from that of excitons bound to neutral donors, as shown in the inset in the figure. That allows an unambiguous determination of the PL decay time for both intrinsic free excitons and neutral-donor bound excitons. The lifetime of the PL decay at 10 K was found to be typically about 30-35 ps for free excitons and 40-55 ps for bound excitons, varying from sample to sample used in this work. The measured decay time is much shorter than the value estimated by theoretical considerations regarding the radiative lifetime of an excited state in a semiconductor, where the radiative lifetime of bound excitons in GaN is expected to be on the order of several hundreds of picoseconds and that of free excitons in the nanosecond domain.[4]

The discrepancy between the measured values of PL decay times and the theoretical estimated ones can be attributed to nonradiative relaxation processes in competition with the radiative channel. The measured PL decay time only yields an effective lifetime (τ_{eff}) for free

excitons and bound excitons. It is related to both the radiative (τ_R) and nonradiative (τ_{NR}) lifetimes with the decay rate expressed as

$$1/\tau_{eff} = 1/\tau_R + 1/\tau_{NR}. \quad (1)$$

In this equation, we have assumed that the nonradiative decay is exponential, so that a lifetime can be defined, and the carriers in the levels which undergo recombination are at thermal equilibrium. When the nonradiative decay rate is larger, the measured decay time is characteristic for the nonradiative processes in accordance with Eq.(1). This situation is typical for recombination from intrinsic states of semiconductors.[6] The nonradiative processes, such as multiphonon emission, capture by deep centers, Auger effect, *etc.*, give rise to fast relaxation of the excited carriers down to lower states from which they decay radiatively or relax nonradiatively. As a result, the measured PL decay time for a given excited state is an effective lifetime and usually much shorter than a radiative one. The slow rise of bound-exciton luminescence intensity compared to that of the free-exciton PL shown in Fig. 1 is an indicator of such nonradiative relaxation processes for free excitons arriving at the bound exciton energy. Therefore, the capture of excitons and trapping of carriers by such nonradiative centers at defects and impurities must play a major role in the recombination processes responsible for the exciton population decay in the GaN samples studied in this work. In fact, the measured PL decay time was found to be directly related to the intensity of broadband emissions lying in the GaN band gap. The broad emission structure referred to as yellow emission in the literature is believed to be associated with the optical transitions between the energy levels involving impurity and/or defect states. The intensity of yellow emission is proportional to the density of some particular defects or impurities present in samples. We found that the stronger the yellow emission, the shorter the PL decay time in a GaN sample. Fig.2 compares free-exciton PL decay between two samples with the relative intensity ratio of 100:1 for the yellow emission under identical

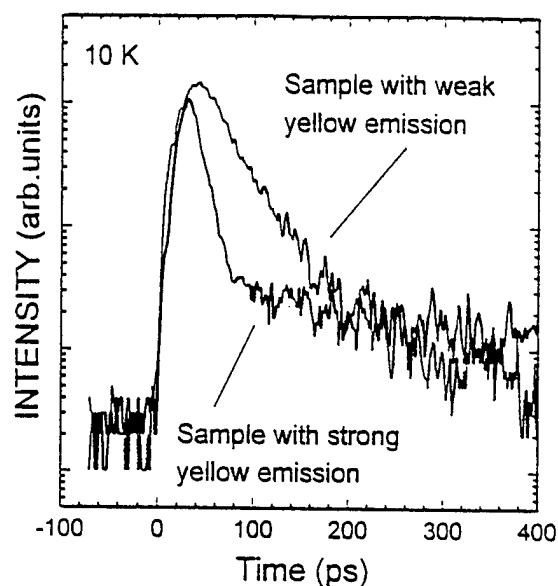


Fig. 2. Comparison of the time decay of free-exciton emission between two GaN epilayer samples on sapphire substrates with the relative intensity ratio of 100:1 for the broadband yellow emission under the same excitation conditions.

excitation conditions. The deduced lifetime of free-exciton emission in the sample with stronger yellow emission is only 15 ps (which is the limit of our instrumental resolution). Therefore, the fast decay behavior of the intensity indicates that the capture of excitons and trapping of carriers at defects and impurities through nonradiative combinations dominate the decay of exciton population. The process of capture therefore must depend on the density of defects and impurities in the GaN samples.

The influence of nonradiative recombination on the measured decay time of exciton luminescence can be further manifested by the effects of sample temperature. It is known that for a radiative recombination dominant system, an increase in the radiative lifetime with temperature is expected for the free excitons[5,7] since their average kinetic energy is increased. The thermal redistribution results in a decreasing number of the excitons close enough to the Brillouin-zone center for radiative recombination. Also the lifetime is expected to be independent of temperature for bound excitons, and only the emission intensity

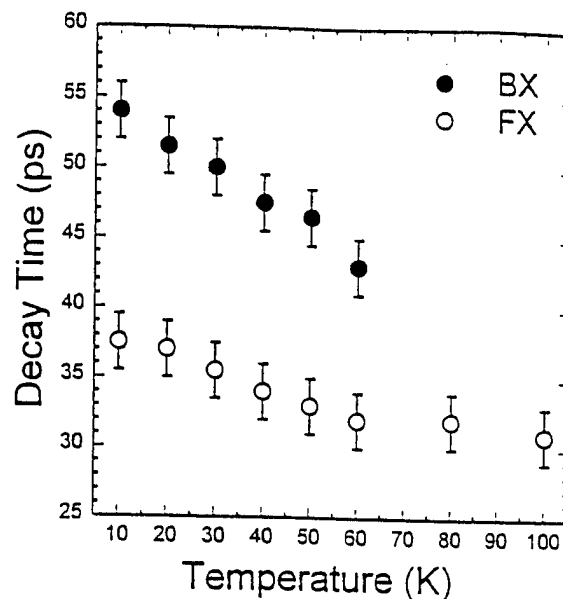


Fig. 3. The measured PL decay times of the free exciton and bound exciton in a GaN samples as a function of temperature.

is expected to decrease because of thermal ionization of the bound excitons. However, the bound-exciton PL decay time was found to decrease with increasing temperature before the emission thermally quenched, and the free-exciton PL decay time measured from the majority of samples used in this work exhibited a slow decrease with temperature, as shown in Fig. 3. Although recombination from excitons bound to extrinsic states such as defects or impurities can often be very efficient at low temperatures as demonstrated by the inset of Fig. 1, the measured decay time is still determined by detailed decay kinetics. The observed decrease of PL decay time with temperature for the bound excitons in the GaN samples indicates that incremental stronger nonradiative relaxations occur as the temperature increases resulting in continued faster decay of the exciton population. The decrease of free-exciton PL in both intensity and decay time with temperature suggests that the nonradiative processes of capture of free excitons at defects or impurities prevail in the competition with the thermally enhanced exciton-exciton and exciton-phonon scatterings.

We have also studied the time decay of

exciton luminescence in GaN/AlGaIn double heterostructures (DHS). Fig. 4 shows the time evolution of bound-exciton emission observed in a GaN/AlGaIn DHS sample compared with that in a GaN epitaxial film. Both samples were deposited on SiC substrates under the identical growth conditions except that the DH structure was grown on one of them. The Al concentration of the AlGaIn cladding layers is about 7%. As shown in the figure, the measured decay time for the bound exciton emission in the DHS sample was found to be (~ 74 ps) twice longer than that in the bulk-like GaN (~ 37 ps). It is known that in a strained heterostructure system such as AlGaIn/GaN, the built-in strain within the uniform elastic limit can significantly reduce the density of defects such as dislocations. The increase in the exciton PL decay time observed in the DHS sample implies that the AlGaIn cladding layers with a small mole fraction could be relatively effective in reducing the density of dislocations in the GaN active layer. In addition, the deposition of cladding layer on the top of GaN active layer could have

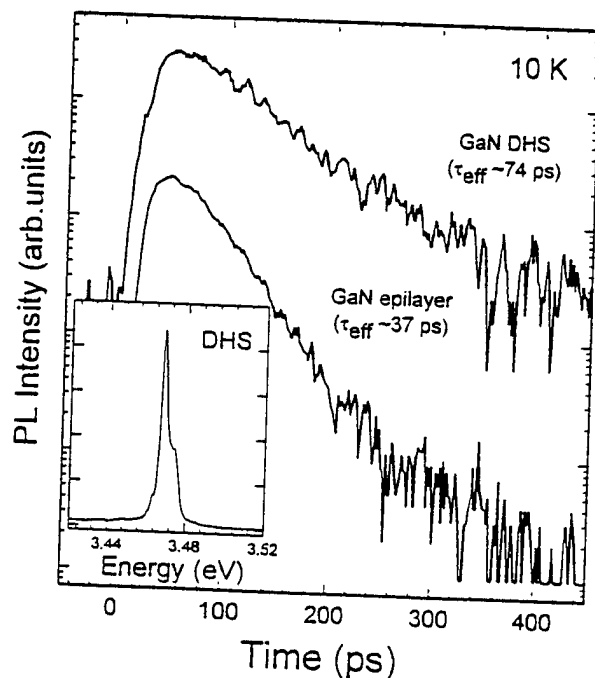


Fig. 4. Comparison of PL decay of bound exciton emissions in a GaN DHS and an epilayer sample. Time-integrated exciton luminescence spectrum associated with GaN active layer taken from a DHS sample is shown in the inset.

passivated the surface states resulting in a reduction of the nonradiative recombination velocity of the photoexcited carriers on the bare surface and in its vicinity. Nevertheless, this is an issue requiring further study.

4. CONCLUSIONS

Time-resolved luminescence spectroscopy has been performed to study the exciton radiative decay in GaN epilayers and double heterostructures grown by MOCVD. The decay time for both free-exciton and bound-exciton emissions was found to be quite short, in the order of a few tens of picoseconds. The results suggest that the lifetime of excitons in the GaN samples is governed by nonradiative recombination. The capture of excitons and trapping of carriers at defects and/or impurities through nonradiative relaxation processes dominate the decay of exciton population. The capture process depends on the density of impurities and defects in the GaN samples. The longer time decay of exciton emissions observed in GaN double heterostructures suggests that the deposition of AlGaIn cladding layers over the GaN active layer reduces the density of the nonradiative recombination centers and results in an increase of the exciton population decay time.

REFERENCES

1. S. Nakamura, T. Mukai, and M. Senoh, *Appl. Phys. Lett.* **64**, 1687(1994).
2. X.H. Yang, T.J. Schmidt, W. Shan, J.J. Song, and B. Goldenberg, *Appl. Phys. Lett.* **66**, 1(1995).
3. A.S. Zubrilov, V.I. Nikovlaev, V.A. Dmitriev, K.G. Irvine, J.A. Edmond, and C.H. Carter, Jr., *Inst. Phys. Conf. Ser.* No.141, 525(1995).
4. W. Shan, X.C. Xie, J.J. Song, and B. Goldenberg, *Appl. Phys. Lett.* **67**, 2512 (1995).
5. G.W. 't Hooft, W.A.J.A. van der Poel, and L.W. Molenkamp, *Phys. Rev.* **B35**, 8281 (1987).
6. M. Voos, R.F. Leheny, and J. Shah, in *Optical Properties of Solids*, edited by M. Balkanski, (North-Holland, Amsterdam, 1980), Chapter 6, p.336.
7. J. Feldmann, G. Peter, E.O. Göbel, P. Dawson, K. Moore, C. Foxon, and R.J. Elliott, *Phys. Rev. Lett.* **59**, 2337(1987).

Microscopic processes during electron cyclotron resonance microwave nitrogen plasma-assisted molecular beam epitaxial growth of GaN/GaAs heterostructures: Experiments and kinetic modeling

Z. Z. Bandić^{a)} and T. C. McGill

Thomas J. Watson, Sr., Laboratory of Applied Physics, California Institute of Technology, Pasadena, California 91125

R. J. Hauenstein^{b)} and M. L. O'Steen

Department of Physics, Oklahoma State University, Stillwater, Oklahoma 74078

(Received 22 January 1996; accepted 16 April 1996)

A set of δ -Ga_{N_yAs_{1-y}}/GaAs strained-layer superlattices grown on GaAs (001) substrates by electron cyclotron resonance (ECR) microwave plasma-assisted molecular beam epitaxy (MBE) was characterized by *ex situ* high resolution X-ray diffraction (HRXRD) to determine nitrogen content y in the nitrided GaAs monolayers as a function of growth temperature T . A first order kinetic model is introduced to quantitatively explain this $y(T)$ dependence in terms of an energetically favorable N for As anion exchange and thermally activated N-surface desorption and surface segregation processes. The nitrogen surface segregation process, with an estimated activation energy $E_s \sim 0.9$ eV appears to be significant during the GaAs overgrowth of Ga_{N_yAs_{1-y}} layers, and is shown to be responsible for strong $y(T)$ dependence. © 1996 American Vacuum Society.

I. INTRODUCTION

In the past few years we have seen a flurry of activity in the development of visible light emitters based on wide band gap refractory semiconductor GaN, related alloys, and heterostructures.¹⁻⁴ Most of the research was concentrated on epitaxial growth techniques of nitrides,⁵ and growth of device structures (LEDs and lasers) on various substrates,⁶ while comparatively little work was done on other materials of potential technological applications, such as mixed anion nitride/arsenide system.⁷⁻⁹ Although limited by a small solubility,¹⁰ even small amounts of N in GaAs can cause unexpected band gap bowing to infrared,^{10,11} while the small amounts of As in GaN can substantially increase valence band spin-orbital splitting which can significantly influence operation of the active layer in the laser structure due to the higher recombination rate.¹² One of the main difficulties in growing such nitride/arsenide structure, for example, in the electron cyclotron resonance plasma-assisted molecular beam epitaxy (ECR-MBE), is controlling the structural and chemical properties of the interface, which is only possible if important microscopic growth processes are fully understood. We have recently shown^{7,8} that it is possible to produce high quality, fully commensurate Ga_{N_yAs_{1-y}}/GaAs strained-layer superlattices (SLS), grown on the GaAs substrate. Initial high resolution X-ray diffraction (HRXRD) and reflection high energy electron diffraction (RHEED) measurements done on such structures revealed existence of several distinct thermally activated processes, but limited by an unavailability of a suitable quantitative model against which these separate experimental observations could be tested

consistently, only semi-quantitative considerations of kinetics and tentative identification of processes have been possible to date.⁸

In this article, we introduce a quantitative model, based on the first order kinetic theory, to examine the initial nitridation (surface N for As exchange), N surface desorption, and N surface segregation processes, observed in ECR-MBE grown Ga_{N_yAs_{1-y}}/GaAs heterostructures, characterized by *ex situ* HRXRD. Through application of our model to an unusually strong growth temperature dependence of y , obtained from X-ray experiments, the existence of a thermally activated N surface segregation mechanism is conclusively established and quantitatively confirmed. Although previously suggested,⁸ the thermally activated N surface segregation mechanism could not be conclusively established without adequate analytical model, which is necessary to describe the concurrent, thermally activated N surface desorption and segregation processes. Activation energies of both surface segregation and desorption processes are numerically estimated, and the impact of the compositional-profile smearing of N, due to the strong N surface segregation effect, to GaN/GaAs heteroepitaxy and interface quality is analyzed and discussed.

II. EXPERIMENTAL DETAILS

A set of 36-period " δ -Ga_{N_yAs_{1-y}}/GaAs" superlattices, with a superlattice period consisting of one Ga_{N_yAs_{1-y}} monolayer (ML) and 75 GaAs monolayers, was grown on a GaAs (100) substrate as a function of temperature (540–580 °C) in an ECR-MBE system. Ga_{N_yAs_{1-y}} monolayers were produced through brief (4 s) N₂ plasma exposure (nitridation) of an As-stabilized GaAs surface. Nitridation was immediately followed by GaAs overgrowth at a fixed

^{a)}Electronic mail: zzbssdp.caltech.edu

^{b)}Electronic mail: rjh@hyper.phy.okstate.edu

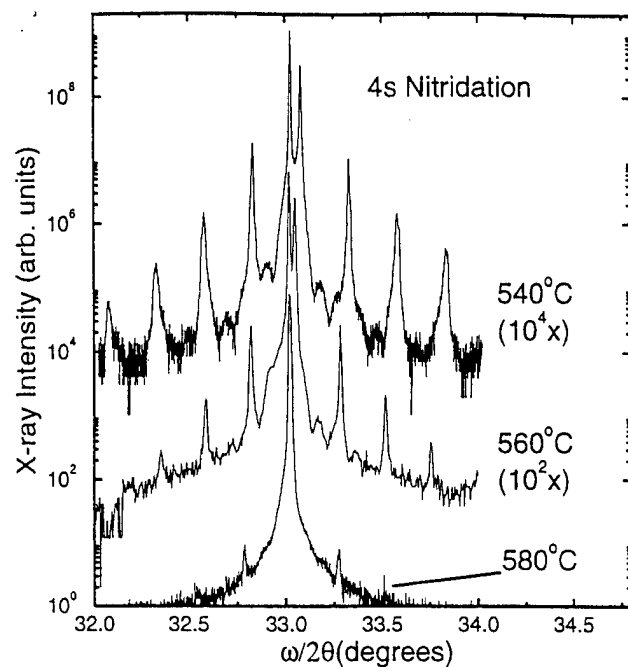


FIG. 1. HRXRD around (004) substrate reflections for $\delta\text{-Ga}_y\text{As}_{1-y}/\text{GaAs}$ superlattices. Results indicate strong dependence of the rocking curves profiles on growth temperature.

growth rate (0.75 ML/s) for 100 s. The surface of GaAs is then As-stabilized through exposing to As_2 flux for only 30 s (As-soak). In addition, one superlattice was grown with 6 s nitridation at 550 °C. Further details about growth system and procedures can be found elsewhere.^{7,8}

To determine strain and concentration profile, the entire sample set is then characterized by *ex situ* HRXRD, with the use of Philips Materials Research Diffractometer (MRD). The standard $\omega/2\theta$ scans are performed in the 4-crystal mode using Ge (220) reflections, around the substrate (004) reflections, while the reciprocal space scans (area scans) around the (115) reflections are done in the same mode, with additional use of a Bonse-Hart collimator in front of the detector. The area scans confirmed that all samples are coherently strained. The resultant $\omega/2\theta$ rocking curves for 4 s nitridations SLS are presented on Fig. 1 (550 °C and 570 °C scans have been omitted for clarity). Results reveal a strong dependence on growth temperature T of the epitaxial structure, indicating a presence of thermally activated microscopic processes. Two-dimensional equivalent alloy compositions (y) are determined from peak positions, and are confirmed through dynamical simulations using Philips High Resolution Simulation (HRS) software package. The agreement typically obtained between experimental rocking curve and simulation is presented on Fig. 2 on the example of the superlattice grown on 550 °C. Figure 3 shows an Arrhenius plot of the resultant compositional dependence on growth temperature, $y(T)$, for 4 s (circles) and 6 s (diamond) nitridations, including experimental uncertainties in temperature, which represent measured variation over a given wafer (i.e., temperature nonuniformity) due to unintended differences in sample mounting. Although not included in the plot, the absolute errors associated with GaN composition can be esti-

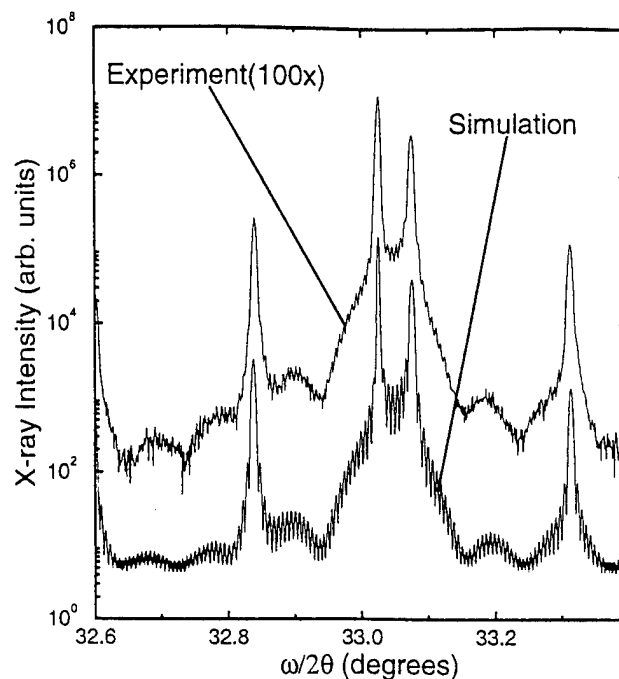


FIG. 2. Typical agreement between experimental rocking curve and HRS simulated rocking curve.

mated to $\pm 0.5\%$. These errors are a result of a Vegard's law approximation and uncertainties in numerical values of elastic properties of the $\text{Ga}_y\text{As}_{1-y}$ layer.

These results suggest existence of two regimes: (i) dose-limited at low temperatures; (ii) kinetically limited at high

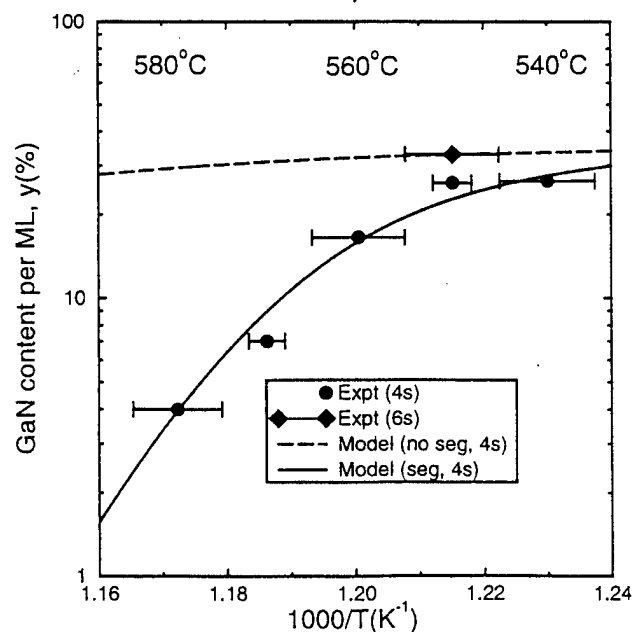


FIG. 3. Growth-kinetics models to explain the strong $y(T)$ dependence observed for ECR-MBE grown $\delta\text{-Ga}_y\text{As}_{1-y}/\text{GaAs}$ strained-layer superlattices. Experimental data points are obtained through HRXRD measurements for 4 s (circles) and 6 s (diamond) nitridations. The dashed curve represents the model neglecting N surface segregation [Eq. (2)], while the solid curve represents the model including segregation effects [Eq. (8)].

temperatures, with unexpectedly strong fall-off in y with increasing growth temperature.

III. KINETICAL MODELING

For the purpose of understanding the physical origin of this $y(T)$ dependence, we have developed a first order kinetic model which explicitly incorporates three phases of our particular SLS growth sequence: (i) nitridation; (ii) overgrowth, and (iii) As-soak, as described in Sec. II.

A. Nitridation

The net rate of surface nitridation is determined by two physical processes which have been previously identified: (i) N-for-As surface anion exchange (N gain), and (ii) surface N desorption (N loss). These processes can be analytically modeled, in the first order in N surface composition y as

$$\frac{dy}{dt} = s\Phi(1-y) - \frac{y}{\tau_d} \quad (1)$$

The first term on the right hand side of Eq. (1) corresponds to the N gain on the As-stabilized GaAs surface due to the energetically favorable anion exchange. This process is modeled as being proportional, in the first order, to the flux Φ of incident physically activated N; to the fraction of available As surface sites to be exchanged with N, and to an overall efficiency factor s (units of area), which in general might depend on surface chemistry, strain, and temperature, but is approximated as constant over the temperature and composition range of interest, for the purpose of our simplified model. The second term in this equation, $-y/\tau_d$, represents the N loss due to surface desorption. It can be simply modeled in terms of thermally activated rate constant $\tau_d^{-1} = \tau_{0d}^{-1} \exp(-E_d/kT)$, with activation energy E_d . Such a process has been directly observed in our RHEED measurements of nitrided GaAs surfaces, and estimates for E_d (~ 2.1 eV) have been previously reported.^{7,8}

If we define an "effective dosing rate" $r \equiv s\Phi$, the solution to Eq. (1) for an initially N-free (As-stabilized) surface can be written as

$$y(t_{\text{exp}}) = y_{\text{ss}}[1 - \exp(-t_{\text{exp}}/\tau)], \quad (2)$$

where $y_{\text{ss}} \equiv r\tau$, $\tau \equiv (\tau_d^{-1} + r)^{-1}$, and t_{exp} is the nitrogen plasma exposure time. If Eq. (2) is considered in the limit of low temperatures so that desorption rate τ_d^{-1} is negligible, then $y \rightarrow 1$ would be obtained. This reflects the assumption that As atoms from the As-enriched (100) GaAs surface, when exposed to N plasma, will be completely exchanged for N atoms in the steady state, since N terminated surface has lower surface free energy, due to a much stronger Ga-N than Ga-As bond (heats of formation 6.81 eV and 5.55 eV, respectively¹³). Although the essential nitridation kinetics is well described by Eq. (2) without unnecessary mathematical complexity, it ignores the subsequent stages of growth of our superlattices, and therefore cannot be used to model directly our experimental results. This can be seen in Fig. 3, where the dashed curve represents the plot of Eq. (2) taking $t_{\text{exp}} = 4$ s and using our RHEED based experimental desorp-

tion parameters, $E_d = 2.1$ eV and $\tau_d = 7$ s at 592 °C.^{7,8} In addition, the dosing rate r is estimated to be approximately 0.1 Hz from experimental values of y at 550 °C for 4 s and 6 s nitridations, such that Eq. (2) describes properly the dose-limited (low temperature) regime of growth.

B. GaAs overgrowth—N segregation

Inspection of Fig. 3 clearly reveals that the processes of anion exchange and N surface desorption *alone* result in the weak fall-off of the model (dashed) curve, and thus cannot account for the strong $y(T)$ dependence in the kinetically limited growth regime. Also, even N surface desorption during the short monolayer deposition time (t_{ML}) required to bury (and freeze-in) the nitrided $\text{GaN}_y\text{As}_{1-y}$ layer cannot result in significant N loss. To overcome this, we hypothesize that thermally activated N surface segregation process, described with the rate constant $\tau_s^{-1} = \tau_{0s}^{-1} \exp(-E_s/kT)$, is occurring concurrently with N desorption, during GaAs overgrowth.⁸ This assumption is supported qualitatively by our experimental observation that GaN-related (3×3) surface reconstruction proceeds faster to GaAs (2×4) reconstruction at a lower substrate temperature during GaAs overgrowth, which is consistent with freeze-out of a thermally activated N segregation process.

Let us assume that (1) segregation occurs from the first subsurface layer upward to the current surface layer; (2) desorption occurs from all currently exposed surfaces, i.e., the current growth surface and the current partially exposed first sub-surface layers; and (3) the segregation and desorption processes are statistically independent, and are occurring concurrently. Also, let S_n represent a relative GaN mole fraction in monolayer n , where by definition the content of the nitrided layer at the end of nitridation process is normalized to unity, $S_0(t=0) \equiv 1$. Under these assumptions, we can relate the N content of monolayers n and $n+1$ through

$$S_{n+1}(0) = [S_n(0) - S_n(t_{\text{ML}})] \frac{\tau_s^{-1}}{\tau_s^{-1} + \tau_d^{-1}}. \quad (3)$$

Equation (3) describes the fraction of lost N $[S_n(0) - S_n(t_{\text{ML}})]$, which segregates rather than desorbs, and becomes the nitrogen content of the next surface layer. Since layer n loses its N content due to both N desorption and segregation, during the time interval $0 \leq t \leq t_{\text{ML}}$, $S_n(t)$ decays exponentially as $\exp(-t/\tau_{\parallel})$, where $\tau_{\parallel}^{-1} \equiv (\tau_s^{-1} + \tau_d^{-1})$. Using this expression in Eq. (3) leads us to

$$S_{n+1}(0) = S_n(0) [1 - \exp(-t_{\text{ML}}/\tau_{\parallel})] \frac{\tau_d}{\tau_{\text{tot}}}, \quad (4)$$

where $\tau_{\text{tot}} \equiv \tau_s + \tau_d$. It is obvious from Eq. (4) that $S_n(0)$ represents geometrical progression. Now, similarly to Eq. (3) we can define δ_n as the amount of initial material lost through desorption from layer n :

$$\delta_n \equiv [S_n(0) - S_n(t_{\text{ML}})] \frac{\tau_s}{\tau_{\text{tot}}}. \quad (5)$$

Therefore, the total loss of N from one superlattice period during overgrowth would be

$$L = \sum_{n=0} \delta_n, \quad (6)$$

which is simply a sum of a geometric progression. Finally, the total amount of the original GaN content retained within one period of a superlattice is $R = 1 - L$, or straightforwardly

$$R = \frac{\tau_{\text{tot}}}{\tau_d + \tau_s e^{t_{\text{ML}}/\tau_l}}. \quad (7)$$

It is important to note that the expression for R given in Eq. (7) gives the correct limiting behaviour in describing the loss of N during the GaAs overgrowth, in the limits of no segregation, or no desorption. If there is desorption, but no segregation, then the only opportunity for N loss would be before nitrated layer is completely buried in GaAs; i.e., $R = \exp(-t_{\text{ML}}/\tau_d)$, which is obtained directly from Eq. (7) in the limit $\tau_s \rightarrow \infty$. Similarly, if there is segregation, but no desorption, then R must be unity, since the only possible mechanism for N loss is desorption process. In that case, where $\tau_d \rightarrow \infty$, one would obtain $R \rightarrow 1$, as it should be.

IV. RESULTS AND DISCUSSION

Using the "segregation correction factor" from Eq. (7), it is clear that in order to consistently incorporate N surface segregation into our model, Eq. (2) must be replaced by

$$y(t_{\text{exp}}) = y_{\text{ss}} [1 - \exp(-t_{\text{exp}}/\tau)] \times \left[\frac{\tau_{\text{tot}}}{\tau_d + \tau_s e^{t_{\text{ML}}/\tau_l}} \right]. \quad (8)$$

Thus, Eq. (8) represents the final result of our model and quantitatively describes the growth sequence (nitridation/overgrowth/soak) of our $\delta\text{-Ga}_x\text{N}_{1-x}\text{As}_{1-y}/\text{GaAs}$ superlattices, taking into account microscopic processes of anion exchange, desorption, and segregation, and is plotted as the solid curve in Fig. 3. This curve is calculated using identical dosing (r) and desorption (E_d and τ_{0d}) parameter values which were used in Eq. (2) to obtain the dashed curve, while adjusting at the same time two segregation parameters, E_s and τ_{0s} . Nonlinear least-squares fit to the experimental data points for 4 s nitridations finally results in the estimate for N surface segregation energy equal to $0.9 \text{ eV} \pm 30\%$. Obviously, from Fig. 3, it is seen that with the corrected Eq. (8) very good agreement with experimental data is obtained, which confirms our N surface segregation hypothesis.

Additionally, the compositional-profile smearing of N along the growth direction would be expected as a natural consequence of the segregation process, which is confirmed in preliminary cross sectional scanning tunneling microscopy (STM) images of one of our superlattices.¹⁴ Unfortunately, such profile smearing effects would tend to limit the abruptness of the GaN/GaAs interface. However, it is possible that smearing effects might be controlled through some of the

MBE techniques which have been successfully used in the problem of dopant-profile smearing in MBE-grown Si.¹⁵ Also, the cross-sectional STM as a direct imaging technique might provide another way to determine E_s , since our model predicts distribution of nitrogen in the superlattice period ($S_n(0)$), as a function of N surface activation energy E_s and growth temperature T .

V. SUMMARY

In conclusion, a simple, but plausible kinetic model have been developed to conclusively establish and quantitatively explain some of the microscopic processes observed in ECR-MBE grown $\delta\text{-Ga}_x\text{N}_{1-x}\text{As}_{1-y}/\text{GaAs}$ strained layer superlattices. Particularly, the strong $y(T)$ dependence, obtained through *ex situ* HRXRD of our superlattices, is fully understood in terms of energetically favorable surface anion exchange and combined, thermally activated N surface-segregation/surface-desorption. Finally, our model predicts for the first time numerical estimates of the kinetic parameters associated with N surface-segregation process, which appears to be significant under typical GaN/GaAs ECR-MBE growth conditions.

ACKNOWLEDGMENTS

This work was supported by Advanced Research Project Agency, and monitored by Office of Naval Research under Grant No. N00014-92-J-1845. Additionally, two of us (R.J.H. and M.L.O.) wish to acknowledge the support of Air Force Office of Scientific Research under Contract Nos. F49620-93-1-0211 and F49620-93-1-0389, and the support of the Advanced Research Projects Agency, monitored through the Army Research Office under Contract No. DAAH04-94-G-0393.

- ¹S. Nakamura, M. Senoh, S. Nagahama, N. Iwasa, T. Yamada, T. Matsushita, H. Kiyoku and Y. Sugimoto, *Jpn. J. Appl. Phys.* **35**, 74 (1996).
- ²S. Nakamura, M. Senoh, N. Iwasa, and S. Nagahama, *Appl. Phys. Lett.* **67**, 1868 (1995).
- ³I. Akasaki, H. Amano, S. Sota, H. Sakai, T. Tanaka, and M. Koike, *Jpn. J. Appl. Phys.* **34**, 1517 (1995).
- ⁴H. Sakai, T. Koide, H. Suzuki, M. Yamaguchi, S. Yamasaki, M. Koike, H. Amano, and I. Akasaki, *Jpn. J. Appl. Phys.* **34**, L1429 (1995).
- ⁵W. Gotz, N. M. Johnson, J. Walker, D. P. Bour, H. Amano, and I. Akasaki, *Appl. Phys. Lett.* **67**, 2666 (1995).
- ⁶S. N. Mohammad, A. A. Salvador, and H. Morkoç, *Proc. IEEE* **83**, 1306 (1995).
- ⁷R. J. Hauenstein, D. A. Collins, X. P. Cai, M. L. O'Steen, and T. C. McGill, *Appl. Phys. Lett.* **66**, 2861 (1995).
- ⁸R. J. Hauenstein, D. A. Collins, M. L. O'Steen, Z. Z. Bandić, and T. C. McGill, *Mater. Res. Soc. Symp. Proc.* **388**, 259 (1995).
- ⁹M. Sato, *Jpn. J. Appl. Phys.* **34**, 1080 (1994).
- ¹⁰J. Neugebauer and C. G. Van de Walle, *Phys. Rev. B* **51**, 10568 (1995).
- ¹¹S. Sakai, Y. Ueta, and Y. Terauchi, *Jpn. J. Appl. Phys.* **32**, 4413 (1993).
- ¹²Z. Z. Bandić and T. C. McGill (unpublished).
- ¹³*CRC Handbook of Chemistry and Physics*, edited by R. C. West (Chemical Rubber, Boca Raton, FL, 1987), p. E102.
- ¹⁴R. M. Feenstra (unpublished).
- ¹⁵H. Jorke, *Surf. Sci.* **193**, 569 (1988).

Atomic-scale structure and electronic properties of GaN/GaAs superlattices

R. S. Goldman^{a)} and R. M. Feenstra^{b)}

Department of Physics, Carnegie Mellon University, Pittsburgh, Pennsylvania 15213

B. G. Briner^{c)}

IBM Research Division, Yorktown Heights, New York 10598

M. L. O'Steen and R. J. Hauenstein

Department of Physics, Oklahoma State University, Stillwater, Oklahoma 74078

(Received 31 July 1996; accepted for publication 1 October 1996)

We have investigated the atomic-scale structure and electronic properties of GaN/GaAs superlattices produced by nitridation of a molecular beam epitaxially grown GaAs surface. Using cross-sectional scanning tunneling microscopy (STM) and spectroscopy, we show that the nitrided layers are laterally inhomogeneous, consisting of groups of atomic-scale defects and larger clusters. Analysis of x-ray diffraction data in terms of fractional area of clusters (determined by STM), reveals a cluster lattice constant similar to bulk GaN. In addition, tunneling spectroscopy on the defects indicates a conduction band state associated with an acceptor level of N_{As} in GaAs. Therefore, we identify the clusters and defects as nearly pure GaN and N_{As} , respectively. Together, the results reveal phase segregation in these arsenide/nitride structures, in agreement with the large miscibility gap predicted for GaAsN. © 1996 American Institute of Physics. [S0003-6951(96)00150-7]

Nitride-based III-V compound semiconductor heterostructures are promising for optoelectronic devices, such as blue light-emitting diodes¹ and lasers.² In principle, mixed anion nitride/arsenide alloys would enable the fabrication of light emitters operating in the entire visible spectrum. However, for the GaAsN system, calculations predict a limited miscibility of N in GaAs,³ and experiments have presented conflicting results concerning the formation of GaAsN alloys. Apparently, thick layers ($>0.5 \mu\text{m}$) of dilute $\text{GaAs}_{1-x}\text{N}_x$ ($x \leq 0.03$) alloys have been produced by nitride growth,^{4,5} and attempts to increase the nitrogen composition in the alloy using GaAs surface nitridation resulted in GaAs/GaN/GaAs thin-layer structures⁶ and $\text{GaAs}_{1-x}\text{N}_x/\text{GaAs}$ superlattices ($0.04 \leq x \leq 0.33$).^{7,8} The identification of the nitride/arsenide structures as binary or ternary alloys has relied upon x-ray diffraction (XRD), which has spatial resolution of hundreds of microns and averages over many surface layers parallel to the interfaces. Thus, standard interpretations may lead to misleading results in terms of ternary alloy formation if the structures are not continuous films of homogeneous material. Therefore, a detailed study of the atomic-scale structure and electronic properties at nitride/arsenide interfaces is essential for the understanding of alloy formation in this materials system.

In this letter, we present cross-sectional scanning tunneling microscopy (STM) and spectroscopy investigations of GaN/GaAs superlattices produced by nitridation of a molecular beam epitaxially grown GaAs surface. Our cross-sectional studies indicate that the nitrided layers are not continuous films, but consist of regions with sparse N content

and larger clusters. Analysis of x-ray diffraction data in terms of fractional area of clusters reveals a cluster lattice constant similar to bulk GaN, indicating that the nitrided regions consist of nearly pure GaN. Spectroscopic studies on the atomic-scale defects reveal a state in the conduction band associated with an acceptor level of N_{As} in GaAs, which allows us to identify the defects as N_{As} . The observed lateral inhomogeneity and lack of ternary alloy formation indicate that phase segregation has occurred, in agreement with the prediction of a large miscibility gap in the GaAsN system.³ In addition, spectroscopy on the clusters reveals band gap narrowing which may be associated with a few percent As in highly strained GaN, and an upward shift of the band edges due to band bending at the cluster/GaAs interface.

The samples were prepared using a combination of solid Ga and As_2 effusion and ECR-plasma-excited N_2 gaseous sources.⁷ Thirty-six period superlattices were produced by a growth and nitridation procedure (based on the principle of N-As surface anion exchange),⁷ with substrate temperatures ranging from 540 to 560 °C. Reflection high energy electron diffraction obtained during surface nitridation revealed a specular, commensurate (3×3) pattern, indicating coherent growth.⁷ Simulations of XRD data suggested that the structures consist of coherently strained superlattices, with monolayer thickness $\text{GaAs}_{0.79}\text{N}_{0.21}$ embedded in 192 Å GaAs layers. For STM studies, the samples were cleaved to expose a (110) surface, in an ultra-high-vacuum chamber with base pressure $<4 \times 10^{-11}$ Torr. STM was performed with electrochemically etched single-crystal $\langle 111 \rangle$ -oriented W tips cleaned by *in situ* electron bombardment and characterized by *in situ* field-emission microscopy. Typically, images were obtained with a constant tunnel current of 0.1 nA. Details of the STM design,⁹ cleavage procedure,¹⁰ and spectroscopic methods¹¹ have been described previously.

Figures 1(a) and 2(a) show STM topographic images of the GaN/GaAs superlattices, displayed with the growth direction from right to left. In these empty state images, the

^{a)}Present address: Department of Materials Science and Engineering, The University of Michigan, Ann Arbor, MI 48109-2136. Electronic mail: rsgold@engin.umich.edu

^{b)}Electronic mail: feenstra+@andrew.cmu.edu

^{c)}Present address: Fritz-Haber-Institut, der Max-Planck-Gesellschaft, Faradayweg 4-6, D-14195 Berlin, Germany.

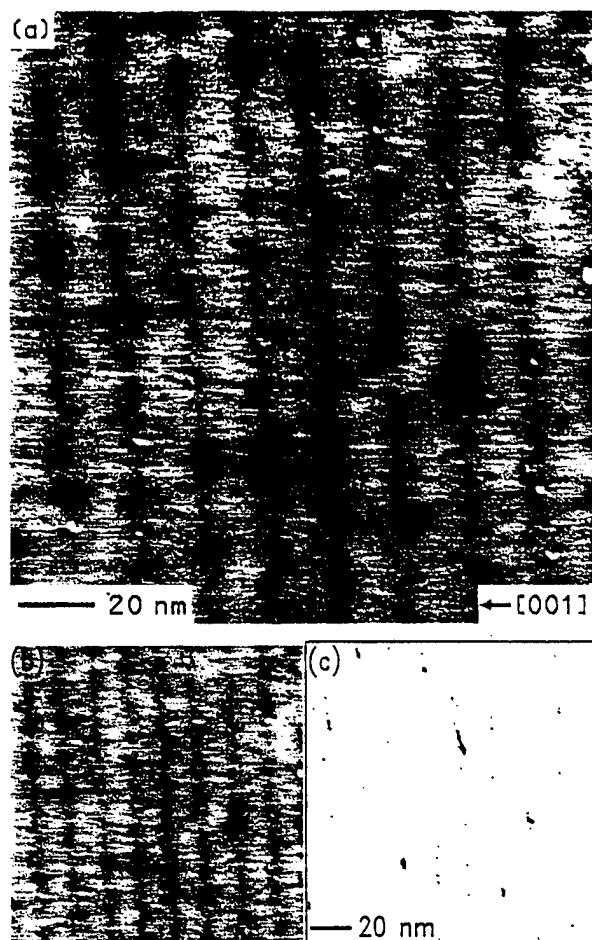


FIG. 1. Large-scale topographic images of GaN/GaAs superlattices, acquired at a sample voltage of +2.2 V. The grey-scale ranges displayed in (a) and (b) are 2.1 and 4.7 Å, respectively. In (c), pixels with tip height more than 2 Å below the nominal GaAs height are displayed as black, while all others are white.

nitrided regions appear as depressions (darker regions) in the surrounding GaAs (brighter regions). The large-scale image in Fig. 1(a), acquired at a sample bias voltage of +2.2 V, indicates that the nitrided layers are not continuous films, but consist of groups of atomic-scale defects and clusters of various sizes. In Fig. 2(a), we present a high-resolution view of the superlattices, acquired at a sample bias voltage of +2.5 V. Fringes with a spacing of 5.65 Å, corresponding to the (001) lattice planes of GaAs, are observed in the bright regions of the image. The image consists primarily of one nitrided layer sandwiched by 160 Å GaAs layers, with tails of additional nitrided layers on the edges of the image. This nitrided layer contains one small cluster and a group of atomic scale defects. It is evident that the extent of nitrogen incorporation in the growth direction is ≥ 30 Å, considerably greater than the simulated monolayer thickness. In filled state images (negative sample bias voltage), the nitrided regions appear bright in comparison with the surrounding GaAs.¹² Since the contrast of the defects and clusters is dependent on the sign of the bias voltage, both features are of electronic rather than topographic origin. In other words, the dark (bright) features in the empty (filled) state images are not pits (protrusions) in the surface but instead regions with different electronic structure.

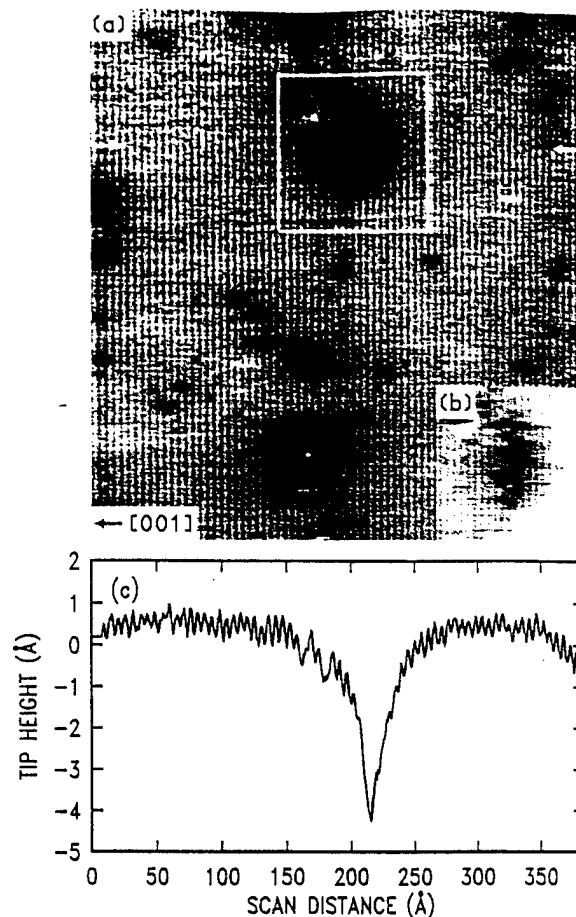


FIG. 2. High resolution topographic image acquired at a sample voltage of +2.5 V. The grey-scale range displayed in (a) is 2.7 Å. A view of the region outlined by a white box in (a) is shown in (b), with a grey-scale range of 4.7 Å. A cut along the line indicated by arrows in (a) is displayed in (c).

In order to quantify the nitrogen content in the structures, we have determined the fractional area of clusters in several large-scale images such as Fig. 1(a). We used an algorithm to count pixels in regions of the image with tip height below a specified value. We estimate a tip height (depth) criterion based on the tip height profile in the vicinity of a cluster. Figure 2(c) is a line cut of the tip height, taken through the center of a cluster, defined by the arrows in Fig. 2(a). The line cut indicates a region of decreased tip height at the cluster, surrounded by a gradual increase in tip height, presumably due to band bending at the cluster/GaAs interface. It is evident from this line cut that the band bending is partly superposed on the GaAs atomic corrugation. This effect is further illustrated for the small cluster outlined by a white box in Fig. 2(a). In Fig. 2(b), the grey scales in the white box region are expanded from 2.7 to 4.7 Å, and the apparent size of the cluster is significantly reduced. Thus, part of the contrast displayed in the clusters in Figs. 1(a) and 2(a) is due to band bending and must be taken into account when counting up the total cluster area. Therefore, the tip height cutoff is defined as the depth at which the atomic corrugation is not observed, approximately 2 Å below the unperturbed GaAs regions. In Fig. 1(b), the grey scales of Fig. 1(a) are expanded from 2.1 to 4.7 Å. In Fig. 1(c), image pixels with tip height more than 2 Å below the nominal GaAs height are displayed as black, while all other image

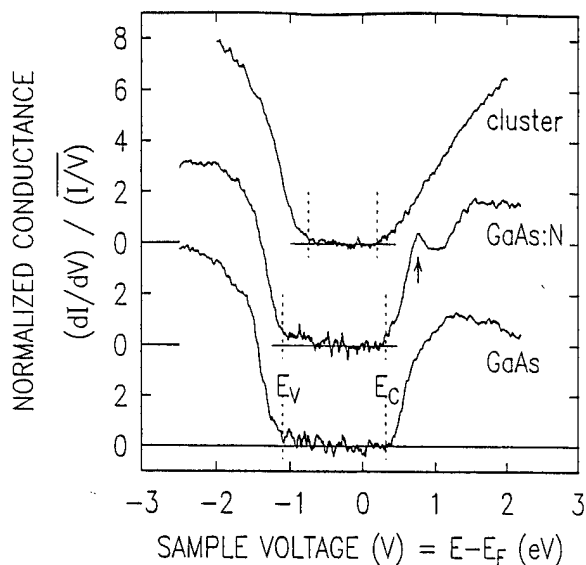


FIG. 3. STM spectra acquired on an atomic scale defect (GaAs:N) and large cluster (lateral extent $> 50 \text{ \AA}$), in comparison with a region of clean GaAs. The valence and conduction band edges are marked by E_V and E_C , respectively. The state associated with an acceptor level of N_{As} in GaAs is indicated by an upward pointing arrow. The sample voltage corresponds to the energy of the state relative to the Fermi level.

pixels are white. The fraction of black regions is $4.45 \pm 0.05 \times 10^{-3}$, which corresponds to only about (1/5) monolayer of GaN per deposited layer, rather than the full monolayer assumed earlier.⁸ A similar fractional area of clusters is obtained in several large-scale images, with total area $> 0.2 \mu\text{m}^2$. High resolution x-ray diffraction data of these GaN/GaAs superlattices indicate an average superlattice lattice constant, 5.6499 \AA , previously interpreted in terms of (continuous) monolayers of $\text{GaAs}_{0.79}\text{N}_{0.21}$ embedded in 192 \AA GaAs layers.⁸ With the knowledge of the fractional area of the clusters, we estimate a cluster lattice constant of $4.6 \pm 0.1 \text{ \AA}$, similar to bulk GaN. Therefore, we conclude that the nitrided regions consist of nearly pure GaN, as opposed to some alloy composition with 20%–30% N.⁸

In order to chemically identify the atomic-scale defects and clusters, we performed spectroscopic measurements on individual defects and clusters of various sizes. In Fig. 3 the normalized conductance versus sample bias voltage are plotted for an atomic scale defect (GaAs:N) and large cluster (lateral extent $> 50 \text{ \AA}$), respectively, and compared with regions of clean GaAs. The GaAs spectrum, shown at the bottom, displays well-defined band edges¹³ with a band gap of $1.43 \pm 0.10 \text{ eV}$, comparable to that of bulk GaAs. The spectrum corresponding to atomic scale defects displays well-defined band edges and band gap similar to GaAs. However, in this case, a state is observed at $0.40 \pm 0.05 \text{ eV}$ above the conduction band edge. The position of this state with respect to the conduction band edge is consistent with the predictions of Wolford *et al.*¹⁴ for N isoelectronic traps in GaAs. Therefore, we associate the state with an acceptor level of N_{As} in GaAs, and identify the atomic-scale defects as N_{As} .

The spectrum corresponding to a large cluster displays several features which are different from the clean GaAs spectrum. The most prominent difference is the reduced band

gap of $1.23 \pm 0.10 \text{ eV}$, which is significantly smaller than band gaps of GaAs (1.43 eV) and GaN (3.5 eV). Recently, a number of theoretical works have predicted band gap bowing in the $\text{GaAs}_{1-x}\text{N}_x$ alloy system.^{3,15–17} The calculated bowing parameters would suggest that the reduced band gap corresponds to a few percent nitrogen or arsenic in $\text{GaAs}_{1-x}\text{N}_x$. However, our analysis of x-ray diffraction data discussed earlier suggests that the clusters are nearly pure GaN. Thus, the band gap reduction may be due in part to a few percent As in GaN with additional reduction due to the high lattice-mismatch strain between the clusters and GaAs.^{12,18–21} In addition to the reduced band gap, the band edges of the cluster spectrum are shifted upward in comparison to the GaAs spectrum. Similar effects are observed in spatially resolved spectroscopy of a small cluster (lateral extent $< 50 \text{ \AA}$), where the band edges are shifted upward as one moves towards the GaAs/cluster interface.¹² The band edge shifts are attributed to electrostatic charging which results in band bending at the cluster/GaAs interface, similar to that observed previously in studies of arsenic precipitates in low-temperature GaAs.²² The upward shift of the band edges of the cluster is consistent with the contrast observed in the bias-dependent images mentioned earlier.¹²

The authors thank C. G. Van de Walle for useful discussions. M.L.O. and R.J.H. acknowledge the support of AFOSR.

- ¹S. Nakamura, T. Mukai, and M. Senoh, *Appl. Phys. Lett.* **64**, 1687 (1994).
- ²S. Nakamura, M. Senoh, S. Nagahama, N. Iwasa, T. Yamada, T. Matsushita, H. Kiyoku, and Y. Sugimoto, *Jpn. J. Appl. Phys.* **1** **35**, L74 (1996).
- ³J. Neugebauer and C. G. Van de Walle, *Phys. Rev. B* **51**, 10568 (1995).
- ⁴M. Weyers, M. Sato, and H. Ando, *Jpn. J. Appl. Phys.* **1** **31**, L853 (1992).
- ⁵M. Kondow, K. Uomi, K. Hosomi, and T. Mozume, *Jpn. J. Appl. Phys.* **1** **33**, L1056 (1994).
- ⁶M. Sato, *Jpn. J. Appl. Phys.* **1** **34**, 1080 (1995).
- ⁷R. J. Hauenstein, D. A. Collins, X. P. Cai, M. L. O'Steen, and T. C. McGill, *Appl. Phys. Lett.* **66**, 2861 (1995).
- ⁸Z. Z. Bandic, R. J. Hauenstein, M. L. O'Steen, and T. C. McGill, *Appl. Phys. Lett.* **68**, 1510 (1996).
- ⁹R. M. Feenstra, *21st International Conference Physics Semiconductors*, edited by P. Jiang and H.-Z. Zheng (World Scientific, Singapore, 1992), p. 357.
- ¹⁰R. M. Feenstra, E. T. Yu, J. M. Woodall, P. D. Kirchner, C. L. Lin, and G. D. Pettit, *J. Vac. Sci. Technol. B* **61**, 795 (1992).
- ¹¹P. Mårtensson and R. M. Feenstra, *Phys. Rev. B* **39**, 7744 (1988).
- ¹²R. S. Goldman, B. G. Briner, R. M. Feenstra, M. L. O'Steen, and R. J. Hauenstein (unpublished).
- ¹³R. M. Feenstra, *Phys. Rev. B* **50**, 4561 (1994).
- ¹⁴D. J. Wolford, J. A. Bradley, K. Fry, and J. Thompson, *17th International Conference Physics Semiconductors*, edited by J. D. Chadi and W. A. Harrison (Springer, New York, 1985), p. 627.
- ¹⁵S. Sakai, Y. Ueta, and Y. Terauchi, *Jpn. J. Appl. Phys.* **1** **32**, 4413 (1993).
- ¹⁶S.-H. Wei and A. Zunger, *Phys. Rev. Lett.* **76**, 664 (1996).
- ¹⁷L. Ballaiche, S.-H. Wei, and A. Zunger, *Phys. Rev. B* (in press).
- ¹⁸K. Kim, W. R. L. Lambrecht, and B. Segall, *Phys. Rev. B* **50**, 1502 (1994).
- ¹⁹C. G. Van de Walle, *Phys. Rev. B* **39**, 1871 (1989).
- ²⁰W. Shan, T. J. Schmidt, R. J. Hauenstein, J. J. Song, and B. Goldenberg, *Appl. Phys. Lett.* **66**, 3492 (1995).
- ²¹C. G. Van de Walle (unpublished).
- ²²R. M. Feenstra, A. Vaterlaus, J. M. Woodall, and G. D. Pettit, *Appl. Phys. Lett.* **63**, 2528 (1993).

Kinetic modeling of microscopic processes during electron cyclotron resonance microwave plasma-assisted molecular beam epitaxial growth of GaN/GaAs-based heterostructures

Z. Z. Bandić^{a)}

T. J. Watson, Sr., *Laboratories of Applied Physics, California Institute of Technology, Pasadena, California 91125*

R. J. Hauenstein^{b)} and M. L. O'Steen

Department of Physics, Oklahoma State University, Stillwater, Oklahoma 74078

T. C. McGill^{c)}

T. J. Watson, Sr., *Laboratories of Applied Physics, California Institute of Technology, Pasadena, California 91125*

(Received 5 September 1995; accepted for publication 4 January 1996)

Microscopic growth processes associated with GaN/GaAs molecular beam epitaxy (MBE) are examined through the introduction of a first-order kinetic model. The model is applied to the electron cyclotron resonance microwave plasma-assisted MBE (ECR-MBE) growth of a set of δ -Ga_yAs_{1-y}/GaAs strained-layer superlattices that consist of nitrided GaAs monolayers separated by GaAs spacers, and that exhibit a strong decrease of y with increasing T over the range 540–580 °C. This $y(T)$ dependence is quantitatively explained in terms of microscopic anion exchange, and thermally activated N surface-desorption and surface-segregation processes. N surface segregation is found to be significant during GaAs overgrowth of Ga_yN_{1-y} layers at typical GaN ECR-MBE growth temperatures, with an estimated activation energy $E_s \sim 0.9$ eV. The observed $y(T)$ dependence is shown to result from a combination of N surface segregation/desorption processes.

© 1996 American Institute of Physics. [S0003-6951(96)01211-3]

The wide band-gap refractory semiconductor, GaN, related alloys, and heterostructures have recently come under active investigation due to their technological promise as light emitters in the blue to UV region.^{1–3} While much recent GaN research has emphasized growth of device structures (blue LEDs and lasers) on various substrates,^{4–6} comparatively little work has concentrated on the microscopic growth processes that are of significance, for example, in the electron cyclotron resonance plasma-assisted molecular beam epitaxial (ECR-MBE) growth of GaN-related heterostructures. Recently, we have shown^{7,8} that it is possible to produce high quality, fully commensurate Ga_yN_{1-y}/GaAs strained-layer superlattices (SLS). Analysis of such structures through time-resolved reflection high energy electron diffraction (RHEED) and high-resolution x-ray diffraction (HRXRD) measurements recently revealed evidence of distinct thermally activated microscopic processes, but, in the absence of a quantitative model to consistently account for these separate RHEED and HRXRD observations, only tentative identification of processes, and at best, semiquantitative assessment of kinetics has been possible to date.⁸

In this letter, we examine the initial nitridation, N surface desorption, and N surface segregation processes observed in ECR-MBE-grown Ga_yN_{1-y}/GaAs heterostructures through the introduction of a quantitative model that is based on first-order kinetic theory. For the first time, the existence of a thermally activated N surface-segregation mechanism, which appears to be significant under typical

GaN/GaAs ECR-MBE growth conditions, is conclusively established and quantitatively assessed. Through application of our model to an unusually strong growth temperature dependence of y in Ga_yN_{1-y}/GaAs superlattices, the existence of a strong N-surface-segregation mechanism, which we suggested previously,⁸ but could not conclusively establish in the absence of a suitable quantitative model (which is necessary to adequately describe the combined effects of concurrent, thermally activated N surface-segregation and surface-desorption processes) is now quantitatively confirmed. Numerical estimates of activation energies for the N surface segregation as well as surface desorption processes are given, within the context of first-order kinetics. Finally, the broader significance of a strong N surface-segregation effect to GaN/GaAs heteroepitaxy is discussed.

The samples and experimental details that are of relevance to the present work have been described in Ref. 8; for convenience, we briefly repeat the most pertinent details here. A set of 36-period " δ -Ga_yN_{1-y}/GaAs" superlattices, each consisting nominally of Ga_yN_{1-y} monolayers (ML) separated by GaAs spacers, was grown on GaAs (100) as a function of substrate temperature (540–580 °C) in an ECR-MBE system. Ga_yN_{1-y} monolayers were produced through brief (4 s) N₂ plasma exposure of an As-stabilized GaAs surface, followed immediately by GaAs overgrowth at a fixed growth rate (0.75 ML/s), and an "As-soak" (30 s). The entire sample set was characterized through HRXRD, which confirmed commensurate growth, and from which N content (y in Ga_yN_{1-y} layers) was determined. The resultant compositional dependence on growth temperature, $y(T)$, from Ref. 8 is reproduced here in Fig. 1. For the purpose of the present work, the key finding is the unexpectedly abrupt

^{a)}Electronic mail: zzb@ssdp.caltech.edu

^{b)}Electronic mail: rjh@hyper.phy.okstate.edu

^{c)}Electronic mail: tcm@ssdp.caltech.edu

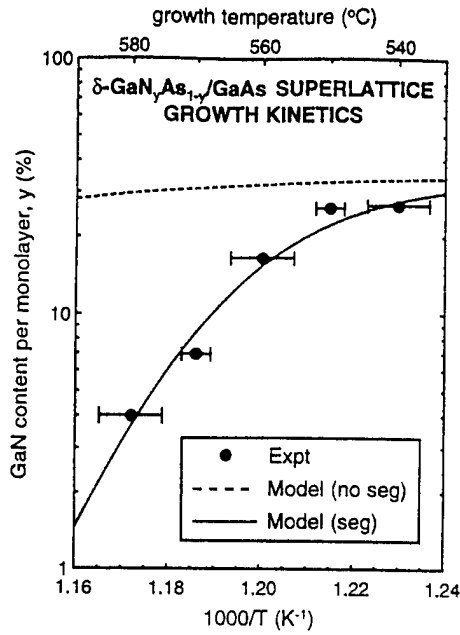


FIG. 1. Growth-kinetic models to explain the strong $y(T)$ dependence observed for ECR-MBE-growth $\delta\text{-Ga}_x\text{N}_{1-x}/\text{GaAs}$ strained-layer superlattices. Experimental data points are reproduced from Ref. 8. Dashed curve: model calculation neglecting N surface segregation [Eq. (2)]. Solid curve: model calculation including segregation [Eq. (4)].

drop in y with increasing growth temperature.

We now wish to understand the physical origin of this $y(T)$ dependence. For this purpose, we devise an analytical model, based on first-order-kinetics arguments, which explicitly incorporates the distinct phases of our particular SLS growth sequence (nitridation/overgrowth/soak) as described above. First, let us consider the nitridation phase. The essential physical processes that describe the net rate of surface nitridation have been previously identified;⁷ they are (i) N-for-As surface anion exchange (N gain), and (ii) surface N desorption (N loss). Mathematically, these processes can be modeled (up to terms linear in N concentration) as

$$\frac{dy}{dt} = s\Phi(1-y) - \frac{y}{\tau_d}. \quad (1)$$

In this equation, the term $-y/\tau_d$ corresponds to N loss due to surface desorption and is described kinetically in terms of a thermally activated rate constant, $\tau_d^{-1} = \tau_{0d}^{-1} \times \exp(-E_d/kT)$, with activation energy E_d . We have directly observed such a process through RHEED observation of nitrided GaAs surfaces at elevated temperatures, and have previously reported estimates for E_d (~ 2.1 eV).⁸

The N gain term [first term on the right hand side of Eq. (1)] represents the N buildup on the As-stabilized GaAs surface due to anion exchange. This process is modeled (again up to terms linear in y) as being proportional to the incident physically activated N flux Φ ; to an overall "efficiency factor" s ;⁹ and, to the fraction of available (As) surface sites, $(1-y)$. Defining an "effective dosing rate" $r \equiv s\Phi$, the solution to Eq. (1) for an initially N-free surface can be written as

$$y(t_{\text{exp}}) = y_{ss}[1 - \exp(-t_{\text{exp}}/\tau)], \quad (2)$$

where $y_{ss} \equiv r\tau$ and $\tau \equiv (\tau_d^{-1} + r)^{-1}$, and t_{exp} is the nitrogen plasma exposure time. Equation (2) models the essential ni-

tridation kinetics without undue mathematical complexity, but ignores the subsequent stages of growth of our superlattices. A comparison of the dashed curve with experimental data points in Fig. 1 graphically illustrates the seriousness of this omission. The dashed curve is a plot of Eq. (2), taking $t_{\text{exp}} = 4$ s, and making use of the RHEED-based experimental desorption parameters, $E_d = 2.1$ eV, and $\tau_d = 7$ s at 592°C .^{7,8} Additionally, the dosing rate r is estimated to be approximately 0.1 Hz from experimental y values at 550°C for 4 and 6 s nitridations.⁸

Upon inspection of Fig. 1 it is evident that the processes of anion exchange and N desorption alone are insufficient to account for the strong falloff of y with increasing growth temperature in our $\delta\text{-Ga}_x\text{N}_{1-x}/\text{GaAs}$ superlattices. The weak falloff of the model (dashed) curve with increasing T results from the negligible N desorption, which would be expected in the short time over which an initially nitrided surface remains exposed; i.e., $(t_{\text{exp}} + t_{\text{ML}}) \leq \tau_d$, where t_{ML} is the monolayer deposition time of the GaAs overlayer. Since surface desorption is the only observed N loss mechanism in our samples, the effective time over which N persists on the (moving) growth surface must be substantially larger than $\sim (t_{\text{exp}} + t_{\text{ML}})$. To explain this, we hypothesize that thermally activated N surface segregation, with rate $\tau_s^{-1} = \tau_{0s}^{-1} \exp(-E_s/kT)$, is occurring during GaAs overgrowth.⁸ This is supported qualitatively by our experimental observation that GaN-related (3×3) RHEED surface reconstructions persist longer at higher substrate temperatures during GaAs overgrowth.

Let us consider explicitly the fractional loss of N from one period of a superlattice during overgrowth. In our model, we shall assume that (1) segregation is allowed only from the current first subsurface to the current surface layer; (2) desorption is allowed from all currently exposed surfaces, i.e., from the current surface and current partially exposed first subsurface layers; and (3) the segregation and desorption processes are statistically independent. It is convenient to define a relative GaN mole fraction S_n in monolayer n where, by definition, the content of the nitrided layer at the end of the nitridation step is normalized to $S_0(t=0) \equiv 1$. Under these conditions, the N content of monolayers n and $n+1$ are related through

$$S_{n+1}(0) = [S_n(0) - S_n(t_{\text{ML}})] \frac{\tau_d}{\tau_{\text{tot}}}, \quad (3)$$

where $\tau_{\text{tot}} \equiv \tau_s + \tau_d$. Also, over the time interval $0 \leq t \leq t_{\text{ML}}$, $S_n(t)$ decays exponentially as $\exp(-t/\tau_{\text{tot}})$, where $\tau_{\text{tot}}^{-1} \equiv (\tau_s^{-1} + \tau_d^{-1})$. Using this expression in Eq. (3), it is straightforward to show that, in order to consistently incorporate N surface segregation into our model, Eq. (2) must be replaced by

$$y(t_{\text{exp}}) = y_{ss} \left[1 - \exp\left(-\frac{t_{\text{exp}}}{\tau}\right) \right] \left(\frac{\tau_{\text{tot}}}{\tau_d + \tau_s e^{t_{\text{ML}}/\tau_d}} \right), \quad (4)$$

where the bracketed factor on the right is merely a dimensionless "correction factor" to Eq. (2) in the range 0 to 1, which physically represents the fraction of the initial N dose that is retained within each (nominally identical) period of the superlattice. Thus, Eq. (4), rather than Eq. (2) above, is

needed to quantitatively describe the nitridation/overgrowth/soak sequence of our $\delta\text{-GaN}_y\text{As}_{1-y}/\text{GaAs}$ superlattices, in terms of microscopic anion exchange, desorption, and segregation processes.

With N surface segregation now properly included in our model, Eq. (4) is plotted as the solid curve in Fig. 1. This curve has been calculated through use of the identical dosing (r) and desorption (E_d and τ_{0d}) parameter values that were used above to obtain the dashed curve while, at the same time, performing a nonlinear least-squares fit to the experimental data points shown in the figure through adjustment of the two segregation parameters E_s and τ_{0s} . The surface-segregation activation energy that results from this procedure is estimated to be $0.9\text{ eV} \pm 30\%$. From the figure it is seen that, with N surface segregation now included in our model, very good quantitative agreement with the experimental data is obtained, thereby tending to confirm our N surface-segregation hypothesis.

Our results imply that a compositional-profile smearing of N along the growth direction should be expected as a natural consequence of the segregation process. Preliminary cross-sectional scanning tunneling microscopy images of one of our superlattices confirm this.¹⁰ Such direct-imaging techniques might provide a means for direct determination of the quantity E_s , since our model predicts the manner in which the spatial extent of profile smearing should increase with increasing growth temperature. Such profile-smearing effects would tend to limit heterojunction abruptness of nitride/arsenide heterostructures (assuming that a given GaN/GaAs-based heterostructure can be stabilized in the first place); however, such smearing effects might possibly be controlled through some of the MBE techniques that have been successfully applied to the problem of dopant-profile smearing in MBE-grown Si.¹¹

In summary, we have developed a kinetic model to help identify and quantitatively assess some of the microscopic processes that are observed in ECR-MBE-grown GaN/GaAs-based heterostructures. Separate experimental observations

of anion exchange, N surface desorption, and an unusually strong decrease in N content with increasing growth temperature for the case of ECR-MBE-grown, coherently strained $\delta\text{-GaN}_y\text{As}_{1-y}/\text{GaAs}$ superlattices, are all quantitatively explained in terms of this single, kinetic model. In particular, the strong $y(T)$ dependence is quantitatively understood for the first time in terms of combined, thermally activated, N surface-segregation/surface-desorption processes. The N surface-segregation process appears to be significant under typical GaN/GaAs ECR-MBE growth conditions. Finally, our model enables for the first time a numerical estimate of the kinetic parameters that are associated with the N surface-segregation process.

This work was supported by the Office of Naval Research under Grant No. N00014-92-J-1845. Additionally, R.J.H. and M.L.O. wish to acknowledge the support of Air Force Office of Scientific Research under Contract Nos. F49620-93-1-0211 and F49620-93-10389, and the support of the Advanced Research Projects Agency, monitored through the Army Research Office under Contract No. DAAH04-94-G-0393.

¹F. Davis, Proc. IEEE **79**, 702 (1991).

²S. Srite and H. Morkoç, J. Vac. Sci. Technol. B **10**, 1237 (1992).

³I. Akasaki and H. Amano, J. Electrochem. Soc. **141**, 2266 (1994).

⁴M. A. Khan, S. Krishnakutty, R. A. Skogman, J. N. Kuznia, D. T. Olson, and T. George, Appl. Phys. Lett. **65**, 520 (1994).

⁵S. Nakamura, T. Mukai, and M. Senoh, Appl. Phys. Lett. **64**, 1687 (1994).

⁶H. Morkoç and B. Sverdlov (unpublished).

⁷R. J. Hauenstein, D. A. Collins, X. P. Cai, M. L. O'Steen, and T. C. McGill, Appl. Phys. Lett. **66**, 2861 (1995).

⁸R. J. Hauenstein, D. A. Collins, M. L. O'Steen, Z. Z. Bandić, and T. C. McGill, Mater. Res. Soc. Symp. Proc. **388**, 259 (1995).

⁹The efficiency factor (defined here with units of area) corresponds to possible physical subprocesses such as adsorption, surface migration, dimerization and re-evaporation, chemical kinetics of As-N exchange, etc., and in general might depend on surface chemistry, strain, and temperature, but in our simplified model, is approximated as constant over the temperature and compositional ranges of interest.

¹⁰R. M. Feenstra (unpublished).

¹¹H. Jorke, Surf. Sci. **193**, 569 (1988).

Reflection high energy electron diffraction study of nitrogen plasma interactions with a GaAs (100) surface

R. J. Hauenstein,^{a)} D. A. Collins,^{b)} X. P. Cai, M. L. O'Steen, and T. C. McGill^{b)}
Oklahoma State University, Stillwater, Oklahoma 74078

(Received 20 October 1994; accepted for publication 7 March 1995)

Effect of a nitrogen electron-cyclotron-resonance (ECR) microwave plasma on near-surface composition, crystal structure, and morphology of the As-stabilized GaAs (100) surface is investigated with the use of digitally image-processed *in situ* reflection high energy electron diffraction. Nitridation is performed on molecular beam epitaxially (MBE) grown GaAs surfaces near 600 °C under typical conditions for ECR microwave plasma-assisted MBE growth of GaN films on GaAs. Brief plasma exposures ($\approx 3\text{--}5$ s) are shown to result in a specular, coherently strained, relatively stable, GaN film approximately one monolayer in thickness, which can be commensurately overgrown with GaAs while longer exposures (up to 1 min) result in incommensurate zincblende epitaxial GaN island structures. Specular and nonspecular film formations are explained in terms of N-for-As surface and subsurface anion exchange reactions, respectively. Commensurate growth of ultrathin buried GaN layers in GaAs is achieved. © 1995 American Institute of Physics.

Recent progress in epitaxial growth techniques has prompted a renewed interest in wide-band-gap, "refractory" compound semiconductor materials based on GaN. In particular, the growth, properties, and technological prospects in blue-to-UV optoelectronic and high temperature electronic device applications of GaN and its related alloys and heterostructures with AlN and InN have been the subject of a number of recent reviews.¹⁻³ Indeed, several recent successes with GaN-based materials, including room-temperature optically pumped blue stimulated emission⁴ and the demonstration of intense emission from blue⁵ and blue-green⁶ light-emitting diode (LED) devices, appear to validate the promise of wide-gap III-V semiconductors as an alternative to II-VI materials for short-wavelength optoelectronic applications. However, despite numerous reports of epitaxial growth of GaN on GaAs, Al₂O₃, Si, and other substrates, primarily through metalorganic chemical vapor deposition⁷ (MOCVD) and molecular beam epitaxial⁸⁻¹⁰ (MBE) techniques, relatively little is known about the underlying phenomena, processes, and kinetics associated with the initial formation of GaN epitaxial films.

In this paper, the initial formation and stability of GaN on GaAs under electron-cyclotron-resonance microwave-plasma-assisted MBE (ECR-MBE) growth conditions is studied with the use of *in situ* reflection high energy electron diffraction (RHEED) techniques. Exposure of GaAs to the nitrogen plasma is seen to result in GaN formation through surface and subsurface anion exchange, *without* the use of codeposited Ga. A preliminary assessment of the anion-exchange kinetics is given. It is shown that limited plasma exposure results in the formation of a specular, *coherently strained*, GaN film, presumed to be close to one monolayer (ML) in thickness, which can be overgrown with commensurate GaAs overlayers, whereas slightly longer plasma ex-

posure results in incommensurate, three-dimensional island formation of zincblende GaN. To our knowledge, this is the first time that commensurate growth has been reported for such a large lattice constant mismatch (25%) in a heteroepitaxial structure.

The samples used in this study were prepared in a manner similar to that followed in the usual ECR-MBE growth of GaN films on GaAs from a combination of conventional solid Ga and As effusion and ECR-plasma-excited N₂ gaseous sources,¹⁰ except that no Ga flux was used in our initial nitride layer formation. All MBE growth, nitridation, and RHEED observations were performed in a Superior Vacuum Technology Model 433R solid-source III-V system, which has been retrofitted with a Wavemat Model MPDR 610iA ECR microwave plasma source and a 2000 l/s cryopump. First, GaAs buffer layers ($\approx 1\text{ }\mu\text{m}$) were epitaxially deposited onto on-axis (100) GaAs epi-ready substrates at a substrate temperature of 600 °C and a growth rate of 0.73 ML/s, following well established *in situ* surface preparation and growth procedures.¹¹ Next, the substrate temperature was lowered to 580 °C, and a steady-state flow (26 sccm, 2×10^{-4} Torr chamber pressure) of filtered, commercial ultra-high purity N₂ gas was established through the ECR source into the growth chamber, while a continuous As₂ flux was used throughout to maintain the As-stabilized GaAs (100) surface condition. At this point, the following basic sequence of events was implemented in each of three MBE runs: nitridation (plasma exposure at 100 W forward microwave power); stability assessment (with or without an As₂ flux); and GaAs overgrowth. Plasma exposure times, substrate temperature, and GaAs growth rate were varied to aid in interpretation of the salient phenomena. RHEED pattern images were recorded throughout these procedures with the use of a CCD camera and S-VHS VCR unit. Subsequently, selected frames were captured digitally on playback through the use of a frame grabber, and analyzed in detail with the aid of custom-developed image processing and analysis software.¹²

^{a)}Electronic mail: rjh@hyper.phy.okstate.edu

^{b)}Also with T. J. Watson Laboratories of Applied Physics, 128-95, California Institute of Technology, Pasadena, CA 91125.

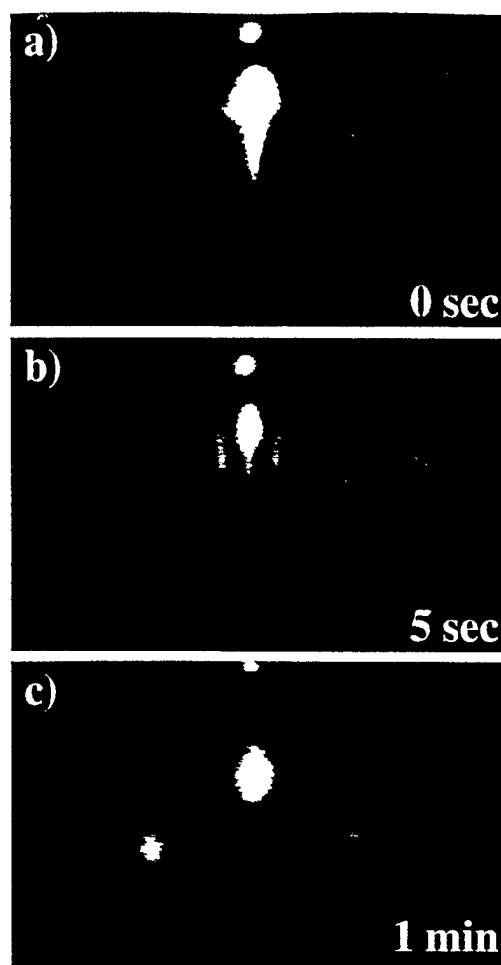


FIG. 1. RHEED patterns along the substrate [110] azimuth, showing surface nitridation of GaAs (100) at 600 °C as a function of exposure time. (a) Initial GaAs (2×4) reconstruction ($t=0$); (b) commensurate, specular GaN (3×3) reconstruction ($1 < t \leq 5$ s); (c) incommensurate, nonspecular zincblende GaN ($t > 5$ s).

The effects of nitridation of a GaAs (100) surface on surface structure and morphology are assessed through RHEED analysis as shown in Fig. 1. Presented in this figure are a sequence of RHEED patterns, taken along the substrate [110] azimuth, that reveal the evolution of surface microstructure and morphology as a function of plasma exposure time. Figure 1(a) shows the un-nitrided GaAs (100) buffer layer surface, which is seen here to exhibit the characteristic As-stabilized (2×4) surface reconstruction. Upon initial plasma exposure, the pattern shifts immediately (~ 1 s) to a new, (3×3) reconstruction pattern shown in Fig. 1(b). This streaked pattern, characteristic of a specular epitaxial surface, upon further plasma exposure quickly (> 5 s at 600 °C) gives way to the spotty pattern shown in Fig. 1(c). The spotty pattern, characteristic of an epitaxial but microscopically rough surface, is recognizable as the diffraction pattern of zincblende GaN, and this pattern persists up to our maximum exposure time of 1 min.

It is possible to recover information about the in-plane lattice constant a_{\parallel} through measurement of the horizontal spacing of the diffraction features shown in Fig. 1. Figure 2 shows a comparison of the diffracted intensity versus horizontal position for the three RHEED images presented in

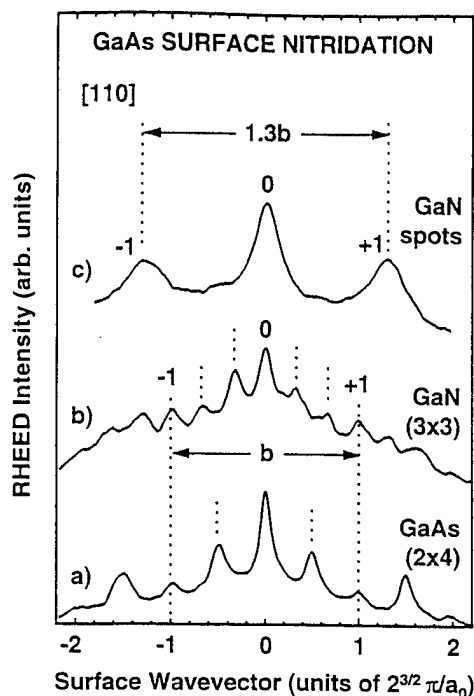


FIG. 2. Horizontal linescans [curves (a)–(c)] for the corresponding RHEED images shown in Fig. 1. Principal and equally spaced fractional-order peaks are indicated. The GaN (3×3) pattern [curve (b)] is commensurate with the substrate (a_0 = GaAs lattice constant) while the peak spacing in curve (c) indicates a partially relaxed zincblende GaN film.

Fig. 1. The abscissa corresponds to surface reciprocal lattice vector G_x , given in units of $(2\pi\sqrt{2}/a_0)$, where a_0 is the bulk GaAs lattice constant. In these units, the diffraction peak indices for curve (a) in Fig. 2 are directly read from the abscissa. We see immediately from Fig. 2 that the RHEED patterns shown in Figs. 1(a) and 1(b) are *commensurate*. In contrast, the more diffuse spotty pattern is clearly *incommensurate* with the substrate. If we define the spacing between the ± 1 GaAs diffraction orders as b , then we see from Fig. 2 that the ± 1 -order peak separation in curve (c) is $1.3b$, corresponding in real space to an in-plane lattice constant of $a_{\parallel}/1.3 = 4.3$ Å, close to the value of $a_0^{\text{GaN}} = 4.52$ Å, the lattice constant of bulk GaN. This slight discrepancy in lattice constants, and the extremely diffuse character of the diffraction spots, suggest the presence of inhomogeneously distributed residual strain in the GaN layer.

The effect of an As_2 flux on the onset and stability of the (3×3) RHEED pattern has also been investigated. Our observations indicate that, once nitrided, in the absence of an As_2 flux, the newly established RHEED patterns are comparatively stable (~ 1 min) even near 600 °C. This is in direct contrast to the case of GaAs at similar temperatures, whereupon removal of As_2 flux results in immediate loss of surface As, followed by a subsequent loss of subsurface As. The above suggests that negligible As is associated with the patterns shown in Figs. 1(b) and 1(c). Additionally, since the time scale of the initial transition to the (3×3) pattern (~ 1 s) is comparable to that of volatilization of surface As from GaAs, it is reasonable to conclude that the pattern in Fig. 1(b) corresponds to a nearly complete replacement of surface As by N while the formation of a GaN pattern of Fig. 1(c) is

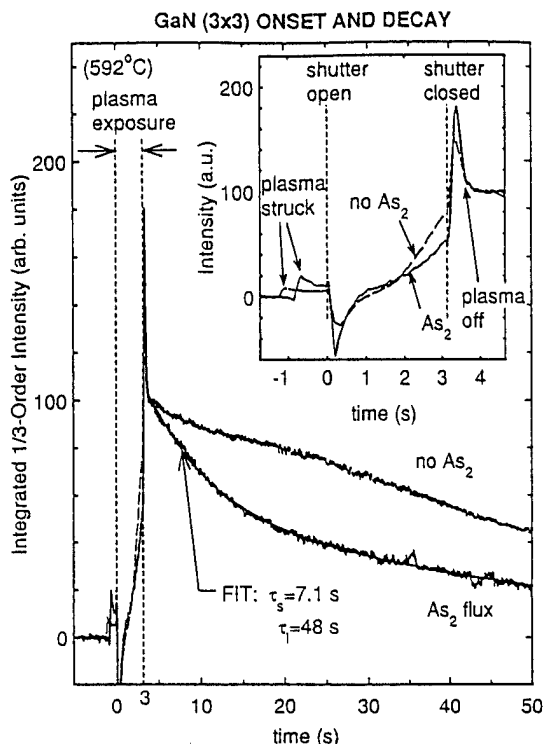


FIG. 3. Effect of As_2 flux on initial formation (inset) and stability (main figure) of the GaN (3 \times 3) surface, as monitored through time dependence of the integrated $\frac{1}{3}$ -order streak. Data for a 3 s plasma exposure at 592 °C are shown. Pertinent timing events and fit to Eq. (1) are indicated.

evidently the result of further (subsurface) atomic exchange.

A quantitative examination of the rates of initial formation and subsequent decay of the GaN (3 \times 3) surface at 592 °C and as a function of differing incident flux conditions is presented in Fig. 3. There, we present the time dependence of the 1/3-order GaN diffraction streak during initial nitridation and subsequent plasma removal. Also indicated are relevant events such as shutter and plasma (de)activation, both of which were observed to induce comprehensible artifacts due to electrostatic perturbation from the plasma source. Figure 3 clearly indicates a pronounced increase in the decay rate of the GaN surface under the presence of an As_2 flux ("As-soak" case) in comparison with the condition in which only background As ("no-soak") is present. Qualitatively, for the As-soak case, the GaN (3 \times 3) pattern slowly evolves back to the GaAs (2 \times 4), suggesting a gradual replacement of the surface N layer by As atoms. (GaAs overgrowth on such a surface immediately exhibits RHEED oscillations.) In contrast, in the no-soak case, the GaN (3 \times 3) again gradually evolves, but this time, into what appears to be a pattern characteristic of a poorly ordered Ga-stabilized GaAs surface. On the other hand, the As_2 flux appears to have a less significant effect upon the initial nitridation rate of the GaAs surface (inset of Fig. 3). This is consistent with the high volatility of As at the temperature noted above, and with the large difference in Ga-N and Ga-As bond strengths (heats of formation 6.81 and 5.55 eV, respectively)¹³ compared to kT . An analogous situation has been previously investigated in the case of As-for-Sb anion exchange.¹⁴ It is interesting to note that the decay of the $\frac{1}{3}$ -order line in the As-soak case of Fig. 3 can be well represented by an equation of the form

$$I = A_s e^{-t/\tau_s} + A_l e^{-t/\tau_l}, \quad (1)$$

involving the superposition of "short" ($\tau_s \approx 7.1$ s) and "long" ($\tau_l \approx 48$ s) decay processes. A very preliminary analysis of our results at 592 and 613 °C suggests an activation energy of ≈ 2 eV for τ_s and ≈ 3 eV for τ_l .

As mentioned above, commensurate buried layers of GaN were readily produced through limited-exposure surface nitridation, followed by commensurate GaAs overgrowth at monolayer deposition times that are short compared with the surface stability lifetime of the GaN top layer. This technique might be applied to the synthesis of "digital alloys" of $\text{GaN}_y\text{As}_{1-y}$ since it is difficult to form the ternary alloy via plasma-assisted MBE growth.¹⁵ Further, such a digital alloy could be grown commensurately, provided that the usual rules for staying below applicable critical thicknesses of a multilayered structure are obeyed.¹⁶

In summary, we have examined the effects of exposing a GaAs surface to a nitrogen plasma under conditions that are typical of the ECR-MBE growth of GaN films. Direct evidence for the near-surface formation of GaN due to N-for-As anion-exchange processes as the result of plasma-surface interactions, rather than the usual codeposition of the constituent source elements, has been presented. It has been shown that limited plasma exposure results in a single, ultrathin, planar, coherently strained, and comparatively stable GaN layer, which can be commensurately overgrown with GaAs. Finally, multilayers might be used in the synthesis of $\text{GaN}_y\text{As}_{1-y}$ digital alloy structures.

This work was supported in part by the Air Force Office of Scientific Research under Contract Nos. F49620-93-1-0211 and F49620-93-1-0389. Additionally, two of us (D. A. C. and T. C. M.) wish to acknowledge the partial support of the Office of Naval Research under Contract No. N000014-92-J-1845.

¹ R. F. Davis, Proc. IEEE 79, 702 (1991).

² S. Strite and H. Morkoç, J. Vac. Sci. Technol. B 10, 1237 (1992).

³ I. Akasaki and H. Amano, J. Electrochem. Soc. 141, 2266 (1994).

⁴ M. A. Khan, S. Krishnakutty, R. A. Skogman, J. N. Kuznia, D. T. Olson, and T. George, Appl. Phys. Lett. 65, 520 (1994).

⁵ S. Nakamura, T. Mukai, and M. Senoh, Appl. Phys. Lett. 64, 1687 (1994).

⁶ H. Morkoç and B. Sverdlov (unpublished).

⁷ K. Ito, K. Hiramatsu, H. Amano, and I. Akasaki, J. Cryst. Growth 104, 533 (1990).

⁸ T. D. Moustakas, T. Lei, and R. J. Molnar, Physica B 185, 36 (1993).

⁹ M. E. Lin, S. Strite, A. Agarwal, A. Salvador, G. L. Zhou, N. Teragochi, A. Rockett, and H. Morkoç, J. Vac. Sci. Technol. B 9, 1924 (1991).

¹⁰ S. Strite, J. Ruan, Z. Li, A. Salvador, H. Chen, D. J. Smith, W. J. Choyke, and H. Morkoç, J. Vac. Sci. Technol. B 9, 1924 (1991).

¹¹ See, for example, J. D. Grange, in *The Technology and Physics of Molecular Beam Epitaxy*, edited by E. H. C. Parker (Plenum, New York, 1985), Chap. 3.

¹² D. A. Collins, M. W. Wang, R. W. Grant, and T. C. McGill, J. Appl. Phys. 75, 259 (1993).

¹³ *CRC Handbook of Chemistry and Physics*, edited by R. C. Weast (CRC, Boca Raton, FL, 1987), p. E102.

¹⁴ M. W. Wang, D. A. Collins, T. C. McGill, and R. W. Grant, J. Vac. Sci. Technol. B 11, 1418 (1993).

¹⁵ J. W. Orton, C. T. Foxon, T. S. Cheng, D. E. Lacklison, S. V. Novikov, D. Johnson, N. Baba-Ali, T. L. Tansley, S. Hooper, and L. J. Challis, presented at the 36th Electronic Materials Conference, Boulder, CO, 1994 (unpublished).

¹⁶ R. Hull, J. C. Bean, F. Cerdeira, A. T. Fiory, and J. M. Gibson, Appl. Phys. Lett. 48, 56 (1986).

Schottky-based band lineups for refractory semiconductors

M. W. Wang, J. O. McCaldin, J. F. Swenberg, and T. C. McGill^{a)}
T. J. Watson, Sr., Laboratory of Applied Physics, California Institute of Technology,
Pasadena, California 91125

R. J. Hauenstein
Physics Department, Oklahoma State University, Stillwater, Oklahoma 74078

(Received 5 December 1994; accepted for publication 26 January 1995)

An overview is presented of band alignments for small-lattice parameter, refractory semiconductors. The band alignments are estimated empirically through the use of available Schottky barrier height data, and are compared to theoretically predicted values. Results for tetrahedrally bonded semiconductors with lattice constant values in the range from C through ZnSe are presented. Based on the estimated band alignments and the recently demonstrated *p*-type dopability of GaN, we propose three novel heterojunction schemes which seek to address inherent difficulties in doping or electrical contact to wide-gap semiconductors such as ZnO, ZnSe, and ZnS. © 1995 American Institute of Physics.

This letter presents Schottky barrier based estimates of band alignments among tetrahedrally bonded semiconductors with lattice constant values in the range from C to ZnSe. This range includes the refractory semiconductors, e.g., GaN and related nitride compounds, of much current interest due to recent successes in short-wavelength light-emitting devices.¹ The band alignments are determined empirically from Au Schottky barrier height data in a manner similar to that found in Refs. 2 and 3. Basis for the connection between band alignments and Schottky barrier height data can be found in Ref. 4. For our study, we use primarily the limited Schottky barrier data currently available, which nonetheless appear sufficient to indicate some striking differences between small and large lattice-parameter semiconductors. These Schottky-based band edge energies are compared to the predictions of Harrison and Tersoff.⁵ Based on our findings for valence band offsets of wide-gap semiconductors, three applications, each involving heterostructures of *p*-type GaN with wide-gap II–VI semiconductors, are proposed as a means of circumventing limitations in *p*-type dopability or electrical contact formation in the latter materials.

The band alignments are summarized in Fig. 1. The data are presented in the form of a “McCaldin” diagram,⁶ which simultaneously displays lattice parameters, band gaps, band alignments, and dopability. Each semiconductor is represented by a vertical line whose length is determined by the band gap of the semiconductor and whose vertical position is determined by experimental Au Schottky barrier height measurements from the literature, where the zero of energy is defined as the Au Fermi level. The *n*-type dopability is indicated by open and filled triangles for either undopable or dopable material, respectively. Similarly, open and filled squares are used to indicate *p*-type dopability. In cases where only the conduction-band Schottky barrier height ϕ_{Bn} was measured, the valence-band Schottky barrier height, ϕ_{Bp} , was determined using $E_g = \phi_{Bn} + \phi_{Bp}$, where E_g is the semiconductor band gap.

Also shown in Fig. 1 are the band lineups as determined from theoretical predictions of Harrison and Tersoff. These values are indicated by horizontal bars representing the valence band edge. When the predicted E_v lies below the experimental E_v , a vertical dotted line connects the horizontal bar to the symbol for the experimental E_v . For clarity, the theoretically determined conduction band edge positions are not shown. It should be noted that with the exception of a few semiconductors, the calculated E_v values of Ref. 5 are in reasonable agreement with the experimental values, and that discrepancies can generally be explained by the lack of *d*-orbitals in the calculation. All of the values used to produce Fig. 1 are also listed in Table I.^{3,5,7–35}

A few points should be made regarding the experimental band lineup values. For AlN and AlP, no Schottky barrier height data were available, so the valence band edge positions were determined from measurements of the AlN/GaN^{26,27} and AlP/GaP³³ valence band offsets, respectively. For InN, no experimental data were found, so only the calculated band alignment is shown. Other non-Schottky-based measurements suggest that GaN and AlN should lie higher in the diagram,^{36,37} but we use the Au Schottky barrier height result.²⁸ Finally, the equilibrium crystal structure of some of the semiconductors is wurzite instead of zinc blende. For these semiconductors, we use the band gap for the wurzite crystal structure; however, for clarity of presentation, we use the lattice constant for the equivalent zinc blende crystal structure. For SiC, the 3C–SiC band gap and lattice parameter are used. We expect little variation of the E_v values with crystal structure, since the SiC Schottky barrier height data do not show a strong dependence of the valence band position on crystal structure, as supported by the recent measurement of a small valence band discontinuity between 3C–SiC and 6H–SiC.³⁸

Figure 1 shows a similar correlation between dopability and band edge position as observed in earlier studies for larger lattice parameter semiconductors.⁶ A notable exception, however, is GaN which is dopable *p*-type to high levels despite a deep valence band edge. Some possible light emit-

^{a)}Electronic mail: tcm@ssdp.caltech.edu

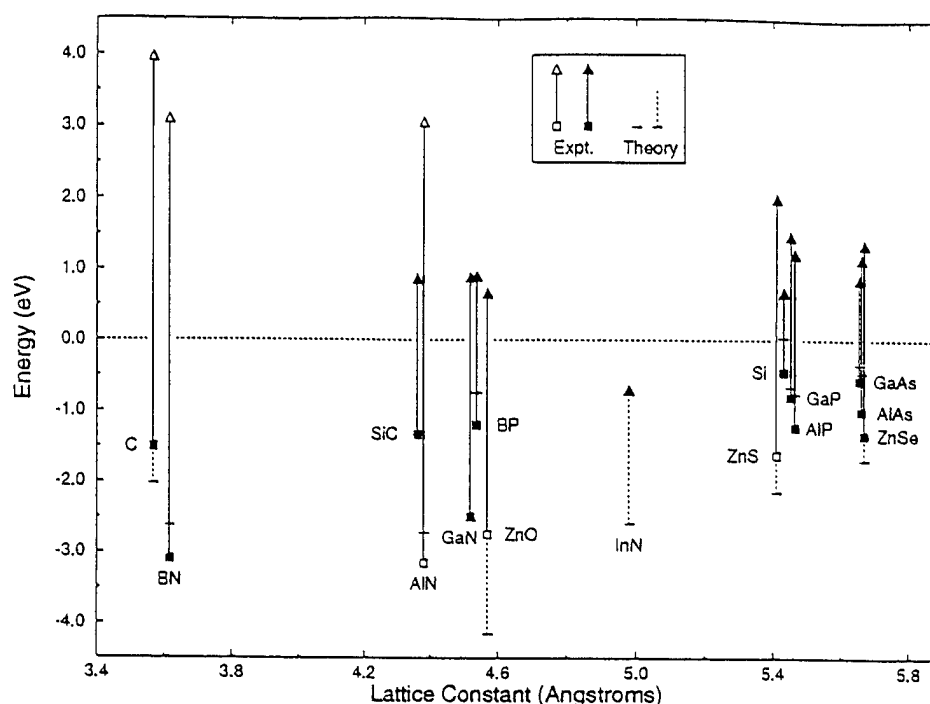


FIG. 1. Diagram for small-lattice parameter tetrahedral semiconductors. Band gaps and band lineups are given by the length and vertical position of the line associated with each semiconductor. Filled and open symbols represent dopable and undopable material, respectively: triangles for *n*-type and squares for *p*-type. Experimental band lineups were determined primarily from Schottky barrier height measurements. The theoretical E_v positions of Harrison and Tersoff (Ref. 5) are indicated by horizontal bars.

ter applications utilizing this *p*-type dopability of GaN are described below.

Graded injector: As explained in detail in Refs. 39 and 40, a suitably designed graded layer near a heterojunction facilitates carrier injection into a semiconductor which is not easily doped with a given carrier type. For example, holes could be injected into ZnO by transport over a small energy barrier from an adjacent layer of GaN, which happens to have a relatively good lattice match to ZnO. The flatband diagram for a *p*-GaN/*n*-ZnO heterojunction shows a moderate barrier for hole injection from *p*-GaN into *n*-ZnO. This barrier can be overcome by grading the GaN into an $\text{Al}_x\text{Ga}_{1-x}\text{N}$ ternary to extend the valence band edge to match that of ZnO at the $\text{Al}_x\text{Ga}_{1-x}\text{N}/\text{ZnO}$ interface. At the same time, the expanded band gap serves to block electron injection from *n*-ZnO into GaN. *p*-GaN/*n*-ZnO is a typical type II heterojunction with barriers to both carrier types, and grading in this manner allows suppression of one carrier flow while enhancing the other. Note that the graded injector approach does not require doping within the graded region.

Type II, no-barrier injector: As has been discussed previously,⁴¹ it is possible to have a type II heterojunction with no barrier for either carrier type when at flatband. Figure 1 indicates excellent prospects for this no-barrier application for *n*-ZnSe/*p*-GaN and *n*-ZnS/*p*-GaN heterojunctions. Of these two, *n*-ZnS/*p*-GaN is particularly attractive because ZnS has not yet been rendered *p*-type. While ZnSe has been made *p*-type, *n*-ZnSe/*p*-GaN could provide an alternative approach to introducing holes into *n*-ZnSe. Both of these examples entail large lattice mismatch at the heterojunction, of the same order as in growing GaN on sapphire. Single-crystal growth has been achieved in the latter case, although

TABLE I. Data for important elemental and binary compound semiconductors with equivalent zinc blende lattice parameters of 5.7 Å or less.

Material	Lat. const (Å) ^a	Band gap ^a (eV)	ϕ_{sp} (eV)	
			Theory ^b	Expt
C	3.567	5.48	2.03	1.5 ^c
SiC	4.360	2.2	1.33	1.3 ^d
Si	5.431	1.12	-0.03	0.45 ^e
Ge	5.658	0.66	-0.32	0.07 ^e
BN	3.616	6.2 ^f	2.62	3.1 ^g
AlN	4.38 ^h	6.2 ^h	2.72	3.15 ⁱ
GaN	4.52 ^h	3.39 ^h	2.55	2.50 ^j
InN	4.98 ^h	1.89 ^h	2.59	...
BP	4.538	2.1 ^k	0.74	1.2 ^l
AlP	5.464	2.45	0.76	1.23 ^m
GaP	5.451	2.27	0.66	0.80 ^e
InP	5.869	1.35	0.77	0.86 ^e
AlAs	5.660	2.15	0.46	1.00 ^e
GaAs	5.653	1.42	0.34	0.56 ^e
ZnO	4.57 ^b	3.4	4.16	2.74 ⁿ
ZnS	5.41	3.62	2.16	1.62 ^o
ZnSe	5.668	2.69	1.69	1.33 ^o

^aReference 7 unless noted otherwise.

^bReference 5

^cReferences 8–14.

^dReferences 8,15–21.

^eReference 3.

^fReferences 22–24.

^gReference 8.

^hReference 25.

ⁱReferences 26,27.

^jReference 28.

^kReferences 22,29–31.

^lReference 32.

^mReference 33.

ⁿReference 34.

^oReference 35.

at a cost in terms of imperfections. However, for some device purposes, such imperfections are tolerable, as demonstrated in recent GaN/sapphire blue light emitters.¹ Furthermore, ZnS as presently used in electroluminescent devices can tolerate grain boundaries and other imperfections.

Ohmic contacts: In principle, *p*-GaN can introduce holes into any material with E_v lying higher in Fig. 1 than E_v (GaN). This means that Ni/Au on *p*-GaN, which forms an Ohmic contact, could be used to contact those materials that are dopable *p*-type, but not to levels sufficient for good Ohmic contact. Two examples are *p*-GaN/*p*-ZnSe and *p*-GaN/*p*-AlP. In practice, such substrate materials should not be heated above the temperatures at which they were processed, a limitation that may possibly be overcome with the improvement of lower-temperature GaN growth methods. As with the other applications described above, energetics are favorable for the proposed devices, but practical problems of fabrication remain.

In conclusion, best estimates of band edge energies for smaller lattice parameter semiconductors, based on Schottky barrier heights, have been presented and compared to theoretical estimates. Based on these data, we have proposed three applications which take advantage of the *p*-type dopability of GaN. A graded injector is proposed to facilitate minority carrier injection into ZnO. Type II, no-barrier injectors are proposed using *p*-GaN/*n*-ZnSe and *p*-GaN/*n*-ZnS heterojunctions. Finally, *p*-GaN is proposed as a possible Ohmic contacting layer to *p*-ZnSe or *p*-AlP.

This work was supported by the Advanced Research Projects Agency monitored under ONR Contract N00014-92-J-1845.

- ¹S. Nakamura, T. Mukai, and M. Senoh, Appl. Phys. Lett. 64, 1687 (1994).
- ²E. T. Yu, J. O. McCaldin, and T. C. McGill, Solid State Phys. 46, 1 (1992), see Figs. 4 and 42, and associated text.
- ³S. Tiwari and D. J. Frank, Appl. Phys. Lett. 60, 630 (1992); Commented on by J. O. McCaldin and T. C. McGill, Appl. Phys. Lett. 61, 2243 (1992).
- ⁴J. Tersoff, in *Heterojunction Band Discontinuities* (North-Holland, Amsterdam, 1987), Chap. 1, p. 5.
- ⁵W. A. Harrison and J. Tersoff, J. Vac. Sci. Technol. B 4, 1068 (1986).
- ⁶J. O. McCaldin, J. Vac. Sci. Technol. A 8, 1188 (1990).
- ⁷Landolt-Börnstein, *Semiconductors* (Springer, Berlin, 1982, 1987), Vols. 17a, 17b, and 22a.
- ⁸C. A. Mead and W. G. Spitzer, Phys. Rev. A 134, 713 (1964).
- ⁹G. H. Glover, Solid State Electron. 16, 973 (1973).

- ¹⁰E. C. Lightowers and A. T. Collins, J. Phys. D 9, 951 (1976).
- ¹¹C. A. Mead and T. C. McGill, Phys. Lett. 58A, 249 (1976).
- ¹²A. Lepek, A. Halperin, and J. Levinson, Phys. Rev. B 19, 2250 (1979).
- ¹³F. J. Himpsel, P. Heimann, and D. E. Eastman, Solid State Commun. 36, 631 (1980).
- ¹⁴M. C. Hicks, C. R. Wronski, S. A. Grot, G. Sh. Gildenblat, A. R. Badzian, T. Badzian, and R. Messier, J. Appl. Phys. 65, 2139 (1989).
- ¹⁵S. H. Hagen, J. Appl. Phys. 39, 1458 (1968).
- ¹⁶S. Y. Wu and R. B. Campbell, Solid State Electron. 17, 683 (1974).
- ¹⁷S. Yoshida, K. Sasaki, E. Sakuma, S. Misawa, and S. Gonda, Appl. Phys. Lett. 46, 766 (1985).
- ¹⁸D. E. Ioannou, N. A. Papanicolaou, and P. E. Nordquist, Jr., IEEE Trans. Electron Devices 34, 1694 (1987).
- ¹⁹Y. Fujii, M. Shigeta, K. Furukawa, A. Suzuki, and S. Nakajima, J. Appl. Phys. 64, 5020 (1988).
- ²⁰J. R. Waldrop and R. W. Grant, Appl. Phys. Lett. 56, 557 (1990).
- ²¹J. R. Waldrop, R. W. Grant, Y. C. Wang, and R. F. Davis, J. Appl. Phys. 72, 4757 (1992).
- ²²V. A. Fomichev and M. A. Rumsch, J. Phys. Chem. Solids 29, 1015 (1968).
- ²³R. M. Chrenko, Solid State Commun. 14, 511 (1974).
- ²⁴N. Miyata, K. Moriki, O. Mishima, M. Fujisawa, and T. Hattori, Phys. Rev. B 40, 12028 (1989).
- ²⁵S. Strite, M. E. Lin, and H. Morkoç, Thin Solid Films 231, 197 (1993).
- ²⁶G. Martin, S. Strite, A. Botchkarev, A. Agarwal, A. Rockett, H. Morkoç, W. R. L. Lambrecht, and B. Segall, Appl. Phys. Lett. 65, 610 (1994).
- ²⁷J. Baur, K. Maier, M. Kunzer, U. Kaufmann, and J. Schneider, Appl. Phys. Lett. 65, 2211 (1994).
- ²⁸P. Hacke, T. Deichprohm, K. Hiramatsu, and N. Sawaki, Appl. Phys. Lett. 63, 2676 (1993).
- ²⁹R. J. Archer, R. Y. Koyama, E. E. Loebner, and R. C. Lucas, Phys. Rev. Lett. 12, 538 (1964).
- ³⁰C. C. Wang, M. Cardona, and A. G. Fischer, RCA Rev. 25, 159 (1964).
- ³¹G. A. Kurbatov, V. K. Sidorin, and A. M. Acheludchenko, Sov. Phys.-Semicond. 17, 7 (1983).
- ³²Y. Kumashiro and Y. Okada, Appl. Phys. Lett. 47, 64 (1985).
- ³³J. R. Waldrop, R. W. Grant, and E. A. Kraut, J. Vac. Sci. Technol. B 11, 1617 (1993).
- ³⁴R. C. Neville and C. A. Mead, J. Appl. Phys. 41, 3795 (1970).
- ³⁵J. O. McCaldin, T. C. McGill, and C. A. Mead, Phys. Rev. Lett. 36, 56 (1976).
- ³⁶G. Martin, S. Strite, J. Thornton, and H. Morkoç, Appl. Phys. Lett. 58, 2375 (1991).
- ³⁷M. C. Benjamin, C. Wang, R. F. Davis, and R. J. Nemanich, Appl. Phys. Lett. 64, 3288 (1994).
- ³⁸K. F. Dombrowski, U. Kaufmann, M. Kunzer, K. Maier, J. Schneider, V. B. Shields, and M. G. Spencer, Appl. Phys. Lett. 65, 1811 (1994).
- ³⁹M. C. Phillips, M. W. Wang, J. F. Swenberg, J. O. McCaldin, and T. C. McGill, Appl. Phys. Lett. 61, 1962 (1992).
- ⁴⁰M. W. Wang, M. C. Phillips, J. F. Swenberg, E. T. Yu, J. O. McCaldin, and T. C. McGill, J. Appl. Phys. 73, 4660 (1993).
- ⁴¹J. O. McCaldin, *Growth and Optical Properties of Wide-Gap II-VI Low Dimensional Semiconductors* (Plenum, New York, 1989), pp. 39-51.

ANION EXCHANGE REACTIONS AND INITIAL GaN EPITAXIAL LAYER FORMATION UNDER NITROGEN PLASMA EXPOSURE OF A GaAs SURFACE

R. J. HAUSTEIN*, D. A. COLLINS**, M. L. O'STEEN*, Z. Z. BANDIC**, AND T. C. MCGILL**

*Oklahoma State University, Dept. of Physics, PS-145, Stillwater, OK 74078

**California Institute of Technology, Dept. of Applied Physics, 128-95, Pasadena, CA 91125

ABSTRACT

Initial nitridation of molecular beam epitaxially (MBE) grown GaAs surfaces by means of an electron cyclotron resonance (ECR) microwave plasma source is investigated *in situ* through time-resolved reflection high energy electron diffraction (RHEED), and *ex situ* high-resolution X-ray diffraction (HRXRD) techniques. Brief ($< 8-10$ s) plasma exposure of GaAs (100) surfaces results in surface N-for-As anion exchange and a new, specular, commensurate (3x3) RHEED pattern which appears to correspond to up to 1 monolayer of coherently strained GaN on GaAs. Anion exchange kinetics is studied through the time-dependence of the onset and decay of the (3x3) RHEED pattern as a function of substrate temperature. For the first time, coherently strained GaN_yAs_{1-y}/GaAs heterostructures are grown and characterized. Direct evidence for thermally activated processes from both RHEED and HRXRD observations is presented, and N desorption and surface-segregation phenomena are proposed to explain the experimental results.

INTRODUCTION

GaN-based wide-gap III-V refractory semiconductors have come under intensely renewed interest as a prospective short-wavelength optoelectronic device material. Several reviews of GaN-based materials have been given recently,¹⁻³ and a number of successful demonstrations of GaN-based blue-green⁴ and blue⁵ light-emitting diode (LED) devices have been reported. Owing to the considerable technological demand for blue-to-UV semiconductor LEDs and lasers, most research on GaN-based wide-gap semiconductors has emphasized light-emitting device structures. In contrast, relatively few reports have concentrated on fundamental investigation of the epitaxial growth process itself. In particular, for the case of electron-cyclotron-resonance microwave plasma assisted molecular beam epitaxial (ECR-MBE) growth of GaN/GaAs structures, the exchange of N and As atoms ("anion exchange") plays a crucial role in the initial stages of epitaxy, but, nonetheless, has received little attention.

In this paper, we investigate anion exchange processes at an initial GaAs (100) surface upon nitrogen plasma (N*) exposure in an ECR-MBE system. Anion-exchange processes are monitored *in situ* through time-resolved reflection high energy electron diffraction (RHEED) techniques. Brief N* exposure is shown to result in the formation of a comparatively stable, coherently strained nitrided surface layer on GaAs, due to N-for-As surface exchange. This layer exhibits a previously unreported (3x3) surface reconstruction, and can be overgrown commensurately with GaAs. In this way, coherently strained GaN_yAs_{1-y}/GaAs strained-layer superlattices are fabricated for the first time, and characterized through high resolution X-ray diffraction (HRXRD). Finally, two important but previously unreported thermally activated

The HRXRD measurements are performed with the use of a Philips Materials Research Diffractometer (MRD) operated in the 4-crystal mode using (220) Ge reflections. Both $\omega/2\theta$ scans, and "area" scans (reciprocal-space mapping), about the substrate (004) and (115) Bragg peaks, respectively, are performed on each sample. Additionally, dynamical simulations of the $\omega/2\theta$ scans, to aid in compositional and strain profile analysis of our superlattices, are computed with the use of the Philips High Resolution Simulation (HRS) software package.

RESULTS AND DISCUSSION

Figure 1 shows schematically the effect of the N^* flux on initial GaAs (100) RHEED pattern. Near 600°C, the characteristic As-stabilized (2x4) GaAs surface reconstruction [Fig. 1(a)] upon N^* exposure immediately changes to the *specular* (3x3) pattern depicted in Fig. 1(b). This reaction is reversible: upon replacement of the N^* flux with an As flux, the pattern again returns to the original (2x4) though *much more slowly* than the forward reaction. We have first reported this behavior elsewhere⁷ where it has been argued that the observed RHEED pattern changes correspond to surface-layer anion exchange of N and As species, for sufficiently brief (< 8-10 s) N^* exposure times. In contrast, we have shown that longer exposure times (up to 1 min) result in the formation strain-relaxed islands of zinc blende GaN.⁷ Together, these observations suggest a *nitridation* of the As-terminated GaAs surface due to incident N^* flux such that first rapid surface, followed by slower subsurface, anion exchange processes, take place.

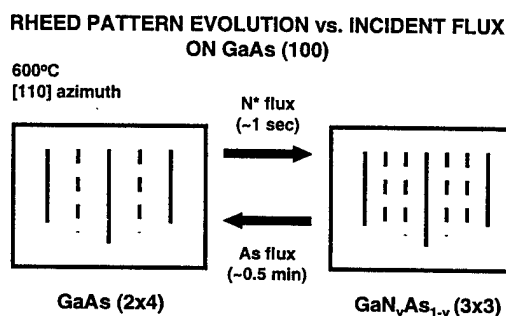


Fig. 1 RHEED Pattern evolution under N^* and As fluxes. Note time scales. GaNAs pattern is *commensurate* w/ substrate. Reaction is reversible, if N^* exposure time is limited to a few sec.

The RHEED pattern dynamics have also been examined quantitatively through time-resolved measurements. The pattern evolution is quantitatively assessed as a function of time through intensity of the 1/3-order reconstruction line. This line, present in the (3x3), but absent from the (2x4) pattern, is taken as a measure of the extent of surface reaction. Assessment of the (3x3) onset and decay are presented in Fig. 2(a). From the inset, it is seen that the presence (absence) of As flux has negligible effect on the rate of surface nitridation (N-for-As replacement), and that the time scale for nitridation is ~1 s. In contrast, the surface, once nitrided, is quite stable, even when all fluxes are removed. Note that the time scale for decay of the (3x3) pattern is *much* longer than that of As-terminated GaAs (2x4) at similar temperature. This result suggests strongly that the (3x3) pattern is primarily associated w/ a N-terminated surface.

strained, as confirmed through (115) area scans. Inspection of the figure clearly reveals a very strong dependence on growth temperature T of the epitaxial structure. Two-dimensional equivalent alloy compositions (y defined above) are determined from XRD peak positions and verified through dynamical simulations; final results are summarized in Table I. Figure 3(b) shows an Arrhenius plot of the resultant ML alloy compositions. The results, within experimental error, clearly suggest two distinct regimes of behavior which act to limit N incorporation: (i) *dose-limited* (low- T); and (ii) *kinetically limited* (high- T). This finding suggests that a thermally activated N surface-segregation process, in addition to the thermally activated N desorption process found above from RHEED data, is active, and can be significant at typical GaN ECR-MBE growth conditions. Extracting an activation energy from the linear portion of the data yields a value which is greater than that found for the desorption processes alone from Fig. 2(b) above, consistent with the existence of an additional thermally activated process. We have developed a kinetic model to account for the observed results, which also quantitatively explains the increased composition observed for the 6 sec exposure (sample OS95.009); this kinetic model will be described in detail elsewhere.⁹

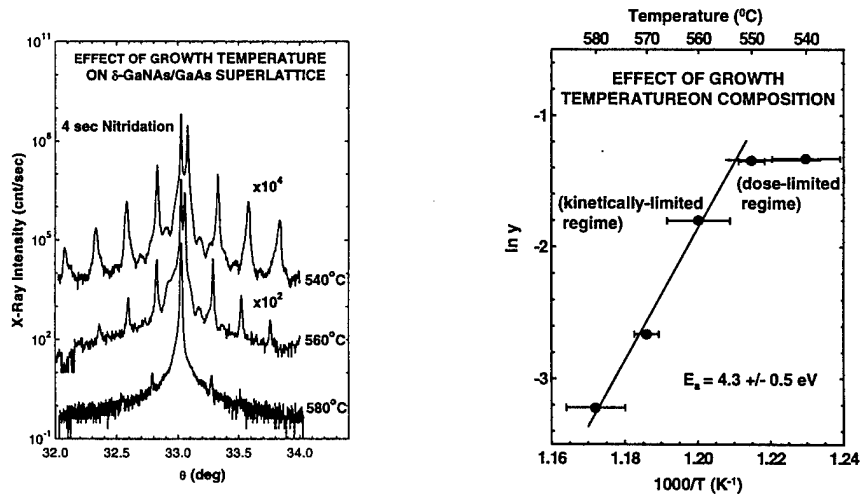


Fig. 3 (a) HRXRD about GaAs (004) for GaN_yAs_{1-y}/GaAs superlattice structures. Results indicate a strong dependence of y on growth temperature. (b) Arrhenius plot, showing the effect of y growth temperature. A thermally activated loss mechanism for the N is suggested. Low- T (dose-limited) and high- T (kinetically-limited) regimes are also seen.

CONCLUSION

In conclusion, we have studied the interaction of a nitrogen ECR microwave plasma and a GaAs surface under typical ECR-MBE growth conditions, and have observed and characterized a number of important new phenomena which are of significance in understanding the initial nucleation kinetics of GaN films on GaAs. Sufficiently brief N* exposure results in the formation of a commensurate, planar surface layer of GaN_yAs_{1-y}, associated with a characteristic (3x3) pattern observable through RHEED, which can be overgrown with GaAs to form a coherently strained GaN/GaAs heterostructure. Finally, direct evidence is presented for the existence of thermally activated N desorption and surface-segregation processes, and preliminary activation energies for these processes are given.

Time-resolved exciton luminescence in GaN grown by metalorganic chemical vapor deposition

W. Shan,^{a)} X. C. Xie, and J. J. Song

Department of Physics and Center for Laser Research, Oklahoma State University,
Stillwater, Oklahoma 74078

B. Goldenberg

Honeywell Technology Center, Plymouth, Minnesota 55441

(Received 26 June 1995; accepted for publication 15 August 1995)

We report the results of time-resolved studies on the exciton radiative decay in single-crystal GaN films grown by metalorganic chemical vapor deposition. Time-resolved photoluminescence (PL) measurements were performed on the samples at various temperatures from 10 to 320 K. The well-resolved near-band-edge luminescence features associated with free excitons and bound excitons in the GaN allow us to unambiguously determine their decay times. We found that the nonradiative recombination processes play an important role and dominate the decay of exciton population. The processes depend on the density of defects and impurities in the GaN samples. © 1995 American Institute of Physics.

GaN-based III-V nitride semiconductors currently attract extensive attention for their potential device applications.¹⁻³ Superbright high-efficient blue LEDs based on nitride structures have been demonstrated by the Nichia group and others.⁴ The observation of optically pumped laser action in GaN with clear resolvable longitudinal lasing modes over a broad temperature range from 10 to 400 K has been recently reported by a few research groups.^{5,6} All this progress has led to much more intense interest in the development of efficient nitride UV-visible light emitters. In this letter, we represent the results of time-resolved studies of nonresonantly excited exciton luminescence in single-crystal GaN epilayer films grown on sapphire substrates by metalorganic chemical vapor deposition. The intrinsic free-exciton (FX) luminescence line in the samples used in this work can be spectrally well resolved from that of excitons bound to neutral donors (BX). This allows us to unambiguously study the recombination dynamics of both intrinsic free excitons and neutral-donor bound excitons.

The GaN samples used in this work were nominally undoped single-crystal films grown by metalorganic chemical vapor deposition on (0001) sapphire substrates.³ The thickness of the GaN epilayers used in this work ranges from 2.5 to 7 μm . Time-integrated photoluminescence (TIPL) measurements were first performed to characterize the GaN samples. The experimental setup for the TIPL measurements consisted of a HeCd laser as an excitation source and a 1.0-M double-grating monochromator with a photon counting and data acquisition system. For time-resolved photoluminescence (TRPL) measurements, the primary excitation source was a pulsed dye laser synchronously pumped by a frequency-doubled mode-locked Nd:YAG laser (82 MHz). The output laser pulses from the dye laser with a pulse duration of less than 5 ps and at the wavelength around 600 nm was then frequency doubled into UV pulses by a nonlinear crystal. The luminescence signals were dispersed by a 1/4 M

monochromator and detected by a synchronscan streak camera with a temporal resolution of 2 ps. The detection system provides the capabilities of simultaneously measuring photoluminescence intensity, time, and wavelength. The overall time resolution of the system is less than 15 ps.

Time-integrated photoluminescence spectra taken from the samples used in this work all exhibit strong, predominant near-band-edge exciton luminescence lines and a weak broadband emission structure peaked at yellow spectral regions. Another weak broadband emission centered at the blue color range could be also detected. The inset of Fig. 1 shows a typical time-integrated PL spectrum taken at 10 K. Two

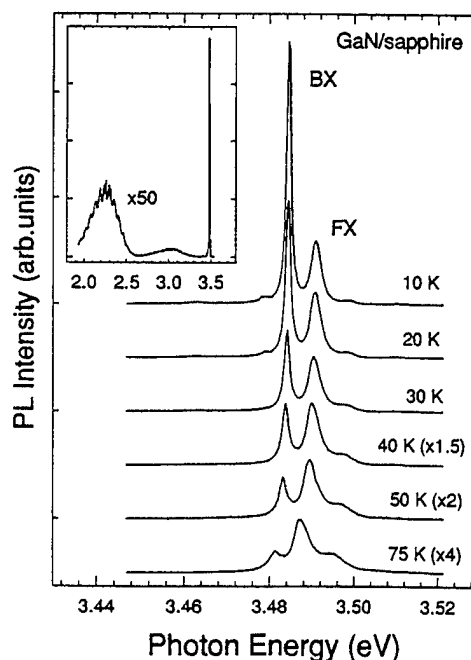


FIG. 1. Time-integrated exciton luminescence spectra of a MOCVD GaN sample taken at different temperatures. The inset shows the 10 K PL spectrum of the sample over a broad spectral range.

^{a)}Electronic mail: wshan@osuunx.ucc.okstate.edu

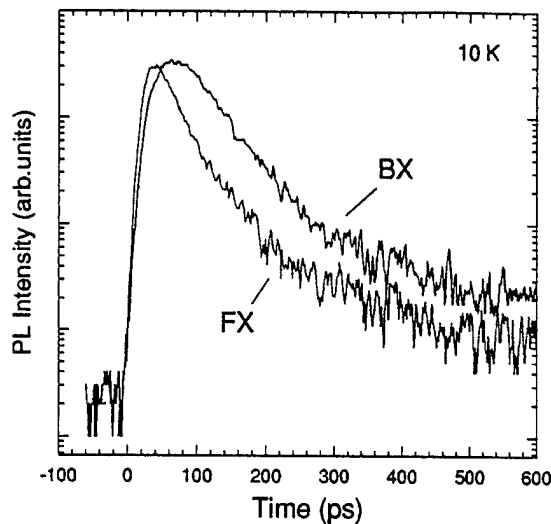


FIG. 2. Temporal variation of spectrally integrated PL for both intrinsic free-exciton and bound-exciton emissions.

sharp luminescence lines dominate near-band-edge emission spectra. The strongest emission line marked by BX in Fig. 1 has a full width at half maximum (FWHM) of less than 1.0 meV at 10 K. The second one labeled FX in the figure shows a FWHM of less than 1.5 meV. The intensity of the BX peak was found to decrease with increasing temperature much faster than that of FX as shown in Fig. 1, where the near-band-edge PL spectral features were plotted as a function of temperature. It became hardly resolvable when the temperature was raised to above 100 K (not shown). Such effects of temperature on the luminescence intensity indicate the emission line resulting from radiative recombination of excitons bound to neutral donors.⁷ The rapid thermal quenching below 100 K implies that the exciton is bound very weakly; hence it must be bound to a shallow neutral donor, not a deep donor, or an acceptor. The second strongest luminescence line (FX), together with the weak emission feature on the higher energy side, can be attributed to intrinsic free-exciton emissions associated with the split-off band states of GaN due to the symmetry of the wurtzite structure.⁸

Figure 2 illustrates the temporal evolution of spectrally integrated exciton luminescence for both free-exciton and bound-exciton emissions observed in a GaN sample at 10 K. The time evolution for both free-exciton and bound-exciton luminescence is dominated by exponential decay. A much weaker long-decay component with an intensity more than two decades smaller compared to the main process could also be observed at low temperatures. The lifetime of the main PL decay was found to be ~ 35 ps for the free-exciton emissions and ~ 55 ps for the bound-exciton emissions for the GaN sample at 10 K. It has to be pointed out that the measurement of luminescence decay time does not provide a direct measurement of radiative lifetime, the measured PL decay time only yields an effective lifetime (τ_{eff}) for free excitons and bound excitons. It involves both the radiative (τ_R) and nonradiative (τ_{NR}) lifetimes with the decay rate expressed as

$$1/\tau_{\text{eff}} = 1/\tau_R + 1/\tau_{\text{NR}}. \quad (1)$$

In this equation we have assumed that the nonradiative decay mechanism is linear, so that a lifetime can be defined. The radiative lifetime for an excited state in a semiconductor can be estimated by considerations of optical transition probability. The radiative lifetime τ_R of the excited state can be described by^{9,10}

$$\tau_R = 2\pi\epsilon_0 m_0 c^3 / \tilde{n} e^2 \omega^2 f, \quad (2)$$

where f is the oscillator strength of the optical transition, \tilde{n} is the refractive index, and the other symbols have their usual meanings. By using $\tilde{n} = 2.4$,¹¹ and $\omega = 5.3 \times 10^{15} \text{ s}^{-1}$ for GaN, one can roughly obtain $\tau_R \sim (800/f) \text{ ps}$. The radiative lifetime of bound excitons in GaN is thus expected to be just a little shorter than 1 ns and on the order of several hundreds of picoseconds if we take the upper limit with its oscillator strength as unity ($f \sim 1$). The oscillator strength of free excitons calculated within the effective-mass approximation is given by $f = E_p / \pi \hbar \omega (V/a_x^3)$, where E_p is the Kane matrix element connecting Bloch states in the valence and conduction bands, V is the volume of unit cell, and a_x is the effective Bohr radius of free exciton. Our result yields $f \sim 0.012$ for the free excitons in GaN using $E_p \sim 18 \text{ eV}$ and $a_x \sim 20 \text{ \AA}$.¹² Thus, the calculated value of the radiative lifetime for free excitons in GaN will be in the several tens of nanoseconds domain.

Generally, the discrepancy between the measured values of PL decay time and the theoretical estimated radiative lifetime can be attributed to nonradiative relaxation processes in competition with the radiative channel. For the case where the nonradiative decay rate is larger, the measured decay time is characteristic for the nonradiative processes in accordance with Eq. (1). This situation is typical for recombination from intrinsic states of semiconductors.¹³ The nonradiative processes such as multiphonon emission, capture by deep centers, Auger effect, etc. give rise to fast relaxation of the excited carriers down to lower states from which they decay radiatively or relax nonradiatively. As a result, the measured PL decay time for a given excited state is an effective lifetime and usually much shorter than a radiative one. This has been observed in a number of semiconductor bulk materials and heterostructures with the measured free-exciton PL decay time decreasing progressively as the density of nonradiative recombination centers increased.¹⁴⁻¹⁶ The slow rise of bound-exciton luminescence intensity compared to that of the free-exciton PL shown in Fig. 2 is an indicator of such nonradiative relaxation processes for free excitons arriving at the bound-exciton energy. Therefore the capture of excitons and trapping of carriers by such nonradiative centers at defects and impurities must play a major role in the recombination processes responsible for the exciton population decay in the GaN samples studied in this work. In fact, the measured PL decay time was found to be directly related to the intensity of broadband emissions lying in the GaN band gap. The broad emission structure referred to as yellow emission in the literature is believed to be associated with the optical transitions between the energy levels involving impurity and/or defect states. The intensity of yellow emission is proportional to the density of some particular defects or impurities present in samples. We found that the

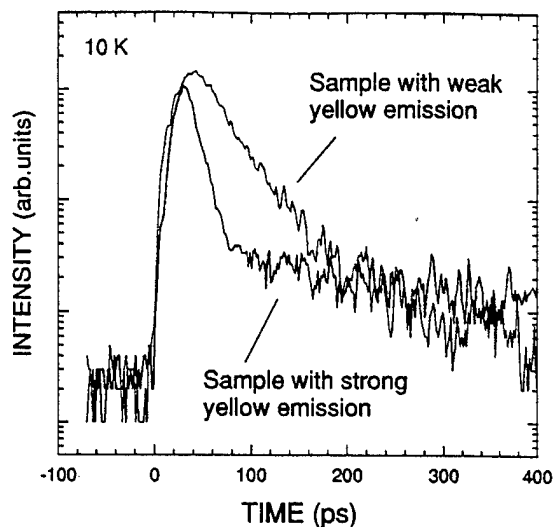


FIG. 3. Comparison of the time decay of free-exciton emission between two GaN samples with the relative intensity ratio of 100:1 for the yellow emission under the same excitation conditions.

stronger the yellow emission, the shorter the PL decay time in a GaN sample. Shown in Fig. 3 is a comparison of free-exciton PL decay between two samples with the relative intensity ratio of 100:1 for the yellow emission under identical excitation conditions. The deduced lifetime of free-exciton emission in the sample with stronger yellow emission is only 15 ps (which is the limit of our instrumental resolution). Therefore, the fast decay behavior of the PL intensity indicates that the capture of excitons and trapping of carriers at defects and impurities through nonradiative combinations dominate the decay of exciton population. The process of capture therefore must depend on the density of defects and impurities in the GaN samples.

The effects of sample temperature on the time decay of exciton luminescence were also examined. The bound-exciton PL decay time was found to decrease slightly with increasing temperature before the emission thermally quenched. The free-exciton PL decay time exhibited slow variations with temperature, either decreasing or increasing, from different samples. It is known that for a radiative recombination dominant system, an increase in the radiative lifetime with temperature is expected for the free excitons^{10,17} since their average kinetic energy is increased. The thermal redistribution results in a decreasing number of the excitons close enough to the Brillouin-zone center for radiative recombination. Also the lifetime is expected to be independent of temperature for bound excitons, and only the emission intensity is expected to decrease because of thermal ionization of the bound excitons. Although recombination from excitons bound to extrinsic states such as defects or impurities can often be very efficient at low temperatures as demonstrated by Fig. 1, the measured decay time is still de-

termined by detailed decay kinetics. The observed decreasing of PL decay time with temperature for the bound excitons in the GaN samples suggests that the incremental stronger non-radiative relaxations occur as the temperature is raised resulting in further faster decay of the exciton population. This can be also evidenced from the decrease of free-exciton PL intensity with temperature. Therefore, the variations of the measured PL decay time for free excitons with temperature in the GaN samples is a result of competition between non-radiative capture of free excitons at defects or impurities and thermally enhanced exciton-exciton and exciton-phonon scatterings.

In summary, we have performed time-resolved luminescence spectroscopy to study the exciton radiative decay in GaN epilayers grown by MOCVD. The decay time for both free-exciton and bound-exciton emissions was found to be quite short compared to the theoretical estimated radiative lifetime. The results suggest that the lifetime of excitons in the GaN samples is governed by nonradiative recombination. The capture of excitons and trapping of carriers at defects and/or impurities through nonradiative relaxation processes dominate the decay of exciton population. The capture process depends on the density of impurities and defects in the GaN samples.

This work was supported by AFOSR, ARPA, and ONR.

- ¹S. Strite and H. Morkoç, *J. Vac. Sci. Technol. B* **10**, 1237 (1992), and references therein.
- ²J. I. Pankove, *Mater. Res. Soc. Symp. Proc.* **162**, 515 (1990), and references therein.
- ³H. Markoç, S. Strite, G. B. Gao, M. E. Lin, B. Sverdlov, and M. Burns, *J. Appl. Phys.* **76**, 1363 (1994), and references therein.
- ⁴See, for example, S. Nakamura, T. Mukai, and M. Senoh, *Appl. Phys. Lett.* **64**, 1687 (1994).
- ⁵X. H. Yang, T. J. Schmidt, W. Shan, J. J. Song, and B. Goldenberg, *Appl. Phys. Lett.* **66**, 1 (1995).
- ⁶A. S. Zubrilov, V. I. Mikolaev, V. A. Dmitriev, I. G. Irvine, J. A. Edmond, and C. H. Carter, Jr., *Inst. Phys. Conf. Ser. No. 141*, 525 (1995).
- ⁷R. Dingle, D. D. Sell, S. E. Stokowski, and M. Ilegems, *Phys. Rev. B* **4**, 1211 (1971).
- ⁸W. Shan, T. J. Schmidt, X. H. Yang, S. J. Hwang, J. J. Song, and B. Goldenberg, *Appl. Phys. Lett.* **66**, 985 (1995).
- ⁹D. L. Dexter, in *Solid State Physics*, edited by F. Seitz and D. Turnbull (Academic, New York, 1958), Vol. 6.
- ¹⁰G. W. 't Hooft, W. A. J. A. van der Poel, and L. W. Molenkamp, *Phys. Rev. B* **35**, 8281 (1987).
- ¹¹*Landolt-Börnstein, New Series, Group III*, edited by O. Madelung (Springer, Berlin, 1982), Vol. 17.
- ¹²The effective Bohr radius of the free exciton in GaN was estimated by $a_x = 0.528(m_0\epsilon/\mu\epsilon_0) \text{ \AA}$, where $\epsilon = \bar{n}^2 (\sim 5.8\epsilon_0)$, and μ is the reduced effective mass, $\sim 0.16m_0$.
- ¹³M. Voos, R. F. Leheny, and J. Shah, in *Optical Properties of Solids*, edited by M. Balkanski (North-Holland, Amsterdam, 1980), Chap. 6, p. 336.
- ¹⁴C. J. Hwang, *Phys. Rev. B* **8**, 646 (1973).
- ¹⁵J. P. Bergman, P. O. Holtz, B. Monemar, M. Sundaram, J. L. Merz, and A. C. Gossard, *Phys. Rev. B* **43**, 4765 (1991).
- ¹⁶J. S. Massa, G. S. Buller, A. C. Walker, J. Simpson, K. A. Prior, and B. C. Cavenett, *Appl. Phys. Lett.* **64**, 589 (1994).
- ¹⁷J. Feldman, G. Peter, E. O. Göbel, P. Dawson, K. Moore, C. Foxon, and R. J. Elliott, *Phys. Rev. Lett.* **59**, 2337 (1987).

Temperature dependence of interband transitions in GaN grown by metalorganic chemical vapor deposition

W. Shan, T. J. Schmidt, X. H. Yang, S. J. Hwang, and J. J. Song
Department of Physics and Center for Laser Research, Oklahoma State University,
Stillwater, Oklahoma 74078

B. Goldenberg
Honeywell Technology Center, Bloomington, Minnesota 55420

(Received 1 August 1994; accepted for publication 9 December 1994)

The interband transitions in single-crystal GaN films grown by metalorganic chemical vapor deposition (MOCVD) have been studied as a function of temperature ($15 \leq T \leq 300$ K) by reflectance and photoluminescence measurements. At low temperatures, well-resolved spectral features corresponding to the GaN band structure were observed. The energies of the excitonic interband $\Gamma_9^V - \Gamma_7^C$, Γ_7^V (upper band) $-\Gamma_7^C$ and Γ_7^V (lower band) $-\Gamma_7^C$ transitions are found to be 3.485, 3.493, and 3.518 eV at 15 K, respectively, for the MOCVD GaN. The spectral features are broadened and shift to lower energy as temperature increases. At room temperature (300 K), the $\Gamma_9^V - \Gamma_7^C$ and Γ_7^V (upper band) $-\Gamma_7^C$ transition energies of this wide band-gap material are determined to be 3.420 and 3.428 eV, respectively. The temperature dependence of these two transitions have been determined using the Varshni empirical relation. Our results yield $E_0(T) = 3.486 - 8.32 \times 10^{-4} T^2 / (835.6 + T)$ eV for the $\Gamma_9^V - \Gamma_7^C$ transition and $E_0(T) = 3.494 - 10.9 \times 10^{-4} T^2 / (1194.6 + T)$ eV for the Γ_7^V (upper band) $-\Gamma_7^C$ transition. © 1995 American Institute of Physics.

GaN-based III-V nitride semiconductors have recently attracted extensive attention because of their importance to both science and technology for the applications toward high-temperature electronics and light emitters and detectors operating in the blue and ultraviolet wavelength range.^{1,2} It is known that GaN has a wurtzite structure in natural form, and has a wide direct band gap of ~ 3.4 eV at 300 K, which provides efficient radiative recombination. The wavelength of radiation from GaN based materials can be tuned over a wide range from visible to ultraviolet by alloying or forming heterostructures such as quantum wells with other nitrides (AlN and InN). Many efforts have been devoted to the preparation of high quality GaN crystals and epitaxial films, the characterization of GaN crystals and films grown by a variety of growth techniques, and the development of devices using GaN based materials.³⁻¹⁴ There have been several reports on the temperature dependence of the GaN band gap.¹⁵⁻²⁴ However, the estimated temperature coefficients reported by the literature vary among the samples prepared by various growth techniques as well as with different optical measurement methods.

In this letter, we present the results of temperature-dependent optical measurements on a single-crystal GaN film grown by metalorganic chemical vapor deposition (MOCVD) on a sapphire substrate. The low-temperature photoluminescence (PL) spectra of the MOCVD GaN samples exhibit a strong, narrow near-band-edge emission structure corresponding to the radiative decay of bound excitons and free excitons. The normally observed donor-acceptor pair recombination spectral signatures could barely be observed, indicating the high quality as well as substantial purity of the samples. The reflection spectra measured at low temperatures consist of a few well-resolved spectral features associated with the free-exciton transitions in the GaN.

While the spectral features are broadened and shift towards lower energy as temperature increases, photoreflectance measurements were employed so as to obtain a better spectral resolution and allow a more precise determination of the transition energies. As a result, the observed interband excitonic transitions [$\Gamma_9^V - \Gamma_7^C$ and Γ_7^V (upper band) $-\Gamma_7^C$] in this MOCVD grown GaN have been mapped out as a function of temperature and the Varshni thermal coefficients²⁵ have been determined.

The GaN sample used in this work was a nominally undoped single-crystal film grown by metalorganic chemical vapor deposition on a (0001) sapphire substrate. A thin AlN buffer layer of ~ 50 nm was deposited on the substrate at about 775 °C before the growth of the GaN epilayer. The 4.2 μm GaN layer was deposited at 1040 °C directly on the AlN buffer. Optical measurements were carried out on the GaN sample over a temperature range from 15 K up to 300 K. Photoluminescence (PL) spectra were measured using an experimental setup consisting of a HeCd laser as an excitation source and a 1-M double-grating monochromator connected with a photon-counting system. For reflectance measurements, quasimonochromatic light dispersed by a 0.5 m monochromator from a halogen tungsten lamp was focused on the sample and the reflection signals were detected by an UV-enhanced Si photodiode or a photomultiplier tube connecting to a lock-in amplification and data acquisition system. In addition, a chopped HeCd laser beam was used to provide optical modulation when the photoreflectance measurements were performed.

To illustrate the quality and purity of the GaN films grown by MOCVD, photoluminescence and reflection spectra of the GaN sample used in this work are shown in Fig. 1 for 15 K. The reflection spectrum (upper curve) has three exciton resonances as indicated by the vertical arrows. The

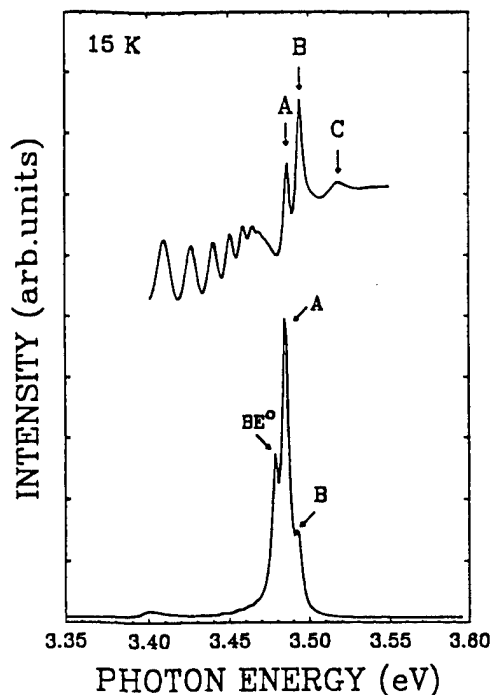


FIG. 1. Reflection (upper curve) and photoluminescence (lower curve) spectra of the MOCVD GaN sample at 15 K are shown for comparison.

excitons referred to as the A, B, and C exciton (Refs. 16 and 22) are related to the $\Gamma_9^V - \Gamma_7^C$, Γ_9^V (upper band) $-\Gamma_7^C$ and Γ_7^V (lower band) $-\Gamma_7^C$ interband transitions in GaN. Their transition energies are 3.485, 3.493, and 3.518 eV, respectively. The oscillations on the lower energy side of the spectrum are caused by interference effects. The PL spectrum (lower curve) exhibits the dominant transitions of the intrinsic free-exciton (FE) emission (A exciton) with the peak energy at 3.4854 eV, together with another FE emission shoulder (B exciton) at a higher energy of 3.4924 and the emission of excitons bound to neutral donors (BE°) at a lower energy of 3.4790 eV. A series of weak luminescence spectral signatures (not shown) at the energy below 3.3 eV was also observed. Temperature-dependent PL measurements were performed to verify the assignments of the emission structures. The intensity of the BE° structure was found to decrease much faster than that of the FE structures (A and B). The emission structure completely disappeared when the temperature was raised to above 100 K, indicating the dissociation of bound excitons due to thermal effects, whereas the structure attributed to the B-exciton emission could be well resolved up to 200 K.

Photoreflectance (PR) spectra measured from the same sample are shown at selected temperatures in Fig. 2. The sharp derivativelike line shapes in the spectra shown in Fig. 2 correspond to the transitions between the edges of different valence bands to that of the conduction band of wurtzite GaN. As the temperature increases, the line shapes of the PR spectral features shift towards lower energy and the sharp features on the lower energy side [corresponding to the $\Gamma_9^V - \Gamma_7^C$ and Γ_7^V (upper band) $-\Gamma_7^C$ transitions] observed at low temperatures gradually broaden and merge together. The weak feature on the higher energy side [corresponding to

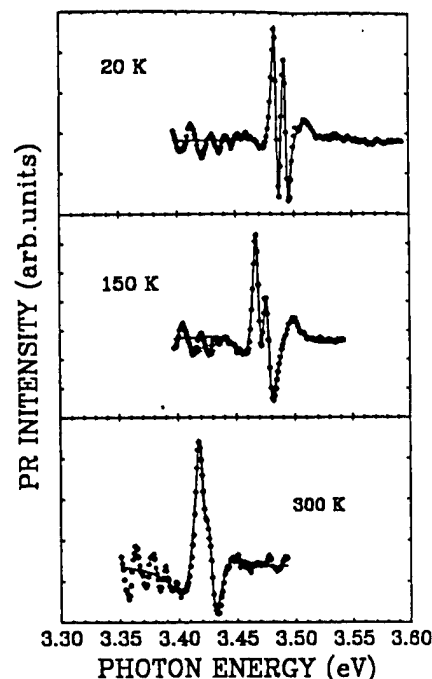


FIG. 2. Photoreflectance spectra of the GaN film at selected temperatures. The solid circles represent experimental data and the solid lines represent the best fits to the data.

Γ_7^V (upper band) $-\Gamma_7^C$ transition] becomes barely resolvable as the temperature increases.

In order to determine the energy positions associated with the optical transitions, the PR spectra were fitted to different line shape functions. The solid lines in Fig. 2 are the best fit to experimental data using the Lorentzian line-shape functional form^{26,27}

$$\Delta R/R = \text{Re}[C e^{i\theta} (E - E_0 + i\Gamma)^{-n}], \quad (1)$$

where C and θ are the amplitude and phase of the line shape, and E_0 and Γ are, respectively, the energy and the empirical broadening parameter of the transitions. The exponent n is a characteristic parameter which depends on the type of critical point in the Brillouin zone and the order of the derivative. While a PR spectrum exhibits sharp derivativelike structures on a featureless background due to the optical modulation, the order of the derivative is not immediately clear. Therefore, it is necessary to use the values of $n=2$ and $n=5/2$, which describe the nature of the interband excitonic transitions and three-dimensional band-to-band transitions, respectively,^{26,27} to fit the PR spectral structures associated with the fundamental band-gap transitions in bulk materials. We found that using $n=2$ (corresponding to the first derivative line shape) results in a better fit to the line positions and widths of the PR spectra than using $n=5/2$ (the third derivative line shape). This was found to be appropriate even at the highest temperature employed. The best fits to the room-temperature (300 K) PR spectral features give an energy of 3.420 eV for the lowest interband ($\Gamma_9^V - \Gamma_7^C$) transition and an energy of 3.428 eV for the second interband [Γ_7^V (upper band) $-\Gamma_7^C$] transition. This suggests that the PR spectra observed at high temperatures are still of the excitonic nature rather than being due to band-to-band transitions, presum-

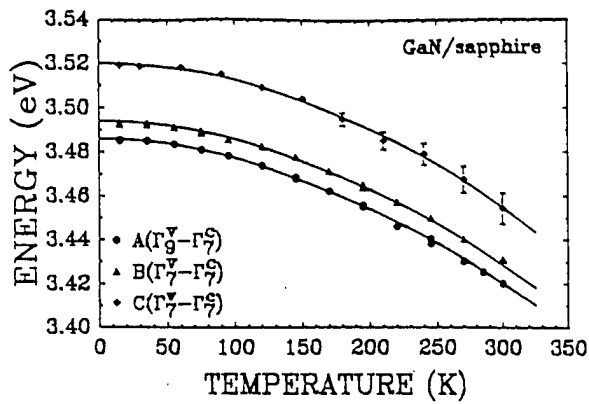


FIG. 3. Temperature dependence of three interband transition energies.

ably because of the large exciton binding energy (~ 28 meV) of this wide band-gap material.¹⁶ It should be pointed out that the PR spectrum taken at room temperature shows a significant phase change compared to others taken at lower temperatures. This might indicate an onset of the occurrence of band-to-band transitions but, as mentioned above, the first derivative functional form of a Lorentzian line shape still produces the best fit to the room-temperature PR spectrum. Attempts were also made to use the functional form for the first derivative of a Gaussian function to fit the experimental data measured at high temperatures. The form describes strong exciton-phonon coupling and inhomogeneous perturbation of a system with a Gaussian absorption profile of excitonic transition.^{28,29} This was done because a Lorentzian absorption profile for an interband excitonic transition at high temperature could be inadequate. However, the fitting results were not as good as the results obtained by using Eq. (1).

Figure 3 plots out the energies as a function of temperature of all three observed interband excitonic transitions in the low-pressure MOCVD GaN. The temperature dependence for the interband transitions was deduced by using the Varshni empirical equation.²⁵

$$E_0(T) = E_0(0) - \alpha T^2 / (\beta + T), \quad (2)$$

where $E_0(0)$ is the transition energy at 0 K, and α and β are constants referred to as Varshni thermal coefficients. The solid lines in the figure represent the least-square fit to the experimental data using Eq. (2). The parameters obtained from the best fit are $E_0(0) = 3.486$ eV, $\alpha = 8.32 \times 10^{-4}$ eV/K, and $\beta = 835.6$ K for the $\Gamma_9^V - \Gamma_7^C$ transition, and $E_0(0) = 3.494$ eV, $\alpha = 10.9 \times 10^{-4}$ eV/K, and $\beta = 1194.7$ K for the Γ_7^V (upper band) $-\Gamma_7^C$ transition. Attempts to fit to Eq. (2) the Γ_7^V (lower band) $-\Gamma_7^C$ transition energies measured at different temperatures yield $E_0(0) = 3.520$ eV, $\alpha = 2.92 \times 10^{-3}$ eV/K, and $\beta = 3698.9$ K. The values of α and β for the Γ_7^V (lower band) $-\Gamma_7^C$ transition are somewhat anomalously larger than those for the $\Gamma_9^V - \Gamma_7^C$ and Γ_7^V (upper band) $-\Gamma_7^C$ transitions. This is primarily due to the relatively large uncertainty in determination of the transition energy at high temperatures ($T > 150$ K) caused by a poor signal-to-noise ratio.

In summary, photoluminescence and reflectance measurements have been performed on MOCVD grown GaN single-crystal films over a temperature range from 15 K up to 300 K. The energies of the $\Gamma_9^V - \Gamma_7^C$, Γ_7^V (upper band) $-\Gamma_7^C$, and Γ_7^V (lower band) $-\Gamma_7^C$ free-exciton transitions in the GaN sample were found to be 3.485, 3.493, and 3.518 eV at 15 K, respectively. The room-temperature interband transition energy values obtained from these measurements are 3.420 eV for the $\Gamma_9^V - \Gamma_7^C$ transition and 3.428 eV for the Γ_7^V (upper band) $-\Gamma_7^C$ transition. By fitting the temperature-dependent energy values of the $\Gamma_9^V - \Gamma_7^C$ and Γ_7^V (upper band) $-\Gamma_7^C$ transitions to the Varshni empirical relation, our result yields $E_0(T) = 3.486 - 8.32 \times 10^{-4} T^2 / (835.6 + T)$ and $E_0(T) = 3.494 - 10.9 \times 10^{-4} T^2 / (1194.7 + T)$ eV, respectively.

This work was supported by AFOSR and ONR. One of the authors (B.G.) is pleased to acknowledge the technical assistance of Maurice Hitchell.

- ¹ S. Strite and H. Morkoç, J. Vac. Sci. Technol. B 10, 1237 (1992), and references therein.
- ² J. I. Pankove, Mater. Res. Soc. Symp. Proc. 162, 515 (1990), and references therein.
- ³ H. Amano, M. Kito, K. Hiramatsu, and I. Akasaki, Jpn. J. Appl. Phys. 28, 2112 (1989).
- ⁴ M. J. Paisley, Z. Sitar, J. B. Posthill, and R. F. Davis, J. Vac. Sci. Technol. A 7, 701 (1989).
- ⁵ S. Strite, J. Ruan, Z. Li, A. Salvador, H. Chen, D. J. Smith, W. J. Choyke, and H. Morkoç, J. Vac. Sci. Technol. B 9, 1924 (1991).
- ⁶ T. Lei, M. Fanciulli, R. J. Molnar, T. D. Moustakas, R. J. Graham, and J. Scanlon, Appl. Phys. Lett. 59, 944 (1991); T. Lei, K. F. Ludwig, Jr., and T. D. Moustakas, J. Appl. Phys. 74, 4430 (1993).
- ⁷ M. Asif Khan, J. M. Van Hove, J. N. Kuznia, and D. T. Olson, Appl. Phys. Lett. 58, 2408 (1991).
- ⁸ T. Detchprohm, K. Hiramatsu, H. Amano, and I. Akasaki, Appl. Phys. Lett. 61, 2688 (1992).
- ⁹ R. C. Powell, N.-E. Lee, Y.-W. Kim, and J. E. Greene, J. Appl. Phys. 73, 189 (1993).
- ¹⁰ I. Akasaki, H. Amano, H. Murakami, M. Sassa, H. Kato, and K. Manabe, J. Cryst. Growth 123, 379 (1993).
- ¹¹ R. Singh, R. J. Molnar, M. S. Ünlü, and T. D. Moustakas, Appl. Phys. Lett. 64, 336 (1994).
- ¹² T. Kozawa, T. Kachi, H. Kano, Y. Taga, M. Hashimoto, N. Koide, and K. Manabe, J. Appl. Phys. 75, 1098 (1994).
- ¹³ M. Asif Khan, J. N. Kuznia, D. T. Olson, M. Blasingame, and A. R. Bhattarai, Appl. Phys. Lett. 63, 2455 (1993).
- ¹⁴ S. Nakamura, M. Senoh, and T. Mukai, Appl. Phys. Lett. 62, 2390 (1993); Appl. Phys. Lett. 64, 1687 (1994).
- ¹⁵ J. I. Pankove, J. E. Berkeyheiser, H. P. Maruska, and J. Wittke, Solid State Commun. 8, 1051 (1970).
- ¹⁶ B. Monemar, Phys. Rev. B 10, 676 (1974).
- ¹⁷ D. L. Camphausen and G. A. N. Connell, J. Appl. Phys. 42, 4438 (1971).
- ¹⁸ T. Matsumoto and M. Aoki, Jpn. J. Appl. Phys. 13, 1804 (1974).
- ¹⁹ K. Osamura, S. Naka, and Y. Murakami, J. Appl. Phys. 46, 3432 (1975).
- ²⁰ A. M. Zykov and G. K. Guido, Sov. Phys. Semicond. 6, 154 (1972).
- ²¹ R. Dingle, D. D. Sell, S. E. Stokowski, and M. Ilegems, Phys. Rev. B 4, 1211 (1971).
- ²² R. Dingle and M. Ilegems, Solid State Commun. 9, 175 (1971).
- ²³ H. Teisseyre, P. Perlín, T. Suski, I. Grzegory, S. Porowski, J. Jun, A. Pietraszko, and T. D. Moustakas, J. Appl. Phys. 76, 2429 (1994).
- ²⁴ G. Ramirez-Flores, H. Navarro-Contreras, A. Lastras-Martinez, R. C. Powell, and J. E. Greene, Phys. Rev. B 50, 8433 (1994).
- ²⁵ Y. P. Varshni, Physica 34, 149 (1967).
- ²⁶ D. E. Aspnes, in *Optical Properties of Solids*, edited by M. Balkanski (North-Holland, Amsterdam, 1980), Chap. 4A.
- ²⁷ F. H. Glembocki and O. J. Glembocki, SPIE Proc. 946, 2 (1988).
- ²⁸ O. J. Glembocki and B. V. Shanabrook, Superlatt. Microstruct. 5, 235 (1987).
- ²⁹ H. Shen, S. H. Pan, F. H. Pollak, M. Dutta, and T. R. AuCoin, Phys. Rev. B 36, 9384 (1987).

Above room temperature near ultraviolet lasing from an optically pumped GaN film grown on sapphire

X. H. Yang, T. J. Schmidt, W. Shan, and J. J. Song

Center for Laser Research and Department of Physics, Oklahoma State University, Stillwater, Oklahoma 74078

B. Goldenberg

Honeywell Technology Center, Bloomington, Minnesota 55420

(Received 9 August 1994; accepted for publication 1 November 1994)

Optically pumped near ultraviolet lasing from single-crystal GaN grown by metalorganic chemical vapor deposition has been achieved over a temperature range from 10 K to over 375 K by using a side-pumping geometry on small barlike samples. The laser emission threshold was measured as a function of temperature and the threshold was found to show weak temperature dependence: ~ 500 kW/cm² at 10 K and ~ 800 kW/cm² at room temperature (295 K) for one particular sample studied. The longitudinal lasing modes were clearly observed. The characteristics of the temperature dependence of the laser emission threshold suggests that GaN is a suitable material for the development of optoelectronic devices required to operate at high temperatures. © 1995 American Institute of Physics.

Recently, III-V nitrides have attracted much attention because of their large energy band gaps, great physical hardness, high thermal conductivities, and high melting temperatures.¹ These properties make III-V nitrides promising for high-temperature electronic and optoelectronic device applications. In particular, GaN has been the most extensively studied material because its large direct band gap of 3.41 eV at room temperature is appropriate for short wavelength (blue-ultraviolet) light emitting diodes and laser diodes.¹⁻³ With the advancement of growth techniques, high quality GaN crystals have been grown and room-temperature optically pumped stimulated emission has been reported by several groups.⁴⁻¹⁰ Also, a commercial light-emitting diode based on an InGaN/AlGaIn double-heterostructure has been successfully fabricated by Nichia Chemical Company in Japan.¹¹ However, thus far clear evidence of lasing from prepared cavities has not been reported from GaN, nor from other nitrides, except an early report by Dingle *et al.*, showing Fabry-Pérot modes superimposed on top of a broad emission background from as-grown GaN needle samples.⁸ This can be partially attributed to difficulties associated with sample preparation and processing. In particular, suitable cavity end mirrors are difficult to obtain when the single-crystal epilayer films are grown on such a hard substrate as sapphire. This makes the observation of laser emission and the resultant longitudinal cavity modes difficult.⁶

In this letter we report the experimental results of optically pumped lasing from single-crystal GaN samples over a temperature range from 10 K to over 375 K. The GaN samples were grown on sapphire substrates by low-pressure metalorganic chemical vapor deposition (MOCVD). By cutting the large sample wafer into small barlike specimens and employing a side-pumping geometry we were able to produce strong near-UV laser emissions from the GaN samples over a temperature range from 10 K to over 375 K. The longitudinal cavity modes of the laser emission could be clearly observed without the need for fine polishing or reflective coating of the samples edge facets. The lasing threshold

pumping power density has been measured in detail as a function of temperature. The characteristics of the temperature dependence of the lasing threshold suggests that this wide band gap material can be used for the development and fabrication of light-emitting devices required to operate at high temperatures. To our knowledge, this is the best experimental evidence of optically pumped near-UV lasing of GaN ever observed.

The GaN samples used in this study were cut from a nominally undoped single-crystal grown by low-pressure MOCVD. The 4.2 μ m thick GaN epilayer was grown on a 1.75 in. (0001) sapphire substrate at 1040 °C. Before the deposition of the GaN film a 50 nm AlN buffer layer was grown on the substrate at 775 °C. The large wafer was cut into small barlike specimens of various thicknesses, ranging from 150 to 1000 μ m. Extreme care was taken to ensure that the quality and parallelness of the cut edge facets were as good as possible. The barlike samples were then mounted on a sapphire heat sink which was then attached to a copper sample holder inside a cryostat. The optical pumping system is very similar to that used in our previous ZnSe lasing work.^{12,13} A tunable dye laser pumped by a frequency-doubled pulsed Nd:YAG laser was used as the primary optical pumping source. The output of the dye laser was then frequency doubled to achieve a near UV pumping frequency. Side-pumping geometry was used in this study. The emission signal from one facet of the GaN sample was collected into a Spex 1.0 m spectrometer and recorded by either a charge coupled device (CCD) camera or a photomultiplier tube used in conjunction with a boxcar averager.

Strong near-UV laser actions from the GaN samples were observed over the broad temperature range from 10 K to over 375 K under the conditions of high-excitation power densities. The laser emission light was found to be transverse electric (TE) polarized (along the direction of the bar). As the temperature was increased, the lasing peak shifted to longer wavelength, from 362 nm at 10 K to 381 nm at 375 K. The room-temperature (295 K) laser emission peak position was

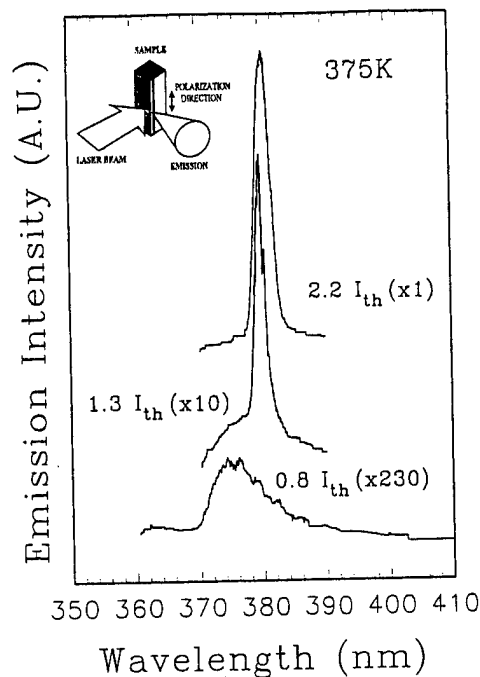


FIG. 1. Emission spectra from a GaN sample with a cavity length of $330\mu\text{m}$ under pump power densities of $2.2 I_{\text{th}}$, $1.3 I_{\text{th}}$, and $0.8 I_{\text{th}}$. The curves are vertically displaced for clarity. The threshold pump power density I_{th} was determined to be 1.2 MW/cm^2 at 375 K . The insert shows the excitation and emission configuration.

found to be 373 nm . The full width at half-maximum (FWHM) of the lasing peak is $\sim 1\text{ nm}$ at 10 K and broadens slightly with increasing temperature. In Fig. 1 we show the emission spectra taken at a temperature well above room temperature (375 K), for pumping power densities above and below the estimated threshold pumping power density. Under the condition of low pump power intensities, only a broad emission spectral structure with an approximate peak position of 376 nm could be observed (lower curve). Its emission intensity was found to be linearly proportional to the pumping power density, indicating that the broad emission structure is of the typical nature of spontaneous emission. As pumping power density increases, a new emission feature with a much narrower line shape appears at the low-energy shoulder of the spontaneous emission structure. The emission intensity of this new spectral feature becomes predominant as the pumping power density is increased to slightly above the lasing threshold (middle curve). The strong, narrow emission exhibits a superlinear increase and the broad emission background is totally suppressed as the pumping power density is increased further, indicating the occurrence of laser action in the sample. For example, the emission intensity increased by almost three orders of magnitude when the pumping power density was increased by less than a factor of 3 (upper curve). Meanwhile, the laser emission peak shifts to a longer wavelength as the pumping power density is increased. In addition, some longitudinal cavity modes could be recognized in the emission spectra shown in Fig. 1. In order to better resolve the longitudinal cavity modes in the emission spectra, a sample with a $200\mu\text{m}$ cavity length was used and different spectra were captured using a CCD cam-

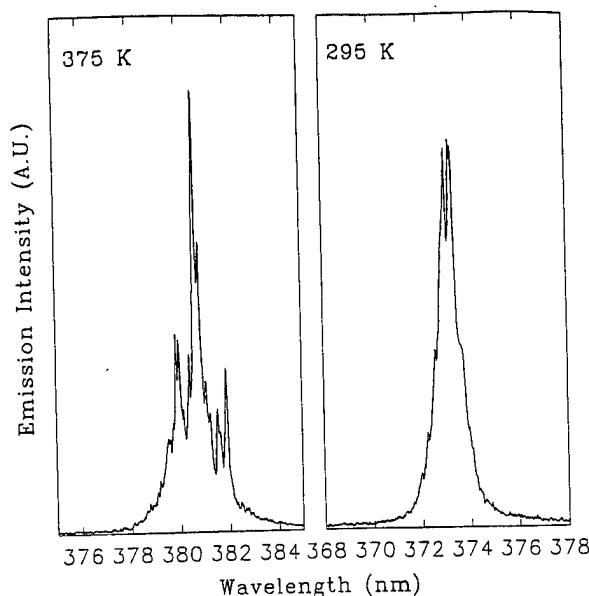


FIG. 2. Lasing spectra taken at two different temperatures from a sample with a cavity length of $200\mu\text{m}$. The longitudinal modes are clearly resolved.

era with a very short integration time (0.1 s). Mode hopping was observed. Figure 2 shows two typical spectra captured at 295 and 375 K . The irregular appearance of the spectra shown in Fig. 2 is primarily a result of imperfections in the samples edge facets. Spectral quality is expected to improve greatly after the samples edge facets are fine polished and reflective coated. The mode spacing caused by the $200\mu\text{m}$ long Fabry-Pérot resonant cavity is about 0.2 nm , which is consistent with the calculated value of the mode spacing determined by the formula^{14,15}

$$\Delta\lambda = \frac{\lambda_0^2}{2L(n - \lambda_0 dn/d\lambda)},$$

where L is the cavity length, λ_0 is the wavelength of one mode, $\Delta\lambda$ is the spacing of an adjacent mode, n is the index of refraction at λ_0 , and $dn/d\lambda$ is the variation of the index of refraction with wavelength.

Figure 3 demonstrates the change in the laser emission intensity for a sample at 10 K and at room temperature (295 K) as the pumping power density is increased. The emission intensity was measured by integrating the area under the emission peak. The lasing threshold of pumping power density for these two different temperatures is well defined by the onset of the increase in slope of the emission intensity versus pumping power intensity curve. The lasing threshold was found to be $\sim 0.5\text{ MW/cm}^2$ at 10 K and $\sim 0.8\text{ MW/cm}^2$ at room temperature. One interesting finding of the study is that the lasing threshold was relatively insensitive to the temperature change. The variation of the lasing threshold as a function of temperatures is plotted in Fig. 4. We note that over the temperature range from 10 to 120 K the lasing threshold is not very dependent on temperature. As the temperature increases further, the lasing threshold increases slowly. The threshold increases by about three times when

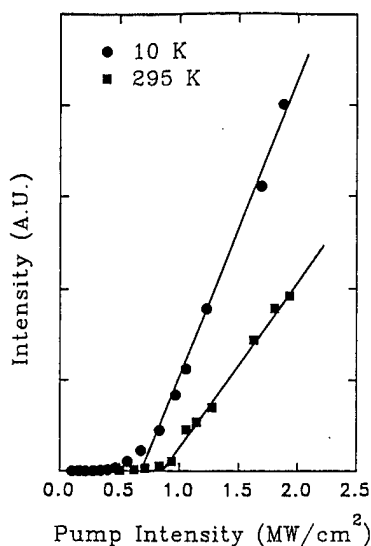


FIG. 3. Emission output vs optical pumping power densities at 10 and 295 K.

the temperature is increased from 10 to 375 K. The solid line in Fig. 4 represents the best fit of the experimental data to the empirical form¹⁶

$$I_{th}(T) = I_0 \exp(T/T_0)$$

for the temperature dependence of the lasing threshold. The characteristic temperature T_0 was estimated to be 230 K over the temperature range from 120 to 375 K for this sample. This value of T_0 is about two times larger than that of II-VI lasers ($T_0 \sim 120$ K for II-VI lasers), indicating that the lasing threshold is less sensitive to changes in temperature.^{17,18} It is well known that high-temperature sensitivity of the lasing threshold usually limits the performance of a laser under high-temperature operation.¹⁶ On the other hand, a weak temperature dependence for the lasing threshold implies that the high-temperature performance limit for

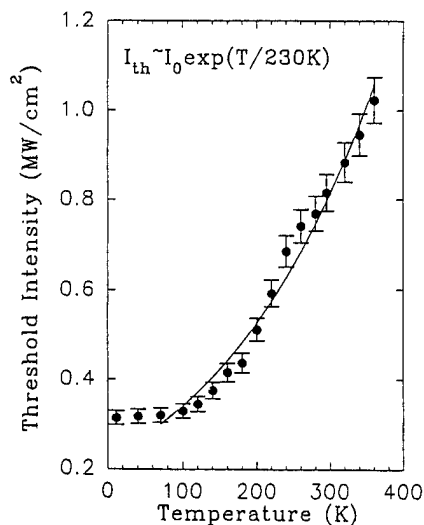


FIG. 4. Variation of the lasing threshold as a function of temperature. The error bars indicate the fluctuations in pump power density. The solid line is the best fit to the experimental data using the formula $I_{th} = I_0 \exp(T/230 \text{ K})$.

laser operation can be significantly expanded. Therefore, our results suggest that GaN-based laser diodes will have a much higher temperature tolerance. We should also mention that laser action was observed at temperatures as high as 425 K. However, due to our current systems limitations, lasing could not be studied in detail at these higher temperatures. Further investigation is underway to study higher temperature lasing effects.

In summary, optically pumped near-UV laser action in single-crystal MOCVD grown GaN samples has been successfully achieved for the first time without reflective coating at temperatures ranging from 10 to over 375 K. The laser action was evidenced by the spectral narrowing of the emission peak, the suppression of the broad emission background, the drastic increase in emission output for pump power intensities above threshold, and the clearly resolved longitudinal lasing modes. This work demonstrates that the laser cavity can be formed by simply cutting the sample into a barlike structure without a need for polishing or reflective coating. The laser emission threshold of pumping power density was measured as a function of temperature and was found to exhibit a weak temperature dependence. The characteristics of the temperature dependence of the lasing threshold suggests that GaN is not only a suitable material for the development of UV light emitters, but that it is also suitable for the development of optoelectronic devices required to operate at high temperature.

The work at OSU was supported by AFOSR, ONR, ARPA, and OCAST. One of the authors (BG) would like to acknowledge the technical assistance of Maurice Hitchell. A portion of this work was presented at the Rare Earth Doped Optoelectronic Materials Workshop held in Malibu, CA, June, 1994.

¹S. Strite and H. Morkoc, J. Vac. Sci. Technol. B **10**, 1237 (1992), and references therein.

²T. Kawabata, T. Matsuda, and S. Koike, J. Appl. Phys. **56**, 2367 (1984).

³J. I. Pankove, Mater. Res. Soc. Symp. Proc. **162**, 515 (1990), and references therein.

⁴M. A. Khan, D. T. Olson, J. M. Van Hove, and J. N. Kuznia, Appl. Phys. Lett. **58**, 1515 (1991).

⁵K. Yung, J. Yee, J. Koo, M. Rubin, N. Newman, and J. Ross, Appl. Phys. Lett. **64**, 1135 (1994).

⁶H. Amano, T. Asahi, and I. Akasaki, Jpn. J. Appl. Phys. **29**, L205 (1990).

⁷H. Amano, T. Asahi, M. Kito, and I. Akasaki, J. Lumin. **48&49**, 889 (1991).

⁸R. Dingle, K. L. Shaklee, R. F. Leheny, and R. B. Zetterstrom, Appl. Phys. Lett. **19**, 5 (1971).

⁹I. M. Catalano, A. Cingolani, M. Ferrara, M. Lugara, and A. Minafra, Solid State Commun. **25**, 349 (1978).

¹⁰C. D. Wang and M. Gershenson, Bull. APS **24**, 343 (1979).

¹¹S. Nakamura, T. Mukai, and M. Senoh, Appl. Phys. Lett. **64**, 1678 (1994).

¹²X. H. Yang, J. Hays, W. Shan, W. Shan, E. Cantwell, and J. Aldridge, Appl. Phys. Lett. **59**, 1681 (1991).

¹³X. H. Yang, J. Hays, W. Shan, J. J. Song, E. Cantwell, and J. Aldridge, Appl. Phys. Lett. **60**, 926 (1992).

¹⁴J. J. Song and W. C. Wang, J. Appl. Phys. **55**, 660 (1984).

¹⁵M. Voos, R. F. Leheny, and J. Shah, in *Optical Properties of Solids*, edited by M. Balkanski (North-Holland, Amsterdam, 1980), Chap. 6.

¹⁶See, for example, G. P. Agrawal and N. K. Dutta, in *Semiconductor Lasers* (Van Nostrand Reinhold, New York, 1993), p. 132.

¹⁷A. M. Glass, K. Tai, R. B. Bylisma, R. D. Feldman, D. H. Olson, and R. F. Austin, Appl. Phys. Lett. **53**, 834 (1988).

¹⁸K. Nakanishi, I. Suemune, Y. Fujii, Y. Kuroda, and M. Yamanishi, Appl. Phys. Lett. **59**, 1401 (1991).

Pressure-dependent photoluminescence study of wurtzite GaN

W. Shan, T. J. Schmidt, R. J. Hauenstein, and J. J. Song

Department of Physics and Center for Laser Research, Oklahoma State University, Stillwater, Oklahoma 74078

B. Goldenberg

Honeywell Technology Center, Bloomington, Minnesota 55420

(Received 18 January 1995; accepted for publication 2 April 1995)

Low-temperature photoluminescence (PL) in single-crystal GaN films grown on sapphire substrates by metalorganic chemical vapor deposition has been studied as a function of applied hydrostatic pressure using the diamond-anvil-cell technique. The PL spectra of the GaN at atmospheric pressure were dominated by two sharp, strong, near-band-edge exciton luminescence lines and a broad emission band in the yellow spectral region. The exciton emission lines were found to shift almost linearly toward higher energy with increasing pressure. While the yellow emission band showed a similar blue shift behavior under applied pressure, a relatively strong sublinear pressure dependence was observed. By examining the pressure dependence of the exciton emission structures, the pressure coefficient of the direct Γ band gap in the wurtzite GaN was determined. The value of the hydrostatic deformation potential of the band gap has also been deduced from the experimental results. © 1995 American Institute of Physics.

GaN-based III-V nitride semiconductors currently attract extensive attention for their potential device applications.¹⁻³ It is known that GaN has a wurtzite structure in natural form, and has a wide direct band gap of ~ 3.4 eV at 300 K, which provides efficient radiation recombination. The wavelength of radiation from GaN-based materials can be turned over a wide range from visible to ultraviolet by alloying or forming heterostructures, such as quantum wells, with other nitrides (AlN and InN). These merits make GaN and its based nitrides very attractive to the short-wavelength optical applications such as light emitters and detectors operating in the blue and ultraviolet wavelength range. The outstanding thermal and chemical stability of the wide band-gap nitrides also allows the GaN-based electronic and optoelectronic devices to operate at high temperatures and in hostile environments.

Recently, a number of theoretical studies on the band structures and electronic structures of impurities and native defects in GaN have been performed.⁴⁻¹⁰ In the course of these studies, the pressure coefficients and the deformation potentials for the band gaps of the III-V nitrides have been estimated.^{4,6,8} So far there have been little experimental determination of the pressure dependence of the band gap for GaN (which is the most important compound among the III-V nitrides). To our knowledge, there has been only two reported studies of the pressure dependence of the absorption edge in GaN.^{6,11} In this report, we present the results of low-temperature photoluminescence (PL) measurements on wurtzite GaN with applied pressures up to over 50 kbar. The samples were single-crystal GaN epilayer films grown by metalorganic chemical vapor deposition (MOCVD) on sapphire substrates. The photoluminescence (PL) spectra of the MOCVD GaN samples were dominated by strong, narrow, near band-edge emission structures corresponding to the radiative decay of bound and free excitons and a broad emis-

sion band in the yellow spectral region (yellow band) with the maxima around 2.25 eV. The exciton emission lines were found to shift almost linearly toward higher energy with increasing pressure. While the yellow emission band showed a similar blue shift behavior under applied pressure, a relatively strong sublinear pressure dependence was observed. The pressure coefficients for the observed excitonic emission lines were found to be 3.9 meV/kbar, which provides a direct measure of the pressure coefficient of wurtzite GaN direct Γ band gap. The experimental value of the hydrostatic deformation potential of the band gap has also been derived from the results.

The GaN sample used in this work was a nominally undoped single-crystal film grown by metalorganic chemical vapor deposition on a (001) sapphire substrate. A thin AlN buffer layer of ~ 50 nm was deposited on the substrate at about 775 °C before the growth of the GaN epilayer. The GaN layer was deposited at 1040 °C directly on the AlN buffer. The thickness of the GaN layer was 4.2 μm . The pressure-dependent photoluminescence (PL) measurements were carried out on the GaN sample using a gasketed diamond anvil cell (DAC). In order to accommodate the dimensions of the DAC, small sample pieces with sizes of $\sim 200 \times 200 \times 50 \mu\text{m}^3$ were prepared by mechanical polishing and cutting and then loaded into the DAC. The cell was mounted onto the cold finger of a closed cycle refrigerator and cooled down to 10 K for the measurements. PL spectra were measured using an experimental setup consisting of a HeCd laser as an excitation source and a 1 M double-grating monochromator connected to a photon-counting system. The applied pressures were determined by the standard method of monitoring the shift of the ruby R1 line.

PL spectra of the GaN measured at 10 K are shown in Fig. 1 for a few selected pressures. The PL spectrum taken at atmospheric pressure from the GaN sample exhibits the dominant near-band-edge exciton transitions and a broad-band emission structure centered in the yellow spectral region. Another weak broadband luminescence in between the

^aElectronic mail: wshan@osuunx.ucc.okstate.edu

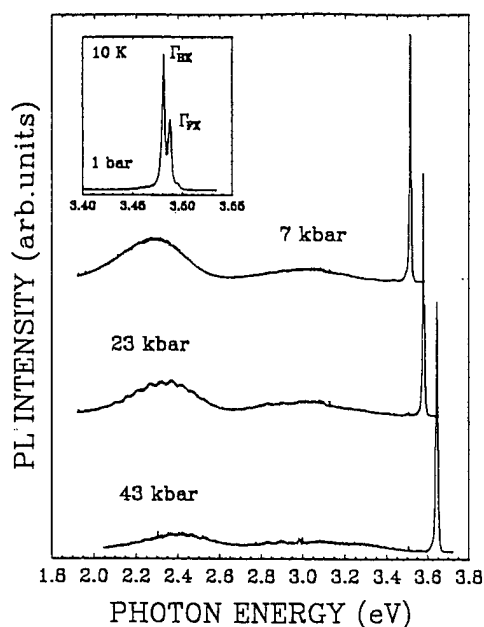


FIG. 1. Photoluminescence spectra of the MOCVD GaN sample at 10 K are shown for selective pressures. The inset details the spectral features associated with the near band-edge exciton transitions.

exciton emission lines and the yellow band was also observed (in the blue-green spectral region). The inset of Fig. 1 details the spectral features of excitons associated with the direct band-gap $\Gamma^C - \Gamma^V$ transitions in GaN. Temperature-dependent PL measurements performed on the sample suggest that the strongest emission line at 3.4808 eV (Γ_{BX}) can be attributed to the radiative recombination of excitons bound to neutral donors and the one at 3.4875 eV (Γ_{FX}), together with the weak emission shoulder on the higher energy side, can be assigned to intrinsic free-exciton emission. The intensity of Γ_{BX} emission was found to decrease much faster than that of the other two structures located at higher energies. It became hardly resolved when the temperature was raised to above 100 K, indicating the dissociation of bound excitons due to thermal effects, whereas the emission structures attributed to free excitons could be still resolved at temperatures higher than 200 K. Under applied pressure, these excitonic spectral features and the broadband emission in the yellow spectral region were found to shift towards higher energy as the GaN band-gap increases. The intensity of the broad yellow emission band relative to that of the exciton emissions was found to decrease with pressure. However, the influence of applied pressure on the broadband emission structure in the blue-green spectral region was too ambiguous to draw any conclusions from due to its very broad and rather complicated line shape.

In Fig. 2 we plot the peak energies of various observed emission structures as a function of pressure. The energy position of the broad yellow emission band maximum was determined by fitting its lineshape to a Gaussian profile. It shows a relatively strong sublinear dependence compared to the exciton emissions. The solid lines in the figure are the least-squares fits to the experimental data using the quadratic-fit function

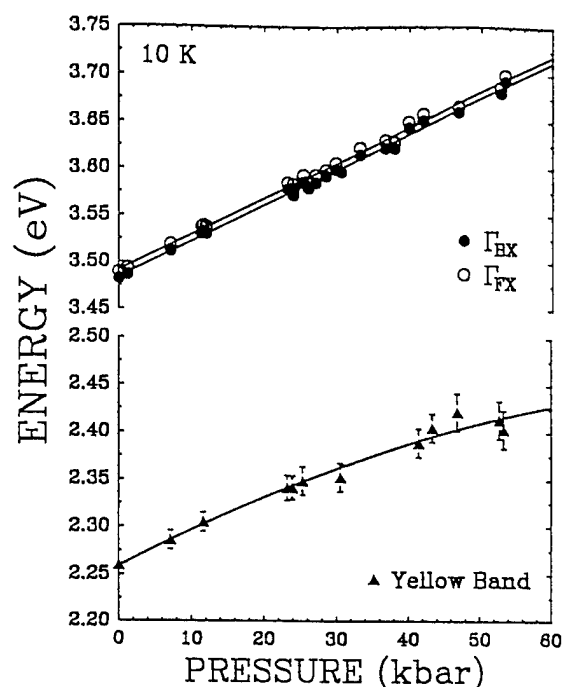


FIG. 2. Dependence of the energy positions on pressure for the various observed PL transitions in the GaN sample.

$$E(P) = E(0) + \alpha P + \beta P^2. \quad (1)$$

It is known that the emission lines associated with the radiative decay of a free exciton or a shallow bound exciton shifts with the host semiconductor band gap under hydrostatic pressure at the same rate. The electron stays in the conduction-band edge state or in the orbit of shallow donor state associated with the conduction-band edge and the excitonic hole bound in the Coulomb field retains the symmetry of the valence-band edges. Therefore, the change of the intense and sharp Γ_{BX} transition with pressure plotted in the figure provides an unmistakable signature of the direct Γ band-gap dependence for wurtzite GaN. The best fits to the data yield a linear slope of 3.86×10^{-3} eV/kbar with an extremely small sublinear term of -8×10^{-7} eV/kbar.² Similar results can be obtained from fitting the Γ_{FX} transition as well. Table I lists the pressure coefficients for the emission energies derived from the fittings. The uncertainty of the linear pressure coefficient is $\sim 5 \times 10^{-5}$ eV/kbar, primarily coming from the error bar of pressure calibration (within ± 0.2 kbar) as well as the possible pressure-induced change of the exciton binding energy, which arises from an increasing electron effective mass and a decrease in the dielectric constant as the band gap increases.^{6,12,13} The pressure coefficient of GaN

TABLE I. Pressure coefficients of the various emission structures observed in the wurtzite GaN sample studied in this work.

	$E(P=0)$ (eV)	$\alpha = dE/dP$ (10^{-3} eV/kbar)	$\beta = d^2E/dP^2$ (10^{-5} eV/kbar ²)
Bound exciton (Γ_{BX})	3.4808	3.86	-0.08
Free exciton (Γ_{FX})	3.4875	3.90	-0.18
Yellow band	2.25 ± 0.01	4.0	-2.0

band gap reported here is smaller than those reported in other studies of GaN involving absorption measurements under pressure,^{6,11} where a linear pressure dependence of 4.2×10^{-3} eV/kbar was obtained at 77 K for pressures below 10 kbar¹¹ and a nonlinear pressure dependence of $E_g(P) = E_g(0) + 4.7 \times 10^{-3}P - 1.8 \times 10^{-5}P^2$ eV was deduced at 300 K for pressures over 50 kbar.⁶ We suggest that the discrepancy between our results and those reported may result from the difficulty in accurately determining the transition energies in broad optical absorption curves. Therefore, we regard the dependence of the direct Γ band gap on pressure derived from Fig. 2 as a more accurate and reliable result.

The application of hydrostatic pressure, inducing a shift of the conduction-band edge relative to the valence-band edge due to a change in the volume, allows a direct estimation of the hydrostatic deformation potential for the direct Γ band gap of wurtzite GaN. The deformation potential is defined as $a = \partial E / \partial \ln V$. The variation of the band gap with pressure can also be appropriately expressed in terms, up to the second order, of the relative volume change,

$$\Delta E = a[(V - V_0)/V] + \gamma[(V - V_0)/V]^2, \quad (2)$$

where V is the volume, V_0 is the volume at atmospheric pressure, a is the hydrostatic deformation potential for the Γ band gap, and γ is the quadratic dependence of the band gap on the relative volume change. The relative volume change caused by applied pressure can be related by the Murnaghan equation of state:¹⁴

$$P = (B_0/B'_0)[(V_0/V)^{B'_0} - 1], \quad (3)$$

where B_0 is the bulk modulus of the wurtzite GaN and B'_0 is its pressure derivative ($= dB/dP$). By fitting the experimental data to Eq. (2), using recently reported values of $B_0 = 2370 \pm 310$ kbar and $B'_0 = 4.3 \pm 2$,¹⁵ the deduced hydrostatic deformation potentials for the direct Γ band gap of wurtzite GaN were found to be $a = -9.2 \pm 1.2$ eV and $\gamma = 16.6 \pm 9$ eV. This experimental value of A is comparable to the theoretical value predicted by self-consistent linear muffin-tin-orbital band-structure calculations.^{6,8} However, it should be pointed out that the estimated experimental value might represent a lower limit of the deformation potential since it was obtained by using the value of the bulk modulus obtained at room temperature to fit experimental data obtained at 10 K. This was done because a low-temperature value is not available at present. The bulk modulus for a given material is generally expected to increase with decreasing temperature.

The broadband yellow emission spectral structure could be commonly observed in the PL spectra of nominally undoped GaN single crystals regardless of the crystal growth technique.^{16–20} More strikingly, this band was observed in samples implanted with a variety of atomic species.²¹ These results have led to the general belief that the broadband emission in yellow spectral region involves defects. Recent theoretical studies on the electronic structures of impurities and native defects in GaN have suggested that point defects, such as antisites and vacancies, play important roles.^{22–25} In particular, Tansley *et al.* attributed the broadband yellow emission to transitions involving $|s\rangle$ -like levels associated

with N_{Ga} antisite defects and the top of the valence band.²³ This attribution seems to be consistent with the dependence of the yellow emission band on pressure reported here. On the other hand, the pressure dependence of the yellow emission is also consistent with the transmissions involving shallow donors and deep acceptors in broad terms. Nevertheless, further theoretical and experimental studies are necessary to investigate the microscopic nature of the broadband yellow emission in GaN.

In conclusion, we have studied low-temperature photoluminescence in wurtzite GaN as a function of pressure. The pressure coefficient and the hydrostatic deformation potential for the direct Γ band gap of GaN have been deduced from the dependencies of the near band-edge impurity-bound and intrinsic exciton transitions on pressure. Our results yield the variation of the Γ band gap with pressure to be $\Delta E_g(P) = 3.9 \times 10^{-3}P - 1.0 \times 10^{-6}P^2$ eV and the value of the deformation potential to be $a = -9.2 \pm 1.2$ eV. The broadband emission observed in the yellow spectral region at atmospheric pressure was found to exhibit a similar, but relatively strong sublinear dependence, on pressure compared to the exciton emissions. The results are consistent with proposals that defect states are responsible for the broadband yellow emission in GaN.

This work was supported by AFOSR, ARPA, and ONR. One of the authors (B.G.) is pleased to acknowledge the technical assistance of Maurice Hitchell.

¹ S. Strite and H. Morkoç, *J. Vac. Sci. Technol. B* **10**, 1237 (1992), and references therein.

² J. I. Pankove, *Mater. Res. Soc. Symp. Proc.* **162**, 515 (1990), and references therein.

³ H. Morkoç, S. Strite, G. B. Gao, M. E. Lin, B. Sverdlov, and M. Burns, *J. Appl. Phys.* **76**, 1363 (1994), and references therein.

⁴ I. Gorczyca and N. E. Christensen, *Solid State Commun.* **80**, 335 (1991); *Physica B* **185**, 410 (1993).

⁵ B. J. Min, C. T. Chan, and K. M. Ho, *Phys. Rev. B* **45**, 1159 (1992).

⁶ P. Perlín, I. Gorczyca, N. E. Christensen, I. Grzegory, H. Teisseyre, and T. Suski, *Phys. Rev. B* **45**, 13307 (1992).

⁷ A. Rubio, J. L. Corkill, M. L. Cohen, E. L. Shirley, and S. G. Louie, *Phys. Rev. B* **48**, 11810 (1993).

⁸ N. E. Christensen and I. Gorczyca, *Phys. Rev. B* **50**, 4397 (1994).

⁹ K. Kim, W. R. Lambrecht, and B. Segall, *Phys. Rev. B* **50**, 1502 (1994).

¹⁰ W. R. L. Lambrecht, B. Segall, S. Strite, G. Martin, A. Agarwal, H. Morkoç, and A. Rockett, *Phys. Rev. B* **50**, 14155 (1994).

¹¹ D. L. Camphausen and G. A. N. Connell, *J. Appl. Phys.* **42**, 4438 (1971).

¹² D. J. Wolford and J. A. Bradley, *Solid State Commun.* **53**, 1069 (1985).

¹³ G. A. Samara, *Phys. Rev. B* **27**, 3494 (1983).

¹⁴ F. D. Murnaghan, *Proc. Natl. Acad. Sci. USA* **30**, 244 (1944).

¹⁵ M. Ueno, M. Yoshida, A. Onodera, O. Shimomura, and K. Takemura, *Phys. Rev. B* **49**, 14 (1994).

¹⁶ T. Ogino and M. Aoki, *Jpn. J. Appl. Phys.* **19**, 2395 (1980).

¹⁷ R. Singh, R. J. Molnar, M. S. Ünlü, and T. D. Moustakas, *Appl. Phys. Lett.* **64**, 336 (1994).

¹⁸ C. Wetzel, D. Volm, B. K. Meyer, K. Pressel, S. Nilsson, E. N. Moknov, and P. G. Baranov, *Appl. Phys. Lett.* **65**, 1033 (1994).

¹⁹ K. G. Fertitta, A. L. Holmes, J. G. Neff, F. J. Ciuba, and R. D. Dupuis, *Appl. Phys. Lett.* **65**, 1823 (1994).

²⁰ Y. Ohba and A. Hatano, *Jpn. J. Appl. Phys. Pt. 2*, **33**, L1367 (1994).

²¹ J. I. Pankove and J. A. Hutchby, *J. Appl. Phys.* **47**, 5387 (1976).

²² D. W. Jenkins and J. D. Dow, *Phys. Rev. B* **39**, 3317 (1989).

²³ T. L. Tansley and R. J. Egan, *Phys. Rev. B* **45**, 10942 (1992); *Physica B* **185**, 190 (1993).

²⁴ J. Neugebauer and C. G. Van de Walle, *Phys. Rev. B* **50**, 8067 (1994).

²⁵ P. Boguslawski, E. Briggs, and J. Bernholc, in *Proceedings of the 22nd International Conference on Physics and Semiconductors*, Vancouver, 1994 (to be published).

Hot-phonon generation in GaAs/Al_xGa_{1-x}As superlattices: Observations and implications on the coherence length of LO phonons

D. S. Kim, A. Bouchalkha, J. M. Jacob, and J. J. Song

Department of Physics and Center for Laser Research, Oklahoma State University, Stillwater, Oklahoma 74078

J. F. Klem

Sandia National Laboratories, Albuquerque, New Mexico 87185

H. Hou and C. W. Tu

Department of Electrical Engineering, University of California at San Diego, La Jolla, California 92093

H. Morkoç

Coordinated Science Laboratory, University of Illinois at Urbana-Champaign, Urbana, Illinois 61801

(Received 3 March 1994; revised manuscript received 3 June 1994)

Using picosecond Raman scattering, hot-phonon occupation numbers (N) of GaAs and GaAs-like LO phonons have been studied over a wide range of structural parameters in more than 30 GaAs/Al_xGa_{1-x}As superlattices. In addition, simultaneous measurements of these LO phonon modes in bulk GaAs and Al_xGa_{1-x}As alloys are made for comparison. N values of both GaAs and GaAs-like modes of the superlattices are comparable to or larger than those of bulk GaAs or Al_xGa_{1-x}As alloys for $x < 0.2$. On the other hand, N values of GaAs or GaAs-like LO phonons are much smaller for $x > 0.35$, unless the barrier widths are very thin (< 15 Å). The implications of our results on spatial properties of LO phonons are discussed and compared with relevant theoretical and experimental studies.

Spatial properties (or coherence lengths) of LO phonons in GaAs/Al_xGa_{1-x}As superlattices (SL's) as a function of x or layer thicknesses have attracted some attention over the last decade.¹⁻¹⁵ There is now general agreement that an infinite-barrier picture can be used for LO phonons in GaAs/AlAs superlattices because of the relatively large energy separation (≈ 100 cm⁻¹) between the optical phonons in GaAs and AlAs.

While phonon properties of GaAs/AlAs SL's have been extensively studied using Raman scattering,¹⁶⁻¹⁸ those of GaAs/Al_xGa_{1-x}As SL's are more complicated because of the two-moded behavior of optical phonons in Al_xGa_{1-x}As alloys. In GaAs/Al_xGa_{1-x}As SL's, GaAs and GaAs-like LO phonons are much more likely to be bulklike and propagating compared with LO phonons in GaAs/AlAs SL's. This is because GaAs-like LO phonons of Al_xGa_{1-x}As lie very close in energy to GaAs LO phonons, so that the barrier height in GaAs/Al_xGa_{1-x}As SL's for $x < 0.3$ is much smaller (for instance, ≈ 10 cm⁻¹ or less for $x < 0.3$).

In this paper, we have measured N for GaAs LO phonons by picosecond Raman scattering in over 30 molecular-beam-epitaxy grown SL's with various x ($0.10 \leq x \leq 1$), well width L_z ($70 \leq L_z \leq 150$ Å), and barrier width L_b ($5 \leq L_b \leq 150$ Å) at 20 K. The laser mainly used was the second harmonic of a mode-locked Nd:YAG (yttrium aluminum garnet) laser (2.33 eV, 1.5 ps), as well as a synchronously pumped dye laser (1.9–2.1 eV, 1.5 ps). With these exciting photon energies, hot-electron relaxation that generates hot phonons occurs

mostly above the alloy barrier in most of the samples investigated. N was found to be sensitive to both x and L_b : when $x \leq 0.2$, bulklike occupation numbers for both GaAs and the GaAs-like LO phonons are observed in all ranges of L_b and L_z , while when $x > 0.35$, N values of GaAs LO phonons are much smaller when $L_b > 15$ Å, typically at 10–20% that of bulk GaAs. These small values are comparable to those of a GaAs/AlAs SL ($L_z = L_b = 100$ Å), where LO phonons are believed to be perfectly confined. When the barriers are very thin (< 15 Å), a bulklike N is again recovered even for $x > 0.35$. These results can be summarized in a two-dimensional phase diagram (Fig. 3) where regions of bulklike N and the (GaAs/AlAs SL)-like N are well separated in the two-dimensional phase diagram of x and L_b . Our results can be explained qualitatively (and also somewhat quantitatively, see Fig. 4) if we assume that the confined Raman-active LO phonons in the well eventually become propagating and Bloch wave functionlike, with their coherence length ξ much larger than the well widths. This interpretation is in good agreement with some of the recent theoretical studies.⁷⁻¹⁰

In Fig. 1(a), the Stokes and anti-Stokes Raman spectra of GaAs and GaAs-like LO phonons of a GaAs/Al_{0.2}Ga_{0.8}As SL ($L_x = L_b = 70$ Å, 20 periods) at 20 K are plotted. GaAs and GaAs-like modes of the GaAs/Al_{0.2}Ga_{0.8}As superlattice are reasonably well resolved with a separation of ≈ 7 cm⁻¹. By comparing the Raman intensities around ± 295 and ± 288 cm⁻¹, or by deconvoluting the spectra, N values of both GaAs and

GaAs-like modes are obtained. Resonant Raman corrections in obtaining N are relatively small in our samples due to the off-resonance excitation conditions used. Both of these modes have values of N that are only slightly smaller than that of bulk GaAs also in the same cryostat and larger than that of $\text{Al}_{0.2}\text{Ga}_{0.8}\text{As}$. Therefore, from the point of view of hot-phonon generation, both GaAs and GaAs-like LO phonons in this SL are essentially bulklike when $x = 0.2$.

In Fig. 1(b), the Stokes and anti-Stokes Raman spectra of GaAs and GaAs-like LO phonons of a $\text{GaAs}/\text{Al}_{0.4}\text{Ga}_{0.6}\text{As}$ SL ($L_x = 100$ Å, $L_b = 50$ Å, 30 periods) at 20 K are plotted. In this sample, the barrier height is ≈ 15 cm^{-1} , as can be readily seen from the Stokes Raman spectrum. N values of both GaAs and GaAs-like LO phonons are much smaller than those of bulk GaAs or the $\text{GaAs}/\text{Al}_{0.2}\text{Ga}_{0.8}\text{As}$ SL, but is comparable to that of a GaAs/AlAs SL with $L_x = L_b = 100$ Å. Thus, N values of both GaAs and GaAs-like LO phonons in this SL are confined phononlike.

Because of the relatively low power densities ($< 10^{17}$ cm^{-3}) we used, N is much less than 1 and linear with the laser power P . Therefore, experimental errors are reduced by comparing the normalized hot-phonon generation efficiency dN/dP between SL's and bulk GaAs instead of comparing N . In Fig. 2, the normalized (to bulk GaAs) hot-phonon generation efficiency dN/dP for

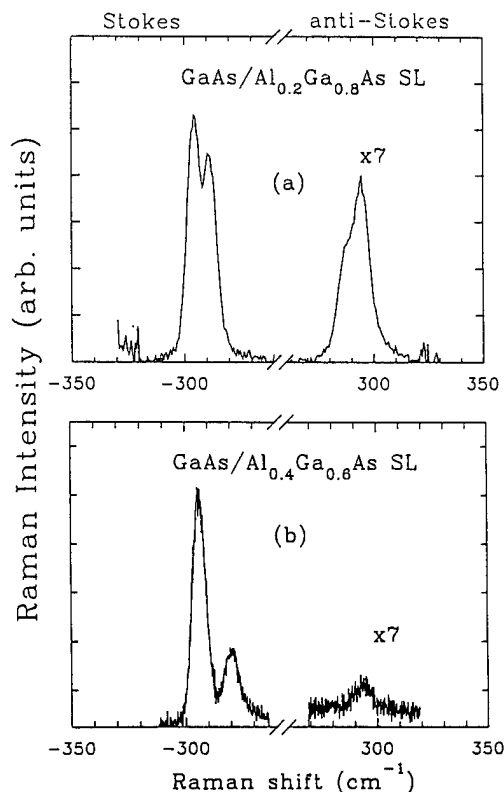


FIG. 1. The Stokes and anti-Stokes Raman spectra of GaAs and GaAs-like LO phonons (a) in a $\text{GaAs}/\text{Al}_{0.2}\text{Ga}_{0.8}\text{As}$ SL ($L_x = L_b = 70$ Å, 20 periods) sample, and (b) in a $\text{GaAs}/\text{Al}_{0.4}\text{Ga}_{0.6}\text{As}$ ($L_x = 100$ Å, $L_b = 50$ Å, 30 periods) SL. Both samples are measured under identical conditions, together with bulk GaAs.

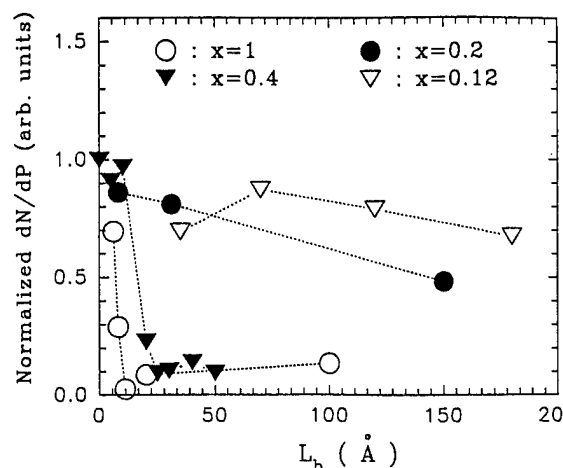


FIG. 2. Hot-phonon generation efficiency normalized to GaAs, plotted as a function of L_b for $x=1$ (empty circle), $x=0.4$ (filled inverted triangle), $x=0.2$ (filled circle), and $x=0.12$ (empty inverted triangle). Broken lines are a guide to the eye.

GaAs LO phonons of SL's are plotted against L_b for four series of SL's ($x=1, 0.4, 0.2$, and 0.12) with fixed $L_x = 100$ Å. There is a clear L_b -dependent transition from bulklike efficiencies to much smaller efficiencies in the two series with $x=0.4$ or 1 . Only bulklike efficiencies, however, are observed for all L_b 's in the two series with $x=0.2$ and 0.12 . GaAs and GaAs-like peaks are well resolved in Raman spectra up to $x=0.2$ [Fig. 1(a)], whereas it is difficult to separate them when $x=0.12$ due to the finite-band width (6 cm^{-1}) of our picosecond pulses. Therefore, dN/dP for the $x=0.12$ series should be regarded as the averaged generation efficiency of GaAs and GaAs-like modes.

For most sample parameters in Fig. 2, the normalized generation efficiency is either bulklike ($dN/dP > 0.6$) or comparable to those of GaAs/AlAs SL's ($dN/dP < 0.2$). This holds true for other series not shown here as well. Therefore, we can easily visualize our results in a parameter space of x and L_b as a phase diagram (Fig. 3), where the line is a guide to the eye, around which N (or dN/dP) changes from bulklike values to confined phononlike values, or vice versa. For comparison, the differences between the energies of GaAs LO phonons (295 cm^{-1}) and the GaAs-like LO phonons, which act as barrier heights, are indicated for several x values in the upper part of Fig. 3. It is clear that when the barrier height is smaller than ≈ 10 cm^{-1} ($x \approx 0.3$), LO phonons become bulklike, at least from the point of view of hot-phonon generation. This critical barrier height (or critical x) of ≈ 10 cm^{-1} (or $x \approx 0.3$) is in good agreement with the theoretical results of Refs. 8 and 10. Furthermore, these results are in qualitative agreement with Ref. 13, where it was found that 1 ML of AlAs can stop the propagation of GaAs LO phonons into the adjacent GaAs layer, while they propagate through $\text{Al}_x\text{Ga}_{1-x}\text{As}$ monolayers with small x 's. From these discussions, it is clear that the confined-to-propagation (or small-to-large ξ) transition of LO phonons as an explanation of our results warrants some further consideration.

It should be noted that for samples with small L_b 's (< 20 Å) in Figs. 2 and 3, the decrease in the effective x , resulting from the diffusion of Al atoms,^{19,20} might be non-negligible. Such decrease in effective x is expected to shift the phase diagram shown in Fig. 3 somewhat, without changing the overall interpretation.

In the following, we perform simple calculations that illustrate that the large increase in N as x or L_b become small can be explained, at least qualitatively, by the confined-to-propagation transition. In Fig. 4(a), a hot-phonon distribution curve at $t = 1$ ps that results from the relaxation of hot electrons in bulk GaAs excited at $t = 0$ by a δ -function pulse is shown, where the hot-phonon occupation number N_q of a phonon mode with a wave vector q is plotted against q .^{21,22} In obtaining this curve, we assumed a parabolic band with an initial excess energy of hot electrons at 500 meV. An instantaneous thermalization was assumed and the intervalley scattering into X and L valleys was included.²² All of the above assumptions or the specific values of the excess energy, electron-LO-phonon scattering times, or intervalley scattering times, can be relaxed without changing the overall hot-phonon distribution curve. This is essentially because the shape of the hot-phonon distribution curve is determined mostly by the energy-momentum conservation of electron-LO-phonon scattering (which explains the cutoff at small q) and the Fröhlich matrix element $1/q^2$ (which explains the rapid decrease in N_q with increasing q). Note that the peak of the hot-phonon distribution curve occurs nearly at $q \approx q_0$, which is the Raman-active wave vector of bulk GaAs ($\approx 9 \times 10^5 \text{ cm}^{-1}$ at the backscattering geometry with photon energy of 2.33 eV). Thus in bulk GaAs, we probe approximately the maximum occupation number of the hot-phonon distribution curve.

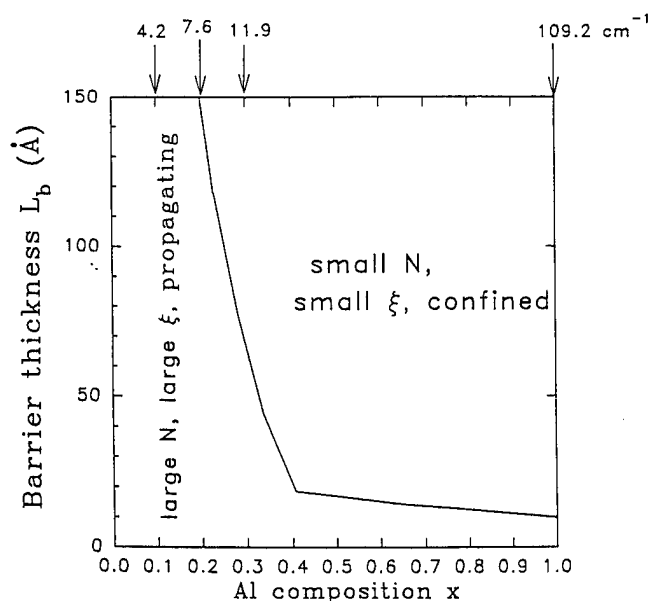


FIG. 3. A phase diagram of sample parameters x and L_b summarizing our results. The lines serve as a guide to the eye, around which N changes rather rapidly. The energy differences of GaAs and GaAs-like LO phonons are denoted as arrows for several x values on top of the figure.

We further assume that hot-electron relaxation in GaAs/ $\text{Al}_x\text{Ga}_{1-x}\text{As}$ SL's is bulklike. This drastic simplification is somewhat justified by the fact that the initial total excess energy (≈ 800 meV above the band gap) far exceeds the alloy barrier height for $0.2 < x < 0.3$ (roughly 200–300 meV). We can then easily calculate the hot-phonon occupation number of an arbitrary phonon mode simply by averaging the hot-phonon distribution curve of Fig. 4(a) weighed by the Fourier transform of the phonon wave function. We now show how phonon confinement and propagation can change the observed N . The Raman-active first confined LO-phonon mode can be represented by the following simple wave function and Fourier transform of it:

$$\Psi_c = \sin \frac{\pi z}{L_z}, \quad 0 < z < L_z, \quad (1)$$

$$|F(q)|^2 = \frac{1 + \cos(qL_z)}{\left[q^2 - \frac{\pi^2}{L_z^2}\right]^2}. \quad (2)$$

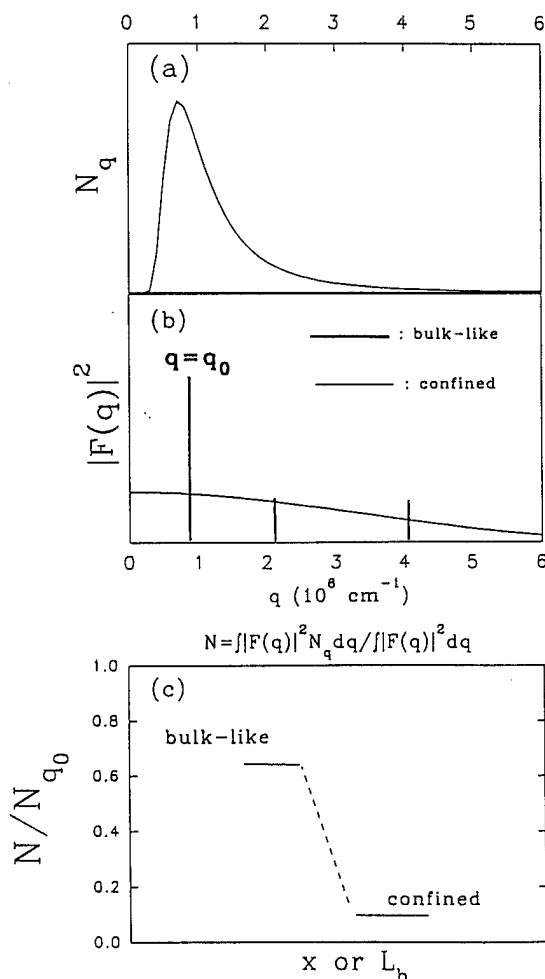


FIG. 4. (a) A hot-phonon distribution curve resulting from hot-electron relaxation in bulk GaAs calculated from Ref. 22. (b) Absolute square of the Fourier-transformed phonon wave function $|F(q)|^2$ for the Bloch wave function (thick lines) or the confined wave function [thin lines, from Eq. (2)] are shown. (c) A schematic diagram illustrating the change in N when a confined-to-propagation transition occurs, calculated from the results plotted in (a) and (b).

From Eq. (2) denoted by thin lines in Fig. 4(b) and the results of Fig. 4(a), we obtain the normalized N of 0.11 for the confined phonon of Eq. (1) [Fig. 4(c)]. Such a small N is a combined result of the relatively wide $|F(q)|^2$ of Eq. (2) resulting from small coherence length ξ of confined phonons, and the sharp decrease of N_q with increasing q . When phonons become propagating and thus can be represented by Bloch wave functions, the dominant Raman-active wave function off resonance can be represented by

$$\Psi_0 = \exp(iq_0 z)U(z). \quad (3)$$

$U(z)$ is an even, periodic function with period of $L_z + L_b$. The Fourier transform $F(q)$ of this wave function would show a dominant peak at q_0 and weaker ones at $|q_0 \pm 2\pi/(L_z + L_b)|$, $|q_0 \pm 4\pi/(L_z + L_b)|$, ..., as shown with thick lines in Fig. 4(b) for $L_z = L_b = 100$ Å. For simplicity, we assume that $|F(q)|^2$ are 1 and 0.3 for q_0 and $|q_0 \pm 2\pi/(L_z + L_b)|$, respectively, and zero for the rest of the Fourier components. The resulting N is much larger than that of the confined phonon, at 65% of the bulk value N_q ($q = q_0$). This results directly from the fact that $|F(q)|$ peaks sharply at q_0 for the Bloch wave function of Eq. (3), so that bulklike N results [Fig. 4(c)]. It should be stressed that this bulklike N is not a result of choosing specific values for $|F(q)|^2$. Rather, any Bloch wave function of Eq. (3) with an even $U(z)$ is dominated by the bulk Raman-active Fourier component $q = q_0$ and, therefore, would result in bulklike N .

The calculations shown in Fig. 4, although simplistic, illustrate that the confined-to-propagating transition of LO phonons is certainly a feasible explanation for the bulklike N observed for small x and L_b . It should be noted that to observe bulklike, large N , it is not necessary to have such a well-defined Bloch wave function of Eq. (3). Rather, any $U(z)$ whose spatial extent is larger than $\pi/q_0 \approx 330$ Å would result in bulklike N , which is self-evident from our Fourier-transform arguments. Thus bulklike or propagating in the context of hot-phonon generation is somewhat relaxed (i.e., $\xi > 330$ Å) from the perfect Bloch wave function. Our hot-phonon technique

and interpretation, compared with the theoretical and experimental cw Raman studies performed on thin SL samples,¹¹⁻¹³ provide a *complementary approach* to the problem of spatial properties of LO phonons. With its large dynamic range, which essentially stems from the rapidly changing hot-phonon distribution curve near the zone center, this technique can be particularly useful for most widely used quantum wells of ≈ 100 Å, where observation of multiple peaks is extremely difficult due to flat dispersion at the zone center.

Our phase diagram shown in Fig. 3, when interpreted as separating regions of confined or propagating LO phonons, is in good agreement with recent theoretical calculations of Colombo, Molteni, and Miglio, where a strong increase in theoretical Raman intensity for $x < 0.3$ is interpreted as the onset of propagating LO phonons.^{8,10} Diagrammatic perturbative studies of Fertig and Reinecke are also in general agreement with our results and interpretation, although a change of LO-phonon properties with x is less abrupt in their studies. Furthermore, the existence of the critical alloy concentration x (≈ 0.3) might suggest that GaAs LO phonons in these SL's propagate via percolation.²³

In conclusion, we have performed an extensive picosecond Raman-scattering study of LO phonons in GaAs/Al_xGa_{1-x}As superlattices. Large, bulklike phonon occupation numbers are observed when $x \leq 0.2$ for all sample parameters, while much smaller values of N comparable to those of GaAs/AlAs SL's are observed for $x \geq 0.3$. These results can be qualitatively explained by assuming that LO phonons undergo confined-to-propagation (or small-to-large ξ) transition around $x \approx 0.2-0.3$. Our results are in good agreement with recent theoretical investigations.

We acknowledge helpful discussions with Professor P. Y. Yu and Professor M. Cardona. This work was supported at Oklahoma State University by the Office of Naval Research. The work at Sandia was supported by the Department of Energy under Contract No. DE-AC04-94AL85000.

¹D. S. Kim and P. Y. Yu, in *Ultrafast Laser Probe Phenomena in Bulk and Microstructure Semiconductors*, edited by R. R. Alfano, SPIE Symposia Proceedings No. 1282 (SPIE, Bellingham, 1990), p. 39.

²D. S. Kim *et al.*, Phys. Rev. Lett. **68**, 1002 (1992).

³D. S. Kim *et al.*, Phys. Rev. Lett. **72**, 1572 (1994).

⁴G. S. Spencer and J. Menéndez, Phys. Rev. Lett. **72**, 1571 (1994).

⁵A. Kobayashi and A. Roy, Phys. Rev. B **35**, 2237 (1987).

⁶C. Colvard *et al.*, Phys. Rev. B **31**, 2080 (1985).

⁷H. A. Fertig and T. L. Reinecke, Phys. Rev. B **49**, 11 168 (1994).

⁸L. Colombo, C. Molteni, and L. Miglio, in *Proceedings of the 21st International Conference on the Physics of Semiconductors*, edited by P. Jiang and H. Z. Zheng (World Scientific, Singapore, 1992), pp. 777-780.

⁹F. Bechstedt *et al.*, Phys. Rev. B **47**, 13 540 (1993).

¹⁰C. Molteni, L. Colomb, L. Miglio, and G. Benedek, Phys.

Rev. B **50**, 11 684 (1994).

¹¹B. Jusserand and D. Paquet, Phys. Rev. B **30**, 6245 (1984).

¹²B. Jusserand *et al.*, Phys. Rev. Lett. **67**, 2803 (1991).

¹³B. Jusserand, D. Paquet, and F. Molloy, Phys. Rev. Lett. **63**, 2397 (1989).

¹⁴K. Huang and B. Zhu, Phys. Rev. B **38**, 13 377 (1988).

¹⁵B. K. Ridley, Phys. Rev. B **39**, 5282 (1989).

¹⁶B. Jusserand and M. Cardona, in *Light Scattering in Solids V*, edited by M. Cardona and G. Güntherodt, Topics in Applied Physics Vol. 66 (Springer, Berlin, 1989), p. 49 and references therein.

¹⁷A. K. Sood *et al.*, Phys. Rev. Lett. **54**, 2111 (1985).

¹⁸D. J. Mowbray *et al.*, Phys. Rev. B **43**, 1598 (1991).

¹⁹D. G. Deppe *et al.*, J. Appl. Phys. **64**, 1838 (1988).

²⁰B. Jusserand *et al.*, Appl. Phys. Lett. **57**, 560 (1990).

²¹C. L. Collins and P. Y. Yu, Phys. Rev. B **30**, 4501 (1984).

²²D. S. Kim and P. Y. Yu, Phys. Rev. B **43**, 4158 (1991).

²³J. Jacob *et al.*, Solid State Commun. **91**, 721 (1994).

Eu-doped CaF_2 grown on Si(100) substrates by molecular beam epitaxy

X. M. Fang, T. Chatterjee, and P. J. McCann

School of Electrical Engineering and Laboratory for Electronic Properties of Materials,
University of Oklahoma, Norman, Oklahoma 73019

W. K. Liu and M. B. Santos

Department of Physics and Astronomy and Laboratory for Electronic Properties of Materials,
University of Oklahoma, Norman, Oklahoma 73019

W. Shan and J. J. Song

Department of Physics and Center for Laser Research, Oklahoma State University, Stillwater,
Oklahoma 74078

(Received 22 May 1995; accepted for publication 23 July 1995)

Eu is incorporated into CaF_2 films grown on Si(100) by molecular beam epitaxy using elemental Eu evaporation. Eu doping as high as 4.05 at. % does not significantly degrade the surface morphology, indicating a relatively high solubility of Eu in CaF_2 . Photoluminescence spectra from Eu-doped CaF_2 show strong blue emissions from Eu^{2+} ions in cubic sites. The inhomogeneous broadening of the zero-phonon line near $24\,190\text{ cm}^{-1}$ is reduced by $\sim 20\%$ upon *in situ* annealing at 1100°C . © 1995 American Institute of Physics.

The increasing interest in the incorporation of rare-earth (RE) elements in epitaxial thin films of the alkaline-earth fluorides is motivated by potential applications in solid state microfilm or microcavity lasers. Growth of these materials on Si substrates offers potential compatibility with Si-based technology. Nd- and Er-doped CaF_2 films grown on Si substrates by molecular beam epitaxy (MBE) have exhibited strong photoluminescence at $1.04\text{ }\mu\text{m}$ and $1.54\text{ }\mu\text{m}$, respectively.¹⁻³ Eu-doped CaF_2 bulk crystals have been extensively investigated⁴⁻⁹ for use as blue emission devices since a strong fluorescence at 420 nm is observed upon UV irradiation. Although laser action in Eu-doped CaF_2 bulk crystals is hindered by excited state absorption,¹⁰ such films can be used as light emitters in multicolor thin-film electroluminescence devices.¹¹ Recently, Eu^{2+} incorporated in CaF_2 films grown on Si(111) substrates by MBE has been used as a sensitive probe of elastic strain in the heteroepitaxial layers.^{12,13} As reported, the growth of the Eu-doped CaF_2 films was carried out by sublimation of a CaF_2 single crystal containing 0.05% divalent Eu.

In this letter, we present the MBE growth of Eu-doped CaF_2 on Si(100) substrates using elemental Eu evaporation. The incorporation of Eu in epitaxial CaF_2 films was investigated by x-ray photoelectron spectroscopy (XPS), reflection high-energy electron diffraction (RHEED), and photoluminescence (PL) measurements. We demonstrate that Eu concentrations as high as 4.05 at. % do not significantly degrade the surface morphology, indicating a relatively high solubility of Eu in the CaF_2 matrix. PL spectra from Eu-doped CaF_2 show a strong blue to violet emission expected from Eu^{2+} ions in cubic sites. *In situ* post-growth annealing improves the morphology of the films and reduces the inhomogeneous broadening of the zero-phonon line of Eu^{2+} interconfiguration transitions.

Growth of Eu-doped CaF_2 on Si(100) was carried out in

an Intevac Modular GEN II MBE system with a background pressure of $\sim 10^{-10}$ Torr throughout the deposition. The 3-inch diameter *p*-type Si(100) substrates (Silicon Sense, Inc.) were cleaned using the Shiraki method.¹⁴ The passivating oxide formed during the *ex situ* cleaning procedure was thermally desorbed in the growth chamber after several minutes at $\sim 1100^\circ\text{C}$. A surface prepared in this manner exhibits no discernible oxygen or carbon traces as examined by Auger electron spectroscopy. High purity polycrystalline CaF_2 was evaporated from a graphite-coated PBN crucible at a typical growth rate of $20\text{ }\text{\AA}/\text{min}$ for a cell temperature of 1300°C . An elemental source of Eu was evaporated from a separate low-temperature effusion cell heated to $300\text{--}400^\circ\text{C}$ to give beam equivalent pressures of 3.5×10^{-10} – 1.9×10^{-8} Torr.

CaF_2 films grown on Si(100) are known to always exhibit a {111} faceted morphology because the surface energy of the $\text{CaF}_2(100)$ face is much larger than for Si(100) and $\text{CaF}_2(111)$ faces.¹⁵ However, growth morphology and crystalline quality can be improved by *in situ* annealing.^{16,17} In our experiments, a $400\text{ }\text{\AA}$ CaF_2 buffer layer, a $3600\text{ }\text{\AA}$ Eu-doped CaF_2 layer, and a $200\text{ }\text{\AA}$ CaF_2 top layer were deposited on a Si(100) substrate at 580°C . Most of the samples in this work were annealed *in situ* at 1100°C for a few minutes at the end of growth.

XPS experiments were conducted at room temperature in an adjoining analysis chamber to eliminate complications caused by exposure to the atmosphere. This chamber is equipped with a VG100AX hemispherical analyzer and a twin-anode x-ray source used in conjunction with a VGX900 data acquisition system (Fisons Instruments). XPS spectra were taken using the $\text{Al K}\alpha_{1,2}$ source ($h\nu=1486.6\text{ eV}$) at a potential of 15 kV and with 10 mA emission current. The binding energies were referenced to F 1s at 684.5 eV . RHEED patterns were produced using a Varian electron gun operated at 9.5 keV and at an angle of incidence of 1° to 3° and digitized using a CCD camera and data acquisition software developed by *k*-space Associates, Inc. Photolumines-

*Electronic mail: fang@mailhost.ecn.uoknor.edu

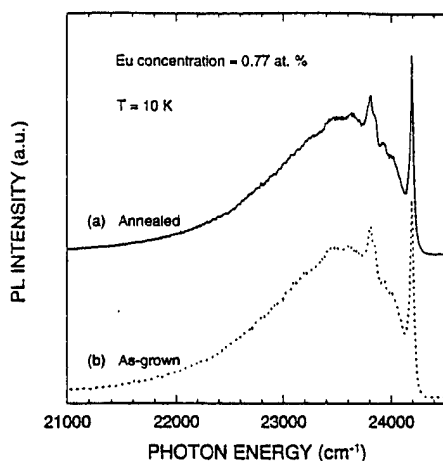


FIG. 4. PL spectra of (a) annealed at $\sim 1100^\circ\text{C}$ and (b) as-grown Eu-doped CaF_2 films grown under the same conditions and with the same Eu concentration of ~ 0.77 at. %. The full widths at half-maximum of the zero-phonon lines are 38 cm^{-1} and 46 cm^{-1} , respectively. Both films are $\sim 4200\text{ \AA}$ thick. Both spectra were taken at 10 K .

cates a smooth surface.¹⁷ While *in situ* annealing improves the growth morphology by smoothing out the $\{111\}$ facets on the surface,¹⁷ it does not alleviate the morphological features attributed to Eu precipitation.

Figure 4(a) shows the PL spectrum of a CaF_2 film with a Eu concentration of ~ 0.77 at. %. A sharp zero-phonon line near 24190 cm^{-1} accompanies a broad vibronic sideband peaking at about 23500 cm^{-1} . This spectrum is very similar to the fluorescence spectra of Eu^{2+} ions in CaF_2 bulk crystals reported previously.^{5,8} The zero-phonon line shown in Fig. 4(a) arises from the electronic transition from the lowest lying $\Gamma_8(4f^65d)$ level of Eu^{2+} to the $^8S_{7/2}(4f^7)$ ground state. The peaks between the vibronic sideband maximum and the zero-phonon line are associated with the density of states maxima of various optical and acoustic phonons. All our samples, grown with various Eu concentrations, exhibit the spectral features shown in Fig. 4(a). No emission indicative of a $^5D_0 \rightarrow ^7F_J$ Eu^{3+} transition was observed in the entire scanned range of $15000\text{--}25000\text{ cm}^{-1}$.

Our PL data demonstrate the predominance of Eu^{2+} ions in cubic symmetry sites of CaF_2 single crystal films prepared by MBE. This differs from previous reports on the preparation of Eu-doped CaF_2 bulk crystals^{6,9} using the Bridgman-Stockbarger technique, where a small amount of Eu mixed with CaF_2 in an excess of fluorine resulted in predominately Eu^{3+} ions in cubic or other lower symmetry sites. Chemical or irradiation reduction processes are required to convert the Eu ions in the bulk crystals from trivalent states to divalent states. Our results suggest that interstitial F^- ions, substitutional O^{2-} ions, or other charged species which are necessary to compensate the additional positive charge of Eu^{3+} in CaF_2 bulk crystals are absent in the MBE-grown Eu-doped CaF_2 films. No excess F^- ions are available because our experiments employ molecular CaF_2 and elemental Eu beams provided by sublimation of CaF_2 and Eu sources in a low background pressure environment. In Nd-doped CaF_2 samples prepared by MBE,¹ NdF_3 was intentionally selected to provide excess F^- ions to enable substitution of Nd^{3+} ions for divalent cations in the CaF_2 matrix. These results imply

that the valence states of RE elements in fluorides can be controlled by using different RE dopant species.

To illustrate the effect of *in situ* annealing on the PL efficiency of Eu^{2+} ions in epitaxial CaF_2 films, the PL spectra of annealed and as-grown films with the same growth conditions and Eu concentration are shown in Figs. 4(a) and 4(b), respectively. The peak intensity of the zero-phonon line remains nearly the same while the line width is narrowed by $\sim 20\%$ and the integral intensity of the vibronic sideband is reduced by $\sim 13\%$ upon annealing. It is evident that *in situ* annealing, which significantly improves the growth morphology, causes only minor changes in the PL efficiency of Eu^{2+} . The insensitivity of the optical activity of Eu^{2+} to *in situ* annealing at temperatures as high as 1100°C suggests that most of the Eu ions entering the CaF_2 matrix are already located substitutionally in divalent cation sites during growth at 580°C . The reduced broadening of the zero-phonon line may result from embedded Eu ions moving closer to their equivalent positions upon annealing.

In summary, the growth of Eu-doped CaF_2 thin films on Si(100) has been realized by MBE using an elemental Eu source and a substrate temperature of 580°C . Good surface morphology is observed in samples with Eu concentration as high as 4.05 at. %. Photoluminescence spectra from these samples show strong blue emissions attributed to Eu^{2+} ions in cubic sites. *In situ* annealing at $\sim 1100^\circ\text{C}$ reduces the inhomogeneous broadening of the zero-phonon line and significantly improves the growth morphology without dramatically changing the PL efficiency of Eu^{2+} ions.

We thank Joel Young for technical support with the MBE laboratory. This work was partially supported by the National Science Foundation through grant number OSR-9108771.

¹L. E. Bausá, R. Legros, and A. Muñoz-Yagüe, *Appl. Phys. Lett.* **59**, 152 (1991).

²C. C. Cho, W. M. Duncan, T. H. Lin, and S. K. Fan, *Appl. Phys. Lett.* **61**, 1757 (1992).

³E. Daran, R. Legros, A. Muñoz-Yagüe, C. Fontaine, and L. E. Bausá, *J. Appl. Phys.* **76**, 270 (1994).

⁴A. A. Kapiyanskii and P. P. Feofilov, *Opt. Spectrosc. (USSR)* **13**, 129 (1961).

⁵M. V. Hobden, *Phys. Lett.* **15**, 10 (1965).

⁶J. L. Merz and P. S. Pershan, *Phys. Rev.* **161**, 217 (1967).

⁷E. Loh, *Phys. Rev.* **184**, 348 (1969).

⁸L. L. Chase, *Phys. Rev. B* **2**, 2308 (1970).

⁹R. J. Hamers, J. R. Wietfeldt, and J. C. Wright, *J. Chem. Phys.* **77**, 683 (1982).

¹⁰J. F. Owen, P. B. Dorain, and T. Kobayasi, *J. Appl. Phys.* **52**, 1216 (1981).

¹¹T. Suyama, K. Okamoto, and Y. Hamakawa, *Appl. Phys. Lett.* **41**, 462 (1982).

¹²N. S. Sokolov, E. Virgilio, S. V. Gastev, S. V. Novikov, and N. L. Yakovlev, *Sov. Phys. Solid State* **31**, 216 (1989).

¹³N. S. Sokolov, N. L. Yakovlev, and J. Almeida, *Solid State Commun.* **76**, 883 (1990).

¹⁴A. Ishizaka and Y. Shiraki, *J. Electrochem. Soc.* **133**, 666 (1986).

¹⁵L. J. Schowalter and R. W. Fathauer, *CRC Crit. Rev. Solid State Mater. Sci.* **15**, 367 (1989).

¹⁶T. Asano, H. Ishiura, and S. Furukawa, *Jpn. J. Appl. Phys.* **27**, 1193 (1988).

¹⁷X. M. Fang, P. J. McCann, and W. K. Liu (unpublished).